UNIVERSITY OF TRENTO
DEPARTMENT OF PHYSICS

Time-resolved optical diagnostics for plasma dissociation of CO_2

Author: Matteo Ceppelli

Tutor: Prof. Paolo Tosi

XXXIV PhD cycle

List of publications

[1] G. Dilecce, L. M. Martini, M. Ceppelli, M. Scotoni, and P. Tosi, "Progress on laser induced fluorescence in a collisional environment: the case of OH molecules in ns pulsed discharges," *Plasma Sources Science and Technology*, vol. 28, p. 025012, 2019

[2] M. Ceppelli, L. M. Martini, G. Dilecce, M. Scotoni, and P. Tosi, "Non-thermal rate constants of quenching and vibrational relaxation in the $\mathrm{OH}(\mathrm{A}^2\Sigma^+, \nu' = 0, 1)$ manifold," *Plasma Sources Science and Technology*, vol. 29, p. 065019, 2020

[3] M. Ceppelli, T. P. W. Salden, L. M. Martini, G. Dilecce, and P. Tosi, "Time-resolved optical emission spectroscopy in nanosecond pulsed discharges," *Plasma Sources Science and Technology*, vol. 30, p. 115010, 2021

[4] M. Budde, L. M. Martini, M. Ceppelli, S. Quercetti. and R. Engeln, "Absolute OH density measurements in a $\mathrm{CO_2} + \mathrm{H_2O}$ glow discharge by laser-induced fluorescence spectroscopy," *submitted to Plasma Sources Science and Technology*, 2022.

Contents

Chapter 1

Introduction

The environmental issue is one of the most crucial problems that humanity needs to face. It includes undertaking drastic measures against environmental degradation, depletion of resources, pollution, climate change, global warming, and many others. The intensive exploitation of fossil fuels gave rise to unprecedented opportunities for humanity in the past two centuries, though often at the expense of the environmental health. Their consumption, in fact, releases vast amounts of heat-trapping species such as carbon dioxide, methane, nitrous oxide, and many others (greenhouse gases). The anthropogenic role in global warming is unequivocal: in its Fifth Assessment Report, dated 2014, the Intergovernmental Panel on Climate Change of the United Nations concluded that there is more than a 95% *probability that human activities have warmed our planet over the past* 50 *years. The only way to mitigate the consequences of the greenhouse effect is by reducing the greenhouse gases in the atmosphere, and ultimately replacing fossil fuels with alternative sources of energy. Direct exploitation of renewable energy sources (RES) cannot represent the definitive solution to the energy task due to limitations of these resources and the existing infrastructures. The storage of renewable energies must then be privileged. In this context, renewable energy could be harvested in the form of portable energy carriers such as liquid carbonaceous fuels or hydrogen, to be used as alternative to fossil fuels or batteries. A promising application is the synthesis of hydrocarbons from captured* $\mathrm{CO_2}$ *and hydrogen (produced by water electrolysis), which has the twofold advantage of simultaneously tackling the greenhouse gases issue and the storage or RES. In this context, non-thermal plasmas (NTPs) are a promising technology that provides an attractive solution for the efficient conversion of* $\mathrm{CO_2}$*, as plasmas have the potential to enable thermodynamically unfavorable chemical reactions at ambient temperature. By suitably 'tailoring' the plasma conditions, the*

energy supplied to the system can be channeled into individual dissociation mechanism of CO_2*, with possible enhancement of the conversion efficiency.*

1.1 Global warming

Ever since the Industrial Revolution, the large-scale exploitation of fossil fuels has ensured easily-accessible energy supply, enduring boost to the economy, and unprecedented wealth to many people. Despite tangible pros in terms of cost and transportation, fossil fuels are acknowledged to cause severe damage to the environment and the health of living species at every stage in their use, with negative repercussions that include land use, air pollution, acid rains, and many others.

Among the consequences of the intensive use of fossil fuels, *global warming* is by far the most evident, since the signs of a changing climate have now more than ever shown up in our everyday life. Global warming appears as an unusually rapid increase in the Earth's average surface temperature, albeit its impact is far more significant than just increasing temperatures. Warming, in fact, modifies rainfall patterns, amplifies coastal erosion, lengthens the growing season in some regions, melts ice caps and glaciers, determines extreme weather events, and even more.

Greenhouse gases (GHGs) Global warming is driven by the release of *greenhouse gases* (GHGs) such as CO_2, CH_4, N_2O, and CFCs, primarily due to anthropogenic activities. The bulk of these emissions is attributable to the combustion of fossil fuels, although also deforestation and changes in land use play a role. Carbon dioxide is the most vilified greenhouse gas, followed by methane and nitrous oxide. Because natural processes only partially compensate these emissions (mostly through absorption by the oceans), a net increase of many billion tons of atmospheric GHGs is observed year by year [1]. Today's levels of GHGs are higher than at any time in the past 800 thousand years, with annual rates of increase being now 100 times faster than natural fluctuations over the past geological eras. Atmospheric levels of CO_2 are estimated to be increased from 280 ppm at the beginning of the industrial age to 417 ppm at the end of 2021 [2] (figure 1.1). Similarly, CH_4 and N_2O concentrations have continued to increase in the atmosphere since pre-industrial values, respectively [3].

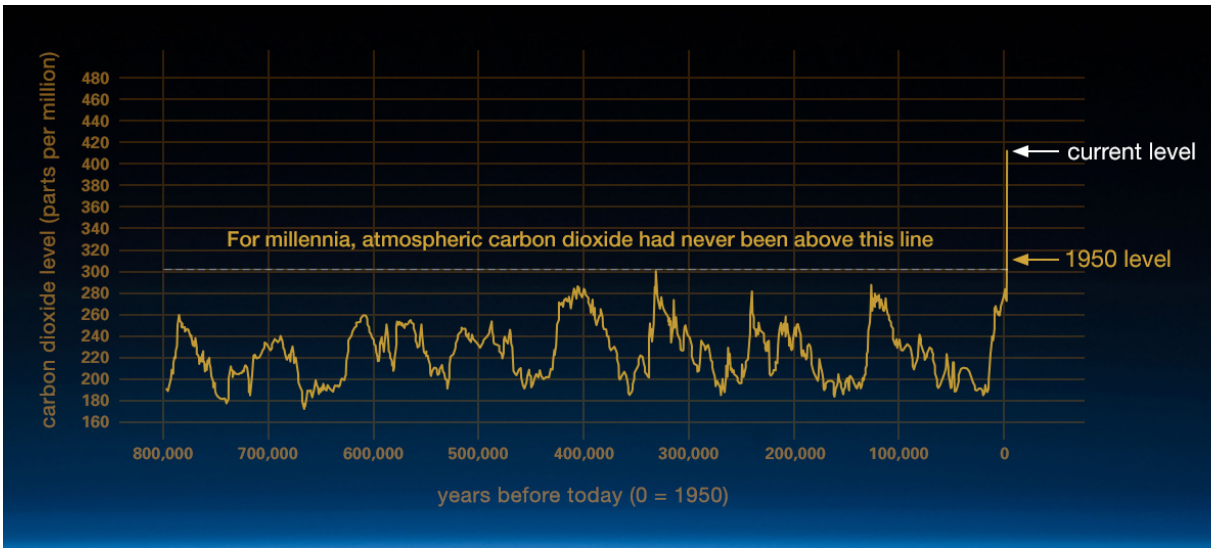

FIGURE 1.1: *Average CO_2 concentration in the mid-troposphere based on the comparison of atmospheric samples contained in ancient ice cores and more recent direct measurements. Figure reported from [2].*

The build-up of GHGs is believed to contribute to global warming through the *greenhouse effect*, as these gases increase *radiative forcing*. Radiative forcing, employed to characterize an externally-imposed perturbation in the total radiative energy balance of the Earth, quantifies the warming influence of each anthropogenic greenhouse gas as a combination of species abundance, lifetime in the atmosphere, and absorbance of IR radiation. At present, the five major greenhouse gases (CO_2, CH_4, N_2O, $CFC-12$ and $CFC-11$) account for about 96% of the total radiative forcing, with CO_2 alone being responsible for about two-thirds of the whole energy imbalance that is causing the Earth's temperature to rise [4].

Based on plausible emission scenarios, the average surface temperatures is expected to rise by at least $2°C$ by the end of the century [2], with severe consequences for the survival of living species. It should be noted that the Earth's climate has changed throughout history, with several cycles of glacial advance and retreat attributable to small variations of the solar activity or slight wobbles in Earth's orbit around the Sun. The current warming trend, however, is of particular significance because it proceeds at a rate that is unprecedented over millennia, and with the unequivocal contribution of human actions.

1.2 The energy challenge

The only way to mitigate the consequences of the greenhouse effect is to prioritize the reduction of the emission of GHGs and, ultimately, the replacement of fossil fuels with alternative sources of energy. Although a general awareness of the harmfulness of GHGs has now been reached, a transition towards alternative and 'carbon-free' energy resources struggles to catch on, as it competes with fossil fuels' cheapness, availability, and thermochemical superiority. In fact, even with marked regional differences at the global level, fossil fuels still sustain the most significant energy demand, accounting in 2020 for a share of about 83% of the global primary energy consumption [5] (table 1.1).

	global	**EU**	**China**	**US**
oil	31	36	20	37
coal	27	11	57	10.5
natural gas	25	25	8.2	34
nuclear	4.3	11	2.2	8.4
hydro	6.9	5.5	8.1	2.9
renewables	5.7	13	5.4	7

	global 2009 − 19
oil	$+1.4$
coal	$+0.9$
natural gas	$+2.9$
nuclear	-0.2
hydro	$+2.1$
renewables	$+13$

TABLE 1.1: *left: Shares of world/EU/China/US primary energy in 2020 (values in %). right: percentage growth rates of global primary energy over the period 2009-2019 (right). Data reported from [5].*

In the view of limiting the effects of global warming, governments all over the world have committed to emissions reduction targets as part of the 2015 Paris Agreement, with the long-term goal of keeping the rise in mean global temperature to well below $2°C$ above the pre-industrial levels. The agreement imposes significant efforts aimed at replacing fossil fuels with renewable energy sources, increasing energy efficiency, and electrifying sectors such as transportation and buildings.

Renewable energy sources (RES) For an energy source to be considered renewable, it must be classified as a naturally-replenishing resource that produces little to zero GHGs emissions. Ultimately provided by the Sun, renewable energy sources are available on the Earth in different forms, most notably sunlight, wind, and water. With

an annual potential of solar energy of about $173000\ \mathrm{TW}$ [6], roughly 10000 times the current primary energy consumption of $18\ \mathrm{TW}$ (2019) [7], we could power our entire society with solar energy. However, even if steadily increasing, RES still sustain less than 15% of the world's energy consumption, primarily due to the costs associated with their large-scale exploitation and the lack of suitable infrastructures.

As research is committed to finding new ways and technologies to produce cleaner and cheaper sustainable electricity, it has become clear that RES are not the definitive solution to the energy issue, as their exploitation exhibits some limitations, notably:

- low energy density, which results in large land consumption. For example, a typical photovoltaic (PV) facility in Italy yields to a production of approximately $150\ \frac{\mathrm{kWh}}{\mathrm{m}^2}$, compared with an electricity demand of about $300\ \mathrm{TWh}$ (2021). Once subtracted the $47\ \mathrm{TWh}$ generated by hydro plants, if PV was to supply the remaining $253\ \mathrm{TWh}$, a surface of about $1700\ \mathrm{km}^2$ would be needed, almost five times the surface of Lake Garda. A similar consideration can be made for wind power generation, as typical wind farms production does not exceed $2-5\ \frac{\mathrm{W}}{\mathrm{m}^2}$, depending on the wind speed;

- unpredictability and temporal intermittency over the daily and annual cycles, which makes a large-scale integration with the power grid challenging due to load matching;

- spatial inhomogeneity, which poses issues in terms of energy transportation;

Energy storage Although RES are potentially in the position to replace completely the use of fossil fuels, the drawbacks mentioned above represent the main obstacles to their massive exploitation. The efficient storage of renewable electricity must then be the way to decouple the supply and demand of energy, as the energy excess can be returned to the grid when production falls below consumption. At present, the storage of (renewable) electric energy is arguably the bottleneck limiting the growth of an infrastructure for the production and utilization of green electricity, which justifies the considerable scientific interest in this field.

Energy storage comes in multiple forms: batteries, pumped hydroelectricity, thermal storage, water electrolysis for hydrogen production, and chemical synthesis (chemical storage). In this context, it has become increasingly more evident that no single

technology will be decisive and universal for all applications, but rather specific solutions to each sector. Energy density is a crucial consideration, particularly in mobile systems such as transportation and aviation, although storage efficiency must also be considered. When possible, direct electrification from decarbonized sources must be privileged, on account of its cheapness, efficiency and well-established technologies. However, there are sectors and applications where direct electrification faces limits that can be overcome by alternative strategies (long-distance aviation, feedstock demand in the chemical industry, primary steelmaking,..).

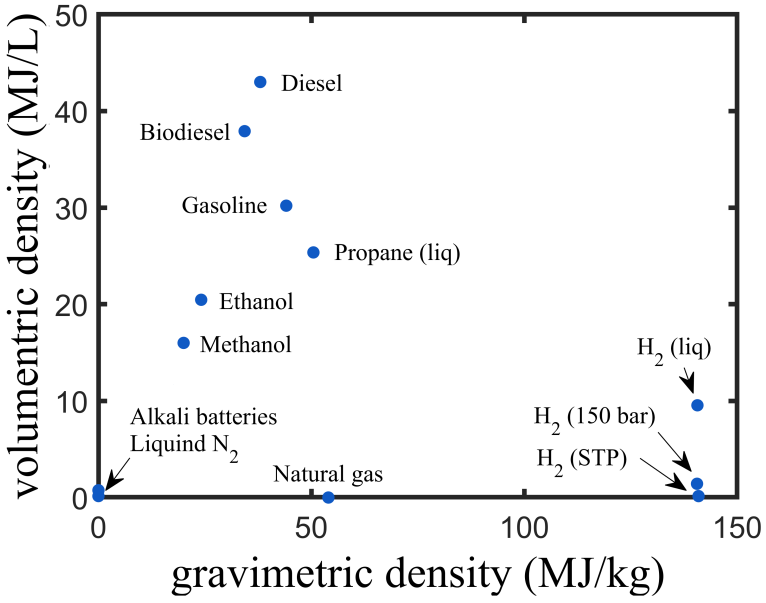

FIGURE 1.2: *Volumetric and gravimetric density of various energy vectors.*

Power-to-chemicals Hydrogen is a potential candidate for the synthesis of carbon-free energy feedstocks, to be employed in the decarbonization of economic sectors which are hard to electrify. Among all production mechanisms [8], the electrolysis of water

$$2H_2O\ (l) \longrightarrow 2H_2\ (g) + O_2\ (g) \tag{1.1}$$

ensures complete sustainable conditions, provided that it is powered by renewable energy sources. Synthetic hydrogen can be used in fuel cells for local electricity generation, offering synergy with unpredictable and intermittent power generation characteristics of RES. Despite its potentialities, several factors prevent the creation of a

large-scale *hydrogen economy*, such as the high reactivity with oxygen in ambient air, the high costs associated with H_2 production, the difficulty of developing long-term storage technologies, and the inadequacy of the existing infrastructures. Due to unfavorable volumetric density (figure 1.2), the use of H_2 is currently limited to those applications in which the volume to mass ratio of the fuel needs to be kept low (aerospace, for instance) or in industrial processes for the production of ammonia and petroleum refining. For a hydrogen energy system, the overall production efficiency is given by the product of the electrolysis efficiency ($\sim 70\%$), the storage efficiency, and the engine efficiency (for fuel cells: $\sim 40 - 60\%$). The number of processes make it difficult to compete for efficiency. To maximize its volumetric energy density, H_2 is commonly compressed or liquefied, at the expense of the overall cost of production.

Nobel Prize George Olah discussed a smart alternative to the hydrogen economy in a seminal paper [9], i.e., the use of renewable electrical power to drive endothermic reactions for the synthesis of liquid carbonaceous chemicals, the so-called *solar fuels*, or *e-fuels*. Typical examples are methanol, ethanol, ammonia, synthetic gasoline, and many others. E-fuels exhibit clear advantages over other energy vectors in terms of compatibility with the existing distribution infrastructures, scalability, and high energy density. Thus, they are particularly suitable for applications such as aviation and transportation. Moreover, they can be produced and stored for later use, when sunlight or wind are not available, in alternative to fossil fuels and batteries. As a term of comparison, typical lithium-ion batteries can reach energy densities ranging from $0.6\ \frac{\mathrm{MJ}}{\mathrm{kg}}$ to $0.9\ \frac{\mathrm{MJ}}{\mathrm{kg}}$, definitely more modest than the energy density of diesel ($\sim 42\ \frac{\mathrm{MJ}}{\mathrm{kg}}$), methanol ($\sim 20\ \frac{\mathrm{MJ}}{\mathrm{kg}}$), or gasoline ($\sim 45\ \frac{\mathrm{MJ}}{\mathrm{kg}}$) (figure 1.2). By exploiting the vast wind and solar potentials of the global sun-belt countries, e-fuels can be globally traded and resolve the geographical mismatch between renewable production and energy demand. However, it should be remarked that the total efficiency is often not competitive with other strategies due to several conversion stages during the overall synthesis process.

A view to the future The synthesis of solar fuels would be even more beneficial if the carbon source were provided by captured CO_2, as this would simultaneously tackle the GHGs issue and energy storage. It should be mentioned, however, that in these cases, the synthesized e-fuels are not rigorously 'carbon free', but more appropriately 'carbon neutral', as their consumption releases previously-captured CO_2 back into the

atmosphere. By *Carbon Capture and Utilization* (CCU), one usually denotes the process of capturing carbon dioxide before it enters the atmosphere, with the aim to store or convert it into an energy source. To achieve it, first CO_2 has to be efficiently captured from natural and anthropogenic sources. As more than half of CO_2 emissions result from small dispersed sources (buildings, heating systems, vehicles,..), the collection of CO_2 often assumes economically-prohibitive costs. Similarly, due to the low CO_2 concentration in the air, its efficient and economic capture from the atmosphere remains a challenge. Far more efficient is the collection from concentrated sources such as fuel-burning power plants or cement and aluminum factories. An extensive review of CO_2 capture methods is given in [9].

The hydrogenation of CO_2 is a potential candidate for the sustainable production of value-added hydrocarbons via the synthesis of methanol, which is the precursor of several chemicals through the Fischer-Tropsch process

$$CO_2 + 3H_2 \longrightarrow CH_3OH + H_2O \qquad \Delta H^0 = -53 \text{ kJ mol}^{-1} \tag{1.2}$$

Liquid methanol exhibits clear advantages in terms of handability of the product and its usability, as it is a well-suited fuel for internal combustion engines operation. Furthermore, reaction (1.2) achieves complete sustainability if hydrogen can be obtained by water electrolysis through renewable energy, albeit direct reforming from fossil fuels is also possible [9]. The overall process is limited by the hydrogen production stage, which poses the issue of large-scale utilization of this technology. Water formation also limits the overall efficiency, as one third of the reacting H_2 is wasted into H_2O. To overcome the high energy costs, contemporary commercial CO_2-to-methanol recycling plants use intense localized energy sources, as in Iceland, where the large availability of geothermal energy makes thermal hydrogenation convenient [10].

1.3 Non-thermal plasmas for CO_2 recycling

In the scenario of CCU, plasma conversion of CO_2 through electrical discharges is an interesting application that offers excellent potentialities for further developments. Renewable electricity can be used to sustain a plasma in which highly non-equilibrium conditions are achieved, often referred to as *non-thermal plasma* (NTP). Unlike thermochemical processes, where energy is supplied as heat and all the molecular degrees of

freedom are equally excited, non-equilibrium conditions allow in principle to induce efficient chemistry at low temperatures, as the energy can be better channeled into the dissociation of CO_2 than in its heating. Besides this crucial property, NTPs are systems with excellent scalability.

1.3.1 Non-equilibrium in plasmas

Equilibrium is an axiomatic concept of thermodynamics describing a condition in which no net flows of matter and energy occur in a physical system. When equilibrium is established, a spatially uniform temperature can be defined as the average energy of the individual degrees of freedom making up the system. Equilibrium is a stationary concept, independent of the time taken by the system to reach it, such that the addition of an energy input calls for the introduction of a kinetic point of view [11]:

- if the rate of energy input is lower than the rate of energy redistribution among all the degrees of freedom, the concept of equilibrium is preserved. More appropriately, a condition of 'quasi-equilibrium' is established in this case;
- if the reverse situation occurs, non-equilibrium is reached and a single temperature ceases to be descriptive for the whole system. An energy (or temperature) hierarchy among the degrees of freedom is established.

In the CO_2 plasmolysis, marked non-equilibrium conditions can be achieved by increasing the energy input rate or decreasing the energy transfer rates by keeping the operating pressure low. With little oversimplification, the energy of the electric field sustaining the plasma is first delivered to the free electrons. The validity of this statement is based on the small mass ratio of the electron and the heavy particles: $\frac{m_e}{m_h} \ll 1$. Once gained by the electrons, energy is transferred to the gas molecules by collisions. Several processes may be induced, depending on the electron energy (figure 1.3). At low electron energies ($\ll 1$ eV), due, again, to the small mass ratio of the colliders, the prevalent elastic collisions do not cause significant energy losses. Consequently, the electrons gain energy up to the inelastic processes thresholds ($T_e \lesssim 1$ eV) while neutrals and ions remain thermalized at room temperature. At these thresholds, electrons can transfer their translational energy efficiently to vibrational and electronic excitations, as well to ionization and dissociation of CO_2. Producing a sufficient population

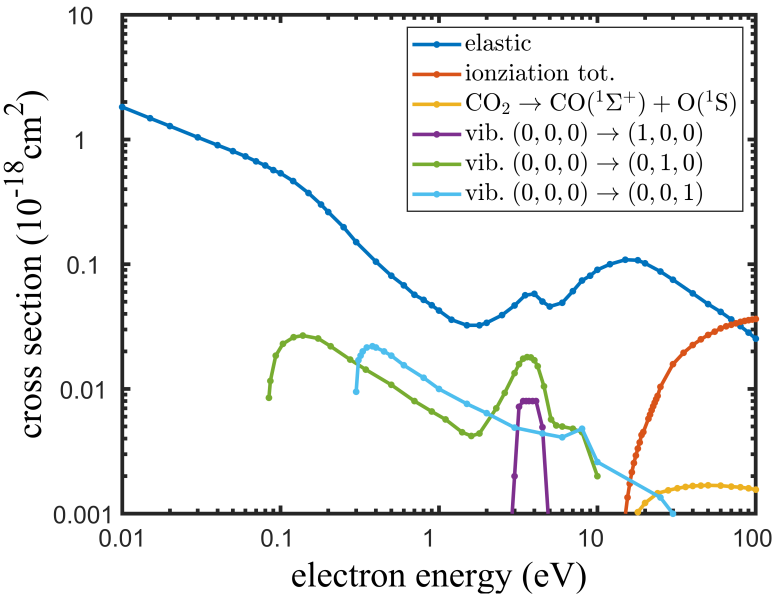

FIGURE 1.3: *Electron collision cross sections for* CO_2*. Data reported from [12] and [13].*

of excited states leads to further energy-transfers between heavy species, with most of the gas heating being generated by the de-excitation of bound states via VT (vibration-to-translation) relaxations.

In summary, the energy of the electric field is primarily given to the electrons, maintaining the kinetic energy of heavy particles low, and so the temperature of the gas. Because the energy is not equally distributed across all the species and their degrees of freedom, it is customary to refer to these systems as *non-equilibrium plasmas* (NEP), or *cold plasmas*. A common way to visualize this condition is by introducing a temperature hierarchy between the degrees of freedom [11]

$$\mathrm{T_e} > \mathrm{T_{vib}} > \mathrm{T_h} \sim \mathrm{T_{rot}} \sim \mathrm{T_{gas}} \tag{1.3}$$

Typical orders of magnitude are: $\mathrm{T_e} \sim 10^4 - 10^5$ K, $\mathrm{T_{vib}} \sim 10^3 - 10^4$ K, $\mathrm{T_{gas}} \sim 300$ K. However, conditions (1.3) should be regarded as indicative of a more detailed description of the system, as the definition of temperature gains a meaning only at equilibrium. Actually, only rotational and kinetic distributions of heavy particles can be described by a temperature. At non-equilibrium, the electron kinetics is rigorously determined by solving the Boltzmann equation (BE), which yields to non-Maxwell electron and vibrational distribution functions. A description of the possible non-

Maxwellian solutions of the BE in non-equilibrium plasmas is found in [11].

1.3.2 Investigation of NTP for CO_2 dissociation

The conversion of CO_2 to CO and O_2 has attracted increasing interest as CO is a crucial chemical feedstock for the synthesis of a range of fuels and chemicals [14] [15]. The major challenge of converting CO_2 is in overcoming its high stability

$$CO_2 \rightarrow CO + O \qquad \Delta H = 5.5 \text{ eV} \cdot \text{molecule}^{-1} \tag{1.4}$$

as the overall process is thermodynamically unfavored. Figure 1.4 shows the fraction of electron energy transferred to the different channels of the excitation, ionization and dissociation of CO_2 as a function of the reduced electric field E/N. The occurrence of

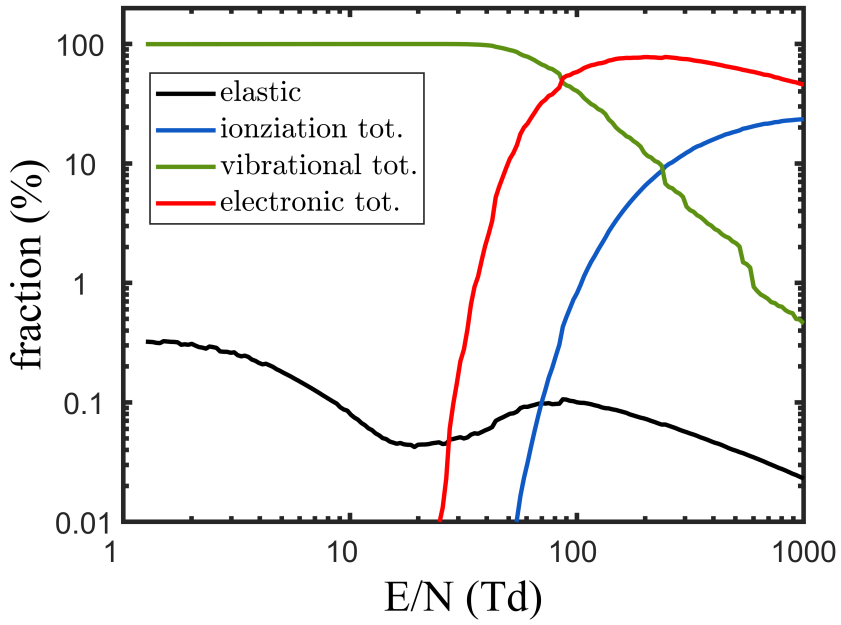

FIGURE 1.4: *Fraction of electron energy transferred to different channels of excitation of* CO_2 *as a function of the reduced electric field. Data reported from [13].*

different discharge conditions through different reduced fields has a significant impact on the electron energy distribution. At low E/N (i.e. at low T_e), electron energy is primarily delivered to vibrational degrees of freedom of the molecule, whereas electronic excitation is favored at higher E/N (high T_e) values. Two different dissociation

mechanisms can then be identified:

$$\mathrm{CO_2 + e \longrightarrow CO + O + e} \tag{1.5}$$

$$\mathrm{CO_2 + e \longrightarrow CO_2(\nu > 0) + e} \overset{\text{collisions}}{\longrightarrow} \mathrm{CO + O + e} \tag{1.6}$$

Process (1.5) proceeds via excitation to electronic states with energy $\gtrsim 7.5\ \mathrm{eV}$ through a predissociative state, a bound state crossing a dissociative state, or a bound state relaxing to one of the previous kinds. One such condition is illustrated in figure 1.5. It should be noted that in this case the transferred energy can substantially exceed the $\mathrm{CO_2}$ bond energy of about $5.5\ \mathrm{eV}$, thus limiting the overall efficiency. Process (1.6) can

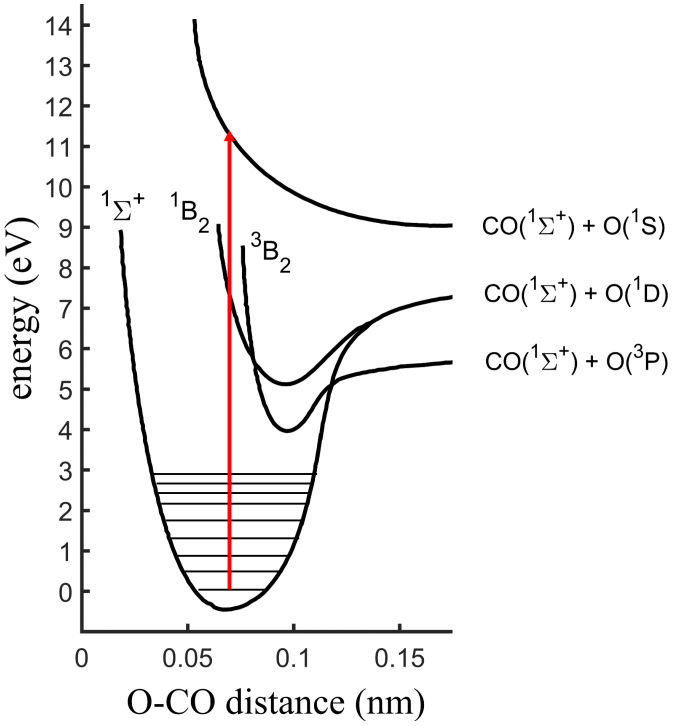

FIGURE 1.5: *Potential energy curve of* $\mathrm{CO_2}$. *Figure freely reported from [16].*

achieve higher efficiencies, as the energy is transferred from the bottom of the potential well to higher vibrational states with successive energy quanta addition till the dissociation limit is reached. This mechanism, often termed *vibrational ladder climbing*, requires two conditions to occur at the same time: an excitation source that populates higher vibrational levels ν of $\mathrm{CO_2}$, usually electron impact, and an energy-transfer process that

allows for gradual climb of the vibrational ladder, i.e., electron impact or vibration-to-vibration (VV) energy- transfers. The latter, in particular, is regulated by a positive energy balance due to the anharmonicity of the potential well.

It follows that different discharge conditions can be exploited to activate individual dissociation mechanisms selectively. For example, a successful strategy for an enhanced role of the vibrational mechanism (1.6) requires 'low' electron temperatures ($\mathrm{T_e} \sim 1 - 2\ \mathrm{eV}$) and a minimal contribution from VT relaxations obtained by reducing the gas temperature. A 'tailoring' of the discharge conditions calls for deep knowledge of the plasma. Macroscopic properties of NTPs such as energy input and gas composition are often insufficient for a complete characterization of the plasma, as the local values of physical observables (e.g. pressure, temperature, electron density,..) can have a decisive role in determining the overall kinetics of the process. In most cases, NTPs exhibit marked spatial and temporal inhomogeneities due to fast pulsing schemes or the discharge morphology.

The complete understanding of the $\mathrm{CO_2}$ dissociation requires dedicated and non-invasive diagnostics suited for the high inhomogeneity and fast transient nature of the plasma discharge. In this regard, only diagnostic methods that operate on timescales that match the plasma kinetics should be employed. This criterion rules out standard analytical techniques such as gas chromatography or mass spectrometrfy since they can only access the long-term products of $\mathrm{CO_2}$ dissociation. Conversely, time-resolved optical diagnostic methods monitor the discharge environment with high spatial and temporal resolution in a non-intrusive way.

A variety of optical diagnostic techniques has been developed in the field of plasma physics/chemistry. In this thesis, Laser-Induced Fluorescence (chapters 2-3) spectroscopy and Time-resolved Optical Emission Spectroscopy (chapter 4) are presented.

Chapter 2

Laser-Induced Fluorescence Spectroscopy

The investigation of non-equilibrium discharge plasmas requires reliable diagnostic methods that can account for their inhomogeneity and transient nature. Laser-Induced Fluorescence (LIF) spectroscopy is a technique suited to extract information from these systems, and it is nowadays widely used for the detection of short-lived intermediate species, trace elements and radicals in many highly 'hostile' environments. LIF diagnostics combines time and space resolution, sensitivity, and selectivity, making it preferable to other techniques such as absorption spectroscopy. In this thesis, LIF is applied to the hydroxyl radical OH*, which can be used as a probe molecule for variations of the gas discharge composition. When dealing with LIF, fluorescence from a laser-prepared state of the probed molecule is the observable. The observed signal comprises information on both the radiating molecule* OH *and the collisional environment around it, since the fluorescence intensity and spectral features are defined by the concurrent role of radiative and collisional processes, which are species-dependent. Collisional processes, although detrimental for the fluorescence quantum yield and the mathematical description of the LIF process, can provide information on the environment in which* OH *molecules are embedded, provided that quantitative knowledge of the relevant collisional rate coefficients is available. In this chapter, the fundamentals of LIF, as well as its features as a diagnostic tool, are presented. The impact of collisional processes on LIF outcomes is also analysed and compared to the collisionless case. At the end of the chapter, the Collisional energy-transfer-LIF (CET-LIF) method is introduced as a promising novel methodology to determine the composition of simple mixtures using LIF spectroscopy and available data on energy-transfer mechanisms.*

2.1 LIF fundamentals

Although the earliest observations of fluorescence date back to the XVI and XVII centuries, complete understanding of the phenomenon has been achieved in the past ten decades. Acknowledged as the pioneer of modern optical spectroscopy, Robert Wood, in 1905, reported on the spectral features of the fluorescence spectrum generated by a lamp-excited sodium vapor sample [17]. This and similar works paved the way to systematic studies on molecular spectroscopy and photochemistry, which successively experienced a significant boost with the advent of lasers in 1960. The selective preparation of atomic and molecular excited states made possible by laser radiation led to rudimentary experiments on Laser-Induced Fluorescence (LIF) in the Sixties. The full pilot report on the topic was published in 1968 by Zare [18]. LIF spectroscopy is nowadays a well-established and powerful technique employed both in fundamental studies and several applications that, in the plasma field, range from plasma-assisted combustions to waste gas treatment and plasma medicine [19] [20] [21] [22].

2.1.1 The LIF process

LIF is substantially an absorption experiment in which the observable is the fluorescence light from a laser-prepared energy level [23]. In standard one-photon LIF, a laser source is tuned so that its frequency ν_{las} matches a dipole-allowed transition of the molecule M (or atom A) under investigation. In the molecular case, an electronically-excited state M^* with definite vibrational and rotational quantum numbers is prepared with the absorption of laser photons. Spontaneous emission $\mathrm{h}\nu_{\mathrm{fluo}}$ from the pumped state to lower levels M^{**} constitutes the spectroscopic observable

$$\mathrm{M} + \mathrm{h}\nu_{\mathrm{las}} \longrightarrow \mathrm{M}^* \longrightarrow \mathrm{M}^{**} + \mathrm{h}\nu_{\mathrm{fluo}} \tag{2.1}$$

In the isolated molecule, $\mathrm{h}\nu_{\mathrm{fluo}}$ is uniquely emitted by the pumped level. In contrast, in the presence of some colliding species, other levels may be populated by collisional energy-transfers, and they too emit [20]. As a consequence, a complete description of the LIF process can only be given if all depopulation channels of M^* are accounted for in scheme (2.1). Two limiting conditions can be identified:

i the *low-pressure regime*, in which collisional relaxations are negligible and radiative de-excitations are the dominant depopulation channels;

ii the *atmospheric pressure or high-pressure regime*, in which collisional processes greatly influence the spectral and temporal characteristics of the LIF outcome, in a way that is sensitive to the gas composition.

LIF in low-pressure regimes

In a collisionless environment, achieved by lowering the operating pressure to a value that makes collisions negligible, molecules are isolated particles that solely undergo radiative processes. When an isolated molecule in its initial state $|\mathrm{i}\rangle$ is resonantly stimulated by laser radiation at frequency $v_{\mathrm{if}} = \frac{1}{\mathrm{h}}(\mathrm{E_f} - \mathrm{E_i})$, absorption can occur and the ro-vibronic transition $|\mathrm{i}\rangle \longrightarrow |\mathrm{f}\rangle$ is induced. $|\mathrm{i}\rangle$ and $|\mathrm{f}\rangle$ label the set of good quantum numbers - electronic, vibrational, rotational - describing the two states. With a mean lifetime τ_{f}, the excited state $|\mathrm{f}\rangle$ undergoes spontaneous emission $|\mathrm{f}\rangle \longrightarrow |\mathrm{k}\rangle$ to lower states $|\mathrm{k}\rangle$ in agreement with the selection rules. Figure 2.1 (left) sketches this situation. The LIF experiment is mathematically described by a set of rate equations for the densities $\mathrm{P}(\mathrm{t})$ of the levels involved in the process

$$\begin{cases} \frac{\mathrm{dP_i(t)}}{\mathrm{dt}} & = -\mathcal{B}_{\mathrm{if}}\ \rho_v(\mathrm{t})\left(\mathrm{P_i(t)} - \frac{\mathrm{g_i}}{\mathrm{g_f}}\mathrm{P_f(t)}\right) \\ \frac{\mathrm{dP_f(t)}}{\mathrm{dt}} & = +\mathcal{B}_{\mathrm{if}}\ \rho_v(\mathrm{t})\left(\mathrm{P_i(t)} - \frac{\mathrm{g_i}}{\mathrm{g_f}}\mathrm{P_f(t)}\right) - \mathcal{A}_{\mathrm{f}}\ \mathrm{P_f(t)} \end{cases} \tag{2.2}$$

- $\mathcal{A}_{\mathrm{f}} = \sum_{\mathrm{k}=1}^{\mathrm{N}} \mathcal{A}_{\mathrm{fk}}$ is the total spontaneous emission Einstein coefficient of state $|\mathrm{f}\rangle$. The sum is performed over the N transitions $|\mathrm{f}\rangle \longrightarrow |\mathrm{k}\rangle$ with nonzero transition probability allowed by the selection rules;
- $\mathcal{B}_{\mathrm{if}}$ is the absorption Einstein coefficient of the transition $|\mathrm{i}\rangle \longrightarrow |\mathrm{f}\rangle$.
- $\mathcal{B}_{\mathrm{fi}} = \frac{\mathrm{g_i}}{\mathrm{g_f}}\mathcal{B}_{\mathrm{if}}$ is the stimulated emission Einstein coefficient of the transition $|\mathrm{f}\rangle \longrightarrow |\mathrm{i}\rangle$ and $\mathrm{g_i}/\mathrm{g_f}$ are the multiplicities of the two states;
- ρ_v is the spectral radiant energy density of the laser field at the frequency v_{if}.

The photon density emitted per unit time and wavelegth by the laser-populated state $|\mathrm{f}\rangle$ is written as

$$\mathcal{S}_{\mathrm{LIF}}(\mathrm{t}, \lambda) = \sum_{\mathrm{k}} \mathcal{A}_{\mathrm{fk}}\ \mathrm{P_f(t)}\ \mathrm{b_{fk}}(\lambda) \tag{2.3}$$

where $\mathrm{b_{fk}}(\lambda)$ is the normalized lineshape (including all broadenings) of the individual allowed $|\mathrm{f}\rangle \longrightarrow |\mathrm{k}\rangle$ transitions.

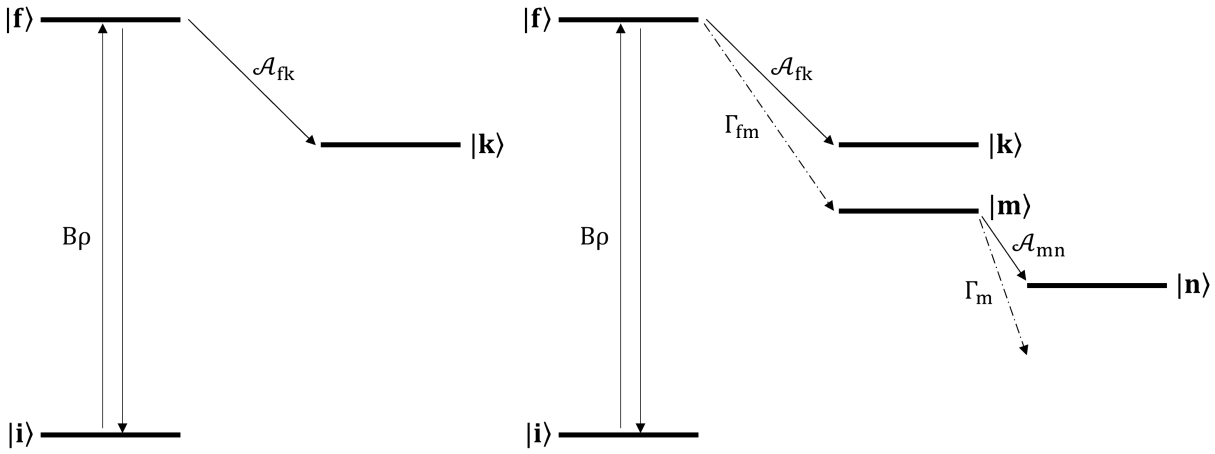

FIGURE 2.1: *Scheme of the LIF process in the low-pressure/collisionless regime (left) and high-pressure/collisional regime (right). Solid arrows: radiative processes. Dashed arrows: non-radiative processes. See text for symbols explanation.*

LIF in high-pressure regimes

The low-pressure regime portrays a theoretical appoximation of a more complete and realistic scenario that incorporates molecular interactions: the collisional regime. In the case of a LIF experiment at high pressure, the selectively-populated $|f\rangle$ state undergoes collisions with the surrounding molecules. If compared to the collisionless case, the fluorescence quantum yield can be dramatically lowered, even by two orders of magnitude, due to non-radiative depopulation of $|f\rangle$. New features appear in the LIF outcomes because energy-transfer processes populate levels other than $|f\rangle$, which successively emit light. Two classes of molecular de-excitation processes concur to define the intensity and profile of the LIF outcomes: *radiative processes*, i.e. the de-excitations of molecular excited states via the emission of a photon, and *collisional processes*, the non-radiative energy losses undergone by molecules upon their interaction with background bodies. In this case, the excess energy is accommodated into the internal degrees of freedom of the molecule or its translational energy. Three collisional processes are possible: rotational energy-transfer, vibrational energy-transfer, and electronic quenching.

When the total non-radiative frequency Γ_f of the emitting state $|f\rangle$ is comparable to,

or larger, than its radiative rate $\mathcal{A}_{\mathrm{f}}$, LIF outcomes are progressively more influenced [23]. As depicted by figure 2.1 (right), equations (2.2) become incomplete and a more thorough description of the LIF process is needed

$$\begin{cases} \frac{\mathrm{dP_i(t)}}{\mathrm{dt}} & = -\mathcal{B}_{\mathrm{if}}\ \rho_v(\mathrm{t})\left(\mathrm{P_i(t)} - \frac{\mathrm{g_i}}{\mathrm{g_f}}\mathrm{P_f(t)}\right) \\ \frac{\mathrm{dP_f(t)}}{\mathrm{dt}} & = \mathcal{B}_{\mathrm{if}}\ \rho_v(\mathrm{t})\left(\mathrm{P_i(t)} - \frac{\mathrm{g_i}}{\mathrm{g_f}}\mathrm{P_f(t)}\right) - \left(\mathcal{A}_{\mathrm{f}} + \Gamma_{\mathrm{f}}\right)\mathrm{P_f(t)} \\ \frac{\mathrm{dP_k(t)}}{\mathrm{dt}} & = \Gamma_{\mathrm{fk}}\ \mathrm{P_f(t)} - \left(\Gamma_{\mathrm{k}} + \mathcal{A}_{\mathrm{k}}\right)\mathrm{P_k(t)} \end{cases} \tag{2.4}$$

- Γ_{fk} denotes the total non-radiative energy-transfer rate from state $|\mathrm{f}\rangle$ to state $|\mathrm{k}\rangle$.
- Γ_{k} is the total non-radiative energy-transfer rate from state $|\mathrm{k}\rangle$.

When collisional relaxations are present, the photon density emitted per unit time and wavelength is the sum of the direct LIF $\mathcal{S}^{\mathrm{d}}_{\mathrm{LIF}}(\mathrm{t},\lambda)$ from the laser-populated state $|\mathrm{f}\rangle$ (see eq. (2.3)) and the collisional LIF $\mathcal{S}^{\mathrm{c}}_{\mathrm{LIF}}(\mathrm{t},\lambda)$ from collision-populated states $|\mathrm{m}\rangle$

$$\begin{aligned} \mathcal{S}_{\mathrm{LIF}}(\mathrm{t},\lambda) &= \mathcal{S}^{\mathrm{d}}_{\mathrm{LIF}}(\mathrm{t},\lambda) + \mathcal{S}^{\mathrm{c}}_{\mathrm{LIF}}(\mathrm{t},\lambda) \\ &= \sum_{\mathrm{k}} \mathcal{A}_{\mathrm{fk}}\ \mathrm{P_f(t)}\ \mathrm{b_{fk}}(\lambda) + \sum_{\mathrm{m}\neq\mathrm{f}}\sum_{\mathrm{n}} \mathcal{A}_{\mathrm{mn}}\ \mathrm{P_m(t)}\ \mathrm{b_{mn}}(\lambda) \end{aligned} \tag{2.5}$$

2.1.2 LIF outcomes and properties

A LIF measurement relies on the detection of the light emitted from either a molecular laser-populated state or nearby states that collisions have populated. The two chief methods of data acquisition are:

- the *fluorescence scan*, in which the laser wavelength is kept constant throughout the whole acquisition and a single quantum state is populated. The collection of light can be performed at different spectral regions;
- the *excitation scan*, in which fluorescence light is collected at a fixed spectral window, while the lasing frequency is scanned through the absorption region of the molecule, so that several transition lines are intercepted.

Two complementary LIF outcomes can be obtained from the collection of the light emitted from a sample volume $\mathcal{V}_{\mathrm{s}}$: the *fluorescence spectrum* $\mathcal{I}(\lambda)$ and the *fluorescence pulse* $\mathcal{S}(\mathrm{t})$. The former is the spectrally-resolved time-integrated signal

$$\mathcal{I}(\lambda) = \mathcal{C}_{\mathcal{I}}\mathcal{V}_{\mathrm{s}} \int_{\Delta\mathrm{t}} \mathcal{S}_{\mathrm{LIF}}(\mathrm{t},\lambda)\ \mathrm{dt}, \tag{2.6}$$

recorded over a time interval of $\Delta \mathrm{t}$ with collection efficiency $\mathcal{C}_{\mathcal{S}}$. The latter is the spectrally-integrated temporally-resolved outcome

$$\mathcal{S}(\mathrm{t}) = \mathcal{C}_{\mathcal{S}} \mathcal{V}_{\mathrm{s}} \int_{\Delta\lambda} \mathcal{S}_{\mathrm{LIF}}(\mathrm{t}, \lambda)\, \mathrm{d}\lambda \tag{2.7}$$

in which $\Delta\lambda$ is the spectral window of observation and $\mathcal{C}_{\mathcal{S}}$ accounts for the light collection efficiency of the detection apparatus. The availability of one or both of these observables supplies information on:

- ground state density of the emitting molecule. The quantitative determination of the ground state population is possible when the intensity and time-profile of $\mathcal{S}(\mathrm{t})$ can be correlated to the ground state properties of the emitting molecule. This is achieved upon calibration of the apparatus and by solving the excitation-relaxation schemes (2.2) or (2.4);

- ground state rotational temperature $\mathrm{T}_{\mathrm{rot}}$ of the emitting molecule, which is informative on the gas temperature $\mathrm{T}_{\mathrm{gas}}$ if a condition of rotational equilibrium is established in the ground state. The rotational temperature is typically inferred from excitation scans, although several different approaches have been described in the literature. A comprehensive review on this topic is available in [24];

- composition of the gas mixture. When a molecule is embedded in a collisional environment, its LIF fluorescence spectrum $\mathrm{I}(\lambda)$ encompasses information on the mixture composition. The determination of the species abundance in the background mixture is submitted to the quantitative knowledge of collisional processes. A clarifying example of the application of this methodology is discussed in section 2.4.

LIF spectroscopy combines high temporal and spatial resolution, sensitivity and selectivity, which make it suitable for detecting transient intermediates, radicals and metastable states in hostile media such as flames, arcs and sparks [25] [22] [26] [27]. Besides providing fundamental spectroscopic and collisional information, LIF is also of more practical importance, notably as a diagnostic tool in the fields of combustion flames, plasma medicine, material science and contaminants detection. The main features of LIF diagnostics are discussed in the following paragraphs.

Sensitivity LIF ensures excellent detection sensitivity because the signal is observed against a dark background and the signal-to-noise ratio can be greatly enhanced [22]. Since the LIF signal is recorded directly and not as the difference between two signals, as in the case of absorption mesurements, the overall sensitivity is only limited by the detectors noise. This scenario compares with typical relative absorptions $\Delta I/I_0 \sim 10^{-4} - 10^{-5}$ attainable with absorption spectroscopy, for which higher sensitivities can only be obtained with intracavity techniques [28] [24]. A further important advantage of LIF is the strength of the resonant absorption process compared with non-resonant Rayleigh and Raman techniques [29]. These two aspects - sensitivity and high cross-section of the process - allow for species detection at the ppm or even sub-ppm level.

Temporal resolution LIF experiments can resolve transient phenomena and follow their progression with high temporal resolution. Fundamental for time-resolved studies is the use of pulsed tunable lasers, since the duration of the laser pulses (typ. $< 10\ \mathrm{ns}$) determines the temporal resolution, whereas the laser repetition rate (typ. $< 50\ \mathrm{Hz}$) gives the sampling frequency.

Spatial resolution Differently from 'line-of-sight' techniques such as absorption spectroscopy, LIF experiments are carried out in a "scattering geometry", with the collection branch disposed perpendicularly to the laser beam propagation direction. The advantage of the right angle configuration is twofold. First, the collection of stray light is minimized; second, small focal volumes can be pinpointed in the sample and the spatial resolution, determined by the intersection volume between the laser beam and the collection cone profiles, is maximum. Typical achievable values of spatial resolution are of the order of $1\ \mathrm{mm}^3$ [24] [19].

Selectivity In a LIF experiment, it is possible to selectively address a species to emit light and spectrally shift the collection to suppress unwanted interferences from stray light or other emissions. The combination of these two aspects more properly features LIF as a doubly selective technique. In common LIF setups, the excitation of a single ro-vibronic line is made possible by tuneable narrow-band lasers, typically Nd:YAG-pumped dye lasers, while the spectral selection of the emitted light is achieved with bandpass filters.

Fluorescence angular distribution Given a linearly polarized laser light, its absorption produces an alignment of the transition dipoles along the laser electric field direction. Therefore, the nascent angular distribution of the fluorescence depends on the angle θ between the direction of observation and the laser electric field. Fluorescence isotropization is reached due to collisions and molecular rotations [19] [30].

Calibration LIF diagnostics requires a calibration for absolute density measurements that accounts for the unknown $\mathcal{CV}_s$ products in formulas (2.6) and (2.7). Getting a reliable calibration of a LIF setup strongly depends on the particular system under investigation, the knowledge of the spectroscopic parameters and the experimental conditions in which the setup operates. Several calibration methods have been proposed in the literature, a survey of which can be found in [19]. However, the royal road to cope with the determination of the calibration constant is to use a second technique, typically Rayleigh scattering or absorption spectroscopy, to calibrate the LIF signal to the signal from a reference gas with known concentration [19].

2.2 LIF on OH

The measurement of OH in atmospheric pressure discharges is a standard application of Laser-Induced Fluorescence spectroscopy. OH, as well as other oxygen reactive species (ROS) such as O, O_3, HO_2, or H_2O_2, contributes to oxidation processes in a countless number of applications that range from waste gas treatment to plasma medicine [31] [32] [33] or plasma-assisted combustions [34] [35]. OH formation is unavoidable when water is present in the mixture to be converted and water is commonly found in CO_2 conversion technology as part of the initial mixture or as a process product. Therefore, monitoring OH, its concentration and time/space distributions is a way to access the microscopic kinetics and chemistry of the discharge. Several studies have been carried out concerning the quantitative detection of OH by LIF. The reader may refer to [36] [37] [38] [39] [40] for corona discharges applications, to [41] [42] [43] for ns discharges, to [44] [45] [46] [47] for plasma-jets and [48] [49] [50] [51] for DBDs.

2.2.1 Spectroscopic scheme

In most cases, the detection scheme applied for OH detection makes use of the transitions of the 3064 Å system

$$\mathrm{OH}(\mathrm{X}\ ^2\Pi, v'', \mathrm{N}'') + \mathrm{h}\nu_\mathrm{L} \longrightarrow \mathrm{OH}(\mathrm{A}\ ^2\Sigma^+, v', \mathrm{N}') \longrightarrow \mathrm{OH}(\mathrm{X}\ ^2\Pi, v) + \mathrm{h}\nu_{\mathrm{N}'} \tag{2.8}$$

in which:

- $(\mathrm{X}, v'', \mathrm{N}'')$ is the set of - electronic, vibrational and rotational - quantum numbers that describe the ground state;
- $(\mathrm{A}, v', \mathrm{N}')$ is the set of - electronic, vibrational and rotational - quantum numbers that identify the excited state;
- $\mathrm{h}\nu_\mathrm{L}$ is the laser energy input;
- $\mathrm{h}\nu_{\mathrm{N}'}$ is the fluorescence generated by the radiative decay of the laser-populated state $\mathrm{OH}(\mathrm{A}\ ^2\Sigma^+, v', \mathrm{N}')$ towards the ground state $\mathrm{OH}(\mathrm{X}\ ^2\Pi, v)$ in agreement with the selection rules.

The details on the adopted nomenclature are reported in section 2.5. In this thesis, as in [49] and [52], LIF is applied to the detection scheme

$$\mathrm{OH}(\mathrm{X}\ ^2\Pi, 0, \mathrm{N}'') + \mathrm{h}\nu_\mathrm{L} \longrightarrow \mathrm{OH}(\mathrm{A}\ ^2\Sigma^+, 1, \mathrm{N}') \longrightarrow \mathrm{OH}(\mathrm{X}\ ^2\Pi, 1) + \mathrm{h}\nu_{\mathrm{N}'} \tag{2.9}$$

with excitation around 2820 Å and collection around 3150 Å. A pictorial representation of scheme (2.9) is given in figure 2.2. Several ro-vibronic transitions are possible. The choice of N'' is dictated by the criteria of 'maximum population and smooth dependence' on the rotational temperature, so that small local changes of the temperature do not influence appreciably the outcome [53]. These constraints usually rule out high rotational levels of a manifold. In this work, the $\mathrm{P}_1(1)$, $\mathrm{P}_1(2)$ and $\mathrm{P}_1(3)$ lines at 2821.70 Å, 2825.80 Å and 2830.09 Å, respectively, are used. These lines, in fact, ensure an almost-constant population in the initial state for a wide temperature range [53]. A scheme of the $\mathrm{P}_1(3)$ line is shown in figure 2.9.

It should be noted that other detection schemes could in principle be used, e.g.

$$\mathrm{OH}(\mathrm{X}\ ^2\Pi, 0, \mathrm{N}'') + \mathrm{h}\nu_\mathrm{L} \longrightarrow \mathrm{OH}(\mathrm{A}\ ^2\Sigma^+, 3, \mathrm{N}') \longrightarrow \mathrm{OH}(\mathrm{X}\ ^2\Pi, 2) + \mathrm{h}\nu_{\mathrm{N}'} \tag{2.10}$$

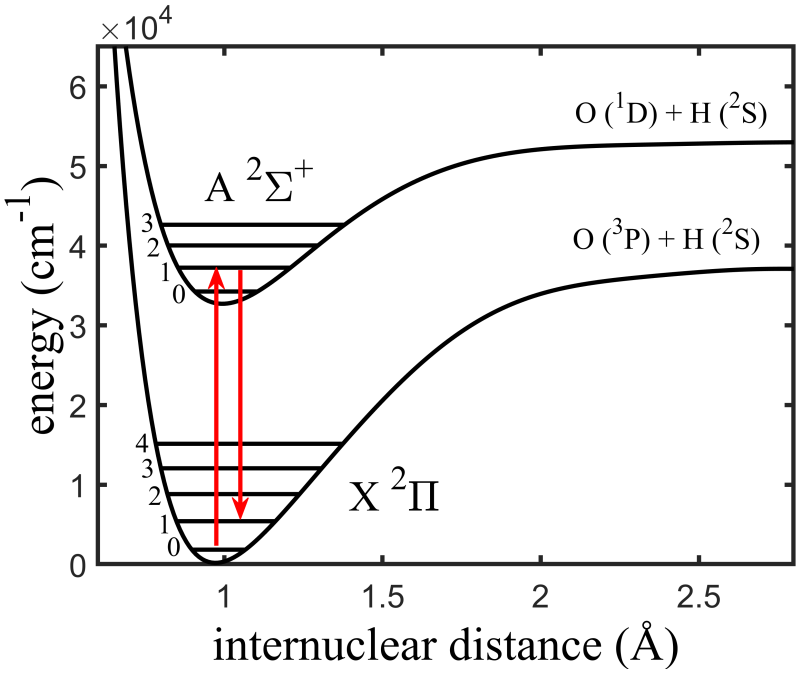

FIGURE 2.2: *Potential energy curves of the* OH *ground state* X $^2\Pi$ *and first excited state* A $^2\Sigma^+$ *[54] [55]. Vibrational energy levels are also sketched. Red arrows refer to diagram (2.9).*

with excitation at 2480 Å and detection around 2970 Å [37], or

$$\mathrm{OH(X\ ^2\Pi, 0, N'')} + \mathrm{h}\nu_{\mathrm{L}} \longrightarrow \mathrm{OH(A\ ^2\Sigma^+, 0, N')} \longrightarrow \mathrm{OH(X\ ^2\Pi, 1)} + \mathrm{h}\nu_{\mathrm{N'}} \tag{2.11}$$

with excitation at 3060 Å and collection at 3090 Å [50]. However, scheme (2.9) is selected over other options because it combines good absorption, high emission coefficients and sufficient spectral separation between the laser and detection wavelengths [19], not to mention that the $\mathrm{OH(A\ ^2\Sigma^+}, v = 1)$ state is well documented in terms of both spectroscopic and collision data. At atmospheric pressure, where the fluorescence duration can be so small to be comparable with the course of the laser pulses, the time separation between the fluorescence and the scattered light is not possible and only their spectral separation ensures the distinction of the two signals. Furthermore, thanks to the spectroscopic characteristics of scheme (2.9), with net separation of the rotational lines and the absence of strong band heads, the absorption on a single ro-vibronic transition is possible and advantageous for a good definition of the LIF process [19].

2.2.2 LIF outcomes in a collisional environment

The applicability of scheme (2.8), and hence of schemes (2.9)-(2.11), is limited to a purely collisionless regime. In the presence of collisional processes, in fact, the de-excitation of the laser-excited states involves both radiative decay and collisional relaxations, and scheme (2.8) needs to be expanded to account for the emission of collision-populated levels

$$\begin{array}{c} \mathrm{OH(X\ ^2\Pi}, v'', \mathrm{N''}) + \mathrm{h}v_{\mathrm{L}} \longrightarrow \mathrm{OH(A\ ^2\Sigma^+}, v', \mathrm{N'}) \longrightarrow \mathrm{OH(X\ ^2\Pi}, v) + \mathrm{h}v_{\mathrm{N'}} \\ \downarrow \mathrm{ET} \\ \mathrm{OH(A\ ^2\Sigma^+}, v''', \mathrm{N'''}) \longrightarrow \mathrm{OH(X\ ^2\Pi}, v) + \mathrm{h}v_{\mathrm{N'''}} \end{array} \tag{2.12}$$

in which:

- $\mathrm{OH(A\ ^2\Sigma^+}, v''', \mathrm{N'''})$ labels any state populated by collisional de-excitation - VET and RET - from the laser-populated state $\mathrm{OH(A\ ^2\Sigma^+}, v', \mathrm{N'})$;
- $\mathrm{h}v_{\mathrm{N'''}}$ is the fluorescence generated upon radiative relaxation of collision-populated states $\mathrm{OH(A\ ^2\Sigma^+}, v''', \mathrm{N'''})$ to the ground state. A broadband detection is used to capture these emissions.

Collisional processes concur to define the intensity and spectral distribution of the emitted light, and for excitation with a pulsed laser, they also affect the temporal decay of the fluorescence. In this section, the impact of energy-transfers is presented through a simulation of the LIF oucomes, reproduced for comparison in both a collisional regime and a collisionless condition.

OH fluorescence spectrum

Figure 2.3 shows the simulated fluorescence spectra, generated by the LIFBASE tool [54] assuming the excitation of the $\mathrm{P_1(3)}$ rotational line. In a collisionless condition, and with a little simplification of the notation, the spectroscopic scheme (2.8) can be rewritten as

$$\mathrm{OH(X}, 0, 3) + \mathrm{h}v_{\mathrm{L}} \longrightarrow \mathrm{OH(A}, 1, 2) \longrightarrow \mathrm{OH(X}, 1, \mathrm{N}) + \mathrm{h}v_{\mathrm{OH(A,1,2)}} \tag{2.13}$$

Under such circumstances, the fluorescence light originates from the sole laser-excited state and the emission preserves a strong reminiscence of the excitation mechanism.

As shown in the top panel of figure 2.3, few isolated lines are observed in the spectrum in this case, corresponding to the dipole transitions allowed by the selection rules (2.40). The details of such transitions are reported in table 2.1. The effect of

	$\mathbf{N'}$	$\mathbf{F'}$	$\mathbf{J'}$	$\mathbf{N}$	$\mathbf{F}$	$\mathbf{J}$	$\mathbf{\Delta J = J' - J}$	**wavelength (Å)**
$\mathrm{R}_1(1)$	2	1	$\frac{5}{2}$	1	1	$\frac{3}{2}$	$+1$	3128.24
$\mathrm{Q}_1(2)$	2	1	$\frac{5}{2}$	2	1	$\frac{5}{2}$	0	3136.18
$\mathrm{Q}_{12}(2)$	2	1	$\frac{5}{2}$	2	2	$\frac{3}{2}$	$+1$	3146.51
$\mathrm{P}_1(3)$	2	1	$\frac{5}{2}$	3	1	$\frac{7}{2}$	-1	3147.41
$\mathrm{P}_{12}(3)$	2	1	$\frac{5}{2}$	3	2	$\frac{5}{2}$	0	3156.19
$\mathrm{O}_{12}(4)$	2	1	$\frac{5}{2}$	4	2	$\frac{7}{2}$	-1	3169.66

TABLE 2.1: *Observed emission lines after excitation of the* $\mathrm{OH}(\mathrm{A}, 1, 2)$ *state in agreement with the selection rule (2.40). All tabled transitions belong to the* $(1, 1)$ *vibrational band of the* OH 3064 *Å system. Primed quantum numbers label the high-energy state of the transition. Data and nomenclature are reported from [54].*

collisional processes is reproduced in the simulation through the addition of a fictitious $[\mathrm{O}_2] = 2.3 \cdot 10^{16}\ \mathrm{cm}^{-3}$ density. In this condition, the spectroscopic scheme (2.13) is expanded to

$$\begin{aligned} \mathrm{OH}(\mathrm{X}, 0, 3) + \mathrm{h}v_{\mathrm{L}} \longrightarrow \mathrm{OH}(\mathrm{A}, 1, 2) \xrightarrow{\mathrm{RET}} \ & \mathrm{OH}(\mathrm{A}, 1) \longrightarrow \mathrm{OH}(\mathrm{X}, 1) + \mathrm{h}v_{(1,1)} \\ & \downarrow \mathrm{VET} \\ & \mathrm{OH}(\mathrm{A}, 0) \longrightarrow \mathrm{OH}(\mathrm{X}, 0) + \mathrm{h}v_{(0,0)} \end{aligned} \tag{2.14}$$

In the presence of a collisional partner, the emission occurs from several states other than the laser-populated, because energy-transfer processes redistribute the excited population. In particular, rotational energy-transfer (RET) populates neighboring rotational states, which then emit, and the 'memory' of the excited state is lost in the fluorescence spectrum. This reflects the formation of the so-called $(1, 1)$ band, or $\mathcal{I}_1(\lambda)$, with R_1 band-head position at 3121.7 Å

$$\mathcal{I}_1(\lambda): \qquad \mathrm{OH}(\mathrm{A}\ ^2\Sigma^+, v' = 1) \longrightarrow \mathrm{OH}(\mathrm{X}\ ^2\Pi, v = 1) \tag{2.15}$$

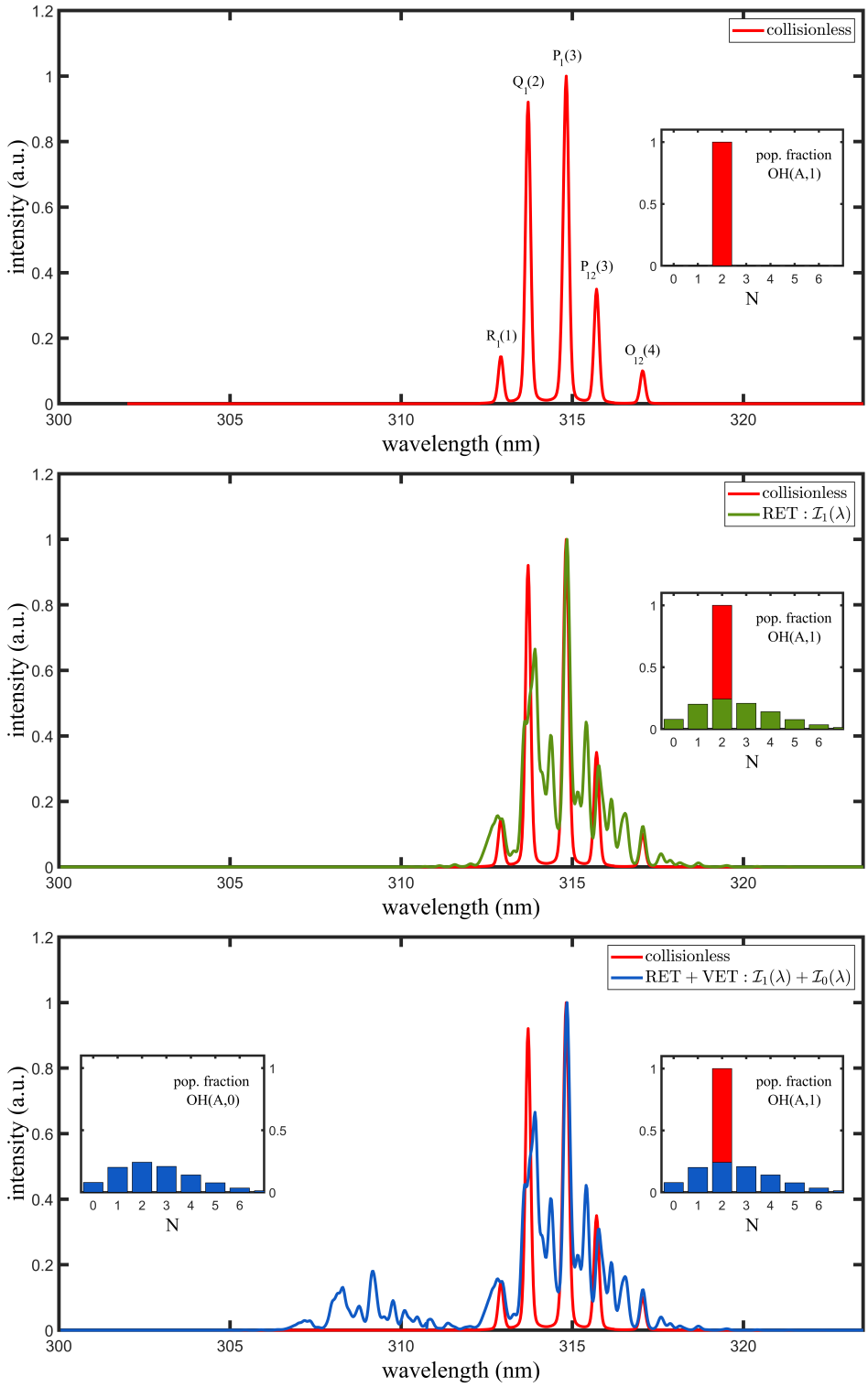

FIGURE 2.3: *Simulation of the* OH *emission spectrum in a collisionless environment (top) and in the presence of a* $[O_2] = 2.3 \cdot 10^{16}$ cm^{-3} *density of collision partner (bottom). The simulations are obtained with the LIFBASE tool [54] with an instrumental resolution of* 0.2 nm *(FWHM). The histograms show the population distributions that generate the spectra.*

The normalized $(1,1)$ band is shown in the central panel of figure 2.3 for a population distribution thermalized at $\mathrm{T_{rot}} = 300\ \mathrm{K}$ (solid green line). Simultaneous to RET, vibrational energy transfer (VET) populates the $\mathrm{OH(A},0)$ manifold, with a rate that depends on the collider species. The decay of $\mathrm{OH(A},0)$ results in the so-called $(0,0)$ band, with $\mathrm{R_1}$ band-head position at 3067.2 Å

$$\mathcal{I}_0(\lambda): \qquad \mathrm{OH(A\ ^2\Sigma^+}, v'=0) \longrightarrow \mathrm{OH(X\ ^2\Pi}, v=0) \tag{2.16}$$

The two bands give rise to an overall emission

$$\mathcal{I}(\lambda) = \mathcal{I}_1(\lambda) + \mathcal{I}_0(\lambda) \tag{2.17}$$

which is shown in the bottom panel of the figure for a thermalized distribution of both $\mathrm{OH(A},1)$ and $\mathrm{OH(A},0)$ (solid blue line). For the sake of completeness, it should be remarked that collisional processes determine a decrease of the fluorescence quantum yield through non-radiative quenching. However, this reduction is not appreciable in the plots, since the simulated signals are normalized to their maxima for comparison.

OH fluorescence pulse

Figure 2.4 shows the simulated fluorescence pulses, obtained by solving the radiative-collisional models (2.2) and (2.4) with the collision data taken from [56]. In a strictly collisionless condition, because non-radiative de-excitation is prevented, the laser-excited state $\mathrm{OH(A},1,2)$ decays through spontaneous emission according to the rate equation

$$\frac{\mathrm{dP_{OH(A,1,2)}(t)}}{\mathrm{dt}} = -\mathcal{A}_{\mathrm{OH(A,1,2)}}\ \mathrm{P_{OH(A,1,2)}(t)} \tag{2.18}$$

where $\mathcal{A}_{\mathrm{OH(A,1,2)}} = 1.2 \cdot 10^6\ \mathrm{s^{-1}}$ is reported from the LIFBASE database [54]. Equation (2.18) gives an exponential decay with time constant $\tau \simeq 830\ \mathrm{ns}$, shown in figure 2.4 (solid red line). With the addition of a collider partner, collisional processes compete with radiative decay, lower the fluorescence quantum yield through non-radiative depopulation and reduce the fluorescence lifetime. In this condition, the total fluorescence pulse $\mathcal{S}(\mathrm{t})$ is the sum of as many terms as the number of radiating states. Under the simulated conditions, the overall emission can be described by two rate equations, one for each of the two radiating vibrational states $\mathrm{OH(A},1)$ and $\mathrm{OH(A},0)$. Solid green and blue lines show the calculated band signals $\mathcal{S}_1(\mathrm{t})$ and $\mathcal{S}_0(\mathrm{t})$. The two bands decay at a different rate:

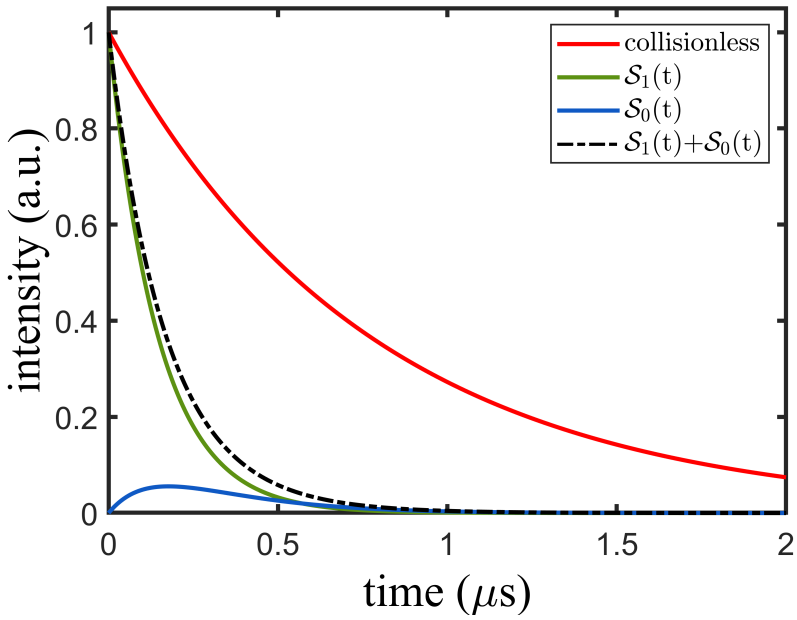

FIGURE 2.4: *Simulation of the fluorescence time decay in a collisionless environment (solid red line) and in the presence of a* $[O_2] = 2.3 \cdot 10^{16}\ \mathrm{cm}^{-3}$ *density of collision partner (solid green and blue lines, dashed black line).*

- the $(1,1)$ decay is a single exponential, as a result of the depopulation of $OH(A,1)$ by total quenching;
- the $(0,0)$ decay is a double exponential, with one term accounting for the depopulation $OH(A,0)$ through total quenching and one term for its refilling by VET.

These give rise to a total fluorescence pulse

$$\mathcal{S}(t) = \mathcal{S}_1(t) + \mathcal{S}_0(t) \tag{2.19}$$

with effective time constant $\tau \simeq 200$ ns (dashed black line). As for the spectra, the variations of the quantum yield are ignored in the simulations and the signals are normalized for comparison.

The simulations presented in this section, although specific for a set of conditions, allow to draw considerations that are applicable generally. First, the correct interpretation of LIF outcomes requires deep knowledge of energy-transfer mechanisms, which frequently confronts the lack of suitable data in the literature. This implies both

a fundamental and experimental characterization of the relevant collision processes. Second, the occurrence of energy-transfers complicates the mathematical description of the LIF process. Developing predictive radiative-collisional models must then prioritized, based on a compromise between the complexity of the model and its computational cost. Both these topics are discussed in the following sections.

2.3 LIF modeling

Quantitative LIF determinations require a rationalization of the LIF process (2.14). Although specific modelizations can be adopted to account for different experimental conditions, all the schemes are based on a set of rate equations that describe the evolution of the population of the involved states. The validity of the rate equations approach over the full quantum Maxwell–Bloch equations has been proven by Daily in [57]. The reader can refer to [57] and [53] for further details on this subject.

The simplest rate equations modelization is presented by Yonemori in [46], where a constant ground state population is assumed, and the two excited states $\mathrm{OH(A,1)}$ and $\mathrm{OH(A,0)}$ are described by rate equations (*two-level model*). A rectangular function is used to characterize the laser beam profile so that an analytical solution of the equations can be found for $\mathrm{t} > \mathrm{t}_0$ after the end of the excitation pulse.

Improvements of the *two-level model* can be implemented to take into account both rotational relaxations and the time evolution of the ground state population. This is the case of the *three-level model* described by Dilecce in [49], where the ground state time evolution is considered, and the *four-level model* presented by Verreycken in [58], in which a fourth level equation is included for the $\mathrm{OH(X,1)}$ state. A further improvement is given by the *six-level model* detailed by Dunn in [59], in which the two laser-coupled states are connected by RET to two additional states - the *lumped states* - that include the remainders of the rotational manifolds, and vibrational relaxations are incorporated in both the excited and the ground states.

Five-level model

Although the *six-level model* is the most thorough modelization of the LIF process, its application is computationally demanding. Several simplifications can be intro-

duced, such as the *five-level model* described by Dilecce in [53], in which VET relaxations $\mathrm{OH(X,1)} \longrightarrow \mathrm{OH(X,0)}$ are neglected because inefficient in refilling the ground state over the measurement cycle. In this thesis work, the *five-level model* (2.20) is adopted. A diagram representation is presented in figure 2.5, where a sixth level (X1) is added for pictorial reasons, albeit not incorporated in the rate equations.

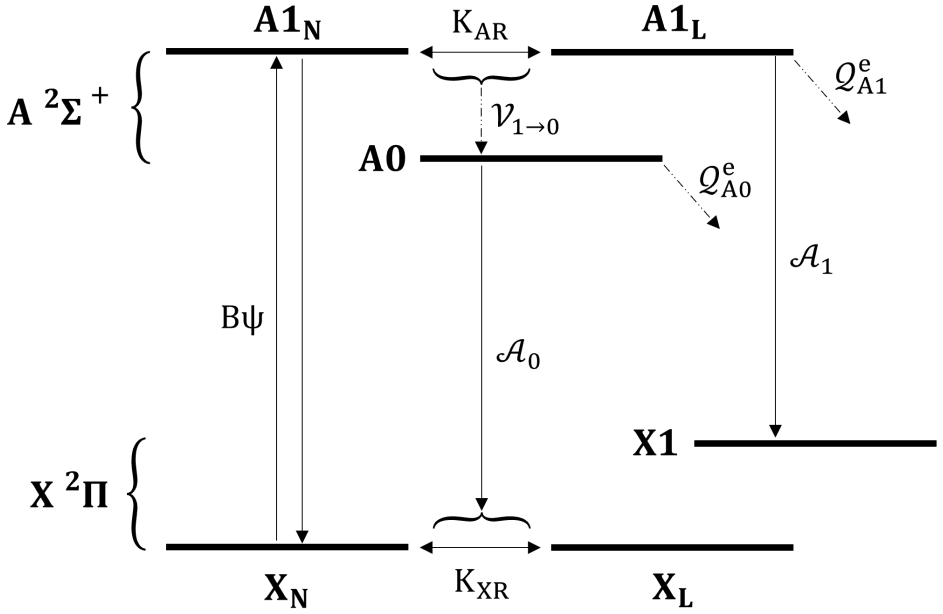

FIGURE 2.5: *Scheme of the five-level model taken from [53] and readapted to include* X1 *state. See text for symbols explanation.*

$$
\begin{cases}
\frac{\mathrm{dP_{X_N}(t)}}{\mathrm{dt}} & = -\mathcal{E}(\mathrm{t})\psi\ \left[\mathcal{B}_{\mathrm{X,A}}\ \mathrm{P_{X_N}(t)} - \mathcal{B}_{\mathrm{A,X}}\ \mathrm{P_{A1_N}(t)}\right] + \left[\mathcal{F}_{\mathrm{X_N}}\ \mathrm{P_X(t)} - \mathrm{P_{X_N}(t)}\right] \mathrm{K_{X,R}} \\
\frac{\mathrm{dP_{X_L}(t)}}{\mathrm{dt}} & = -\left[\mathcal{F}_{\mathrm{X_N}}\ \mathrm{P_X(t)} - \mathrm{P_{X_N}(t)}\right] \mathrm{K_{X,R}} \\
\frac{\mathrm{dP_{A1_N}(t)}}{\mathrm{dt}} & = \mathcal{E}(\mathrm{t})\psi\ \left[\mathcal{B}_{\mathrm{X,A}}\ \mathrm{P_{X_N}(t)} - \mathcal{B}_{\mathrm{A,X}}\ \mathrm{P_{A1_N}(t)}\right] - \Gamma_1\ \mathrm{P_{A1_N}(t)} + \\
& \qquad - \left[\mathrm{P_{A1_N}(t)} - \mathcal{F}_{\mathrm{A_N}}\ \mathrm{P_{A1}(t)}\right] \mathrm{K_{A1,R}} \\
\frac{\mathrm{dP_{A1_L}(t)}}{\mathrm{dt}} & = \mathrm{K_{A1,R}} \left[\mathrm{P_{A1_N}(t)} - \mathcal{F}_{\mathrm{A_N}}\ \mathrm{P_{A1}(t)}\right] - \Gamma_1\ \mathrm{P_{A1_L}(t)} \\
\frac{\mathrm{dP_{A0}(t)}}{\mathrm{dt}} & = \mathcal{V}_{1\to 0}\ \mathrm{P_{A1}(t)} - \Gamma_0\ \mathrm{P_{A0}(t)}
\end{cases}
\tag{2.20}
$$

where $\mathrm{P_X} = \mathrm{P_{X_N}} + \mathrm{P_{X_L}}$ and $\mathrm{P_{A1}} = \mathrm{P_{A1_N}} + \mathrm{P_{A1_L}}$ are the shorthand notation for the population densities in the ground and excited state, respectively. The five states included in the model are defined as follows:

- $\mathrm{X_N}$ is the rotational state that absorbs laser radiation: $\mathrm{OH(X, 0, N'')}$;
- $\mathrm{X_L}$ is the remainder of the rotational manifold of $\mathrm{OH(X, 0)}$, i.e. the *lumped state* constituted by all the rotational levels but $\mathrm{N''}$;
- $\mathrm{A1_N}$ is the laser-populated excited state: $\mathrm{OH(A, 1, N')}$;
- $\mathrm{A1_L}$ is the *lumped state* made up of the rotational levels of $\mathrm{OH(A, 1)}$ except for $\mathrm{N'}$;
- $\mathrm{A0}$ is the $\mathrm{OH(A, 0)}$ state.

Optical and collisional processes concur to define LIF outcomes:

- $\mathrm{X_N}$ is depleted by the absorption of laser light and repopulated by stimulated emission from $\mathrm{OH(A, 1)}$ and by RET collisions from $\mathrm{X_L}$. RET refilling is described by an effective rate $\mathrm{K_{X,R}}$, which can be interpreted as an average of the state-to-state RET rates. Under this approximation, the RET refilling of $\mathrm{X_N}$ is proportional to the discrepancy between the actual population $\mathrm{P_{X_N}}$ and its equilibrium population $\mathcal{F}_{\mathrm{X_N}}\mathrm{P_X}$, where $\mathcal{F}_{\mathrm{X_N}}$ is the rotational population fraction of $\mathrm{X_N}$ at a given temperature. The introduction of the $\mathcal{F}$ function constitutes an approximation, justified by the fact that state-to-state RET rate coefficients are typically not known and a state-to-state approach would represent a daunting computational task;
- $\mathrm{A1_N}$ is populated by optical absorption from the ground state and depopulated by stimulated emission, spontaneous emission, and collisional energy-transfers. $\Gamma_1 = \mathcal{A}_1 + \mathcal{Q}_1^{\mathrm{e}} + \mathcal{V}_{1\to0}$ is the radiative plus electronic quenching plus vibrational relaxation rate of state $\mathrm{A1}$, or its 'total quenching frequency'. $\mathcal{Q}_1 = \mathcal{Q}_1^{\mathrm{e}} + \mathcal{V}_{1\to0}$ labels, instead, the 'total non-radiative quenching frequency' of the state. The coupling between $\mathrm{A1_N}$ and $\mathrm{A1_L}$ is described by an effective RET rate $\mathrm{K_{A1,R}}$ as for the ground state;
- $\mathrm{A0}$ is the vibrational state $(\mathrm{A}, 0)$, populated by VET from $(\mathrm{A}, 1)$ with rate $\mathcal{V}_{1\to0}$ and depopulated by electronic plus radiative quenching with rate $\Gamma_0 = \mathcal{Q}_0^{\mathrm{e}} + \mathcal{A}_0$. Γ_0 is termed 'total quenching frequency' of the state. The tautological identity $\mathcal{Q}_0 = \mathcal{Q}_0^{\mathrm{e}}$ introduces the 'total non-radiative quenching frequency' of the state $\mathrm{A0}$;

- $\mathcal{E}(\mathrm{t})$, with units $[\frac{\mathrm{J}}{\mathrm{m}^3}]$, is the laser radiant energy density, defined as $\mathcal{E}(\mathrm{t}) = \mathrm{W}(\mathrm{t})/\mathrm{cS}$. c is the speed of light, S is the laser section and $\mathrm{W}(\mathrm{t})$ the laser power. The power can be obtained by normalizing the measured one so that the integrated $\mathrm{W}(\mathrm{t})$ equals the laser pulse energy;

- ψ, with units $[\mathrm{s}]$, is the spectral overlap integral of the absorption line and laser line, calculated as
$$\psi = \int_{-\infty}^{+\infty} \mathrm{b}(v - v_{\mathrm{a}})\ \epsilon(v - v_{\mathrm{L}})\ \mathrm{d}v \tag{2.21}$$
v_{L} and v_{a} are the positions of the laser and the absorption lines, respectively, while $\mathrm{b}(v - v_{\mathrm{a}})$ and $\epsilon(v - v_{\mathrm{L}})$ are the two normalized profiles;

- $\mathcal{B}_{\mathrm{X,A}}$ and $\mathcal{B}_{\mathrm{A,X}}$ are the Einstein coefficient for absorption and stimulated emission, respectively. Because the product $\mathcal{E}(\mathrm{t})\psi$ has the units of a spectral radiant energy density $[\frac{\mathrm{Js}}{\mathrm{m}^3}]$, and $\mathcal{B}$ has the units of $[\frac{\mathrm{m}^3}{\mathrm{Js}^2}]$, the multiplication $\mathcal{B}\mathcal{E}(\mathrm{t})\psi$ has the correct unit of a frequency.

Measured signal

Thanks to the spectroscopic characteristics of the detection scheme, two bands can be recorded simultaneously: the $(1,1)$ band, resulting from the emission of the $\mathrm{A1}$ state, and the $(0,0)$ band, generated by the emission of the $\mathrm{A0}$ state. The fluorescence light is collected by two distinct sensors which, in combination, allow for the simultaneous recording of both LIF outcomes. A spectrograph+ICCD setup measures the fluorescence spectrum $\mathcal{I}(\lambda)$, which can be expressed as

$$\begin{aligned}\mathcal{I}(\lambda) &= \mathcal{I}_1(\lambda) + \mathcal{I}_0(\lambda) \\ &= \mathcal{C}_{\mathcal{I}}\mathcal{V}_s\left[\Psi_{(1,1)}(\lambda)\int_{\mathrm{t_0}}^{\mathrm{t_0+t_g}} \mathrm{P_{A1}}(\mathrm{t})\ \mathrm{dt} + \Psi_{(0,0)}(\lambda)\int_{\mathrm{t_0}}^{\mathrm{t_0+t_g}} \mathrm{P_{A0}}(\mathrm{t})\ \mathrm{dt}\right]\end{aligned} \tag{2.22}$$

where $\mathcal{C}_{\mathcal{I}}$ is the transfer function of the collection apparatus, $\mathcal{V}_{\mathrm{s}}$ is the sampled volume and $\mathrm{t_g}$ is the integration time. $\Psi_{(1,1)}(\lambda)$ and $\Psi_{(0,0)}(\lambda)$ are the normalized emission spectra of the $(1,1)$ and $(0,0)$ bands, defined as

$$\Psi_{(1,1)}(\lambda) = \sum_{\mathrm{n}} \mathcal{A}_{\mathrm{n}}^{(1,1)}\ \mathrm{F}_{\mathrm{n}}^{\mathrm{A1}}\ \mathrm{b_n}(\lambda) \qquad\qquad \Psi_{(0,0)}(\lambda) = \sum_{\mathrm{n}} \mathcal{A}_{\mathrm{n}}^{(0,0)}\ \mathrm{F}_{\mathrm{n}}^{\mathrm{A0}}\ \mathrm{b_n}(\lambda) \tag{2.23}$$

For a given rotational state n:

- $\mathcal{A}_{\mathrm{n}}^{(\cdot)}$ is the spontanous emission Einstein coefficient for the $|\mathrm{n}\rangle \longrightarrow |\mathrm{k}\rangle$ transitions that emit within the observation band $(\cdot)$;
- $\mathrm{F_n}$ is the rotational population fraction;
- $\mathrm{b_n}$ is the normalized emission profile (including all broadenings).

The rotational population fractions $\mathrm{F_n}$ are derived by fitting high-resolution fluorescence spectra. $\mathrm{F_n}$ should then be more properly regarded as an effective population fraction over the integration time $\mathrm{t_g}$. A fast photomultiplier detects the time-resolved fluorescence pulse $\mathcal{S}(\mathrm{t})$, expressed as

$$\mathcal{S}(\mathrm{t}) = \mathcal{S}_1(\mathrm{t}) + \mathcal{S}_0(\mathrm{t}) = \mathcal{C}_{\mathcal{S}}\mathcal{V}_{\mathrm{s}}\left(\mathcal{A}_{(1,1)}\ \mathrm{P_{A1}}(\mathrm{t}) + \mathcal{A}_{(0,0)}\ \mathrm{P_{A0}}(\mathrm{t})\right) \tag{2.24}$$

where $\mathcal{C}_{\mathcal{S}}$ is the transfer function of the collection apparatus and $\mathcal{V}_{\mathrm{s}}$ is the sampled volume. $\mathcal{A}_{(1,1)}$ and $\mathcal{A}_{(0,0)}$ are the effective radiative rates of vibrational states $\mathrm{A1}$ and $\mathrm{A0}$, calculated as

$$\mathcal{A}_{(1,1)} = \sum_{\mathrm{n}} \mathcal{A}_{\mathrm{n}}\ \mathrm{F_n^{A1}} \qquad\qquad \mathcal{A}_{(0,0)} = \sum_{\mathrm{n}} \mathcal{A}_{\mathrm{n}}\ \mathrm{F_n^{A0}} \tag{2.25}$$

2.4 Collisional energy-transfer-LIF on OH (CET-LIF)

Collisional processes, although detrimental for the fluorescence quantum yield and the mathematical description of the LIF process, can be a boon to infer information on the environment in which OH molecules are embedded. This method, termed in [60] Collisional Energy Transfer-LIF (CET-LIF), was developed as a way to derive the gas the composition of simple gas mixtures using LIF spectroscopy, based on the dependence of LIF outcomes on collisional processes, which are species-specific.

In this perspective, CET–LIF is conceptually different from the standard LIF since the molecule excited by the laser becomes the probe of the environmental composition rather than the target. In fact, provided that energy-transfer mechanisms undergone by OH with the surrounding particles are known, the variations in the OH fluorescence spectra can be quantitatively related to variations in the enviromental composition [23]. This use of LIF was first applied by Riès in [61] to the case of a humified atmospheric pressure He plasma jet, with the possibility of independently estimating air and water

penetration inside the jet, based on a strong dependence of OH LIF outcomes on air and water collisional rate coefficients.

The CET-LIF method allows to quantify the composition of simple mixtures of known components from a measured LIF fluorescence spectrum $\mathcal{I}(\lambda)$, based on the knowledge of the collisional rate coefficients of the species involved. Two practical applications of this method are presented in section 3.4. In the case of OH detection, the simultaneous recording of the $(1,1)$ and $(0,0)$ bands gives access to the band ratio

$$\mathrm{R_B} = \frac{\int \mathrm{I_0}(\lambda)\ \mathrm{d}\lambda}{\int \mathrm{I_1}(\lambda)\ \mathrm{d}\lambda} = \frac{\int \Psi_{(0,0)}(\lambda)\ \mathrm{d}\lambda \int_{\mathrm{t_0}}^{\mathrm{t_0+t_g}} \mathrm{P_{A0}(t)}}{\int \Psi_{(1,1)}(\lambda)\ \mathrm{d}\lambda \int_{\mathrm{t_0}}^{\mathrm{t_0+t_g}} \mathrm{P_{A1}(t)}} \overset{\text{(a)}}{=} \frac{\mathcal{A}_{(0,0)} \int_{\mathrm{t_0}}^{\mathrm{t_0+t_g}} \mathrm{P_{A0}(t)}}{\mathcal{A}_{(1,1)} \int_{\mathrm{t_0}}^{\mathrm{t_0+t_g}} \mathrm{P_{A1}(t)}} \tag{2.26}$$

in which the equality (a) is justified by the normalization condition $\int \mathrm{b_n}(\lambda)\ \mathrm{d}\lambda = 1$ in equations (2.22) and (2.23). The band ratio $\mathrm{R_B}$ provides an estimate of the population ratio

$$\mathrm{R_P} = \frac{\int_{\mathrm{t_0}}^{\mathrm{t_0+t_g}} \mathrm{P_{A0}(t)}\ \mathrm{dt}}{\int_{\mathrm{t_0}}^{\mathrm{t_0+t_g}} \mathrm{P_{A1}(t)}\ \mathrm{dt}} \tag{2.27}$$

once the $\mathcal{A}_{(1,1)}$ and $\mathcal{A}_{(0,0)}$ are determined. $\mathrm{R_P}$ can be linked to the collisional frequencies involved in the OH relaxation via the *five-level model* (2.20). For times $\mathrm{t} > \mathrm{t_0}$ after the end of the excitation pulse, the rate equations for $\mathrm{P_{A1}(t)}$ and $\mathrm{P_{A0}(t)}$ can be solved analytically

$$\begin{cases} \mathrm{P_{A1}(t)} & = \mathrm{P_{A1}(t_0)e^{-\Gamma_1(t-t0)}} \\ \mathrm{P_{A0}(t)} & = \left[\mathrm{P_{A0}(t_0)} + \frac{\mathcal{V}_{1\to0}}{\Gamma_1-\Gamma_0}\mathrm{P_{A1}(t_0)}\right] \mathrm{e^{-\Gamma_0(t-t0)}} - \frac{\mathcal{V}_{1\to0}}{\Gamma_1-\Gamma_0}\mathrm{e^{-\Gamma_1(t-t0)}} \\ & \simeq \frac{\mathcal{V}_{1\to0}}{\Gamma_1-\Gamma_0}\mathrm{P_{A1}(t_0)}\left(\mathrm{e^{-\Gamma_0(t-t0)}} - \mathrm{e^{-\Gamma_1(t-t0)}}\right) \end{cases} \tag{2.28}$$

in which the approximation assumes a negligible $\mathrm{P_{A0}(t_0)}$. The integration of equations (2.28) returns the population ratio

$$\begin{aligned} \mathrm{R_P} &= \frac{\int_{\mathrm{t_0}}^{\mathrm{t_0+t_g}} \mathrm{P_{A0}(t)}\ \mathrm{dt}}{\int_{\mathrm{t_0}}^{\mathrm{t_0+t_g}} \mathrm{P_{A1}(t)}\ \mathrm{dt}} \\ &= \frac{\mathcal{V}_{1\to0}}{\Gamma_0} = \frac{\mathcal{V}_{1\to0}}{\mathcal{Q}_0+\mathcal{A}_0} \overset{\text{(a)}}{=} \frac{\mathrm{k}_{\mathcal{V}_{1\to0}} \cdot \mathrm{n_{coll}}}{\mathrm{k}_{\mathcal{Q}_0} \cdot \mathrm{n_{coll}} + \mathcal{A}_0} \end{aligned} \tag{2.29}$$

in which equality (a) is due to the definition of quenching frequencies as the product between the collisional rate coefficients (small k) and the collider density $\mathrm{n_{coll}}$

$$\mathcal{V}_{1\to0} = \mathrm{k}_{\mathcal{V}_{1\to0}} \cdot \mathrm{n_{coll}} \qquad \mathcal{Q}_0 = \mathrm{k}_{\mathcal{Q}_0} \cdot \mathrm{n_{coll}} \tag{2.30}$$

In systems at atmospheric pressure, with predominance of molecular gases, it is frequently achieved that $\mathcal{A}_0 \ll \mathcal{Q}_0$. Under such circumstances, equation (2.29) can be approximated to

$$\mathrm{R_P} \simeq \frac{\mathrm{k}_{\mathcal{V}_{1\to0}}}{\mathrm{k}_{\mathcal{Q}_0}} \tag{2.31}$$

and for a mixture with N components equation (2.31) is generalized to

$$\mathrm{R_P} \simeq \frac{\sum_{\mathrm{i}=1}^{\mathrm{N}} \mathrm{k}^{\mathrm{i}}_{\mathcal{V}_{1\to0}}\ \chi_{\mathrm{i}}}{\sum_{\mathrm{i}=1}^{\mathrm{N}} \mathrm{k}^{\mathrm{i}}_{\mathcal{Q}_0}\ \chi_{\mathrm{i}}} \tag{2.32}$$

where χ_{i} are the molar fractions of the single gas components and k^{i} are the collisional rate coefficients of the i-th species. With this appoximation, the population ratio (2.32) is determined by the total VET over $\mathcal{Q}_0$ frequencies ratio. Since both frequencies depend linearly on the gas density, the ratio is independent of the total gas pressure and depends on the gas composition and temperature via the temperature dependence of the rate coefficients. This fact can be exploited when the gas components have markedly different $\mathrm{k}_{\mathcal{V}_{1\to0}}$ and $\mathrm{k}_{\mathcal{Q}_0}$ values, so that the measured population ratio is sensitive to variations in the gas composition and molar fractions χ_{i} can be derived.

The CET-LIF procedure is completed by measuring the LIF fluorescence pulse $\mathcal{S}(\mathrm{t})$, which is informative on the absolute concentration of the gas. However, equation (2.32) is established even when the fluorescence pulse is shorter or comparable to the laser pulse duration t_0, i.e. when no solutions of (2.28) extending beyond t_0 can be found and the LIF pulse is not accessible for absolute determinations. This is the case of an AP NRP discharge, in which the non-radiative quenching rates shorten the fluorescence pulse to a sub ns time-scale, well below the laser pulse duration achievable with standard instrumentation.

2.4.1 CET-LIF in an AP CO_2 NRP discharge

Atmospheric pressure NRP discharges are promising devices for both $\mathrm{CO_2}$ conversion and dry-reforming [62] [63] [56] [64]. Because $\mathrm{CO_2}$ dissociation is the main obstacle to any process dealing with $\mathrm{CO_2}$ conversion into value-added products, a full understanding of its mechanisms is crucial. Investigation of NRP discharges in $\mathrm{CO_2}$ with a small amount of water represents the perfect field of application of the CET-LIF method, on account of the relatively simple gas mixtures that are formed in these systems and the presence of OH as dissociation product.

In the specific case of a $CO_2 + H_2O$ mixture at atmospheric pressure treated by NRP discharges, the gas composition is defined by the dissociation reaction

$$2CO_2 \longrightarrow 2CO + O_2 \tag{2.33}$$

The components of the gas mixture are then given by

$$\begin{aligned} \chi_{CO_2} &= \frac{(1-\alpha)\,\chi^0_{CO_2}}{\left(1+\frac{\alpha}{2}\right)\chi^0_{CO_2} + \chi^0_{H_2O}} \qquad & \chi_{CO} &= \frac{\alpha\chi^0_{CO_2}}{\left(1+\frac{\alpha}{2}\right)\chi^0_{CO_2} + \chi^0_{H_2O}} \\ \chi_{O_2} &= \frac{\frac{\alpha}{2}\chi^0_{CO_2}}{\left(1+\frac{\alpha}{2}\right)\chi^0_{CO_2} + \chi^0_{H_2O}} \qquad & \chi_{H_2O} &= \frac{\chi^0_{H_2O}}{\left(1+\frac{\alpha}{2}\right)\chi^0_{CO_2} + \chi^0_{H_2O}} \end{aligned} \tag{2.34}$$

where $\chi^0_{CO_2}$ and $\chi^0_{H_2O}$ are the initial molar fractions of water and carbon dioxide, respectively. α is the dissociation degree of CO_2 defined by the formula

$$CO_2 \longrightarrow (1-\alpha)\ CO_2 + \alpha\ CO + \frac{\alpha}{2}\ O_2 \tag{2.35}$$

In the stoichometric mixture (2.34), the measurable band ratio can be expressed as a function of the sole α in agreement with

$$R_B \simeq \frac{\mathcal{A}_{(0,0)}}{\mathcal{A}_{(1,1)}} \frac{\left[(1-\alpha)\ k^{CO_2}_{\mathcal{Q}_0} + \alpha\ k^{CO}_{\mathcal{Q}_0} + \frac{\alpha}{2}\ k^{O_2}_{\mathcal{Q}_0}\right]\chi_{CO_2} \quad + \ k^{H_2O}_{\mathcal{Q}_0}\chi_{H_2O}}{\left[(1-\alpha)\ k^{CO_2}_{\mathcal{V}_{1\to0}} + \alpha\ k^{CO}_{\mathcal{V}_{1\to0}} + \frac{\alpha}{2}\ k^{O_2}_{\mathcal{V}_{1\to0}}\right]\chi_{CO_2} + k^{H_2O}_{\mathcal{V}_{1\to0}}\chi_{H_2O}} \tag{2.36}$$

where k quantities are the OH collisional rate coefficients of the correspondent energy trasfer processes.

The validity of the CET-LIF methodology relies on the possibility of unambiguously calculating the dissociation α from the measurement of R_B, provided the collisional rate coefficients and the chemical composition of the mixture are known quantitatively. A plot of equation (2.36) for various $CO_2 + H_2O$ mixtures is displayed in figure 2.6, based on the rate coefficients measured in [52].

As clearly shown in the figure, R_B is a marker of the dissociation degree α since it decreases with increasing α. This behavior is due to the lower $\frac{k_{\mathcal{V}_{1\to0}}}{k_{\mathcal{Q}_0}}$ ratio for both CO and O_2 with respect to CO_2. Because the relation between R_B and α is monotonous, the only limitation to this method is given by its sensitivity, i.e. the rate of variation of R_B with α. The sensitivity of CET-LIF methodology is most pronounced when the gas components have markedly different rate coefficient values so that single species peculiarities are most distinguishable in the fluorescence spectra. Water addition, on

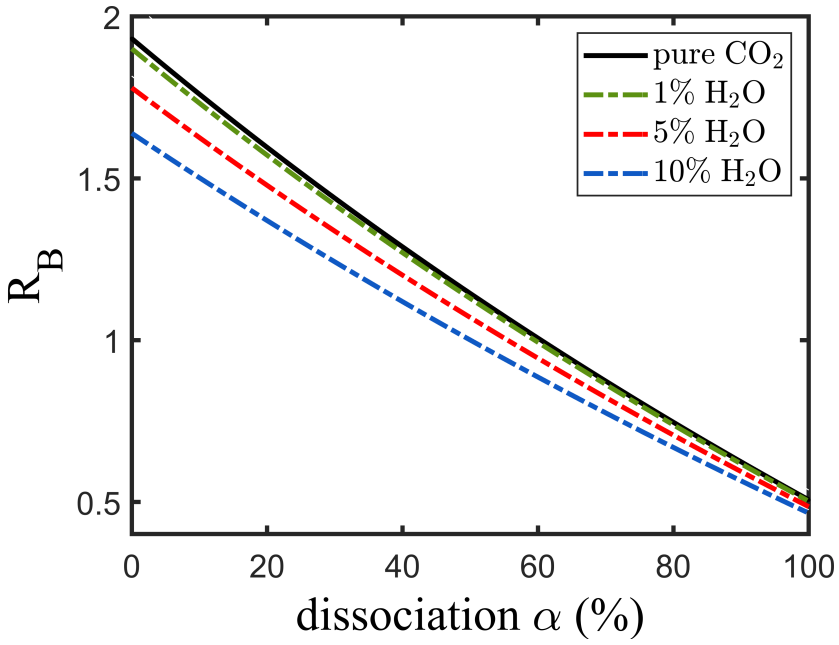

FIGURE 2.6: *Simulation of the band ratio* $\mathrm{R_B}$ *as a function of* $\mathrm{CO_2}$ *dissociation* α *for different water additions:* 1%, 5% *and* 10%. *Simulation temperature* 300 K.

the other hand, although necessary for OH generation, has the effect of lowering the diagnostics sensitivity. This is shown in figure 2.6, in which smaller dynamic ranges are gradually observed upon increasing the water content in the mixture. Besides, water presence alters the band ratio value on account of its very low $\frac{k_{\nu_{1\to0}}}{k_{Q_0}}$ ratio than CO_2, CO, and O_2 ones. This fact is critical when water amount is not known precisely since α gets underestimated in a not quantifiable way. For these reasons, it is advisable to lower the water content in the mixture to a level that ensures OH detection but limits deviations from the pure CO_2 condition.

The application of the CET-LIF method to a NRP CO_2 discharge, as well as the derivation of formula (2.36), assumes that reaction (2.33) completely defines the gas mixture composition. The robustness of the CET-LIF method might then be prejudiced if other species were formed in the discharge environment, since this would impact on the $\mathrm{R_B}$ values and the estimated conversions in an uncontrolled way. Take for instance the formation of O atoms, which results directly from CO_2 dissociation. It is reasonable to assume that a fraction of such oxygen atoms does not recombine to form O_2,

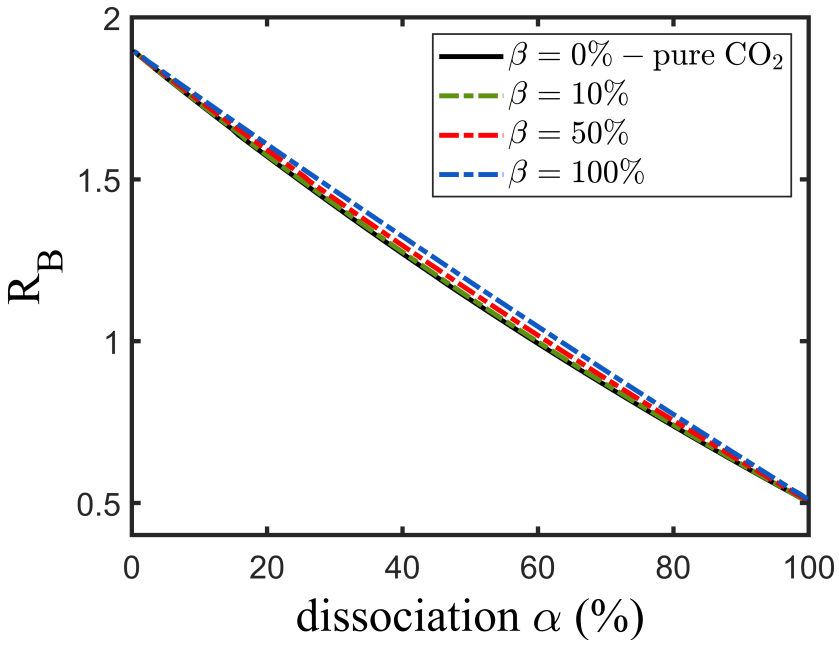

FIGURE 2.7: *Simulation of the band ratio* $\mathrm{R_B}$ *as a function of* $\mathrm{CO_2}$ *dissociation* α *for different* $\mathrm{O_2}$ *dissociations* β*:* 10%*,* 50% *and* 100%*. Simulation temperature* 300 K*.*

but survives in the plasma region since oxygens are lost more effectively via surface recombinations [65] [66]. The fraction β of unrecombined O atoms is defined by the formula

$$\mathrm{O} \longrightarrow \beta\ \mathrm{O} + \frac{1-\beta}{2}\ \mathrm{O_2} \tag{2.37}$$

In the presence of residual atomic oxygen, equation (2.36) must be modified to account for a different mixture composition, parametrized by both α and β. Illustrative plots of $\mathrm{R_B}$ for various β values are shown in figure 2.7, obtained under the hypothesis that light atomic species, including O, have negligible collisional rate coefficients with respect to molecular species [67]. Given the small impact of oxygen formation on the total conversion rates ($< 4\%$), the assumption of the stoichometric mixture (2.34) is justified. Finally, it should be remarked that oxygen atoms could, in principle, be formed by CO dissociation as well. However, due to the similar $\frac{\mathrm{k}_{\mathcal{V}_{1\to 0}}}{\mathrm{k}_{\mathcal{Q}_0}}$ ratios between $\mathrm{O_2}$ and CO, the effect of the two reactions on the measurable band ratio would be comparable.

2.5 Spectroscopic nomenclature

The nomenclature adopted for states and transitions follows the one used by Luque and Crosley in the LIFBASE tool [54] and by Brown and Carrington in [68]:

- $\hat{\mathbf{L}}$ denotes the electronic angular momentum operator. As opposed to atoms, the lack of spherical symmetry in a diatomic molecule invalidates the relation $[\hat{\mathbf{L}}^{\mathbf{2}},\hat{\mathrm{H}}] = 0$, and L ceases to be a good quantum number. The precession of $\hat{\mathbf{L}}$ about the internuclear axis leads to defined components of its projection along the axis, $\hat{\mathbf{\Lambda}}$, which assume the values

  $$\Lambda = 0, 1, 2, .., \mathrm{L}$$

  States with $\Lambda = 0, 1, 2, 3, ..$ are termed $\Sigma, \Pi, \Delta, \Phi, ..$ states;

- $\hat{\mathbf{S}}$ is the electronic spin angular momentum operator, with quantum number S. In all the states with nonzero angular momentum ($\Lambda \neq \Sigma$), $\hat{\mathbf{S}}$ is coupled to the internal magnetic field resulting from the orbital motion of the electrons. The precession of $\hat{\mathbf{S}}$ about the internuclear axis results in defined components of its projection along the axis, $\hat{\mathbf{\Sigma}}$, with values

  $$\Sigma = -\mathrm{S}, -\mathrm{S}+1, .., \mathrm{S}-1, \mathrm{S}$$

- $\hat{\mathbf{J}}$ is the total electronic angular momentum operator, obtained by adding $\hat{\mathbf{L}}$ and $\hat{\mathbf{S}}$. Because the vectors $\hat{\mathbf{\Lambda}}$ and $\hat{\mathbf{\Sigma}}$ both lie along the internuclear axis, the axial component of $\hat{\mathbf{J}}$, $\hat{\mathbf{\Omega}}$, assumes the values

  $$\Omega = |\Lambda + \Sigma|$$

- $\hat{\mathbf{N}} = \hat{\mathbf{J}} - \hat{\mathbf{S}}$ is the total angular momentum operator apart from spin;

- $\hat{\mathbf{R}}$ is the rotational angular momentum operator of the nuclei;

- $\hat{\boldsymbol{\sigma}}$ is the reflection operator with respect to any plane containing the internuclear axis, which are planes of symmetry in diatomic molecules. The electronic wavefunction of a non-degenerate state (Σ states) remains either unchanged or only changes sign when reflected at any of these planes. In the first case the state is termed a Σ^+ state, in the second case a Σ^- state.

- $\hat{\mathbf{I}}$ is the inversion operator through a centre of symmetry of the molecule. For molecules with a center of inversion, the electronic wavefunction remains either unchanged or only changes sign when reflected at the centre. In the first case the wavefunction is said to be in an even state, or *gerade* (g), in the second case in an odd state, or *ungerade* (u).

The state of a diatomic molecule is defined by the term symbol

$$^{2\mathrm{S}+1}\Lambda^{(+/-)}_{\Omega,(\mathrm{g/u})} \tag{2.38}$$

An additional letter $\mathrm{X}, \mathrm{A}, \mathrm{B}, \mathrm{C}, ..$ preceding the state denotes the ground state, the first, second, third,.. excited state, respectiely.

2.5.1 Hund's cases

The mutual interaction between the electronic motion and the nuclear rotation determines different coupling conditions between the angular momenta in the molecule. The possible coupling cases, known as *Hund's cases*, are outlined in [69]. A brief description of (a) and (b) cases is given in the following paragraphs.

Hund's case (a) In this scheme, shown in figure 2.8 (left), the electronic motion is coupled very strongly to the internuclear axis through spin-orbit coupling, while the interaction between the nuclear rotation and the electronic motion is weak. Both $\hat{\mathbf{L}}$ and $\hat{\mathbf{S}}$ precess rapidly about the internuclear axis with defined axis components Λ and Σ, respectively. The total angular momentum $\hat{\mathbf{\Omega}}$ is then also well defined with axial component Ω. $\hat{\mathbf{\Omega}}$ adds to $\hat{\mathbf{R}}$ to give the total angular momentum $\hat{\mathbf{J}}$. Basis functions in this coupling scheme are written in the form $|\Lambda, \Sigma, \Omega, \mathrm{J}\rangle$ and J describes the rotational kinetics [68]. Each fine-structure state with a given Ω has a pattern of rotational levels

$$\mathrm{J} = \Omega, \Omega + 1, \Omega + 2, ..$$

Hund's case (b) In this scheme, shown in figure 2.8 (right), a weak or zero coupling exists between $\hat{\mathbf{S}}$ and the internuclear axis. In this case, $\hat{\mathbf{L}}$ precesses rapidly about the internuclear axis with a well-defined axis component Λ. $\hat{\mathbf{\Lambda}}$ adds to $\hat{\mathbf{R}}$ to form $\hat{\mathbf{N}}$. The coupling between $\hat{\mathbf{N}}$ and $\hat{\mathbf{S}}$ gives the total angular momentum including spin $\hat{\mathbf{J}}$. Basis functions in this coupling scheme are written in the form $|\Lambda, \mathrm{S}, \mathrm{N}, \mathrm{J}\rangle$ and the

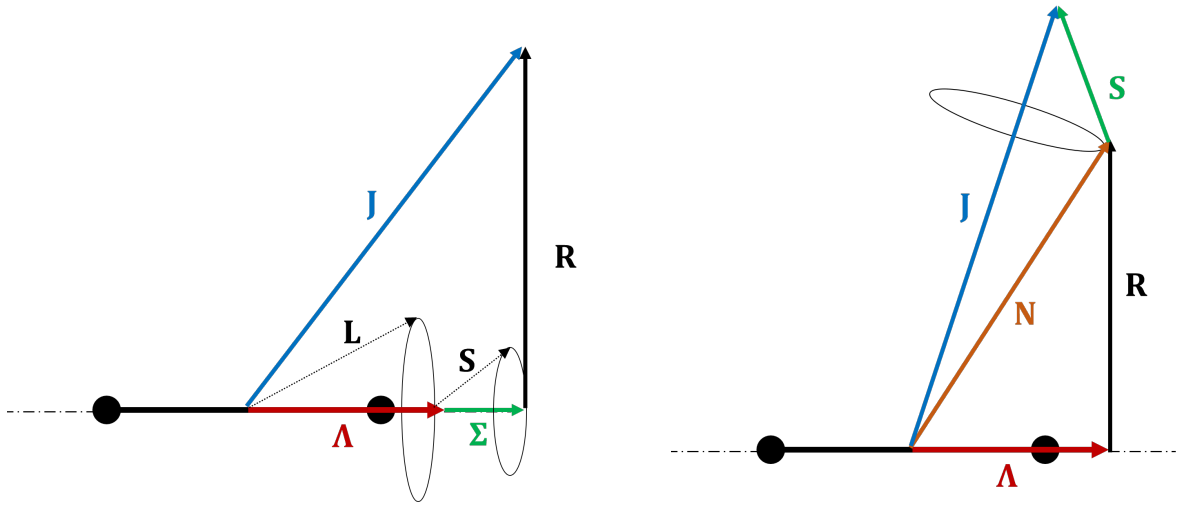

FIGURE 2.8: *left: Hund's coupling case (a). right: Hund's coupling case (b). See text for symbols explanation.*

quantum number N describes the rotational kinetics [68]. Because of the existing coupling between $\hat{\mathbf{N}}$ and $\hat{\mathbf{S}}$, each level with a given N consists of $2\mathrm{S}+1$ components according to

$$\mathrm{J} = \mathrm{K}+\mathrm{S}, \mathrm{K}+\mathrm{S}-1, ..., |\mathrm{K}-\mathrm{S}|$$

2.5.2 OH A $^2\Sigma^+ \leftrightarrow$ X $^2\Pi$ transitions

In the case of X $^2\Pi \leftrightarrow$ A $^2\Sigma^+$ transitions of OH, A $^2\Sigma^+$ belongs to Hund's case (b), while X $^2\Pi$ is intermediate between cases (a) and (b), depending on the operating temperature. Case (b) provides a reasonably good description of X $^2\Pi$ in the investigated temperature conditions [69]:

- the OH ground state X $^2\Pi$ is split by a weak spin-rotation coupling into the two sub-manifolds $\mathrm{J} = \mathrm{N} \pm \frac{1}{2}$. Typical in Hund's case (b) is that the $\mathrm{F}_1 - \mathrm{F}_2$ separation is small compared to the Ns separation. Λ-doubling further splits each level into $+/-$ levels, yielding to four rotational manifolds for a each N [69].;
- the OH first excited state A $^2\Sigma^+$ is split into the two sub-manifolds $\mathrm{J} = \mathrm{N} \pm \frac{1}{2}$, but no further doubling occurs because $\Lambda = 0$.

In Hund's case (b), the classification of ro-vibronic transitions is in the form [54]

$$\Delta N_{F'F''}(N'') \tag{2.39}$$

where primed $(')$ and doubly-primed $('')$ quantum numbers refer to the high-energy and low-energy state of the transition, respectively. $\Delta N = N' - N''$ is termed *rotational branch* of the transition. Five branches are allowed by the selection rules

$$\Delta N = -2, -1, 0, 1, 2 \equiv O, P, Q, R, S \tag{2.40}$$

The F subscripts label the sub-manifolds generated by the spin-rotation coupling in the two states. $F = 1$ (or F_1) corresponds to the series $J = N + \frac{1}{2}$, $F = 2$ (or F_2) to the $J = N - \frac{1}{2}$ series. Figure 2.9 gives a pictorial out-of-scale representation of the $P_1(3)$ transition line at 2830.09 Å, following the selection rules detailed in [69].

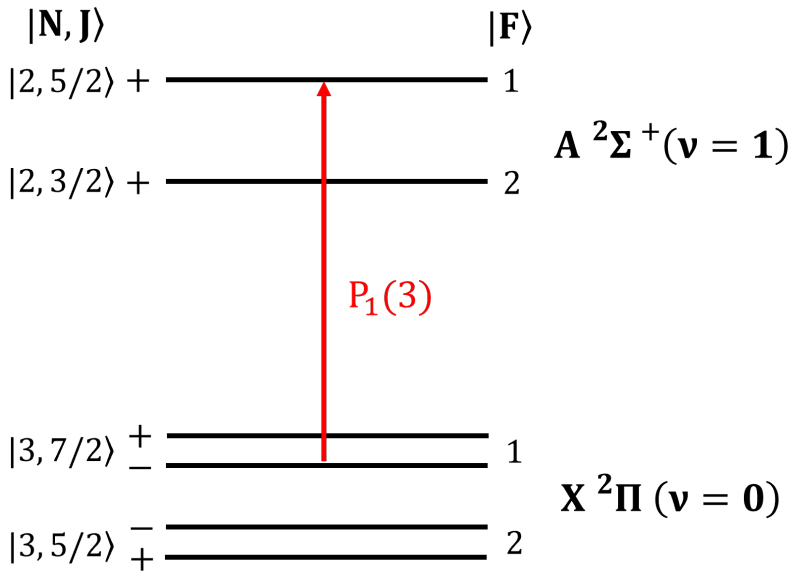

FIGURE 2.9: *Scheme of the* $P_1(3)$ *transition line at* 2830.09 *Å.* N, J *and* F *quantum numbers are reported, with parity labels of the states [69].*

Chapter 3

Measurement of non-thermal collisional rate coefficients

Knowledge of energy-transfer processes is essential for the application of CET-LIF in a quantitative way. Rate coefficients of energy-transfer processes have a marked dependence on the rotational state. Consequently, the degree of rotational thermalization of the emitting state conditions the choice of the right set of rate coefficients that should be employed for quantitative determinations. Rotational thermalization is ruled by the balance between rotational energy-transfer (RET), which redistributes the population within a rotational manifold, and electronic quenching (EQ), which depopulates the state. In a thermalized condition, the emission of a whole vibrational band decays with an effective rate determined by the fast-decaying states, as energy redistribution within the manifold is fast. By contrast, the absence of rotational thermalization results in the almost-independent emission of each rotational state. Application of CET-LIF to $\mathrm{CO_2}$ *discharges suffers from a lack of suitable collisional data, since the available rate coefficients refer to a thermalised condition at* $300\ K$*, which is not met in* $\mathrm{CO_2 + CO + O_2}$ *mixtures. Furthermore, the temperature dependence of the rate coefficients, which needs to be considered to account for the large temperature changes observed in an electrical discharge, is not present in the literature. In this chapter, the measurement of collisional rate constants of the* $\mathrm{OH(A\ ^2\Sigma^+}, v = 0, 1)$ *manifold and their temperature dependence over a wide range is presented in the case of poor rotational thermalization of the emitting state. The new set of collisional data is then used to infer levels of* $\mathrm{CO_2}$ *dissociation in both an atmospheric pressure NRP* $\mathrm{CO_2}$ *discharge and a low-pressure* $\mathrm{CO_2 + H_2O}$ *glow discharge by CET-LIF.*

3.1 State rotational thermalization

Collisional rate coefficients have a marked dependence on the rotational state [70] [71]. Because of this, a definite rotational distribution must be specified to assign a collision rate constant to a given vibrational level [52]. Two counteracting processes rule the thermalization of an excited molecular state: total quenching and RET, with rates Γ and $\mathrm{K_R}$, respectively. The former prevents thermalization from occurring, as it depopulates the levels non radiatively and shortens the state lifetime. The latter drives thermalization, since it redistributes the population within the rotational manifold. The balance between the two defines the degree of thermalization of the state. Two collisional regimes can be classified:

I. *collisional, thermal*. $\mathcal{Q}^{\mathrm{e}}, \mathcal{V} \gtrsim \mathcal{A}$; $\mathrm{K_R} \gg \Gamma = \mathcal{Q}^{\mathrm{e}} + \mathcal{V} + \mathcal{A}$
The quick occurrence of energy-transfer within the excited state lifetime greatly influences the spectral and temporal characteristics of LIF outcomes. Suppose atomic gases like He or Ar are prevalent in a mixture, while molecular gases are present in relatively small amounts. In that case, all emission bands show a Boltzmann rotational distribution thermalized with the gas temperature, because atomic species ensure fast rotational relaxation with negligible contribution to the electronic quenching [53] [72]. Few collisions during the state lifetime are necessary to achieve rotational thermalization. In this condition, the excitation process quickly loses memory of the specific rotational level that is excited within the manifold and the emission of each band decays with an effective rate mostly determined by the fast-decaying rotational states.

II. *collisional, non-thermal*. $\mathcal{Q}^{\mathrm{e}}, \mathcal{V} \gtrsim \mathcal{A}$; $\mathrm{K_R} \lesssim \Gamma = \mathcal{Q}^{\mathrm{e}} + \mathcal{V} + \mathcal{A}$
Because few RET relaxations occur during the state lifetime, thermalization is never achieved during the fluorescence pulse. In this condition, thermal collisional rate coefficients cease to be descriptive as each rotational state radiates independently with its rate. The emission bands show reminiscences of the excitation processes, and LIF outcomes strongly depend on the excitation line used in the detection scheme. This condition is met in discharges in which molecular gases with large quenching rates, such as $\mathrm{CH_4}$, CO or $\mathrm{CO_2}$, are the dominant component.

3.1.1 OH thermal fluorescence spectra

In the LIF process (2.20), the collisional regime (I) is satisfied when conditions

$$\mathrm{K_{A1,R}} \gg \Gamma_1 = \mathcal{A}_1 + \mathcal{Q}_1 \qquad \mathrm{K_{A0,R}} \gg \Gamma_0 = \mathcal{A}_0 + \mathcal{Q}_0 \tag{3.1}$$

are met, with $\mathrm{K_{A1,R}}$ and $\mathrm{K_{A0,R}}$ symbolizing the RET relaxation rates of $\mathrm{A1}$ and $\mathrm{A0}$, respectively. A pictorial representation is given in figure 3.1, which shows the normalized OH LIF spectrum obtained from a mixture containing 4 Torr $\mathrm{CO_2} + 0.75$ Torr $\mathrm{H_2O}$ and He as a buffer gas. The data refer to the atmospheric pressure NRP-DBD described

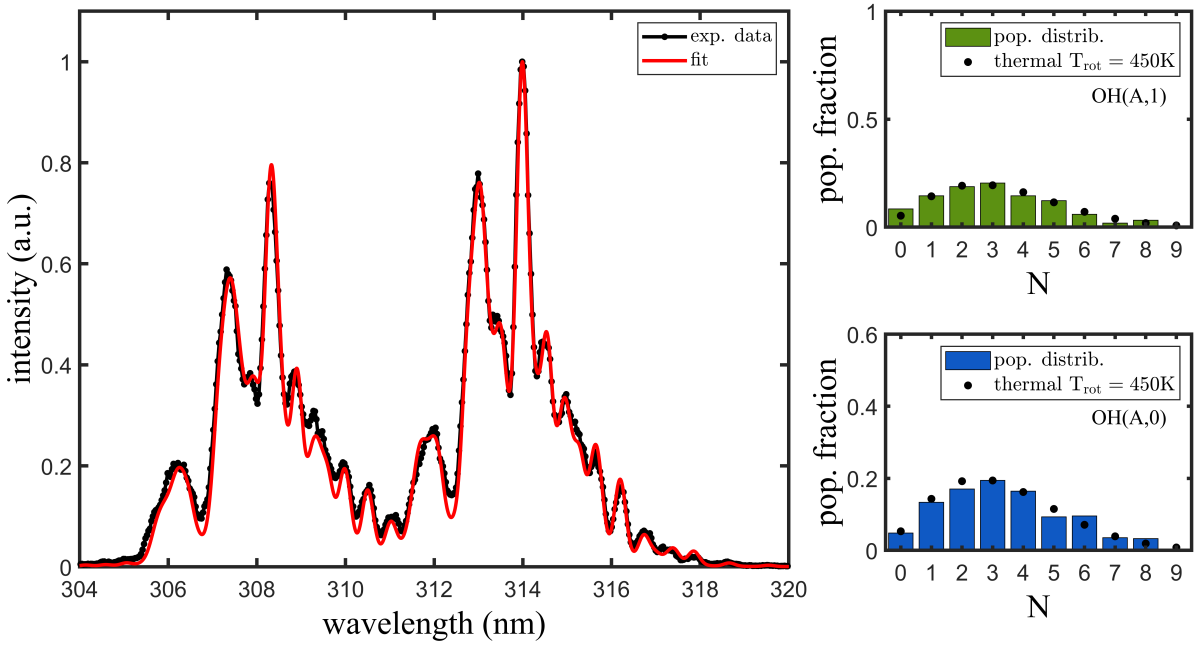

FIGURE 3.1: OH *fluorescence spectrum in a* 4 Torr $\mathrm{CO_2} + 0.75$ Torr $\mathrm{H_2O}$ *mixture in an AP NRP-DBD with He buffer gas. The spectrum is collected at* 200 μs *after the discharge breakdown. Excitation of the* $\mathrm{Q_2(3)}$ *line at* 2829.37 *Å is performed. The solid red line shows the fit of the experimental data. The histograms show the fitted rotational distributions of* $\mathrm{OH(A,1)}$ *and* $\mathrm{OH(A,0)}$ *states. The black dots display the Boltzmann distribution with* $\mathrm{T_{rot}} = 450$ K.

in [60], in which the $\mathrm{Q_2(3)}$ line at 2829.37 Å is excited. A routine that uses the spectroscopic data taken from LIFBASE tool [54] determines the population distributions of $\mathrm{OH(A,1)}$ and $\mathrm{OH(A,0)}$ that better reproduce the experimental spectrum. With this procedure, the histograms of figure 3.1 are obtained. Because the emitting states are

rotationally thermalized, both bands are well reproduced by a population distribution at the gas temperature T_{gas}, in this case $T_{rot} \simeq T_{gas} = 450$ K. No markers of the excitation process are noticeable in the population distribution of state $OH(A, 1)$. Realization of conditions (3.1) is fulfilled thanks to

- total RET frequencies

$$K_{A1,R} = K^{He}_{A1,R} + K^{CO_2}_{A1,R} + K^{H_20}_{A1,R} > 2.4 \cdot 10^9 \text{ s}^{-1}$$

$$K_{A0,R} = K^{He}_{A0,R} + K^{CO_2}_{A0,R} + K^{H_20}_{A0,R} > 2.4 \cdot 10^9 \text{ s}^{-1}$$

for states $OH(A, 1)$ and $OH(A, 0)$, respectively. Tables 3.1-3.2 summarize the individual species contributions to the total rates, calculated, when possible, as

collider	**rate coefficient k_R (cm^3s^{-1})**	**density (cm^{-3})**	**rate K_R (s^{-1})**
He	$(1.0 - 2.0) \cdot 10^{-10}$ [53]	$2.4 \cdot 10^{19}$	$(2.4 - 4.8) \cdot 10^9$
CO_2	not known	$1.3 \cdot 10^{17}$	not known
H_2O	$9.1 \cdot 10^{-10}$ [73]	$2.4 \cdot 10^{16}$	$2.2 \cdot 10^7$

TABLE 3.1: *Individual species contributions to total RET* $K_{A1,R}$. *Considered partial pressures are* $p^{He} = 755.25$ Torr, $p^{CO_2} = 4.00$ Torr *and* $p^{H_2O} = 0.75$ Torr.

collider	**rate coefficient k_R (cm^3s^{-1})**	**density (cm^{-3})**	**rate K_R (s^{-1})**
He	$(1.0 - 2.0) \cdot 10^{-10}$ [53]	$2.4 \cdot 10^{19}$	$(2.4 - 4.8) \cdot 10^9$
CO_2	not known	$1.3 \cdot 10^{17}$	not known
H_2O	not known	$2.4 \cdot 10^{16}$	not known

TABLE 3.2: *Individual species contributions to total RET* $K_{A0,R}$. *Considered partial pressures are* $p^{He} = 755.25$ Torr, $p^{CO_2} = 4.00$ Torr *and* $p^{H_2O} = 0.75$ Torr.

the product of the collisional rate coefficient and the collider density. The contributions of dissociation products CO and O_2 are neglected in the calculation. This can be safely assumed, as the estimated CO_2 dissociation lays around only 5% [60], and collisional rate coefficients of both CO and O_2 are of the same order of magnitude of the CO_2 ones;

- total quenching frequencies

$$\Gamma_1 = \mathcal{A}_1 + \mathcal{Q}_1^{\mathrm{He}} + \mathcal{Q}_1^{\mathrm{CO_2}} + \mathcal{Q}_1^{\mathrm{H_2O}} \simeq 9.6 \cdot 10^7 \ \mathrm{s}^{-1}$$

$$\Gamma_0 = \mathcal{A}_0 + \mathcal{Q}_0^{\mathrm{He}} + \mathcal{Q}_0^{\mathrm{CO_2}} + \mathcal{Q}_0^{\mathrm{H_2O}} \simeq 7.8 \cdot 10^7 \ \mathrm{s}^{-1}$$

for states $\mathrm{OH(A,1)}$ and $\mathrm{OH(A,0)}$, respectively. $\mathcal{A}_1 = 1.3 \cdot 10^6 \ \mathrm{s}^{-1}$, $\mathcal{A}_0 = 1.5 \cdot 10^6 \ \mathrm{s}^{-1}$ [53]. Tables 3.3-3.4 summarize the individual species contributions to the total rates.

collider	**rate coefficient $\mathbf{k_{\mathcal{Q}_1}}$ ($\mathbf{cm^3 s^{-1}}$)**	**density ($\mathbf{cm^{-3}}$)**	**rate $\mathcal{Q}_1$ ($\mathbf{s^{-1}}$)**
He	$4.0 \cdot 10^{-14}$ [53]	$2.4 \cdot 10^{19}$	$9.6 \cdot 10^5$
CO_2	$6.1 \cdot 10^{-10}$ [42]	$1.3 \cdot 10^{17}$	$7.9 \cdot 10^7$
H_2O	$6.1 \cdot 10^{-10}$ [42]	$2.4 \cdot 10^{16}$	$1.5 \cdot 10^7$

TABLE 3.3: *Individual species contributions to total quenching Γ_1. Considered partial pressures are $\mathrm{p^{He}} = 755.25$ Torr, $\mathrm{p^{CO_2}} = 4.00$ Torr and $\mathrm{p^{H_2O}} = 0.75$ Torr.*

collider	**rate coefficient $\mathbf{k_{\mathcal{Q}_0}}$ ($\mathbf{cm^3 s^{-1}}$)**	**density ($\mathbf{cm^{-3}}$)**	**rate $\mathcal{Q}_0$ ($\mathbf{s^{-1}}$)**
He	$4.0 \cdot 10^{-14}$ [53]	$2.4 \cdot 10^{19}$	$9.6 \cdot 10^5$
CO_2	$4.6 \cdot 10^{-10}$ [42]	$1.3 \cdot 10^{17}$	$6.0 \cdot 10^7$
H_2O	$6.6 \cdot 10^{-10}$ [42]	$2.4 \cdot 10^{16}$	$1.6 \cdot 10^7$

TABLE 3.4: *Individual species contributions to total quenching Γ_0. Considered partial pressures are $\mathrm{p^{He}} = 755.25$ Torr, $\mathrm{p^{CO_2}} = 4.00$ Torr and $\mathrm{p^{H_2O}} = 0.75$ Torr.*

3.1.2 OH non-thermal fluorescence spectra

Figure 3.2 shows the OH normalized LIF spectrum obtained from a mixture containing 8.25 Torr $CO_2 + 0.15$ Torr H_2O. OH is produced by photofragmentation of H_2O_2 before LIF detection. The $P_1(3)$ line at 2830.09 Å is used. Except for He content, this mixture resembles the collisional nature of the thermalized condition described in figure 3.1, as the same colliders ratio is maintained. Therefore, differences between the two are ascribable to the He contribution.

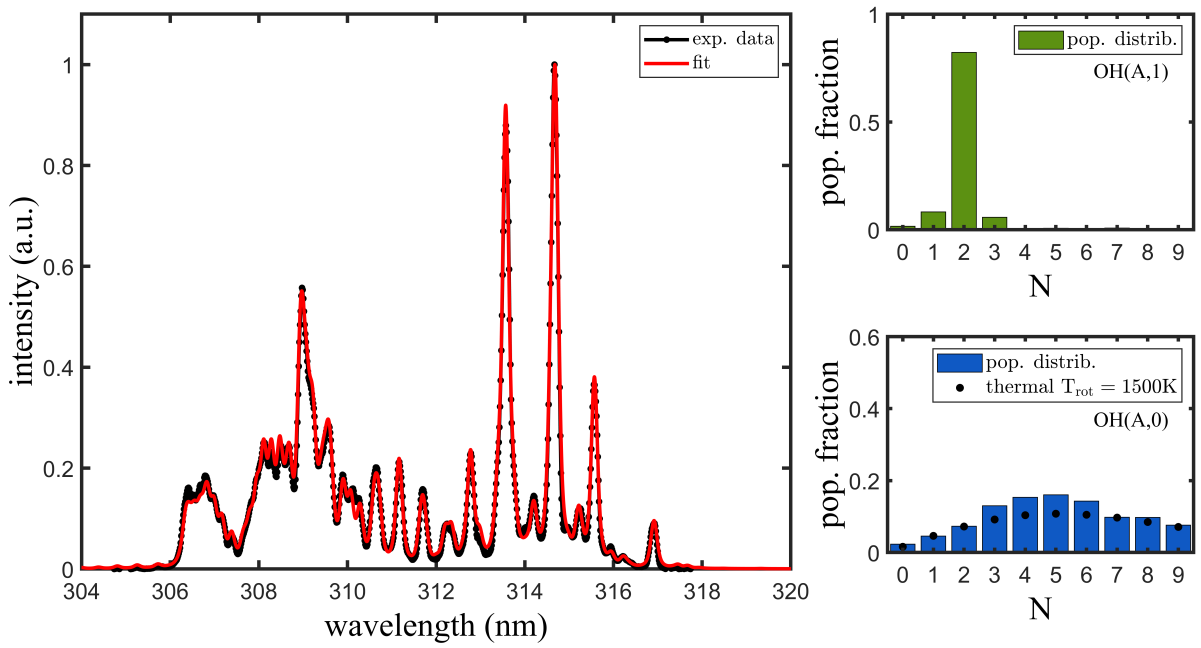

FIGURE 3.2: OH *fluorescence spectrum in a* 8.25 Torr $\mathrm{CO_2} + 0.15$ Torr $\mathrm{H_2O}$ *mixture at room temperature* $\mathrm{T} = 300$ K. *Excitation of the* $\mathrm{P_1(3)}$ *line at* 2830.09 *Å is performed. The simulated spectrum is marked with solid red line and the histograms of the simulated population distributions of* $\mathrm{OH(A,1)}$ *and* $\mathrm{OH(A,0)}$ *are reported. The Boltzmann distribution with* $\mathrm{T_{rot}} = 1500$ K *is shown for comparison with the* $\mathrm{OH(A,0)}$ *distribution.*

OH(A,1) With about 80% of the population emitting from the laser-populated rotational state, the $\mathrm{OH(A,1)}$ distribution presents a strong reminiscence of the excitation process, i.e., the rotational distribution remains 'quasi-nascent' throughout the fluorescence lifetime. This is illustrated in figure 3.3, where three different excitation lines are used. In all cases, the laser-excited state is prominent in the histograms, while RET poorly populates adjacent rotational levels. The degree of rotational thermalization in the three cases seems to depend on the laser-pumped state, most likely due to different quenching rates of the individual rotational states. It is worth pointing out that a deep explanation of the underlying physics would require the knowledge of the RET rate constants, which is not available. Hence, only qualitative interpretations can be given.

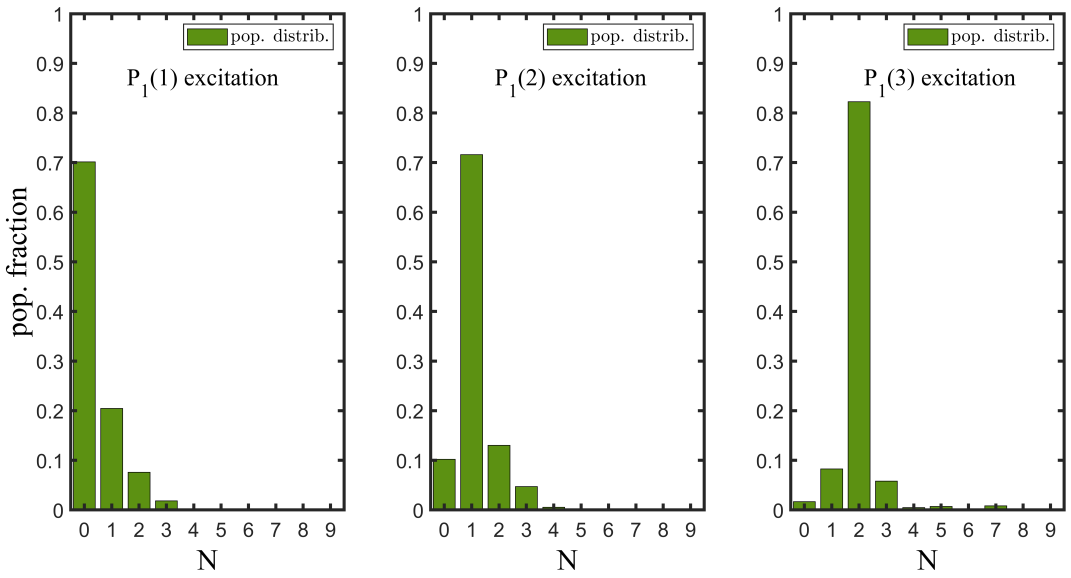

FIGURE 3.3: *Histograms of the simulated* $\mathrm{OH(A,1)}$ *population distributions after excitation of three different* OH *transition lines:* $\mathrm{P_1(1)}$, $\mathrm{P_1(2)}$ *and* $\mathrm{P_1(3)}$. *Data refer to a* 8.25 Torr $\mathrm{CO_2} + 0.15$ Torr $\mathrm{H_2O}$ *mixture at* $\mathrm{T} = 300$ K.

OH(A,0) The histograms corresponding to $\mathrm{OH(A,0)}$ (see figure 3.4), show the 'quasi-nascent' distribution of VET, which populates $\mathrm{OH(A,0)}$. Because the spectrum is time-integrated over the entire fluorescence decay, rotational relaxations affect the fluorescence features within the observation time, and the histogram includes a contribution from both VET and RET. This fact prevents the observation of a purely nascent VET distribution. The rotational distribution of $\mathrm{OH(A,0)}$ presents a supra-thermal behavior, which is only roughly reproduced by a Boltzmann distribution with $\mathrm{T_{rot}} > \mathrm{T_{gas}}$. Because conditions (3.1) are not met, rotational thermalization is inefficient, and a single $\mathrm{T_{rot}}$ ceases to be descriptive. This finding had already been reported in William's work [74], in which the authors could fit the $\mathrm{OH(A,0)}$ rotational distribution with two temperatures.

The supra-thermal nature of the $\mathrm{OH(A,0)}$ distribution results from the accommodation of vibrational quanta into rotational excitation of OH, which inevitably involves high-$\mathrm{N'}$ states, as they are more likely resonant with the vibrational quantum involved. Figure 3.4 compares the $\mathrm{OH(A,0)}$ distributions obtained for excitation of the $\mathrm{P_1(1)}$, $\mathrm{P_1(2)}$ and $\mathrm{P_1(3)}$ transitions. A weak dependence on the pumped level is observed,

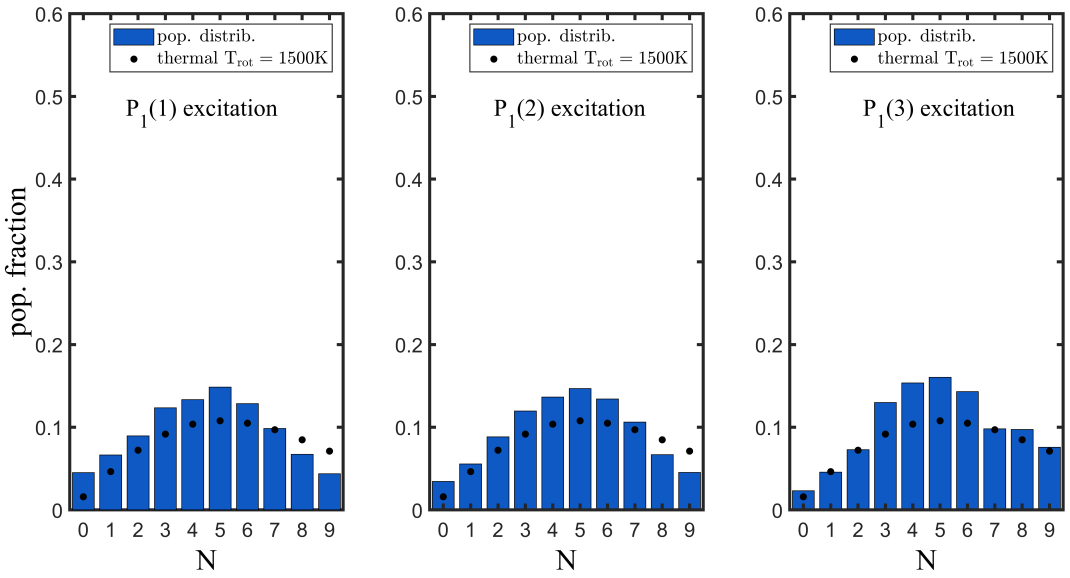

FIGURE 3.4: *Histograms of the simulated* $\mathrm{OH(A,0)}$ *population distributions after excitation of three different* OH *transition lines:* $\mathrm{P_1(1)}$, $\mathrm{P_1(2)}$ *and* $\mathrm{P_1(3)}$. *Data refer to an* 8.25 Torr $\mathrm{CO_2} + 0.15$ Torr $\mathrm{H_2O}$ *mixture at* $\mathrm{T} = 300$ K. *The Boltzmann distribution with* $\mathrm{T_{rot}} = 1500$ K *is shown for comparison.*

partly due to the fitting uncertainty, partly due to a different energy exchange between $\mathrm{OH(A,1)}$ and $\mathrm{OH(A,0)}$ because of different initial distributions in the $\mathrm{OH(A,1)}$ manifold. Again, a complete understanding of the phenomenon would require the knowledge of RET rates for all the colliders.

Collider specificities Non-thermal spectra are measured with $\mathrm{O_2}$, $\mathrm{CH_4}$, CO and $\mathrm{H_2}$ as colliders and the laser wavelength tuned to three lines of the $\mathrm{P_1(N'')}$ branch, $\mathrm{N''} = 1, 2, 3$. The measurements are carried out in a condition in which the collider component is dominant over the $\mathrm{H_2O} + \mathrm{H_2O_2}$ one. Figure 3.5 shows the measured LIF fluorescence spectra, while figure 3.6 displays the simulated population distributions of $\mathrm{OH(A,1)}$ and $\mathrm{OH(A,0)}$. In both figures, excitation of the $\mathrm{P_1(3)}$ line is shown. The reader can refer to the supplementary material file of [52] for the complete dataset. Differences between diverse molecules are ascribable to the nature of the interaction between OH and the colliding partner, and ultimately to a more or less pronounced quenching, VET and RET relaxation condition. The unlike band ratios and distributions in figures 3.5

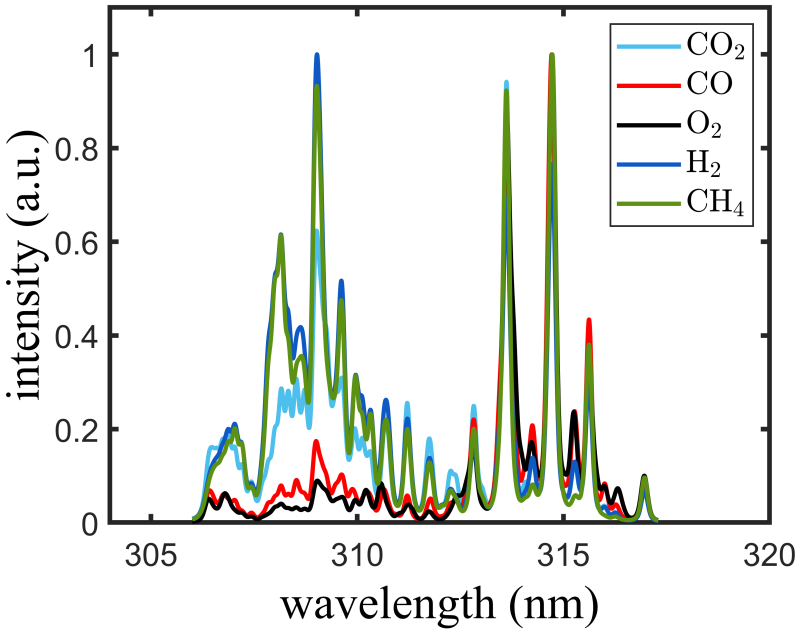

FIGURE 3.5: *Normalized non-thermal fluorescence spectra measured in a cell filled with* 0.15 Torr *of* H_2O_2 *as source of* OH *and about* 1.5 Torr *of collider.* CO_2, CO, O_2, H_2 *and* CH_4 *are used as collider species.*

and 3.6 support this evidence.

Because there is currently no complete understanding of the energy-transfers mechanisms, only the qualitative overall features of the experimental data can be described. For example, different $OH(A, 0)$ rotational distributions seem to be connected with the diverse VET efficiencies of the various colliders. 'Colder' population distributions, like those of H_2 and CH_4, may result from a fast VET exchange between OH and these species. Indeed, VET is fastest when two quasi-resonant states are involved in the exchange so that only little residual energy is available for rotational and translational excitation. $OH(A, 0)$ distributions appear 'colder' in this condition. Conversely, as in the case of O_2 and CO, slow VET can only partially accommodate the OH vibrational energy. A considerable fraction of such excitation then results in rotational excitation, and $OH(A, 0)$ distributions appear 'hotter'. The $OH(A, 1)$ distributions corresponding to various colliders seem to be species-specific, too. Differences might be ascribed to quenching efficiencies for those colliders. Studies on this subject reveal that the formation of complexes by attractive long-range forces governs quenching mechanisms of

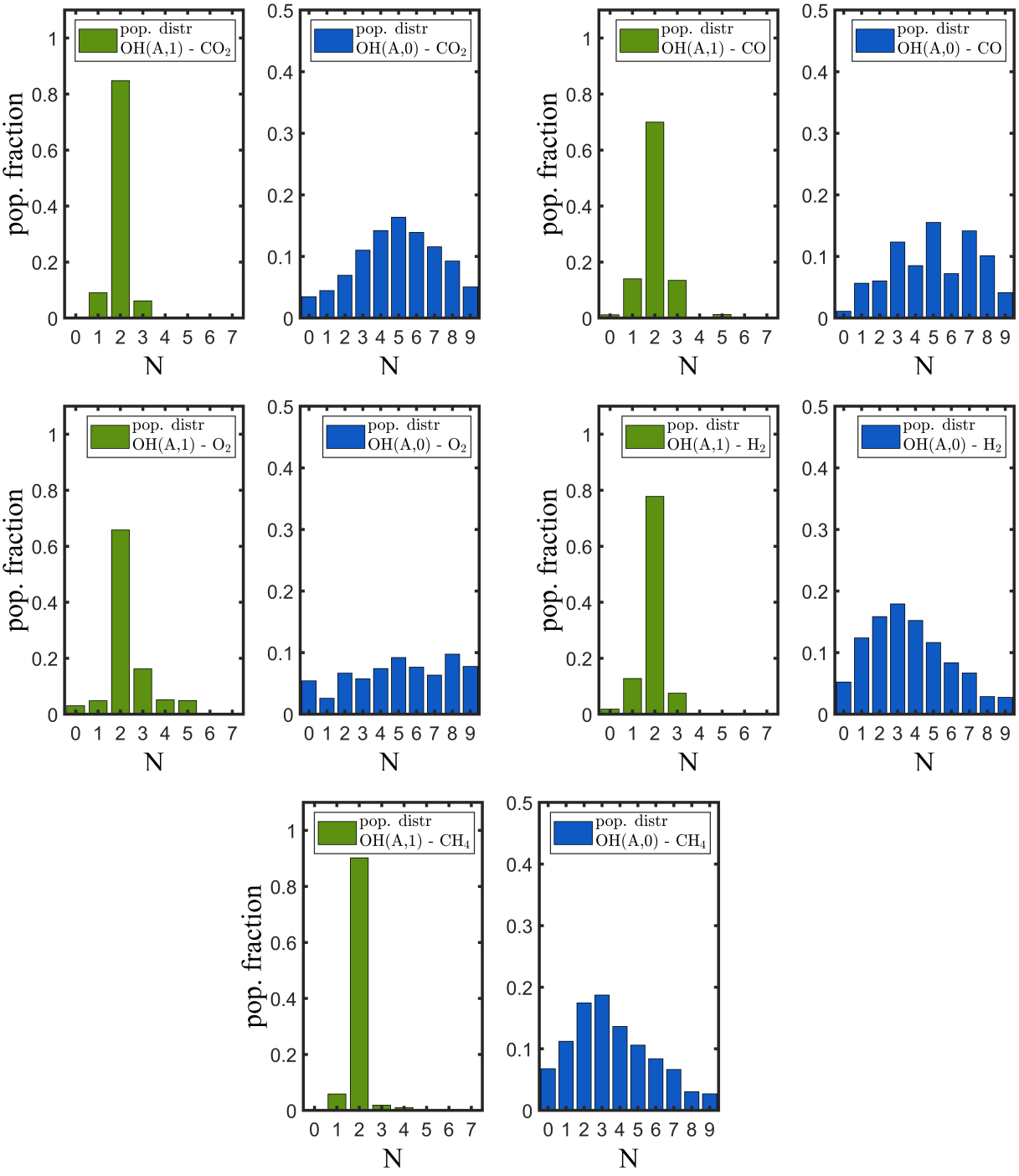

FIGURE 3.6: *Histograms of the simulated population distributions of* $\mathrm{OH(A,1)}$ *(green) and* $\mathrm{OH(A,0)}$ *(blue) states. Measurements are performed in a collisional cell with* 0.15 Torr *of* $\mathrm{H_2O}$ *and approximately* 1.5 Torr *of collider. The* $\mathrm{P_1(3)}$ *transition line is excited at* $\mathrm{T} = 300$ K.

both $\mathrm{OH(A\ ^2\Sigma^+}, v = 0)$ and $\mathrm{OH(A\ ^2\Sigma^+}, v = 1)$ [71] [74]. The potential energy surface of each collider molecule affects the complex-formation in a different way. Species with little tendency to interact with OH are expected to prevent the formation of a complex that leads to quenching. This results in a higher rotational relaxation of the population distributions of OH . This fact is particularly evident for $\mathrm{O_2}$.

3.2 Measurement of collisional rate coefficients of OH

The knowledge of collisional energy-transfer processes is essential to apply LIF quantitatively. However, the current availability of such collisional data is incomplete or absent, as they are often limited to species relevant for atmospheric chemistry only [74] [70] [71] [75]. Documented information on species related to $\mathrm{CO_2}$ dissociation and dry reforming comes from studies performed in combustion research at high temperatures [76], hence not suitable for low-temperature plasma chemistry.

Atmospheric pressure discharges exhibit marked non-equilibrium conditions, with poor rotational thermalization of both $\mathrm{OH(A}, 1)$ and $\mathrm{OH(A}, 0)$ and the impossibility of defining effective rate coefficients of a whole band in a rigorous way [23]. Furthermore, AP NRP discharges with bare metallic electrodes are spark events followed by a quick rise of the gas temperature $\mathrm{T_{gas}}$ in a few hundreds of ns. In [56], LIF thermometry was used to assess the gas temperature evolution in a $\mathrm{CO_2}$ NRP discharge. It was found that $\mathrm{T_{gas}}$ varies in the range from around $2500\ \mathrm{K}$ at $5\ \mu\mathrm{s}$ after the ns voltage pulse down to $1400\ \mathrm{K}$ at $150\ \mu\mathrm{s}$. The full application of CET-LIF to NRP discharges confronts the lack of the suitable non-thermal collisional data in the literature, since the existing collisional data have been measured for a thermalized condition only, mostly at $\mathrm{T} = 300\ \mathrm{K}$ [42]. In this chapter, the measurement of a new set of non-thermal collisional rate constants that includes their temperature dependence is presented.

3.2.1 Experimental procedure and setup considerations

The LIF setup is shown in figure 3.7. The measurements are carried out in a steel cell, with two long-arm Brewster angle windows for laser beam IN and OUT and two short-arm windows for fluorescence collection. The experimental environment is con-

stituted by a fixed amount of $H_2O_2 + H_2O$ vapor in a mixture with a collider gas, whose concentration can be varied to extract kinetic information on $OH(A\ ^2\Sigma^+, v = 0, 1)$ collisions from LIF outcomes. CO_2, CO, O_2, CH_4 and H_2 are used as colliders, due to their significance for both CO_2 conversion and dry reforming studies. The current experiment setup makes use of two separate lasers: the fourth harmonic of a Nd:YAG laser at $266\ \mathrm{nm}$ is used to generate OH by photodissociation of H_2O_2, whereas a second beam tuned to $282\ \mathrm{nm}$ allows for LIF detection according to scheme (2.14). The $P_1(1)$, $P_1(2)$ and $P_1(3)$ rotational lines are alternatively used.

The quantitative determination of the collisional rate coefficients requires that, at a given collider concentration n_{coll}, the OH fluorescence pulse $\mathcal{S}(t)$ (2.24) including the $(1, 1)$ and $(0, 0)$ bands and the spectrum $\mathcal{I}(\lambda)$ (2.22) are measured. The outcomes are then fitted by solving the *five-level model* (2.20), which allows inferring the collisional frequencies and, hence, the collisional rate coefficients. The details of the data analysis procedure are described in section 3.2.2

Laser light generation and manipulation A Spectra-Physics Quanta-Ray GCR-190 Q-switched Nd:YAG laser is used to generate $10\ \mathrm{Hz}$ pulsed radiation at $266\ \mathrm{nm}$ with two thermally-stabilized KDP crystals. The beam energy is approximately $10\ \mathrm{mJ/pulse}$. A second beam, at about $282\ \mathrm{nm}$ and energy of around $150\ \mu\mathrm{J/pulse}$, is obtained by an Nd:YAG-pumped Quantel TDL50 dye laser after frequency doubling. The dye is Rhodamine 590 chloride in a solution with methanol. The beam linewidth is measured to be approximately Lorentzian with an FWHM of about $10^{-3}\ \mathrm{nm}$. The two beams are spatially overlapped by a thin film polarizer (TFP, Eksma Optics 420-1270 UVFS) and sent to the collision cell, where they travel axially. The TFP allows transmitting a single state of polarisation of light while reflecting light with the orthogonal state of polarisation. The geometry of the apparatus is chosen so that the $266\ \mathrm{nm}$ beam is reflected by the polarizer, while the $282\ \mathrm{nm}$ is transmitted. A set of pinholes inside and outside the collision cell avoids scattered light propagation. A delay generator allows for adjustable delay τ_d between the two beams, with a minimum step of $2.5\ \mathrm{ns}$.

Vacuum cell and gas handling A constant flow of H_2O_2 is injected into the cell by bubbling $3\ \mathrm{sccm\ He}$, Φ_{He}, through a vessel filled with $10\ \mathrm{mL}$ of $50\%\ \mathrm{wt}$ aqueous solution of H_2O_2. A proportional-integral-derivative controller (PID) runs a thermal heater that

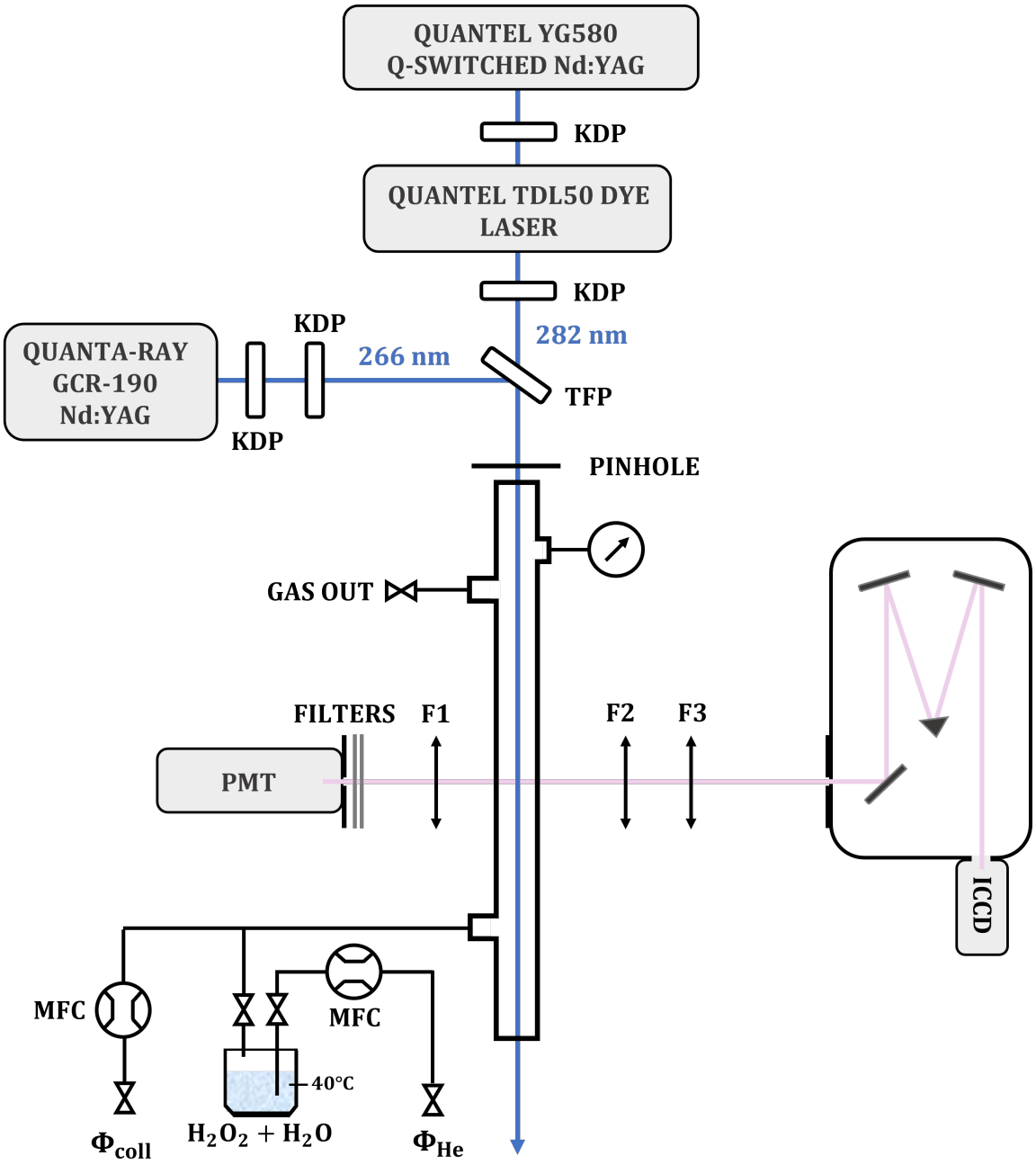

FIGURE 3.7: *Scheme of the experimental apparatus. See text for explanation.*

stabilizes the temperature of the solution at $40\ ^{\circ}\mathrm{C}$ so that the empty region of the vessel is saturated with a constant vapour pressure of $H_2O_2 + H_2O$. A variable flux of collision partner gas Φ_{coll} is added at room temperature. The flows are regulated by MKS mass flow controllers (MFC). The pressure is monitored by a Varian Ceramicel (10 Torr FS)

and a $80\ \frac{\mathrm{m}^3}{\mathrm{h}}$ Edwards two-stage rotary vane pump maintains the cell at a low pressure of few Torr. The collisional partner concentration is determined by the ratio

$$\mathrm{n_{coll}} = \mathrm{n_{tot}}\ \frac{\Phi_{\mathrm{coll}}}{\Phi_{\mathrm{coll}} + \Phi_{\mathrm{He}}} \tag{3.2}$$

where $\mathrm{n_{tot}} = \frac{\mathrm{p}}{\mathrm{k_B\ T}}$ is the total number density in the collision cell. To ensure ideal measurement conditions, it is essential to exclude the formation of any additional species via photodissociation by the laser photons at $266\ \mathrm{nm}$. This possibility is ruled out for all the colliders by examining their dissociation energy values and absorption cross sections at the excitation wavelength of $266\ \mathrm{nm}$ [69] [77] [78] [79].

Detection system Two sensors detect simultaneously the fluorescence light. A photomultiplier (PMT) records the time-resolved, spectrally-integrated LIF pulse $\mathcal{S}(\mathrm{t})$. Two dielectric bandpass filters (Semrock 320-40 and Semrock 315-15) and a bandpass coloured glass filter (Thorlabs FGUV11) are placed in front of the PMT to select the OH $(0,0)$ and $(1,1)$ emission bands. A set of metallic filters (Thorlabs NDUV**B) is also used to avoid saturation effects of the PMT and to maintain it within its linear response regime. The fluorescence light is focused by a $38\ \mathrm{mm}$ focal length lens (F1), which is placed at a distance $2\mathrm{f}$ from both the cell axis and the entrance of the PMT. This ensures that a one-to-one image is projected on the PMT sensor. A slit parallel to the axis propagation direction is placed at the entrance of the PMT to avoid collection of laser scattered light. The signal is measured as a voltage drop across a $50\ \Omega$ resistance of an Agilent Infiniium 54831B oscilloscope, with $600\ \mathrm{MHz}$ bandwidth, sampling at $8\ \mathrm{bit}$ and $4\ \mathrm{GSa/s}$. An Andor DH334-T-18U-03, 1024×1024 pixel intensified CCD detects the spectrally-resolved, time-integrated LIF spectrum $\mathcal{I}(\lambda)$. The ICCD, operated in full vertical binning and with a gating time of $2\ \mu\mathrm{s}$, is coupled with a Shamrock 303i $300\ \mathrm{mm}$ focal length monochromator, equipped with a $2400\ \mathrm{grooves/mm}$ reflective grating. The fluorescence light is collimated by a $50\ \mathrm{mm}$ focal length lens (F2) and focussed onto the spectrograph entrance slit by a $75\ \mathrm{mm}$ positive lens (F3).

3.2.2 Data analysis

The experimental data are analysed by an in-house-developed MATLAB code. The routine requires some preparatory pre-processing steps:

1. both $\mathcal{S}(\mathrm{t})$ and $\mathcal{I}(\lambda)$ are obtained as averages of the raw data. Few thousand averages ensure a sufficiently good signal-to-noise ratio;

2. the LIF spectrum $\mathcal{I}(\lambda)$ is rescaled to account for the spectral response $\mathrm{T}(\lambda)$ of the ICCD, yielding to a modified spectrum according to

$$\mathcal{I}(\lambda)^{\mathrm{mod}} = \frac{\mathcal{I}(\lambda)}{\mathrm{T}(\lambda)} \tag{3.3}$$

This operation is essential to prevent errors in the estimation of both the band ratio and the solution of the *five-level model*. The characterization of the ICCD is achieved by selectively illuminating different regions of the detector by a constant light source, provided by A UVTOP305-FW-SMD LED. The light intensity measured at different pixels is then normalized to its maximum, and the transmission function can be calculated. The plot of the measured $\mathrm{T}(\lambda)$ is shown in figure 3.8 (left);

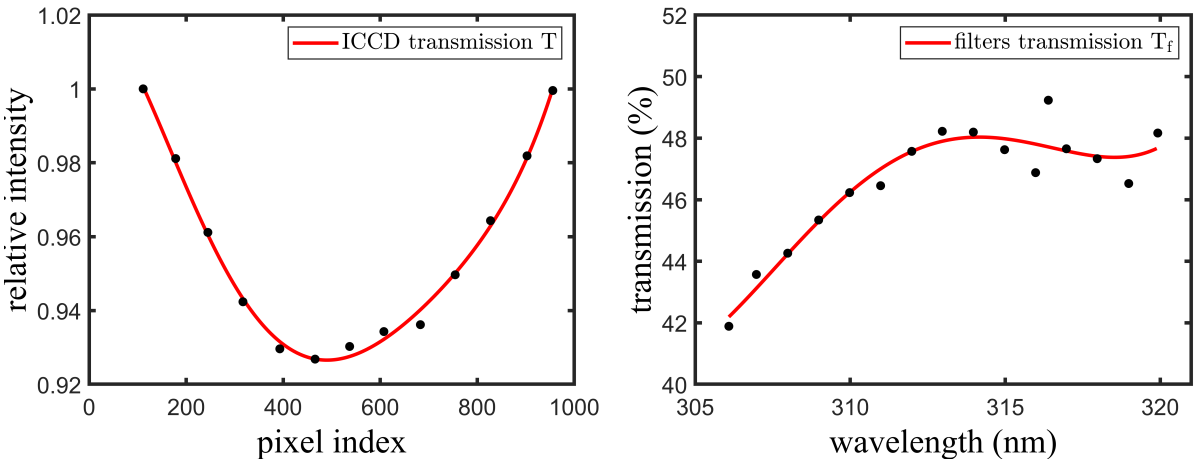

FIGURE 3.8: *left: Spectral response of the ICCD obtained by a UVTOP305-FW-SMD LED as illumination source. The* $2400\ \mathrm{grooves/mm}$ *diffraction grating is used. Black dots are the experimental points, the red solid line is a fit obtained with a five-order polynomial function. right: Total transmission of the set of filters used for spectral selection at the PMT entrance slit: Thorlabs FGUV11, Semrock 320-40, Semrock 315-15. The black dots are obtained by a UV-VIS spectrometer. The red solid line is a fit obtained with a four-order polynomial function.*

3. the modified spectrum $\mathcal{I}(\lambda)^{\mathrm{mod}}$ is fitted by a routine written in the python language that uses LIFBASE data for transition probabilities, line positions and instrumental broadening to simulate the experimental spectrum. The rotatational distributions of $\mathrm{OH(A,0)}$ and $\mathrm{OH(A,1)}$ are used as free parameters. The routine proceeds along two phases, in which the two rotational distributions are fitted separately to deconvolve the signal in the region where the bands overlap. This is achieved by imposing a fixed distribution to one band while leaving the other unrestricted. The fitted population distributions allow calculating the population ratio as

$$\mathrm{R_P^{exp}} = \frac{\mathrm{P_{A0}}}{\mathrm{P_{A1}}} \tag{3.4}$$

from which the band ratio is inferred

$$\mathrm{R_B^{exp}} = \frac{\mathcal{A}_{(0,0)}}{\mathcal{A}_{(1,1)}} \cdot \mathrm{R_P^{exp}} \tag{3.5}$$

An example of one such fit is shown in figure 3.9 (right).

4. the temporal evolution of the laser pulse, needed for the solution of *five-level model* (2.20), is measured by feeding some scattered light to the PMT;

5. the non-flat transmission $\mathrm{T_f}$ of the interference filters is used to re-scale the Einstein coefficient of the $(0,0)$ band $\mathcal{A}_{(0,0)}$, in order to account for the different collection efficiency with which the two bands are recorded. Figure 3.8 (right) shows the filters transmission $\mathrm{T_f}$, measured by a UV-VIS spectrometer. The rescaling factor t is calculated as

$$\mathrm{t} = \frac{\int_0^\infty \mathcal{I}_0(v)\ \mathrm{d}v}{\int_0^\infty \mathcal{I}_0(v) \cdot \mathrm{T_f}(v)\ \mathrm{d}v} \tag{3.6}$$

from which a modified Einstein coefficient $\mathcal{A}^{\mathrm{mod}}_{(0,0)} = \mathrm{t} \cdot \mathcal{A}_{(0,0)}$ can be used to replace $\mathcal{A}_{(0,0)}$ in equation (2.24).

Following steps $1. - 5.$, the LIF pulse $\mathcal{S}(\mathrm{t})$ is simulated by solving the differential equations (2.20). For a given set of collisional frequencies, the complete set of five equations is solved for times $\mathrm{t} \leq 4 \cdot 10^{-8}\ \mathrm{s}$, with the time origin centred to the laser peak. Afterwards, the simplified set of two equations without laser contribution

$$\begin{cases} \frac{\mathrm{dP_{A1}(t)}}{\mathrm{dt}} & = -\Gamma_1\ \mathrm{P_{A1}(t)} & \Gamma_1 = \mathcal{A}_1 + \mathcal{Q}_1 \\ \frac{\mathrm{dP_{A0}(t)}}{\mathrm{dt}} & = \mathcal{V}_{1\to 0}\ \mathrm{P_{A1}(t)} - \Gamma_0\ \mathrm{P_{A0}(t)} & \Gamma_0 = \mathcal{A}_0 + \mathcal{Q}_0 \end{cases} \tag{3.7}$$

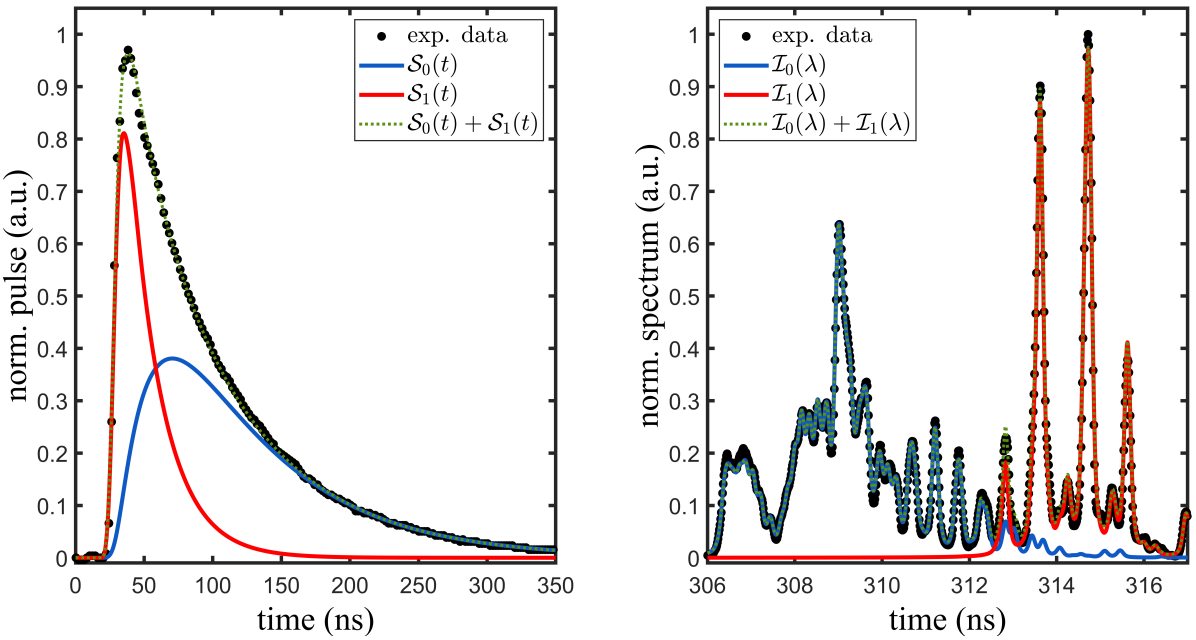

FIGURE 3.9: *Experimental LIF pulse (left) and LIF spectrum (right) with fitting simulation. Instrumental function:* 0.75 *Å gaussian +* 0.43 *Å lorentzian. Experimental conditions:* 0.14 Torr *of* $H_2O_2 + H_2O$ *as source of* OH *and* 1.7 Torr *of* CO_2 *as collider.* $P_1(3)$ *rotational line excitation.*

is solved for $4 \cdot 10^{-8} < t \leq 3 \cdot 10^{-6}$ s. This routine outputs the time-resolved emission profiles $g_{(0,0)}(t)$ and $g_{(1,1)}(t)$ of the $(0,0)$ and $(1,1)$ bands, which are used to simulate and fit the band ratio

$$R_B^{sim} = \frac{\int_{t_0}^{t_g} g_{(0,0)}(t)\ dt}{\int_{t_0}^{t_g} g_{(1,1)}(t)\ dt} \tag{3.8}$$

to its experimental value (3.5). A simulated pulse is shown in figure 3.9 (left), where individual bands contributions are reported. The procedure, embedded in a Levenberg–Marquardt algorithm, is iterated to infer the collisional frequencies $\mathcal{Q}_0$, $\mathcal{Q}_1$ and $\mathcal{V}_{1\to0}$ that better reproduce the experimental LIF pulse, with the constraint of the fixed band ratio (3.5).

Stern-Volmer plots

For each collider species and LIF excitation line, the procedure described above is repeated for a series of collider concentrations n_{coll}. This allows for construction of the

so-called *Stern-Volmer plots*, in which the collisional frequencies are displayed as a function of the collider concentration. Examples of such plots are presented in figure 3.13. The error on collisional frequency values is obtained by letting $\mathrm{R_B}$ vary within the error ϵ_f of the spectral fitting. This error is calculated as the standard deviation of repeated fits on the same experimental conditions. and taking the standard deviation of the fitted $\mathrm{R_B}$ values. A linear regression of the *Stern-Volmer plots* yields the slope and the intercept of the lines. The former give the collisional rate coefficients according to their definition

$$\begin{cases} \mathcal{Q}_1 = \mathrm{k}_{\mathcal{Q}_1} \cdot \mathrm{n_{coll}} \\ \mathcal{Q}_0 = \mathrm{k}_{\mathcal{Q}_0} \cdot \mathrm{n_{coll}} \\ \mathcal{V}_{1\to0} = \mathrm{k}_{\mathcal{V}_{1\to0}} \cdot \mathrm{n_{coll}} \end{cases} \tag{3.9}$$

The latter is a value including all the collider-independent contributions to quenching, e.g. the OH spontaneous emission Einstein coefficient or the water contribution to the total collisional rates. Inverse square errors for both the frequencies and the collider concentrations are used as weights in the fitting algorithm. The error on the collider concentration values is determined by the accuracy with which flows, temperature, and pressure are known, in agreement with equation (3.2). Depending on the MFC type, the repeatability error of the flows accounts for 0.3% of the set value or 0.2% of the full scale value, while the accuracy is equal to 1%. The errors on the pressure and temperature measurements are 0.5% of the capacitive gauge readout and 1% of the measured temperature, respectively. The errors on rate constant values are calculated as twice as the standard deviation returned by the fitting procedure.

3.2.3 Kinetic collision temperature

In the single-photon photolysis of $\mathrm{H_2O_2}$ at $266\ \mathrm{nm}$

$$\mathrm{H_2O_2}(\tilde{\mathrm{X}}\ ^1\mathrm{A}) + \mathrm{h}v \longrightarrow \mathrm{H_2O_2}(\tilde{\mathrm{A}}\ ^1\mathrm{A}) \longrightarrow \mathrm{OH}(\mathrm{X}\ ^2\Pi) + \mathrm{OH}(\mathrm{X}\ ^2\Pi), \tag{3.10}$$

about 90% of the $2.57\ \mathrm{eV}$ excess energy is converted into the translation energy of the OH fragments. The rest is accommodated into their internal energy in the form of vibrational and rotational excitation. This results in translationally hot nascent OH fragments, with temperatures above $2000\ \mathrm{K}$, and a nascent rotational Boltzmann distribution with $\mathrm{T_{rot}} = 1530 \pm 150\ \mathrm{K}$ [80]. The photolysis of $\mathrm{H_2O_2}$ by linearly polarized

light preferentially excites those molecules with a transition dipole moment parallel to the polarization of the radiation. Because the lifetime of $H_2O_2(\tilde{A}\ ^1A)$ is < 60 fs [80], process (3.10) is instantaneous on the time scale of the present experiment and the anisotropy of the parent molecules is transferred to the fragments motion. A detailed investigation of the dissociation reaction (3.10) is carried out in [80].

Elastic collisions with the surrounding gas re-equilibrate the OH velocity towards a Maxwellian isotropic distribution that approaches room temperature after few hundreds of ns, depending on the collider gas. The evolution of the OH translational temperature T_{OH} is ruled by the number of collisions undergone by OH molecules. This depends on the collision frequency (i.e. the collider pressure p_{coll}) and the time t available for the molecule to collide. Therefore, the product $p_{coll} \cdot t$ defines the relaxation degree of OH molecules.

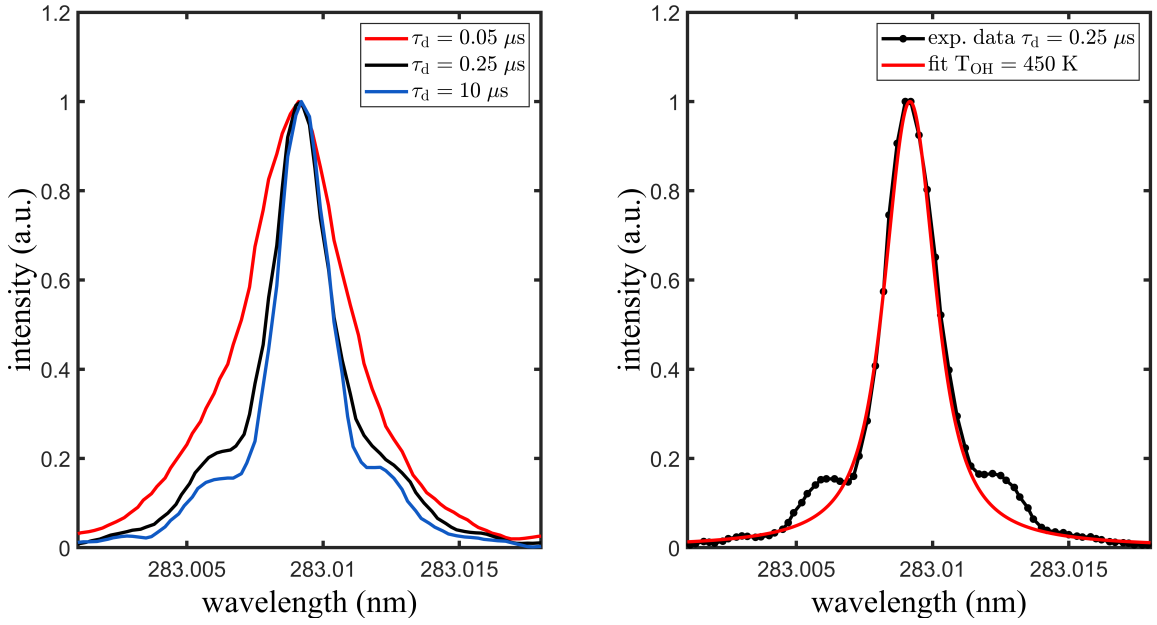

FIGURE 3.10: *left: Doppler profiles of the* $P_1(3)$ *line for different delays* τ_d *after the photophragmentation of* H_2O_2*. In both plots, the measurements refer to a mixture containing* 0.14 Torr *of* $H_2O_2 + H_2O$ *as source of* OH *and* 1.3 Torr *of* CO_2 *as collider. right: Fit of the* $P_1(3)$ *line profile with a Voigt function, obtained by convolution of the laser line profile and a Doppler gaussian profile with* $T_{OH} = 450$ K*.*

In this thesis, $\mathrm{T_{OH}}$ is monitored at variable delays τ_d after the photofragmentation event by excitation LIF on the $\mathrm{P_1(3)}$ line, at a constant collider pressure $\mathrm{p_{coll}}$. This method is chosen over the *Stern-Volmer plot* method, in which $\mathrm{p_{coll}}$ is varied and τ_d is kept constant because of the practical advantage of controlling the laser synchronization than the pressure stabilization. Examples of excitation spectra taken at different τ_d for CO_2 collider are shown in figure 3.10 (left). The lowest τ_d value is determined in such a way to allow for a sufficient isotropization of OH velocity. In fact, for τ_d typically shorter than $50\ \mathrm{ns}$, the line profile reflects a velocity distribution close to the nascent of photodissociation, which is anisotropic and not Maxwellian. Moreover, low τ_d values might cause the detection of laser scattered light, which is detrimental for the fitting of lines profiles. Because the efficiency of energy relaxation processes is species-dependent, different minimum τ_d thresholds are expected for the various colliders and, accordingly, different upper limits to the collision temperature $\mathrm{T_{OH}}$.

When the ejected OH fragments are observed with a laser propagating along direction $\mathbf{k_{las}}$, absorption occurs at a Doppler-shifted frequency given by $v = v_0\left(1 \pm \frac{\mathrm{v_k}}{\mathrm{c}}\right)$, where $\mathrm{v_k} = \mathbf{k_{las}} \cdot \mathbf{v}$ is the projection of the fragment velocity $\mathbf{v}$ onto the direction of laser light propagation. $\mathrm{T_{OH}}$ is determined by fitting the line profiles with a function obtained by convoluting the Doppler line profile $\mathrm{D}(\lambda)$ and the laser line profile $\mathrm{L}(\lambda)$, which is well approximated by a Lorentzian function with width parameter $\mathrm{w} = 0.017$ Å. The normalized fitting function is

$$(\mathrm{D} * \mathrm{L})(\lambda) = \exp\left[\frac{-\mathrm{m}\ \mathrm{c}^2\ (\lambda - \lambda_0)^2}{2\ \mathrm{k_B}\ \mathrm{T_{OH}}\ \lambda_0^2}\right] * \frac{\mathrm{w}^2}{\mathrm{w}^2 + 4\ (\lambda - \lambda_0)^2} \tag{3.11}$$

where c is the speed of light and m is the OH mass. The fitting of the line is restricted to its central core, so two avoid including the two shoulders appearing on both sides on the main peak. The nature of these features is not understood. An example of such fits is presented in figure 3.10 (right), where a good agreement with the experimental data is obtained for a $\mathrm{T_{OH}} = 450 \pm 150\ \mathrm{K}$. The error on temperature values accounts for both the fitting error and the uncertainty with which $\mathrm{L}(\lambda)$ is known.

Collisions between translationally hot OH at $\mathrm{T_{OH}}$ and cold collider molecules at $\mathrm{T_{coll}} = 300\ \mathrm{K}$ are described by an 'equivalent collision temperature' $\mathrm{T_{eq}}$ corresponding to the condition in which both OH and the collider gas have the same temperature. $\mathrm{T_{eq}}$

is obtained from the average kinetic energy in the centre of mass as

$$T_{eq} = T_{OH} \frac{M_{OH}}{M_{coll} + M_{OH}} + T_{coll} \frac{M_{coll}}{M_{coll} + M_{OH}} \tag{3.12}$$

where the M_{OH} and M_{eq} are the molar masses of OH and the collider molecules, respectively. A sample plot of T_{OH} and T_{coll} is shown in figure 3.11 for a fixed pressure of

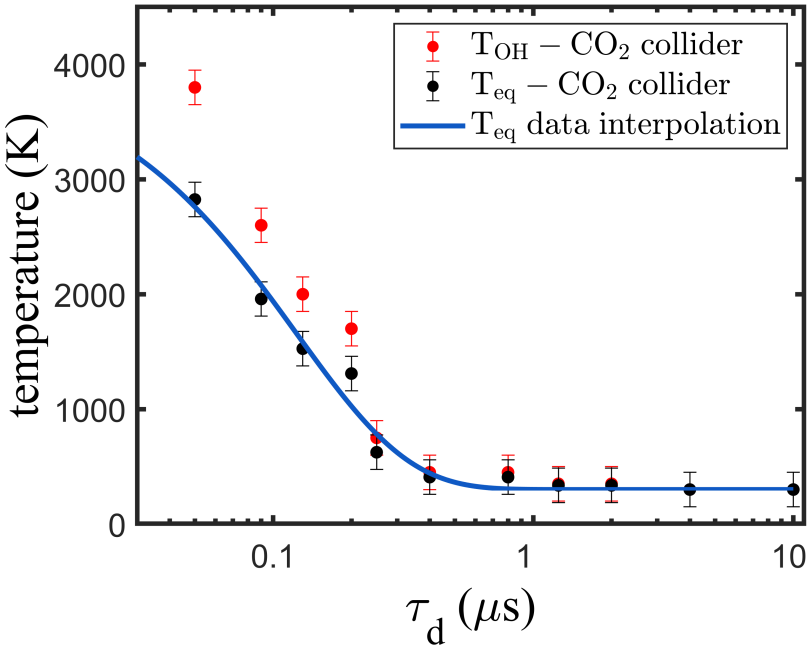

FIGURE 3.11: *Doppler temperature* T_{OH} *and equivalent collision temperature* T_{eq} *as a function of* τ_d. *Experimental conditions:* 0.14 Torr *of* $H_2O_2 + H_2O$ *as source of* OH *and* 1.3 Torr *of* CO_2 *as collider. Interpolation of* T_{eq} *with a single exponential function is also reported.*

CO_2. The same figure displays the interpolation of T_{eq} data with a decaying exponential function, which allows for the construction of a continuous (T_{eq}, τ_d) set. However, no physical meaning is related to this choice. The time-evolutions of T_{eq} for the different colliders are shown in figure 3.12. For all the investigated species, full thermalization of the translational motion with room temperature is achieved around 1 μs after photophragmentation of H_2O_2, with no clear dependence on the collider species being observed.

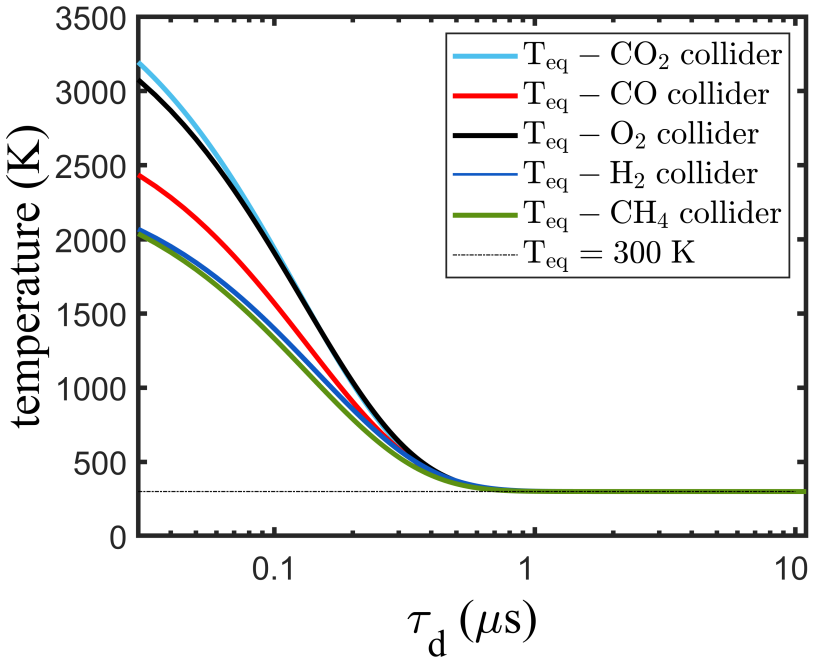

FIGURE 3.12: *Time evolution of* $\mathrm{T_{eq}}$ *for the set of investigated colliders. The* $\mathrm{T_{eq}} = 300$ K *line is reported for reference.*

3.3 Results

3.3.1 Non-thermal rate coefficients at T=300 K

For each collider, the non-thermal collisional rate coefficients at $\mathrm{T} = 300$ K are measured at a fixed delay τ_d, of 10 μs, that ensures that the OH fragments are thermalized at room temperature. The corresponding *Ster-Volmer plots* are shown in figure 3.13. Tables 3.5-3.9 summarize the collisional rate coefficients determined from the slope of the *Stern-Volmer plots*.

3.3.2 Literature comparison

Literature data on the non-thermal collisional rate coefficients of $\mathrm{OH}(\mathrm{A}\ ^2\Sigma^+, v = 0, 1)$ are limited to a few rotational states and colliders, since most of the available studies concern with a rotationally thermalized condition, or a condition of partial rotational thermalization (see [42] and references therein). Pertinent data for comparison

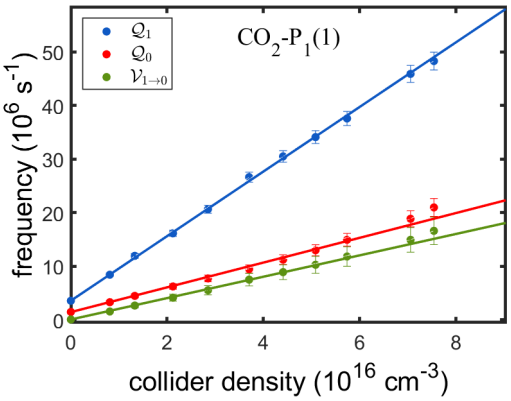
$\mathcal{Q}_1$
$\mathcal{Q}_0$
$\mathcal{V}_{1\to0}$
CO_2-P_1(1)
frequency (10^6 s^{-1})
collider density (10^{16} cm^{-3})

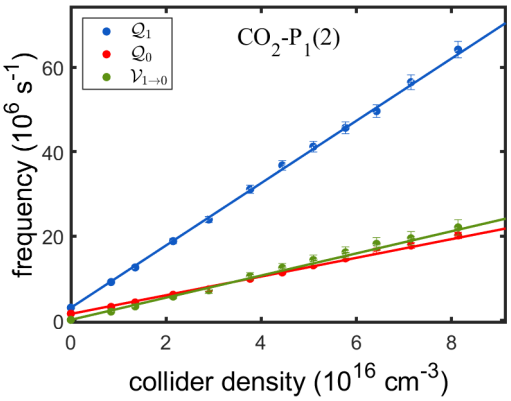
$\mathcal{Q}_1$
$\mathcal{Q}_0$
$\mathcal{V}_{1\to0}$
CO_2-P_1(2)
frequency (10^6 s^{-1})
collider density (10^{16} cm^{-3})

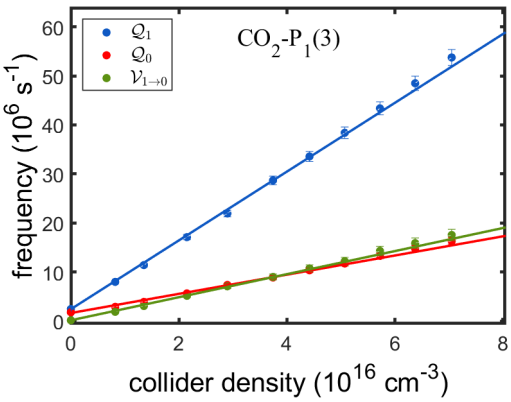
$\mathcal{Q}_1$
$\mathcal{Q}_0$
$\mathcal{V}_{1\to0}$
CO_2-P_1(3)
frequency (10^6 s^{-1})
collider density (10^{16} cm^{-3})

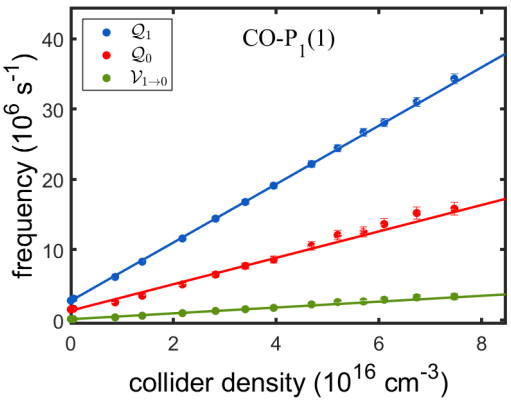
$\mathcal{Q}_1$
$\mathcal{Q}_0$
$\mathcal{V}_{1\to0}$
CO-P_1(1)
frequency (10^6 s^{-1})
collider density (10^{16} cm^{-3})

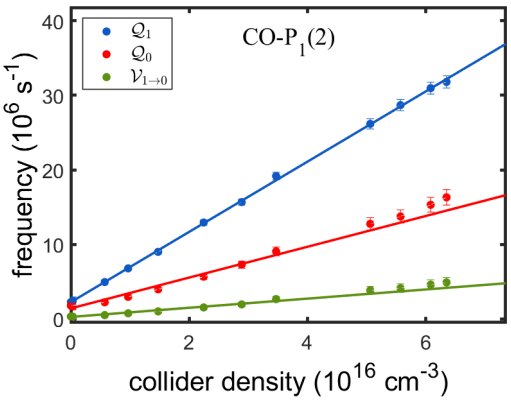
$\mathcal{Q}_1$
$\mathcal{Q}_0$
$\mathcal{V}_{1\to0}$
CO-P_1(2)
frequency (10^6 s^{-1})
collider density (10^{16} cm^{-3})

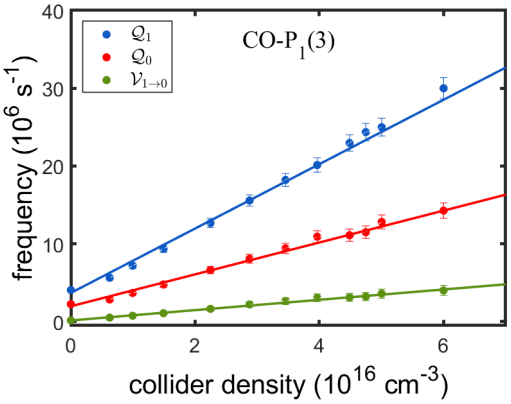
$\mathcal{Q}_1$
$\mathcal{Q}_0$
$\mathcal{V}_{1\to0}$
CO-P_1(3)
frequency (10^6 s^{-1})
collider density (10^{16} cm^{-3})

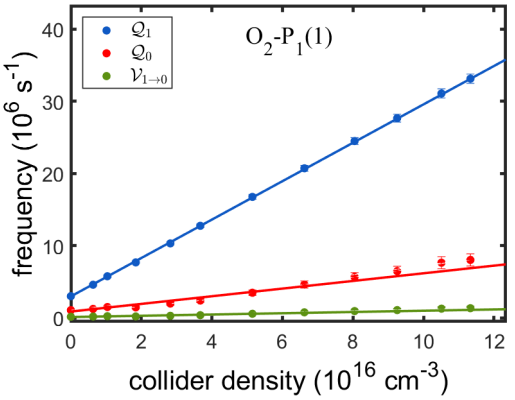
$\mathcal{Q}_1$
$\mathcal{Q}_0$
$\mathcal{V}_{1\to0}$
O_2-P_1(1)
frequency (10^6 s^{-1})
collider density (10^{16} cm^{-3})

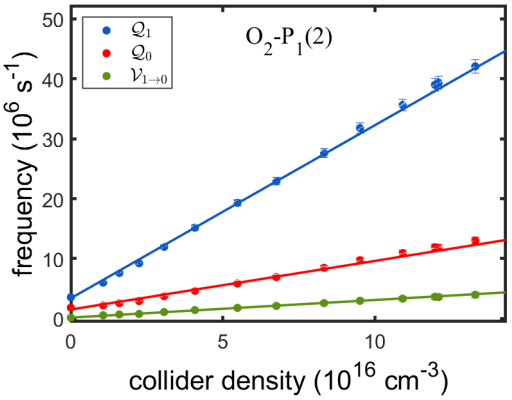
$\mathcal{Q}_1$
$\mathcal{Q}_0$
$\mathcal{V}_{1\to0}$
O_2-P_1(2)
frequency (10^6 s^{-1})
collider density (10^{16} cm^{-3})

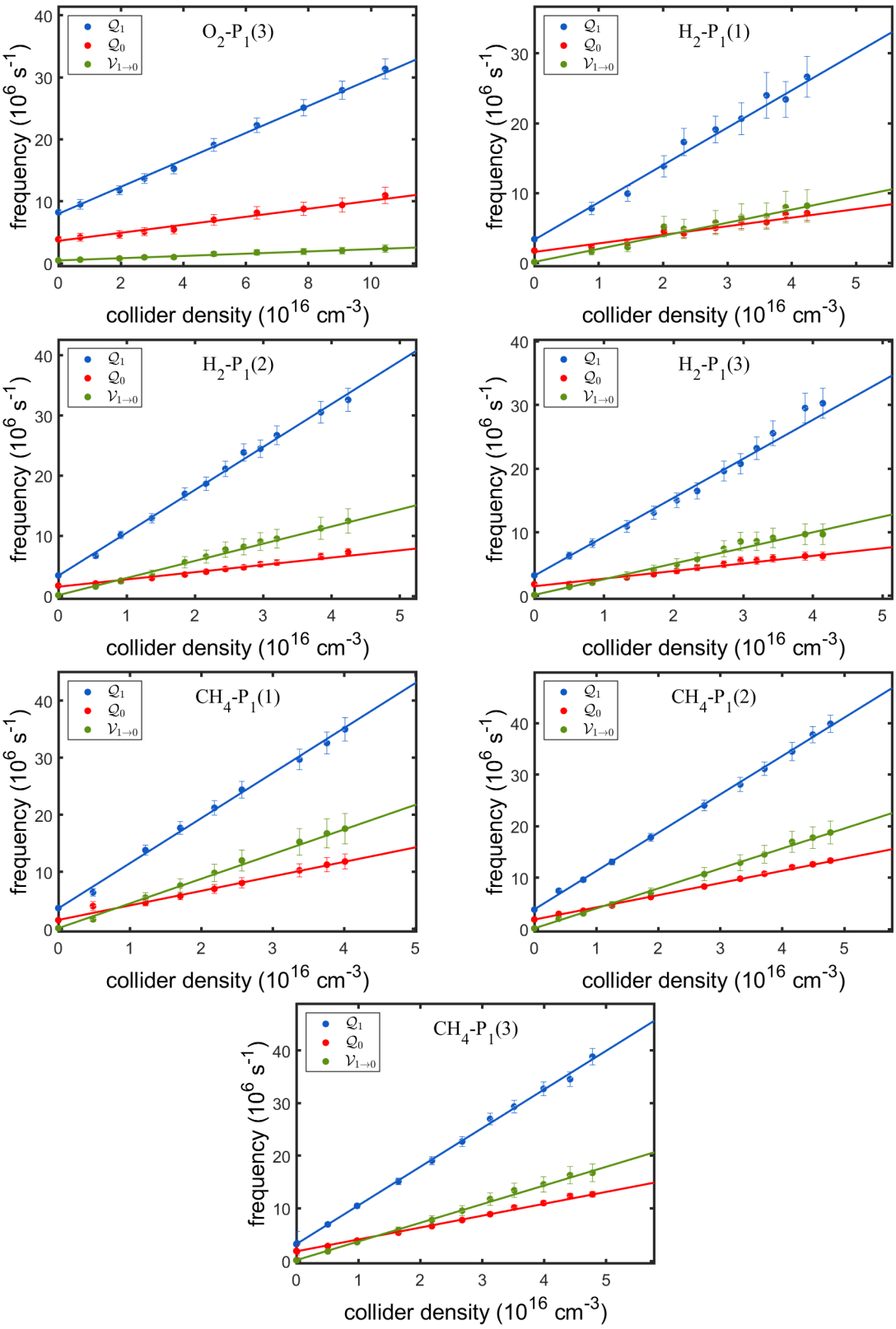

FIGURE 3.13: *Stern-Volmer plots of* $\mathrm{k}_{\mathcal{Q}_1}$, $\mathrm{k}_{\mathcal{Q}_0}$ *and* $\mathrm{k}_{\mathcal{V}_{1\to0}}$ *for several colliders and* $\mathrm{P}_1(1)$, $\mathrm{P}_1(2)$ *and* $\mathrm{P}_1(3)$ *rotational lines excitation.*

pumped level N'	reference	k_{Q_1}	k_{Q_0}	$k_{V_{1\longrightarrow 0}}$
0	this work	60.3 ± 0.9	23.1 ± 1.1	19.9 ± 0.7
0	[71]	61 ± 2	$-$	31 ± 6
1	this work	73.9 ± 1.1	22.2 ± 0.9	26.2 ± 1.3
2	this work	70.1 ± 1.6	19.5 ± 1.3	23.5 ± 0.9
2	this work	67.9 ± 1.8	19.8 ± 0.9	24.1 ± 0.5
thermal	[42]	61.4 ± 3.5	45.5 ± 1.1	26.7 ± 0.7

TABLE 3.5: *Measured non-thermal rate coefficients at* $T_{gas} = 300$ K *for* $N' = 0, 1, 2$ *states excitation in* 10^{-11} cm^3s^{-1} *units.* CO_2 *is used as collider. Thermal rate coefficients are reported from [42]. Copeland's non-thermal data [71] are reported for* $N' = 0$ *state.*

pumped level N'	reference	k_{Q_1}	k_{Q_0}	$k_{V_{1\longrightarrow 0}}$
0	this work	41.5 ± 0.5	18.8 ± 1.4	4.16 ± 0.33
1	this work	47.1 ± 0.6	20.7 ± 2.6	6.15 ± 0.85
2	this work	41.4 ± 2.0	20.5 ± 1.7	6.63 ± 0.33
thermal	[42]	40.1 ± 1.5	38.9 ± 0.6	7.09 ± 0.11

TABLE 3.6: *Measured non-thermal rate coefficients at* $T_{gas} = 300$ K *for* $N' = 0, 1, 2$ *states excitation in* 10^{-11} cm^3s^{-1} *units.* CO *is used as collider. Thermal rate coefficients are reported from [42].*

pumped level N'	reference	k_{Q_1}	k_{Q_0}	$k_{V_{1\longrightarrow 0}}$
0	this work	26.6 ± 0.3	5.30 ± 0.98	0.87 ± 0.21
0	this work	26.3 ± 1.6	5.77 ± 0.45	0.92 ± 0.08
1	this work	28.9 ± 0.9	8.11 ± 0.70	2.94 ± 0.11
2	this work	21.7 ± 1.1	6.47 ± 0.85	1.82 ± 0.19
2	[74]	20.6 ± 1.5	9.6 ± 1.2	2.1 ± 0.2
thermal	[42]	24.15 ± 0.48	13.50 ± 0.27	2.32 ± 0.07

TABLE 3.7: *Measured non-thermal rate coefficients at* $T_{gas} = 300$ K *for* $N' = 0, 1, 2$ *states excitation in* 10^{-11} cm^3s^{-1} *units.* O_2 *is used as collider. Thermal rate coefficients are reported from [42]. William's partially non-thermal data [74] are reported for* $N' = 2$ *state.*

pumped level N'	reference	k_{Q_1}	k_{Q_0}	$k_{V_1 \longrightarrow 0}$
0	this work	53.5 ± 3.6	12.3 ± 1.9	18.7 ± 2.1
1	this work	71.3 ± 2.3	12.1 ± 1.1	28.5 ± 1.3
2	this work	61.3 ± 2.7	12.0 ± 1.5	24.6 ± 1.1
thermal	[42]	53.5 ± 1.8	20.8 ± 0.5	23.05 ± 0.33

TABLE 3.8: *Measured non-thermal rate coefficients at* $T_{gas} = 300$ K *for* $N' = 0, 1, 2$ *states excitation in* 10^{-11} $cm^3 s^{-1}$ *units.* H_2 *is used as collider. Thermal rate coefficients are reported from [42].*

pumped level N'	reference	k_{Q_1}	k_{Q_0}	$k_{V_1 \longrightarrow 0}$
0	this work	79.0 ± 4.0	25.5 ± 2.1	43.3 ± 3.2
0	[71]	68 ± 7	$-$	44 ± 1.3
1	this work	74.4 ± 2.1	23.7 ± 0.8	38.8 ± 1.8
2	this work	73.5 ± 1.1	22.6 ± 0.8	35.5 ± 1.0
thermal	[42]	71.3 ± 2.4	34.6 ± 0.5	37.8 ± 0.6

TABLE 3.9: *Measured non-thermal rate coefficients at* $T_{gas} = 300$ K *for* $N' = 0, 1, 2$ *states excitation in* 10^{-11} $cm^3 s^{-1}$ *units.* CH_4 *is used as collider. Thermal rate coefficients are reported from [42]. Copeland's non-thermal data [71] are reported for* $N' = 0$ *state.*

are reported by Copeland [71] and Williams [74], where the excitation of the $OH(A, 1)$ state was studied. In these works, the OH $(0, 0)$ and $(1, 1)$ bands were spectrally separated and fitted by exponential functions to infer the collisional quenching frequencies. However, this method revealed issues concerning the isolation of the partially overlapping vibrational bands. Copeland and Williams' data are reported in tables 3.5-3.9 for comparison on account of the similar thermalization conditions achieved in those works. Data concerning the $OH(A, 0)$ manifold are reported by Copeland [70], Tamura [76] and Wysong [75]. In these works, a direct measurement of the k_{Q_0} rate coefficients was performed by pumping the $OH(A, 0)$ vibrational level and fitting an exponential function to the time resolved fluorescence signal. However, the rate coefficients measured in these studies are descriptive of rotational distributions that are not

comparable to the highly supra-thermal observed in this thesis because of different $OH(A, 0)$ population mechanisms. For this reason, the data are not reported in tables 3.5-3.9 for reference. Finally, although not rigorously comparable to the non-thermal measures, the thermal rate constants reported by Martini in [42] are tabled owing to the similar procedure adopted for their determination.

k_{Q_1} The measured non-thermal k_{Q_1} values are of the same magnitude, or slightly larger, than the corresponding thermal ones. This picture is consistent with the non-thermal nature of the $OH(A, 1)$ rotational distribution, connoted by the overpopulation of the fast-quenched low-N' states. On the contrary, thermal rotational distributions should be regarded as effective rates that include a contribution from higher rotational levels, which have smaller rate coefficients [70]. A clear dependence of k_{Q_1} on the pumped N' state is observed, with a maximum rate at $N' = 2$ for all the colliders except for CH_4, whose maximum is at $N' = 1$. The limited size of the dataset does not allow for further conclusions.

k_{Q_0} The non-thermal values of k_{Q_0} are lower, even by a factor of two or more, than the corresponding thermal ones [52]. This can be attributed to the largely supra-thermal nature of the $OH(A, 0)$ rotational distribution and the overpopulation of high-N' states, in combination with the decrease of quenching rate coefficients with increasing rotational quantum number. Such a decrease has to be ascribed to the nature of the interaction between OH and the colliders, which is governed by attractive forces and complex formation. According to [70], as an increasing rotation is imparted to the OH, the probability to form a complex is reduced due to the strong interaction anisotropy. This picture received encouragement from ab-initio calculations performed on the potential energy surfaces of $OH\ (A\ ^2\Sigma^+)$ [81]. The degree of the difference with the thermal rate coefficients is peculiar to the collider species, due to specific VET nascent distributions and rotational level dependence of the quenching [70]. Finally, apart from the singular exception of O_2, no significant differences are observed when changing the excitation line, although further investigation would be required to confirm this behavior for a wider set of transitions.

$\mathbf{k_{\mathcal{V}_{1\to 0}}}$ VET rate coefficients are less clearly comparable to the corresponding thermal ones and certainly exhibit a stronger species-dependence than $\mathrm{k}_{\mathcal{Q}_1}$ and $\mathrm{k}_{\mathcal{Q}_0}$. The highly non-thermal nature of $\mathrm{OH(A,1)}$, with over-population of a single $\mathrm{N'}$ state, makes VET rates depend on how individual $\mathrm{N'}$ states interact with the collider. The small size of the dataset, combined with the lack of comparable literature data, does not allow to draw conclusive statements at this stage.

3.3.3 Temperature dependence of the collisional rate coefficients

The temperature dependence of the collisional rate coefficients needs to be accounted for to apply CET-LIF quantitatively. This theme is crucial for an NRP discharge, where strong temperature variations are observed. A comprehensive investigation over a wide temperature range and in a condition of poor rotational thermalization is missing to date. In [82], the collisional rate coefficients were measured between 195 and $295\ \mathrm{K}$ by cooling the flowing gases with a temperature-regulated chiller. A He buffer flow was used to ensure a condition of rotational thermalization. The same methodology was applied in [83] for the charachterization of $\mathrm{OH}(\mathrm{A}\ ^2\Sigma^+, v=0)$ quenching in flash-photolysis tube in the range $200-344\ \mathrm{K}$ and in [84] for the temperature range $204-294\ \mathrm{K}$ with various colliders. In [85], collision quenching of $\mathrm{OH}(\mathrm{A}\ ^2\Sigma^+, v=1)$ was investigated in the range $1000-1400\ \mathrm{K}$ by direct decay time measurements at various pressures of the collider. Finally, LIF spectroscopy was used in [86] to measure $\mathrm{k}_{\mathcal{V}_{1\to 0}}$ and $\mathrm{k}_{\mathcal{Q}_1}$ in a shock tube at $1900\ \mathrm{K}$ and $2300\ \mathrm{K}$.

In this thesis, the temperature dependence of the collisional rate coefficients of the $\mathrm{OH}(\mathrm{A}\ ^2\Sigma^+, v=0,1)$ manifold has been measured for various colliders in a condition of poor rotational thermalization of the emitting state. The temperature evolution of the system is probed via τ_d, with the results shown in figures 3.11 and 3.12. At each τ_d, the LIF fluorescence pulse and spectrum are measured and fitted according to the procedure described in section 3.2.2 to infer the collisional frequencies. As the temperature of the OH fragments at a fixed τ_d varies with the collider density, it is not possible to obtain a *Stern-Volmer plot* in which each point is at the same temperature. Instead, the collider pressure $\mathrm{p_{coll}}$ is fixed, and only τ_d is varied to change the temperature. Unlike with a *Stern-Volmer plot*, the residual water contribution to both the measured

total quenching and VET frequencies must be subtracted manually according to the nominal water content in the mixture. Despite this complication, this method has the advantage of allowing for the exploration of a wider temperature range with greater control.

For CO_2, the evolution of the rate coefficients with temperature can be seen in figure 3.14. The complete dataset comprising all colliders is reported in [52]. In order to minimize the contribution from water to the measured collisional frequencies, and thus reduce the total uncertainty, the collider pressure is set to a pressure value an order of magnitude larger than that of the background water. Other sources of error are the uncertainty on the band ratio, temperature and mixture composition, as discussed in section 3.2.2. The observed dependence of the rate coefficients on the kinetic temperature $\mathrm{T_{eq}}$ is intrinsically related to their definition as

$$\mathrm{k(T_{eq})} = \int \sigma(\mathrm{v})\ \mathrm{v}\ \mathrm{f(v, T_{eq})}\ \mathrm{dv} \tag{3.13}$$

where $\mathrm{f(v, T_{eq})}$ is the distribution of the relative velocities of the interacting molecules and $\sigma(\mathrm{v})$ is the cross section of the process. However, the lack of fundamental knowledge on collisional processes prevents conclusions from being drawn.

3.3.4 Temperature dependence of the population ratio

For all the studied colliders, the fluorescence spectra exhibit a population ratio (2.31) that changes with τ_d and, hence, with the collision temperature $\mathrm{T_{eq}}$. For CO_2 this is shown in figure 3.15. The graph displaying the temperature evolution of $\mathrm{R_P}$ over the whole temperature domain is shown in figure 3.16. In each case, the population ratio shows a monotone increase with increasing kinetic temperature, with the highest variation being observed for O_2 ($\sim \frac{+21\%}{1000\ \mathrm{K}}$) and the lowest change for CO ($\sim \frac{+13\%}{1000\ \mathrm{K}}$). The sole exception to this behavior is H_2, which exhibits a decrease of the population ratio with increasing the temperature of approximately $\frac{-10\%}{1000\ \mathrm{K}}$.

The temperature dependence of the population ratio is in principle attributable to a change of both $\mathrm{k}_{\mathcal{V}_{1\to0}}$ and $\mathrm{k}_{\mathcal{Q}_0}$, which individually depend on the kinetic temperature $\mathrm{T_{eq}}$ according to equation (3.13). As well as the expected 'kinetic' dependence of $\mathrm{R_P}$ on the temperature, an additional component arises from the change in the rotational distribution of $\mathrm{OH(A, 0)}$ manifold. For CO_2, this is shown in figure 3.17, where the rota-

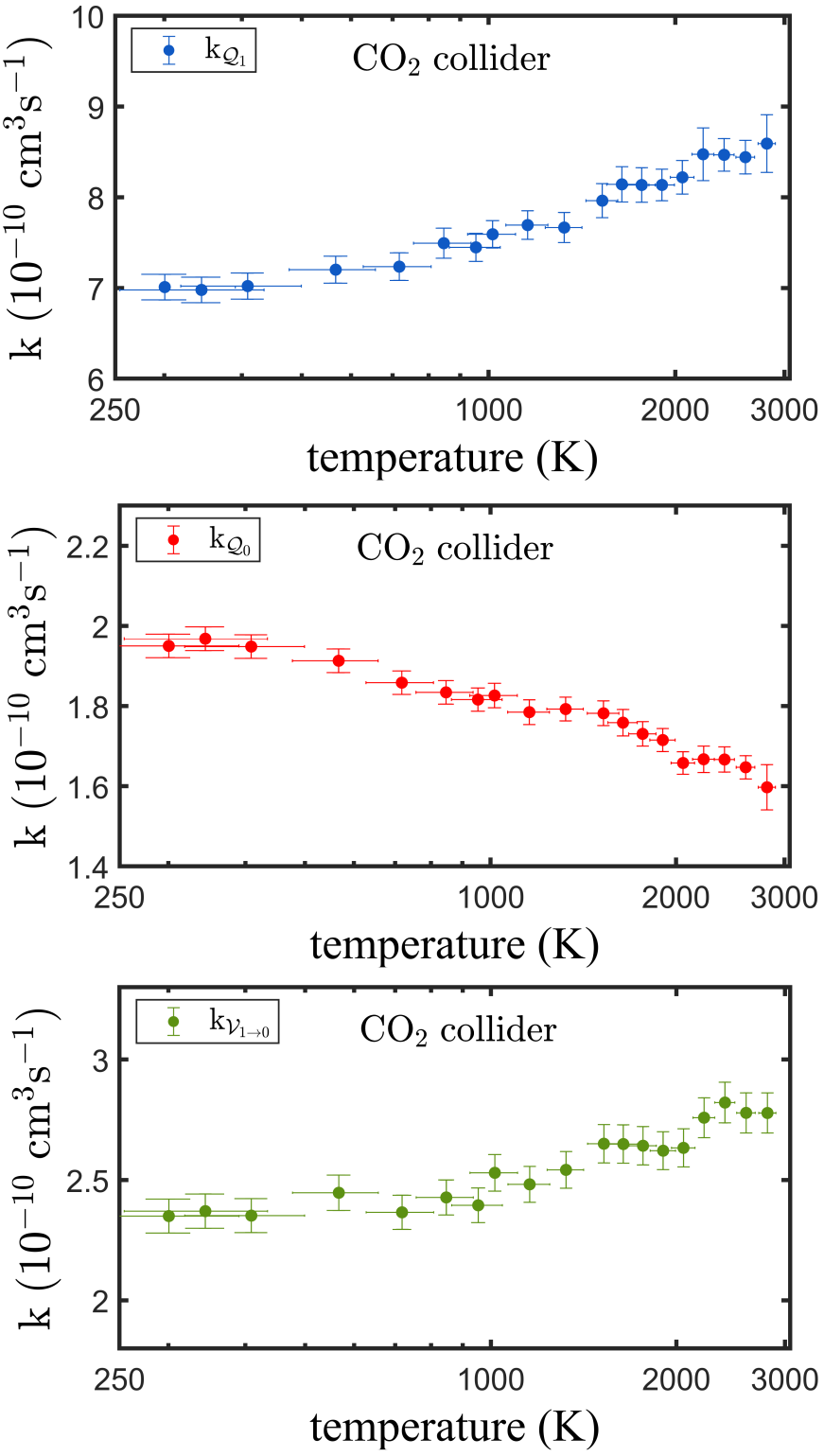

FIGURE 3.14: *Collisional rate coefficients* $k_{\mathcal{Q}_1}$, $k_{\mathcal{Q}_0}$ *and* $k_{\mathcal{V}_{1\to0}}$ *at various kinetic temperatures* T_{eq}. *Experimental conditions:* 0.14 Torr *of* $H_2O_2 + H_2O$ *and* 1.3 Torr *of* CO_2. $P_1(3)$ *rotational line excitation.*

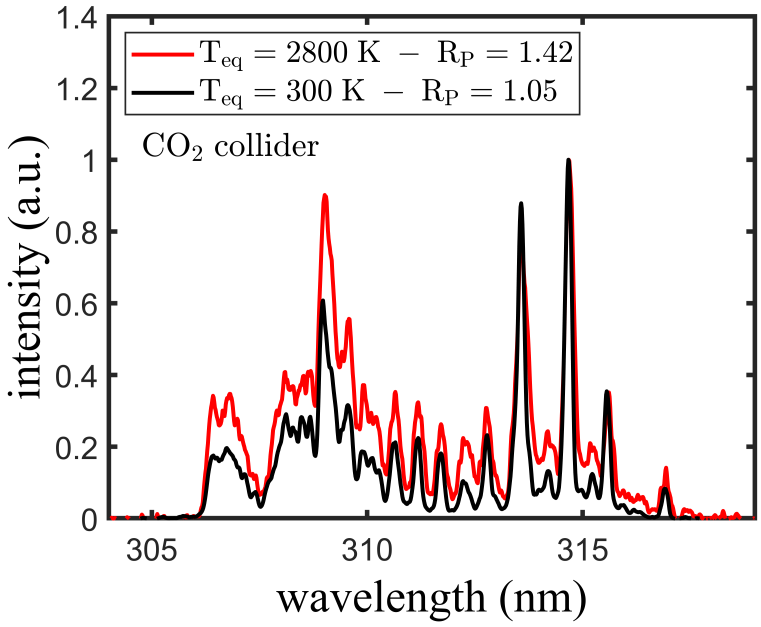

FIGURE 3.15: *Fluorescence spectra at two fixed delays τ_d (or kinetic temperatures T_{eq}). Experimental conditions:* 1.3 Torr *of* CO_2 *and* 0.14 Torr *of* $H_2O_2 + H_2O$. $P_1(3)$ *excitation.*

tional distributions of $OH(A, 0)$ are displayed for three values of T_{eq}. The distribution appears 'hotter' at low T_{eq} (or, equivalently, at low τ_d), likely due to the strong coupling between translational excitation and rotations existing upon photofragmentation of H_2O_2. Because low-N′ states have typically higher quenching rate coefficients [70], the effective quenching of $OH(A, 0)$ decreases at high temperatures and partly explains the increase of R_P. Conversely, the rotational distributions of $OH(A, 1)$ do not change significantly, as evidenced by figure 3.18. With most of the population confined in the laser-populated rotational state, the temperature dependence of $k_{\mathcal{V}_{1\to 0}}$ is not attributable to reasons other than the kinetic temperature.

The discovery of the temperature evolution of R_P contrasts with what is reported in [23], where the invariance of R_P was verified for three mixtures of $H_2O_2 + H_2O$ for a fixed $\tau_d = 0.06$ μs. This incongruity potentially arises from the limited temperature range studied in [23], which may not allow for appreciation of different population ratios in the diverse conditions. As shown in figure 3.19 (top panel), the measurements in [23] explored the temperature range between 1300 K and 3100 K, which corresponds to a variation of R_P of about 13%. This is better visualized in the bottom panel of

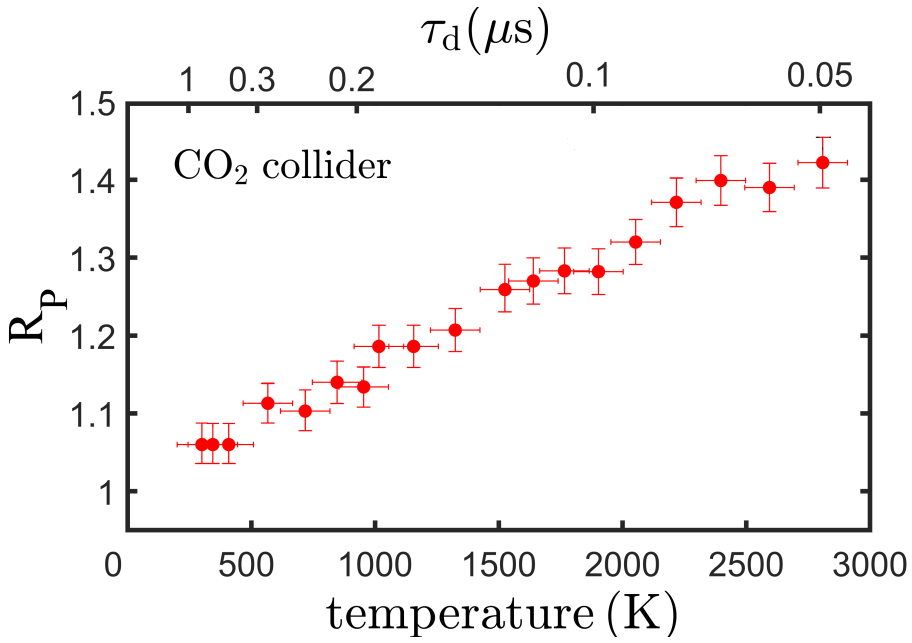

FIGURE 3.16: *Population ratio as a function of the kinetic collision temperature* T_{eq} *and* τ_d. *About* 1.3 Torr *of* CO_2 *is used as collider in a mixture with* 0.14 Torr *of* $H_2O_2 + H_2O$. $P_1(3)$ *line excitation.*

the figure, where R_P values are plotted versus T_{eq}. Because R_P percentage errors are approximately 7%, assigning a constant value to the limited dataset of [23] is possible within the experimental error, and the invariance of R_P with T_{eq} can be erroneously assumed.

3.3.5 Caveat

The procedure adopted for temperature determinations is rigorous if the kinetic temperature, T_{eq}, does not change during the fluorescence lifetime. A change in the kinetic temperature would be observed if the excited OH molecules undergo elastic collisions during their lifetime. However, as the quenching collision frequencies are of the same order of magnitude as the gas kinetic frequencies, OH collisions can be treated as purely inelastic, therefore leading to a depopulation of the excited states. Consequently, the observed fluorescence signal arises only from those molecules that have not undergone any collisions and, therefore, that have maintained the same kinetic energy of the OH fragment at the moment of laser light absorption.

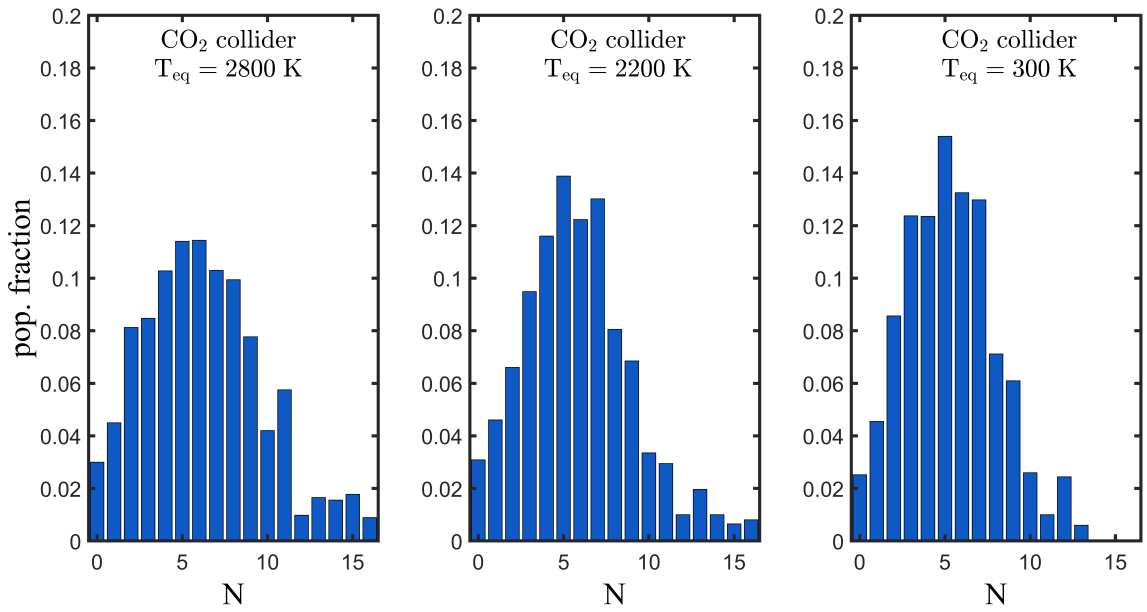

FIGURE 3.17: *Rotational distributions of* $\mathrm{OH(A\ ^2\Sigma^+}, v = 0)$ *at different* $\mathrm{T_{eq}}$. *The rotational distributions are obtained by fitting high-resolution fluorescence spectra (see section 3.2.2).*

A clear evidence supporting this assumption is displayed by figure 3.20, which shows the evolution of the rotational distribution of $\mathrm{OH(A\ ^2\Sigma^+}, v = 0)$ during the fluorescence lifetime. The population distributions are obtained by fitting the LIF fluorescence spectra recorded at consecutive time windows during the fluorescence duration (see section 3.2.2). These can be selected by reducing the ICCD gating time $\mathrm{t_g}$ and repetitively shifting the initial integration time $\mathrm{t_0}$ according to equation (2.22). No significant changes are observed between the rotational distributions, thus supporting the thesis that the kinetic temperature is constant during its measurement.

3.3.6 Temperature-averaged cross sections

In molecular energy transfer studies, it is common to characterize bi-molecular processes via their cross section $\sigma(\mathrm{v})$, i.e. the effective area for successive collisions. From a measured rate constant at thermal equilibrium $\mathrm{k(T)}$, the cross section is more conveniently determined as the ratio of $\mathrm{k(T)}$ and the average collision velocity $\langle \mathrm{v} \rangle$ [87]

$$\sigma(\mathrm{T}) = \frac{\mathrm{k(T)}}{\langle \mathrm{v} \rangle} \tag{3.14}$$

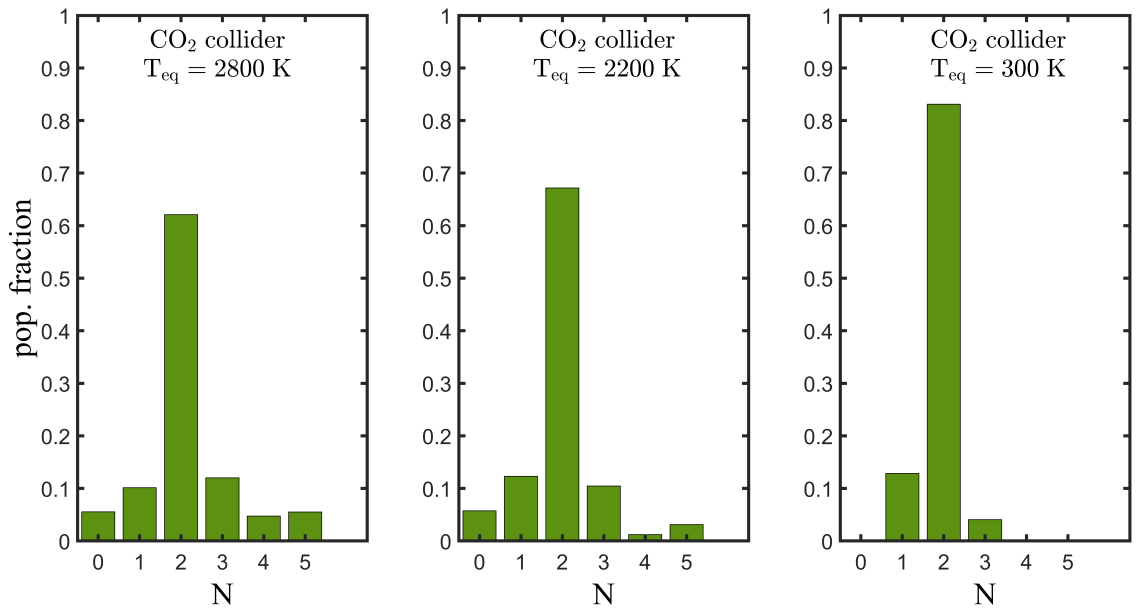

FIGURE 3.18: *Rotational distributions of* $\mathrm{OH(A\ ^2\Sigma^+}, v = 1)$ *at different* $\mathrm{T_{eq}}$. *The rotational distributions are obtained by fitting high-resolution fluorescence spectra (see section 3.2.2).*

This quantity, known as the *temperature/thermally-averaged cross section*, provides description of the collisional processes from the experimental perspective if $\sigma(\mathrm{v})$ is not accessible over the entire velocity spectrum. The *thermally-averaged cross section* is not, in general, equivalent to the 'true' average cross section

$$\langle \sigma(\mathrm{T}) \rangle = \int \sigma(\mathrm{v})\ \mathrm{f}(\mathrm{v}, \mathrm{T})\ \mathrm{dv} \tag{3.15}$$

which is calculated from the distribution $\mathrm{f}(\mathrm{v}, \mathrm{T})$ of the relative velocities of the colliders. The only case yielding to $\sigma(\mathrm{v}) = \langle \sigma(\mathrm{T}) \rangle$ is when the cross section $\sigma(\mathrm{v})$ is independent of v. At thermal equilibrium, the proper distribution of relative velocities is the Maxwell-Boltzmann distribution

$$\mathrm{f_{MB}}(\mathrm{v}, \mathrm{T}) = 4\pi \left(\frac{\mu}{2\pi \mathrm{k_B T}} \right)^{3/2} \mathrm{v}^2 \exp\left[-\frac{\mu \mathrm{v}^2}{2\mathrm{k_B T}} \right] \tag{3.16}$$

which allows rewriting equation (3.14) as

$$\sigma(\mathrm{T}) = \frac{\mathrm{k(T)}}{\langle \mathrm{v} \rangle} = \frac{\mathrm{k(T)}}{\int \mathrm{v}\ \mathrm{f_{MB}}(\mathrm{v}, \mathrm{T})\ \mathrm{dv}} = \sqrt{\frac{\pi \mu}{8 \mathrm{k_B T}}}\ \mathrm{k(T)} = \frac{\mathrm{k(T)}}{\mathrm{dT}^{1/2}} \tag{3.17}$$

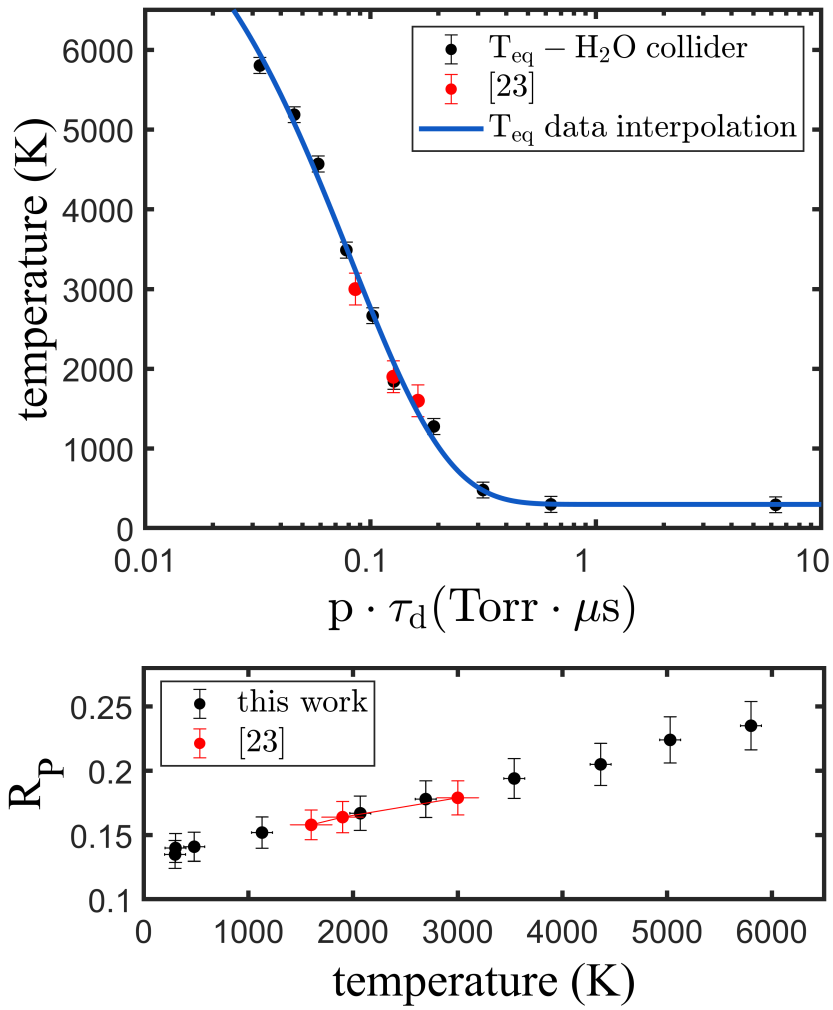

FIGURE 3.19: *top: Equivalent collision temperature* T_{eq} *as a function of the product* $p \cdot \tau_d$. *Measurements refer to a mixture containing* 0.65 Torr *of* $H_2O_2 + H_2O$. *Interpolation of* T_{eq} *with a single exponential function is also reported. Red dots are obtained from [23]. bottom: Population ratio as a function of the kinetic collision temperature* T_{eq}. *Red dots are obtained from [23], where three* $H_2O_2 + H_2O$ *mixtures at different pressures are investigated. The blue dashed line corresponds to a population ratio of* 0.17.

In this thesis, the *thermally-averaged cross sections* $\sigma_{\mathcal{Q}_1}(T)$, $\sigma_{\mathcal{Q}_0}(T)$ and $\sigma_{\mathcal{V}_{1\to0}}(T)$ of total quenching and vibrational energy transfer are determined from the rate coefficients $k_{\mathcal{Q}_1}(T)$, $k_{\mathcal{Q}_0}(T)$ and $k_{\mathcal{V}_{1\to0}}(T)$ via equation (3.17). The d factors are reported in table 3.10 for each collider. For CO_2, the measured cross sections are shown in figure 3.21. The

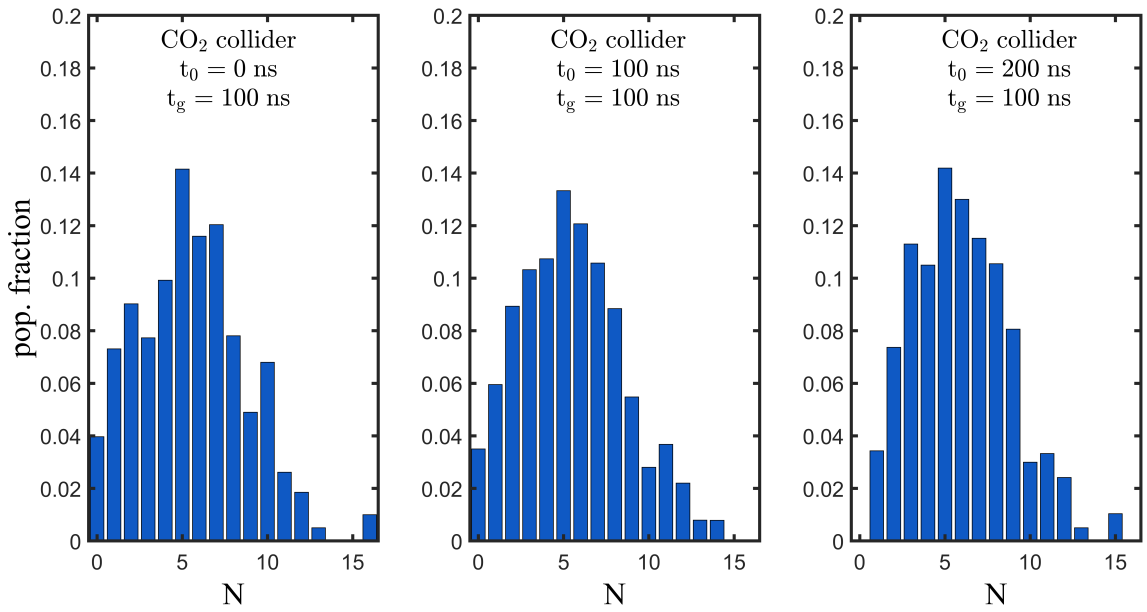

FIGURE 3.20: *Rotational distributions of* $\mathrm{OH(A\ ^2\Sigma^+}, v = 0)$ *at* $\mathrm{T_{eq}} = 2200$ K *(*$\tau_\mathrm{d} = 0.08$ μs*), taken with a fixed integration time* $\mathrm{t_g} = 100$ ns *and different initial integration times* $\mathrm{t_0}$.

collider	d $(\mathbf{cm^3 s^{-1} Å^{-2} K^{-\frac{1}{2}}})$
CO_2	$4.15 \cdot 10^{-13}$
CO	$4.47 \cdot 10^{-13}$
O_2	$4.37 \cdot 10^{-13}$
H_2	$10.84 \cdot 10^{-13}$
CH_4	$5.06 \cdot 10^{-13}$
H_2O	$4.92 \cdot 10^{-13}$

TABLE 3.10: d *factors for formula (3.14) for all the investigated colliders. No error is assumed on* d. *Data are reported from [52].*

reader is invited to refer to [52] for the complete dataset comprising the other studied colliders. The cross sections are well fitted by the formula

$$\sigma_1(\mathrm{T}) = \mathrm{A}\ \exp\left(-\epsilon_1 \mathrm{T}\right) + \mathrm{B}\ \exp\left(-\epsilon_2 \mathrm{T}\right) \tag{3.18}$$

The fitting parameters are listed in table 3.11 for each collision partner. As equation (3.18) is not based on a theoretical model, its validity must be restricted to the tem-

collider	parameter	$\sigma_{\mathcal{Q}_1}$	$\sigma_{\mathcal{Q}_0}$	$\sigma_{\mathcal{V}_{1\to0}}$	T range (K)
CO_2	A	95.80	29.73	33.67	$300-2800$
CO_2	B	64.24	16.87	20.47	
CO_2	ϵ_1	$3.30\cdot10^{-3}$	$3.10\cdot10^{-3}$	$3.14\cdot10^{-3}$	
CO_2	ϵ_2	$1.83\cdot10^{-4}$	$3.05\cdot10^{-4}$	$1.72\cdot10^{-4}$	
CO	A	60.24	26.42	10.21	$300-2200$
CO	B	22.78	16.44	3.31	
CO	ϵ_1	$2.34\cdot10^{-3}$	$2.72\cdot10^{-3}$	$2.17\cdot10^{-3}$	
CO	ϵ_2	$0.30\cdot10^{-4}$	$2.66\cdot10^{-4}$	$0.41\cdot10^{-4}$	
O_2	A	27.59	14.59	2.50	$300-2900$
O_2	B	18.16	6.11	1.44	
O_2	ϵ_1	$3.04\cdot10^{-3}$	$4.87\cdot10^{-3}$	$2.75\cdot10^{-3}$	
O_2	ϵ_2	$1.88\cdot10^{-4}$	$4.80\cdot10^{-4}$	$2.10\cdot10^{-4}$	
H_2	A	44.01	6.90	16.67	$300-1800$
H_2	B	27.29	3.55	9.02	
H_2	ϵ_1	$5.39\cdot10^{-3}$	$2.82\cdot10^{-3}$	$3.99\cdot10^{-3}$	
H_2	ϵ_2	$4.35\cdot10^{-4}$	$1.12\cdot10^{-4}$	$3.35\cdot10^{-4}$	
CH_4	A	97.05	29.87	65.02	$300-1700$
CH_4	B	57.98	18.45	30.65	
CH_4	ϵ_1	$4.02\cdot10^{-3}$	$4.05\cdot10^{-3}$	$5.64\cdot10^{-3}$	
CH_4	ϵ_2	$1.87\cdot10^{-4}$	$3.02\cdot10^{-4}$	$2.28\cdot10^{-4}$	
H_2O	A	60.61	43.56	5.47	$300-5800$
H_2O	B	34.61	21.64	2.92	
H_2O	ϵ_1	$1.96\cdot10^{-3}$	$2.35\cdot10^{-3}$	$2.12\cdot10^{-3}$	
H_2O	ϵ_2	$0.84\cdot10^{-4}$	$1.14\cdot10^{-4}$	$0.15\cdot10^{-4}$	

TABLE 3.11: *Fitting parameters for formulas (3.18) and (3.21).* A *and* B *are in units of* $Å^2$*;* ϵ_1 *and* ϵ_2 *are dimensionless. Data are reported from [52].*

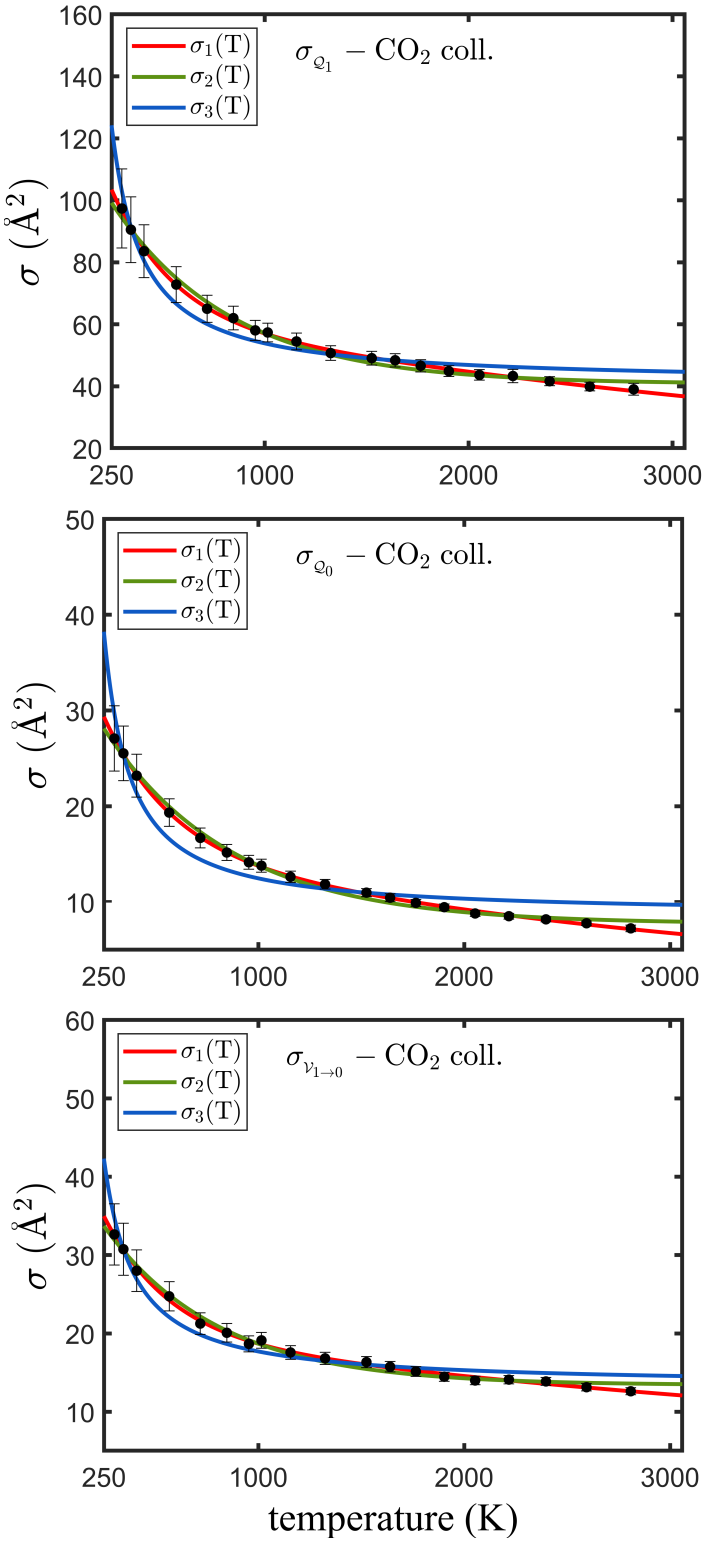

FIGURE 3.21: *Temperature-averaged cross sections $\sigma_{\mathcal{Q}_1}$, $\sigma_{\mathcal{Q}_0}$ and $\sigma_{\mathcal{V}_{1\to0}}$ as a function of the kinetic collision temperature T_{eq}. CO_2 is used as collider. Red fits are obtained by formula (3.18), blue fits by formula (3.19), green fits by formula (3.20).*

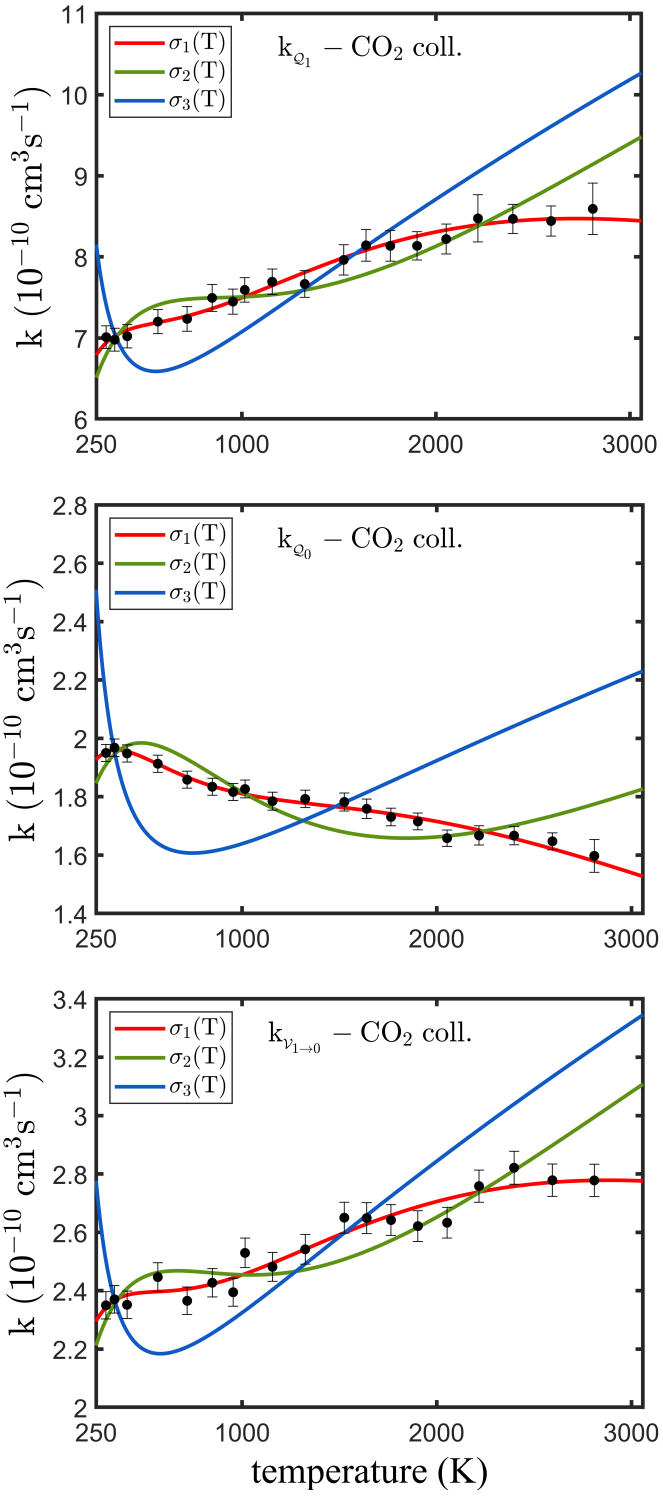

FIGURE 3.22: *Rate coefficients* $k_{\mathcal{Q}_1}$, $k_{\mathcal{Q}_0}$ *and* $k_{\mathcal{V}_{1\to0}}$ *as a function of the kinetic collision temperature* T_{eq}. CO_2 *is used as collider. Colored curves are obtained by recalculating the rate coefficients from equation (3.21). Red curves are obtained with formula (3.18), blue curves by formula (3.19), green curves by formula (3.20).*

perature range investigated for each species, and extrapolations to higher/lower temperatures are discouraged. The temperature validity range is reported in table 3.11 for each species. Fits by the functions

$$\sigma_2(\mathrm{T}) = \mathrm{a}\left[1 + \mathrm{b}\ \exp\left(-\frac{\mathrm{cT}}{296}\right)\right] \tag{3.19}$$

$$\sigma_3(\mathrm{T}) = \sigma_\infty\ \exp\left(\frac{\epsilon}{\mathrm{k_B T}}\right) \tag{3.20}$$

are also plotted in figure 3.21 for comparison with the available literature [76] [83]. As a cross-check, the rate constants are recalculated for the three fitting functions by inverting equation (3.17)

$$\mathrm{k(T)} = \mathrm{dT}^{1/2}\ \sigma(\mathrm{T}) \tag{3.21}$$

These calculations are shown in figure 3.22. The good match with formula (3.18) seems to contradict the picture of a cross section $\sigma(\mathrm{T})$ that approaches a constant value at high T, as suggested by equations (3.19) and (3.20). A possible explanation might be simply given by the definition of $\sigma(\mathrm{T})$ as an average over the kinetic energies of all the colliders, in contrast with the 'theoretical' $\sigma(\mathrm{T})$ defined as the average over the kinetic energy of a single collider.

3.4 Applications

In this section, the application of CET-LIF to two study cases is presented: a $\mathrm{CO_2}$ NRP discharge and a $\mathrm{CO_2 + H_2O}$ glow discharge.

3.4.1 $\mathrm{CO_2}$ dissociation in a $\mathrm{CO_2}$ NRP discharge

The new set of non-thermal rate coefficients is used to reinterpret the fluorescence spectra and band ratios measured in [56] in the post-discharge of a $\mathrm{CO_2}$ NRP discharge. In [56], the authors investigated the $\mathrm{CO_2}$ plasmolysis in a quartz reactor arranged in a pin-to-sphere configuration. An HV ns-pulsed power supply delivered adjustable amplitude, $10\ \mathrm{ns}$-FWHM pulses at a maximum inter-pulse frequency of $3\ \mathrm{kHz}$. The details of the setup arrangement can be found in the original publication [56].

The $\mathrm{CO_2}$ fragmentation kinetics was assessed by CET-LIF on OH, made possible by the dilution of the $\mathrm{CO_2}$ gas input flow with 1.35% of water vapor as a source of OH.

The discharge pattern was made of pulse bursts repeated at a frequency of 300 Hz, each burst being composed by 4 pulses repeated at 3 kHz. The average energy per pulse was 10 mJ. A digital delay generator synchronized LIF detection of OH at variable delays T in the afterglow of the last pulse of the burst to probe the variation of the gas mixture composition. In the late post-discharge, the analysis of the effluent gas composition through gas chromatography was used to validate the CET-LIF measurements.

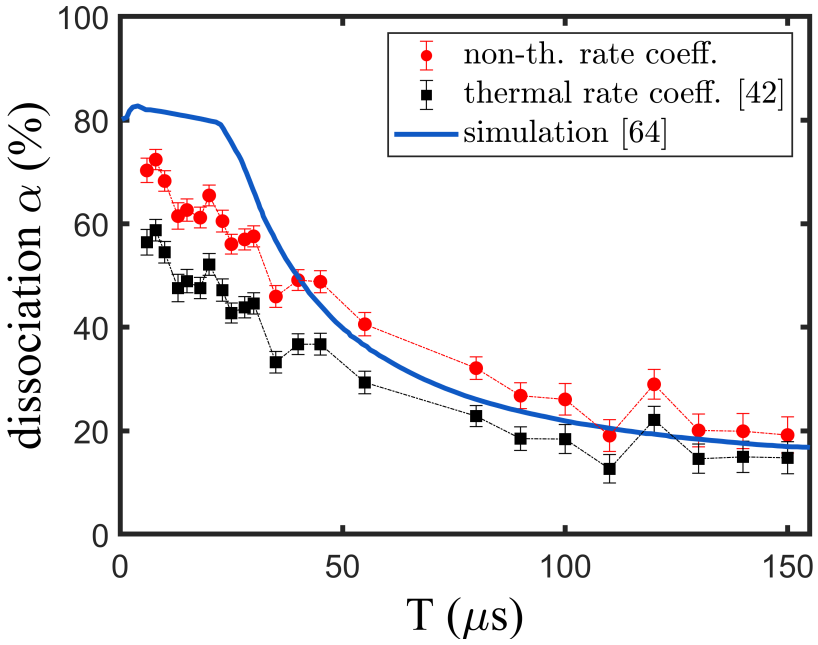

FIGURE 3.23: CO_2 *dissociation* α *in the post-discharge of a* ns *discharge pulse. Experimental conditions:* 725 Torr $CO_2 + 10$ TorrH_2O, *total flow* 100 sccm. *Energy per pulse* 10 mJ. *Red dots are obtained from formula (2.36) and the non-thermal rate coefficients inferred from equation (3.21). Black dots are obtained from thermal rate coefficients reported in [42]. Calculations from [64] are also reported for comparison.*

In [56], CO_2 dissociation was assessed by formula (2.36) with the thermal rate coefficients measured in [42] (black dots in figure 3.23). The calculation was performed under the hypothesis of a temperature-independent band ratio. CO_2 conversion was found to be considerable at the end of the pulse ($\sim 60\%$), and to drop significantly in the afterglow, yielding to a final conversion of about 15% when the gas reached the outlet of the grounded electrode. This decrease has to be attributed to recombination

reactions (mainly $CO + O + M \longrightarrow CO_2 + M$) and VT relaxations, which depopulate CO_2 vibrational levels responsible for most of the dissociation [64].

The reinterpretation of the R_B values using the temperature-dependent non-thermal rate coefficients confirms the decreasing conversion in the post-discharge, although higher absolute values are observed (see red dots in figure 3.23). The band ratio values and the gas temperature measurements are reported in figure 3.24 for reference. The new conversion data better match the simulation described in Heijkers' work [64], which is reported in figure 3.23 for comparison. However, it should be realized that the

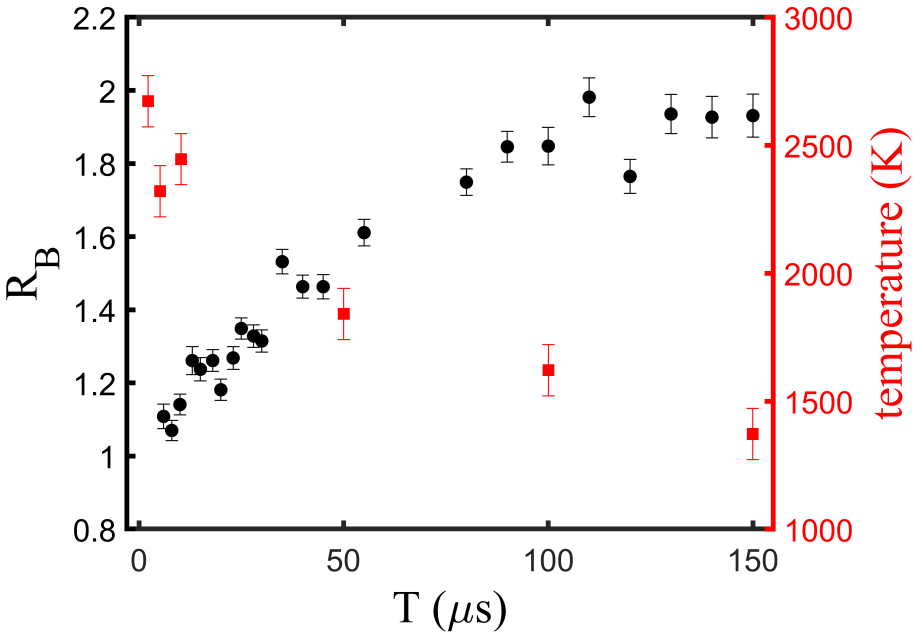

FIGURE 3.24: *Band ratio* R_B *(black) and gas temperature (red) evolution in the post-discharge of a* ns *HV pulse. Experimental conditions:* 725 Torr CO_2 + 10 Torr H_2O, *total flow with* 100 sccm. *Energy per pulse* 10 mJ. *Data reported from [56].*

model applies to pure CO_2, while experiments need to be carried out in the presence of some water content to make CET-LIF possible. Water addition may partly explain the overestimation of the modeled dissociation over the measured one, as suggested by several recent studies. The combined conversion of CO_2 and H_2O has been investigated in various discharge types, including dielectric barrier discharges [88], corona discharges [89], nanosecond repetitively pulsed discharges [56], and surface-wave mi-

crowave discharges [90] [91]. In the next section, the case of a glow discharge will be presented. The CO_2 conversion drops significantly if water vapor is added to the discharge in most cases. This may result jointly from several factors: first, the reduction in the maximum electron density by electron attachment to atomic oxygen [88]; secondly, the activation of the back reactions such as

$$\begin{aligned} CO + OH &\longrightarrow CO_2 + H \\ CO + OH &\longrightarrow COOH \end{aligned} \tag{3.22}$$

which are favored at high temperatures (see rates in [92] and [48]); finally, the stong VV relaxations induced by water depopulate the asymmetric stretch mode responsible for some of the CO_2 dissociation [93].

3.4.2 CO_2 dissociation in a CO_2+H_2O glow discharge

As a further application of CET-LIF, the case of a $CO_2 + H_2O$ glow discharge is presented in this section. The measurements, reported in a recently-submitted paper [94], have been carried out at the PMP group of the Eindhoven University of Technology (The Netherlands) with the setup schematized in figure 3.25.

The plasma reactor is a $23\ \mathrm{cm}$-long Pyrex cylinder with an inner diameter of about $2\ \mathrm{cm}$ and an inter-electrode distance of $17\ \mathrm{cm}$. The electrodes are placed perpendicular to the axis of the cylinder to allow for laser light injection. The discharge is generated by a high-voltage DC power-supply, connected in series with a $50\ \Omega$ resistance to prevent arcing. A current of $50\ \mathrm{mA}$ is supplied during the plasma ON time. A CO_2 flow is combined with a controlled flow of water from a He-pressurized vessel containing distilled water, for a total flow of $7.4\ \mathrm{sccm}$ and water admixture of 20%. The pressure inside the reactor is maintained at $6.7\ \mathrm{mbar}$. A waveform generator triggers the laser firing with the plasma cycle, consisting of $5\ \mathrm{ms}$ ON time and $11.67\ \mathrm{ms}$ OFF time, and allows for LIF detection of OH at variable delays T during both the ON and OFF phases. Further details on the experimental setup can be found in the original paper [94].

CET-LIF is used to assess the extent of CO_2 dissociation throughout the plasma cycle evolution. The gas temperature is determined through LIF thermometry with excitation of the closely-spaced $Q_{12}(1)$, $Q_2(1)$, $Q_1(6)$, $Q_{12}(3)$ and $Q_2(3)$ rotational lines of OH. The temporal evolution of the temperature is shown in figure 3.26 (left panel),

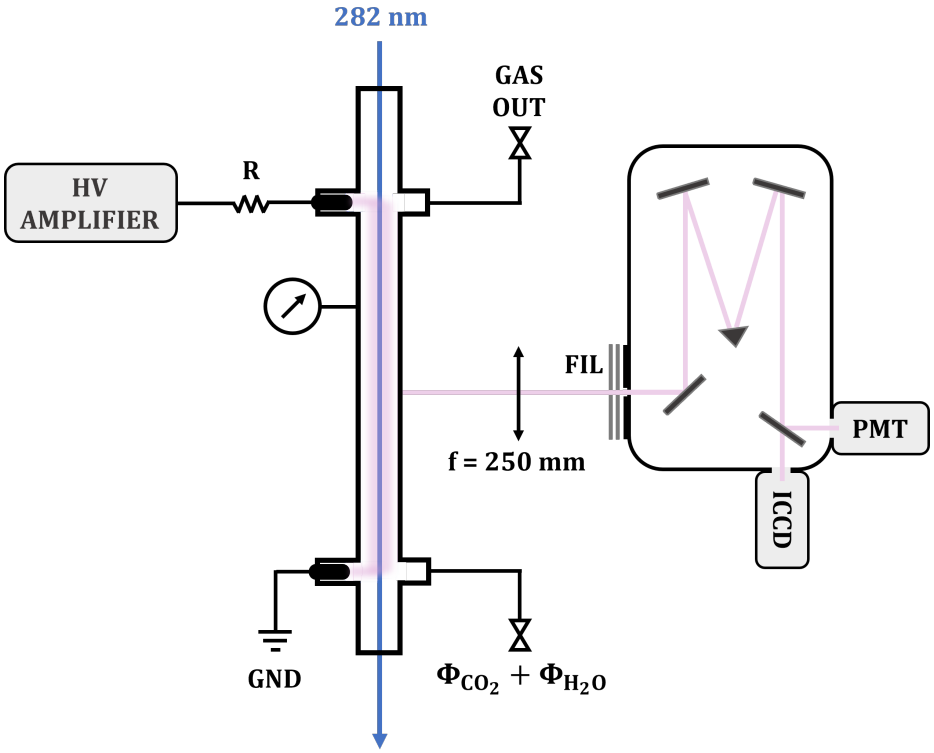

FIGURE 3.25: *Scheme of the glow discharge apparatus. See text and [94] for explanation.*

whereas the CO_2 conversion data are shown in the right panel. The trend exhibited by the CO_2 dissociation, with lower conversion rates during the plasma ON phase, has been observed in the same setup with TALIF spectroscopy on CO [95] and Raman spectroscopy on CO_2 [96]. However, no solid justification has yet been found. α lies between 5% and 25%, significantly deviating from the literature data, where a conversion of 6.2% was obtained for a water admixture of 10% [93]. Besides, the total conversion rate is expected to decrease further with larger water admixtures. This can be mainly ascribed to the uncertainty introduced with water addition, as the water content is not measured in situ, but at the injection stage. As evidenced by figure 2.6, the sensitivity of the diagnostic method decreases with water addition, so that underestimating the water content has the effect of overestimating the resulting conversion. From formula (2.36), it can be calculated that water content of 22% corresponds to a conversion of $\simeq 5\%$ for the same measured band ratio. Hence, it is reasonable to assume an underestimation of water content in the mixture of the order of a few percent, most likely due to uncontrollable condensation or OH adsorption onto the reactor walls.

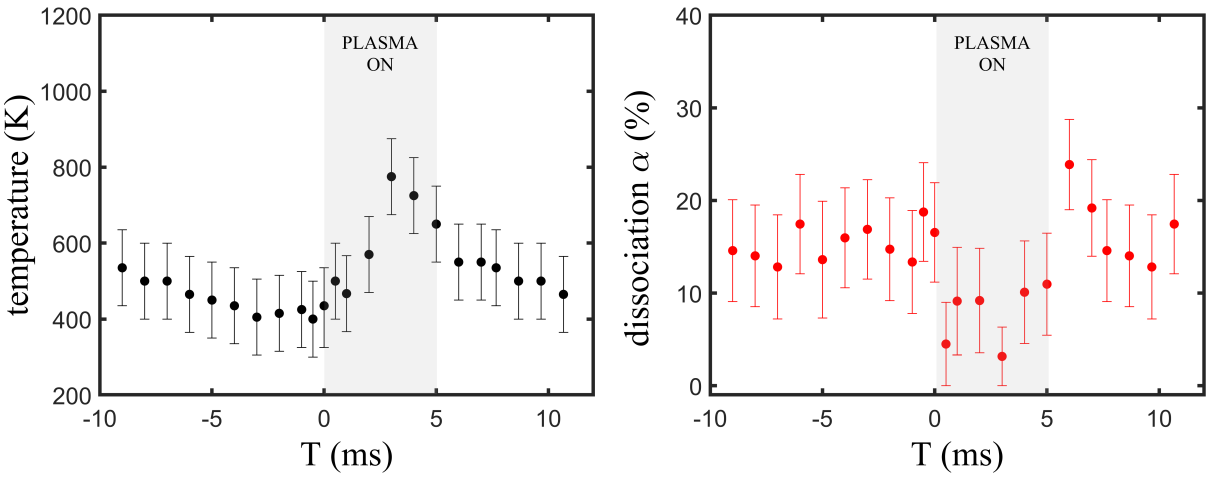

FIGURE 3.26: *Temporal evolution of the gas temperature (left) and the* CO_2 *dissociation during the plasma cycle and its afterglow. Conversion data are obtained from formula (2.36) and the temperature-dependent collisional rate coefficients inferred from equation (3.21). Experimental conditions:* 5.34 mbar CO_2 + 1.33 mbar H_2O, *total flow* 7.4 sccm, *plasma current* 50 mA. *Data reported from [94].*

Chapter 4

Time-resolved optical emission spectroscopy

Atmospheric pressure nanosecond repetitively pulsed (AP NRP) discharges have shown good performances in the reduction of $\mathrm{CO_2}$ *to* CO *and* $\mathrm{O_2}$*, both in pure* $\mathrm{CO_2}$ *and dry reforming of methane. Despite great scientific interest in these systems, a complete understanding of the underlying dissociation mechanisms is still absent. The transient nature of NRP discharges calls for time-resolved diagnostic techniques that can probe the temporal evolution of the discharge and access the microscopic kinetics in a non-invasive way. Time-resolved optical emission spectroscopy (TR-OES) has proven to be a suitable tool for the investigation of NRP discharges, as the emission features can be correlated with the discharge characteristics in a relatively easy way. However, TR-OES studies of* $\mathrm{CO_2}$ *NRP discharges are not available in the literature, as most of the investigated conditions are concerned with different devices or plasma conditions. The application of TR-OES to a* $\mathrm{CO_2}$ *NRP discharge, presented in this chapter, reveals a complex temporal structure along a* ns *pulse for both the emitted light and the discharge characteristics. The addition of a small fraction of* $\mathrm{N_2}$ *to the* $\mathrm{CO_2}$ *gas feed is used to estimate the gas temperature via the Second Positive System bands of nitrogen, as they arise exclusively due to electron impact excitation. The Stark broadening of the* O $(3\mathrm{s}\ {}^5\mathrm{S}^0_2 \leftarrow 3\mathrm{p}\ {}^5\mathrm{P}_{1,2,3})$ *triplet is used to infer the electron density evolution, which reveals a significant degree of ionization in the spark phase with a peak electron density around* $10^{18}\ \mathrm{cm}^{-3}$*. Finally, the intensity ratio of the* C^+ *and* C^{++} *emission lines can assess the electron temperature evolution, owing to an electron excitation kinetics (EEK) condition being established in the plasma. The overall picture that arises from the observations is of a fast breakdown phase, dominated by electron impact*

dissociation of CO_2 from the ground state, followed by a spark phase, where a long-lasting dissociation mechanism of CO_2 is active, most likely related to vibrational excitation.

4.1 Setup considerations

The scheme of the experimental apparatus is shown in figure 4.1. The plasma conversion of CO_2 is carried out in a stainless steel vacuum-tight reactor with the electrodes maintained in a pin-to-pin configuration. Three arms allow for light collection and, if needed, for laser injection at the center of the reactor. The HV and ground pin electrodes are narrow stainless steel tubes that also act as inlet and outlet for the gas flow, respectively. The HV anode, with an internal diameter of $1.07\ \mathrm{mm}$ and an external diameter of $1.47\ \mathrm{mm}$, is kept at a fixed inter-electrode $5\ \mathrm{mm}$ distance above the cathode, which extends from the reactor assembly for a few mm with an internal diameter of $2\ \mathrm{mm}$ and external diameter of $3.2\ \mathrm{mm}$. The reactor is embedded in a Faraday cage to suppress the electromagnetic noise.

Vacuum cell and gas handling A variable CO_2 flow Φ_{CO_2} is injected into the reactor cavity by a MKS mass flow controller (MFC1). For some applications, a variable flux of a second gas Φ_{GAS2} is admixed to Φ_{CO_2} before its injection into the cell. The control range of the mass flow controllers ranges between 2% and 100% of full scale. The accuracy, including non-linearity and hysteresis, is 1%. The repeatability error is 0.2% of the full scale. The pressure is stabilized to $745\ \mathrm{Torr}$ by a proportional-integral-derivative (PID) control that acts on a second mass flow controller (MFC2) at the exit of the reactor. The pressure is monitored by a Varian Ceramicel capacitive gauge ($1000\ \mathrm{Torr}$ FS). The error on pressure values is 0.5% of the gauge readout. Evacuation of the reactor is achieved by a $80\ \frac{\mathrm{m}^3}{\mathrm{h}}$ Edwards two-stage rotary vane pump and a mechanical booster.

Discharge generation and operation The discharge is run by a Megaimpulse Ltd. NPG18/100k ns-pulsed power supply, externally triggered by a Rigol DG4062 waveform generator. The full width at half maximum (FWHM) of the ns pulses is about 10 ns and the rise time < 4 ns on a 75 Ω matched load. The generator supplies a maximum of 4000 HV pulses per second up to a frequency of $100\ \mathrm{kHz}$ and a maximum peak voltage of $18\ \mathrm{kV}$ on a matched load. The output voltage is selected by a knob

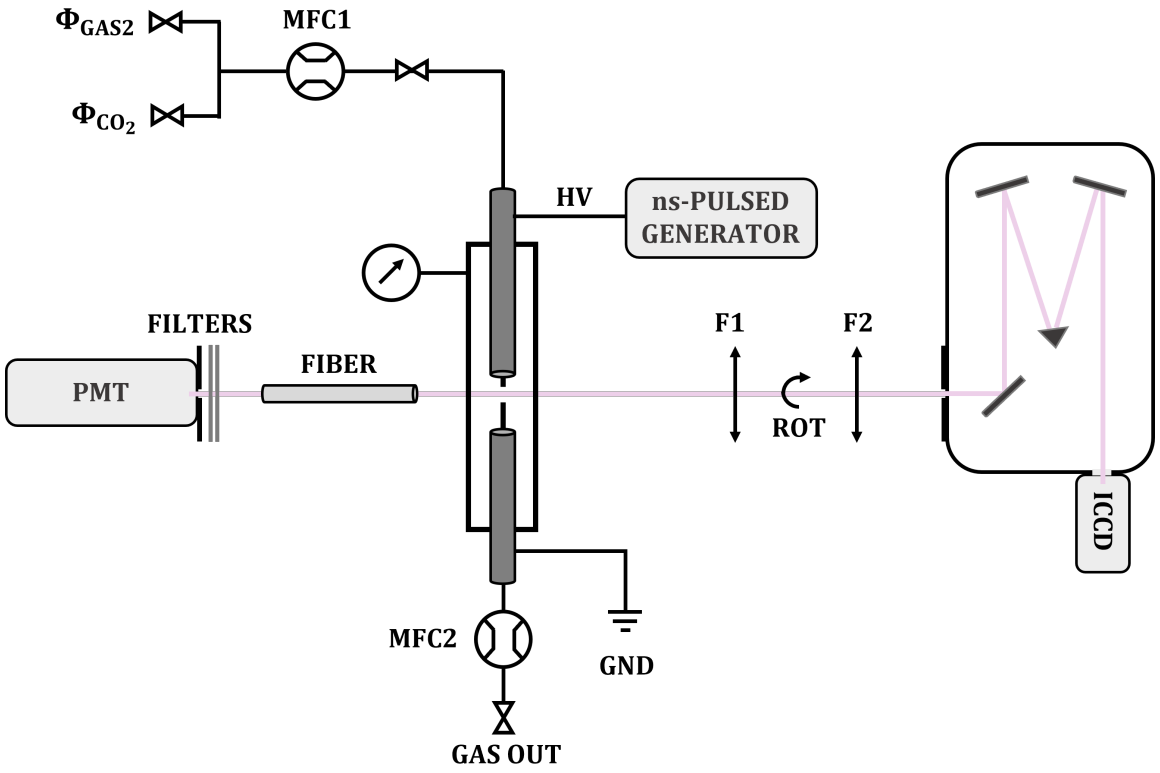

FIGURE 4.1: *Scheme of the experimental apparatus. See text for explanation.*

that allows spanning from 50% to 100% of the maximum ratings of the power supply. Voltage and current signals are measured by a high voltage probe (P6015A Tektronix probe, bandwidth=75MHz) and an $\mathrm{I/V}$ converter (CT-D-1.0 Magnelab, bandwidth=20-500MHz). The traces are collected by a LeCroy HDO9100 digital oscilloscope.

Detection system The light emitted by the discharge is detected simultaneously by two sensors. A Hamamatsu R2949 PMT allows recording the time-resolved, spectrally-integrated emission profile. A set of Thorlabs NDUV**B neutral filters is used to prevent saturation of the PMT and an optical fiber (SQS Vlaknova Optika MM BFL37 $\varnothing = 400\ \mu\mathrm{m}$) couples the emitted light with the entrance slit of the detector. The signal is measured as a voltage drop across a $50\ \Omega$ resistance of a Lecroy HDO9100 digital oscilloscope. An Andor DH334-T-18U-03 intensified gateable CCD detects the spectrally-resolved emission light, i.e. the *emission spectrum*. The ICCD, sized $13.3 \times 13.3\ \mathrm{mm}$, is a 1024×1024 pixels array operated in full vertical binning. The ICCD can be gated

down to $2\ \mathrm{ns}$ and an external trigger signal allows for synchronization between the gate and the ns discharge pulse. The sensor is coupled with a Shamrock 303i $300\ \mathrm{mm}$ focal length monochromator, which is equipped with a set of three reflective gratings: $600\ \mathrm{grooves/mm}$, $1200\ \mathrm{grooves/mm}$ and $2400\ \mathrm{grooves/mm}$. These can be alternatively used to get different spectral resolutions. The spectrograph is calibrated for relative irradiance by an Avantes Avalight-DH-BAL-CAL calibration lamp. The emitted light is collimated by a $200\ \mathrm{mm}$ focal length lens (F1) placed at a distance $\mathrm{f} = 200\ \mathrm{mm}$ from the reactor vertical axis and focussed onto the spectrograph entrance slit by a $75\ \mathrm{mm}$ positive lens (F2). A periscope (ROT) images the inter-electrode axis orthogonally to the slit. The collection system captures about $130\ \mu\mathrm{m}$ of the discharge gap. If needed, two Thorlabs bandpass filters (FEL 0400, FEL 0550) are used to suppress the higher orders of the diffraction gratings.

4.2 Discharge characteristics

Nanosecond repetitively pulsed (NRP) discharges have shown good performances in the reduction of CO_2 through both dry reforming of methane [63] [97] and pure CO_2 [62] [56]. Improvement of the conversion efficiency was achieved in [62] and [97] by changing the temporal pattern of the excitation, exploiting the possibility of varying the time separation between pulses while keeping the total energy input constant.

To explore different excitation time-scales, two pulsing schemes were adopted by the authors, a representation of which is given in figure 4.2:

1. continuous mode: series of equally-spaced ns pulses at a constant repetition frequency $\mathrm{f_p}$. The minimum achievable inter-pulse time in this operation mode, $\mathrm{T_p}$, was $250\ \mu\mathrm{s}$, corresponding to a maximum of 4000 deliverable pulses per second;

2. burst mode: sets of a fixed number N of high-frequency ns pulses repeated at a frequency $\mathrm{f_p}$ and grouped into low frequency bursts of frequency $\mathrm{f_b}$. The minimum achievable inter-pulse time between two successive pulses in the burst, $\mathrm{T_p}$, was $10\ \mu\mathrm{s}$. The burst mode is a technical expedient to explore the effect of short inter-pulse times at a relatively low average energy consumption, since the total number of delivered pulses is kept lower than in continuous mode operation.

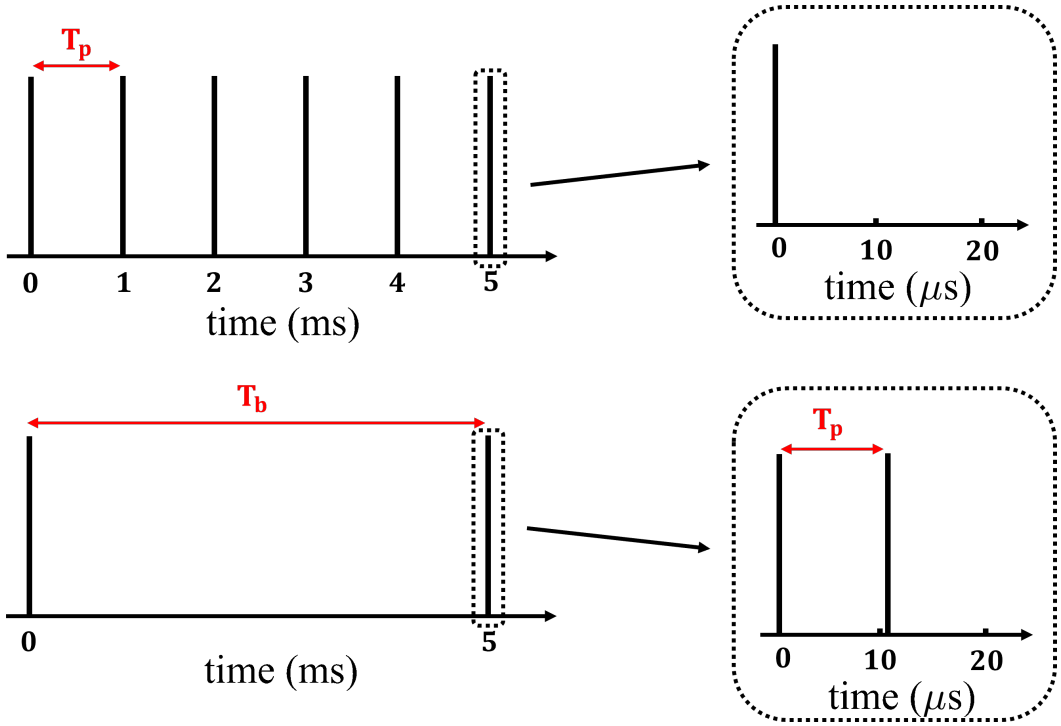

FIGURE 4.2: *top: Scheme of the continuous operation mode at a* $f_p = 1$ kHz ($T_p = 1$ ms)*. bottom: Burst of* $N = 2$ *pulses at* $f_p = 90$ kHz ($T_p = 11$ μs) *and repetition burst frequency* $f_b = 200$ Hz ($T_b = 5$ ms)*.*

For the same energy input, the analysis of effluent gas composition carried out in [62] revealed an improvement of the dissociation performances with the high-frequency burst mode operation with respect to the continuous mode, both in the conversion and the energy efficiency. This behavior was attributed to a *memory effect* appearing between successive pulses in a burst, as the subsequent pulses intercept an already partially-ionized and warm gas composition, as opposed to the untreated gas mixture intercepted by the first pulse of the burst. Evidence supporting this thesis was found in both the analysis of the current/voltage characteristics of the discharge and its imaging. In this thesis, time-resolved optical emission spectroscopy (TR-OES) is employed alongside these two techniques, allowing for further characterization of the discharge pulses and the microscopic processes responsible for the dissociation of CO_2.

4.2.1 Electrical diagnostics and imaging

From the inspection of current and voltage profiles, two kinds of discharge pulses can be identified:

- *type I* pulses, i.e., the first pulse of a burst ($\mathrm{n} = 1$), which exhibits the same characteristics of all the pulses in continuous mode operation if the pulsing frequency is sufficiently low ($\mathrm{f_p} \lesssim 10\ \mathrm{kHz}$);
- *type II* pulses, i.e., the $\mathrm{n} \geq 2$ pulses of a high-frequency burst ($\mathrm{f_p} \gtrsim 10\ \mathrm{kHz}$).

The voltage and current characteristics of the first (*type I*) and the second pulse (*type II*) of a two-pulse burst at $\mathrm{f_p} = 90\ \mathrm{kHz}$ are shown in figure 4.3 for comparison. In a high-frequency burst, the marked differences between the two pulse types suggest that the nth pulse characteristics are influenced by a strong reminiscence of the $(\mathrm{n}-1)$th pulse. This effect gradually vanishes as the inter-pulse time increases, up to a condition in which subsequent pulses are completely independent. Experimental evidence from [62] allow setting the threshold between these two conditions at an inter-pulse time of about $100\ \mu\mathrm{s}$ ($\mathrm{f_p} \simeq 100\ \mathrm{kHz}$).

An indirect confirmation of a strong correlation between closely-spaced pulses is given by the I/V characteristics of both pulse types, which show a significant drop in the breakdown voltage peak and a net increment of the discharge current when transitioning from a *type I* to a *type II* pulse (see figure 4.3). These two facts are clear indicators of the different plasma conditions intercepted by subsequent pulses in a burst. It may therefore be stated that a *type II* pulse is generated when the pulse acts on a discharge gap that retains a memory of the previous pulse, in the form of changed gas composition and a higher temperature or, in other words, when the pulse encounters a different load impedance that changes the way electric power is deposited into the plasma.

The existence of different discharge conditions along the burst suggests that the electron energy distribution function (EEDF) also evolves with time, with the consequence that successive pulses in a burst might be characterized by different dissociation mechanisms. Although the EEDF cannot be estimated directly by spectroscopic means, it is reasonable to conclude that an indirect 'tailoring' of the discharge conditions can be achieved by using high-frequency bursts. Within this context, TR-OES

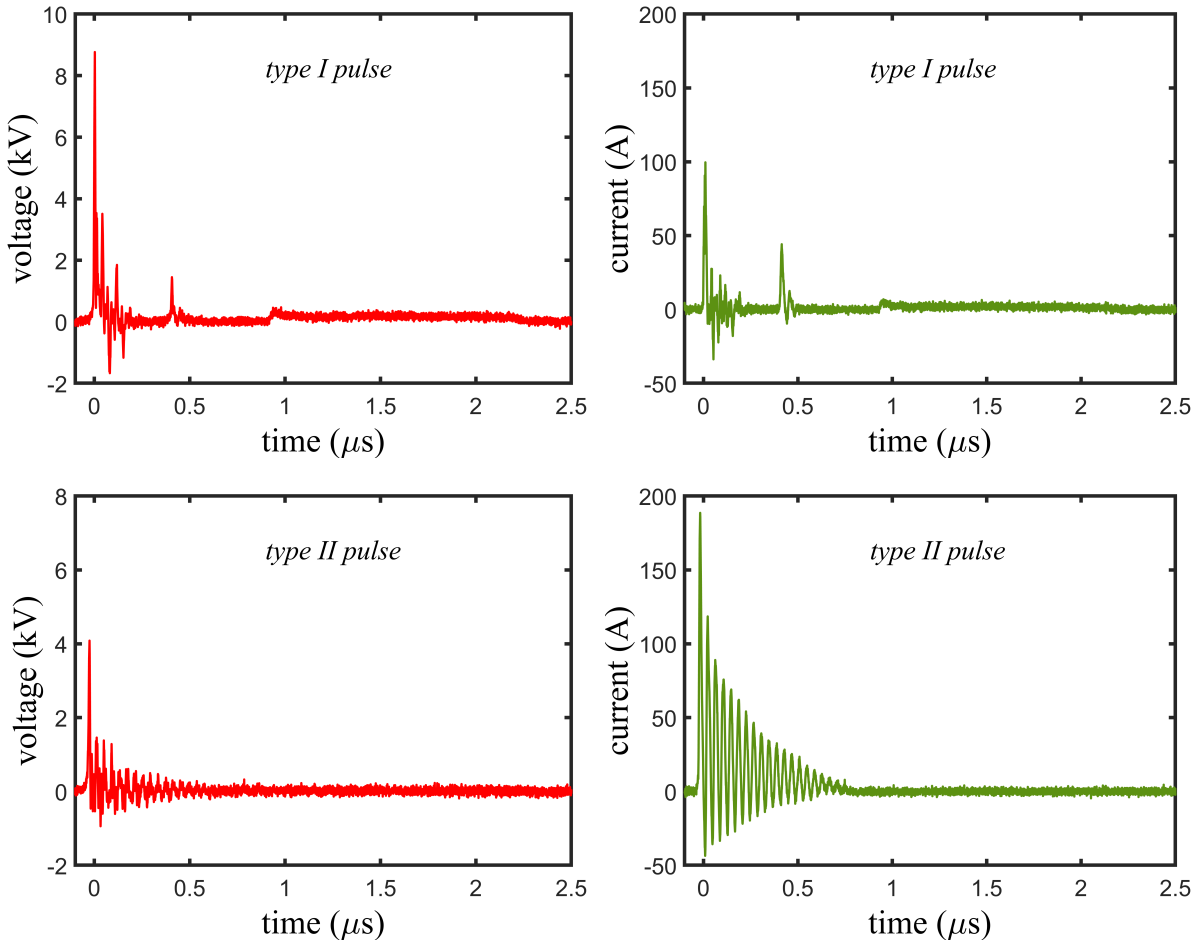

FIGURE 4.3: *Voltage (left) and current (right) profiles of type I pulses (top panels) and type II panels (bottom panels). The discharge is operated in burst mode,* $\mathrm{N} = 2$*, with pulse frequency* $\mathrm{f_p} = 90$ kHz *and burst frequency* $\mathrm{f_b} = 200$ Hz*. Total burst energy of* 9.3 mJ*.*

offers the possibility to access the temporal evolution of the plasma parameters and support these evidences.

A further manifestation of the *memory effect* is the spatial distribution of subsequent discharge events in the electrode gap, which can be investigated by imaging the discharge. In figure 4.4, two illustrative conditions are presented: a three-pulse burst at 10 kHz (left panel) and a three-pulse burst at 90 kHz (right panel). In the first case, the streamers are spread in the discharge gap, with each pulse opening its own discharge channel; instead, the three pulses reproduce the same discharge channel in the high-

frequency burst. This is an additional indicator that if the inter-pulse time is short enough, the pulses in the burst are strongly affected by the previous ones in terms of a residual ionization, a different gas composition and pressure gradients.

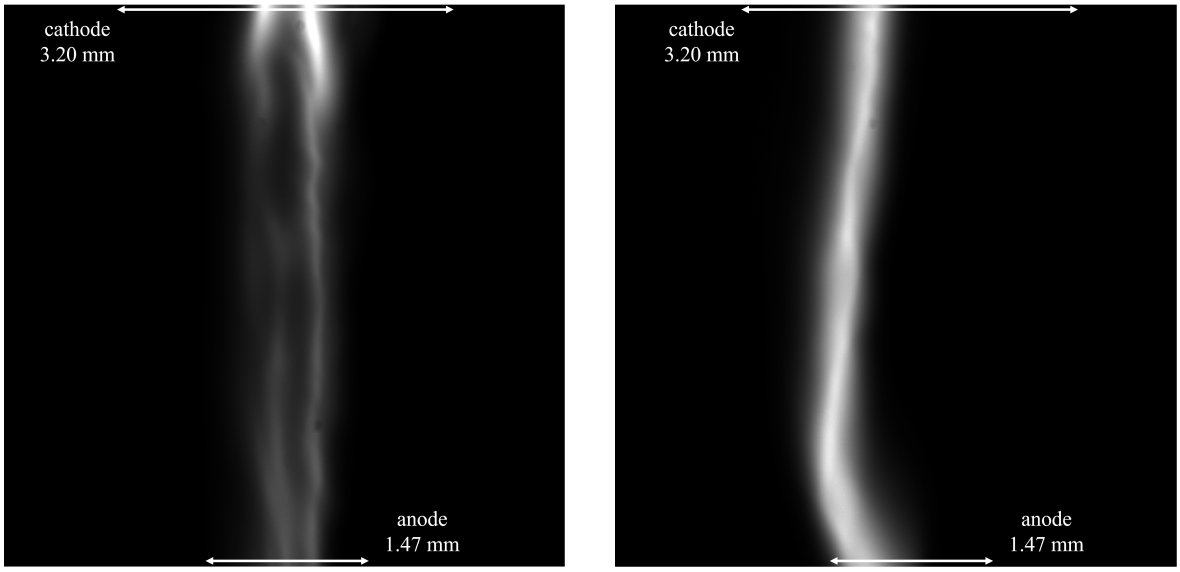

FIGURE 4.4: *Images an NRP discharge operated in burst bode,* $\mathrm{N} = 3$, $\mathrm{f_p} = 10$ kHz *(left) and* $\mathrm{f_p} = 90$ kHz *(right),* $\mathrm{f_b} = 200$ Hz. *Experimental conditions:* 100 sccm CO_2, *total pressure* 745 Torr, .

4.2.2 Pulse characteristics

Figure 4.5 shows the measured voltage, the spectrally-unresolved emission and the discharge energy evolution for both pulse types in a two-pulse burst at 90 kHz. Details on the pulse energy determination are given in section 4.2.3. Four temporal regions can be recognized in a *type I pulse*:

- *Region I*: the breakdown event, with a duration of about 15 ns and a high voltage peak that initiates the discharge. Most of the pulse energy is dissipated at this stage, with values ranging between 70% and 90% of the total energy depending on the discharge parameters. The light profile is spike-like and traces the time

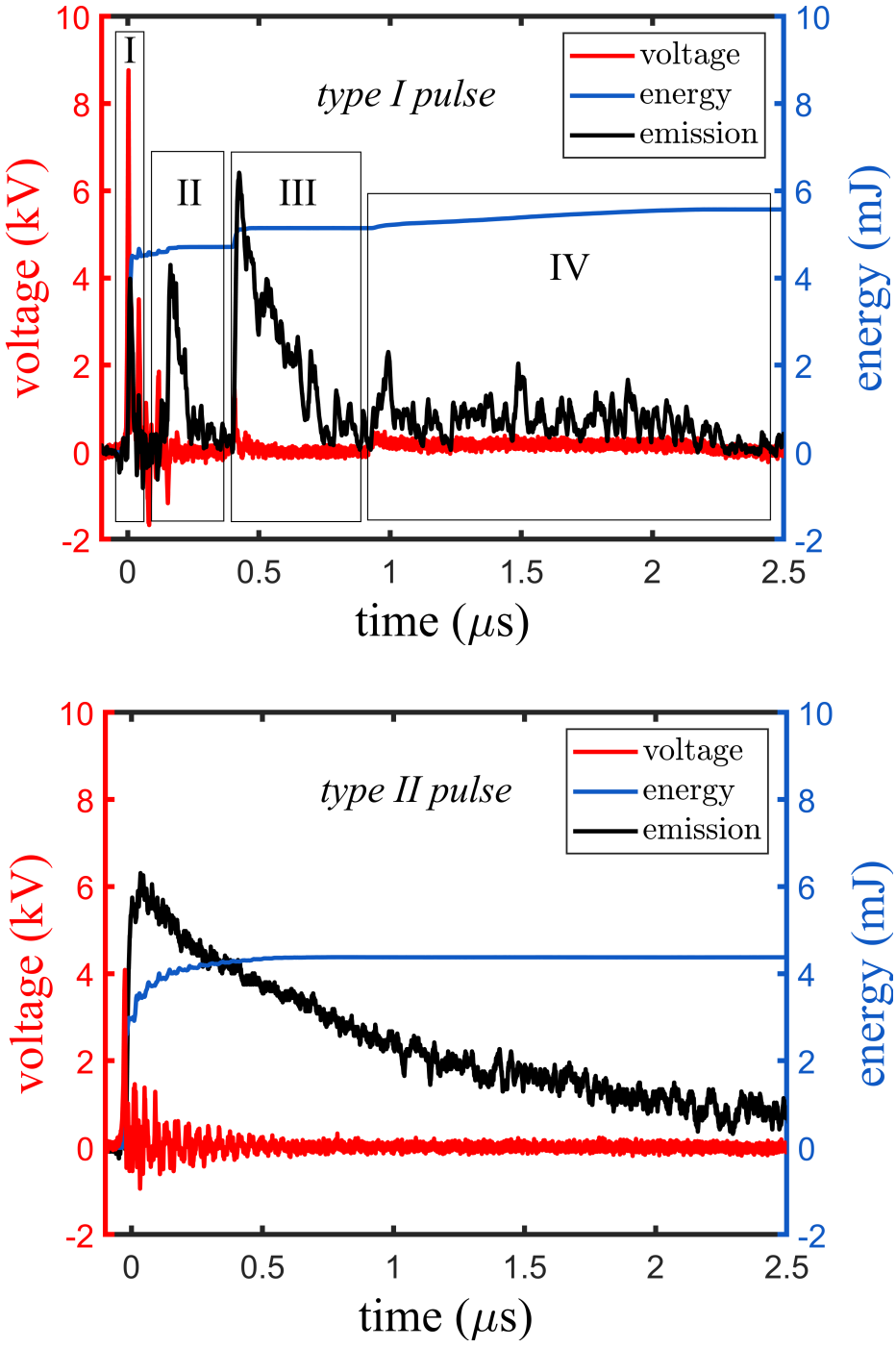

FIGURE 4.5: *Time-resolved voltage, dissipated energy and spectrally unresolved emission profiles of a type I pulse (top) and a type II pulse (bottom). The emission is arbitrarily rescaled to fit into the plot. The discharge is operated in burst mode,* $\mathrm{N} = 2$*, with pulse frequency* $\mathrm{f_p} = 90$ kHz *and burst frequency* $\mathrm{f_b} = 200$ Hz*. Total burst energy of* 9.3 mJ*.*

evolution of the current peak. This suggests that electron-impact might be the dominant excitation mechanism in this initial phase of the discharge;

- *Region II*: multiple discharge events caused by the reflected power traveling back and forth the output cable. In fact, with a propagation velocity of approximately $2 \cdot 10^8 \ \frac{\mathrm{m}}{\mathrm{s}}$ and a cable length of $3 \ \mathrm{m}$, the period of these oscillations ($30 \ \mathrm{ns}$) is consistent with the time taken by the signal to cover the whole length of the output cable back and forth. A low-voltage suffices to ignite these discharges because of a residual ionization degree from the breakdown pulse and a lower gas density. A long-lasting emission extending after the current has dropped to zero is detected. This indicates that microscopic processes other than electron impact might characterize the discharge kinetics in this phase;

- *Region III*: sequence of discharge events begun by a self re-triggering of the power supply: at about $400 \ \mathrm{ns}$ after the breakdown onset, the external switch of the power supply is re-triggered in an uncontrollable way, so that further residual power is let into the circuit. Similarly to *Region II*, a long-lasting and intense emission is observed;

- *Region IV*: slight increase of the voltage and current at approximately $1 \ \mu\mathrm{s}$ after the breakdown. A weak emission of light determined by long-lived excited species is detected.

In *type II pulses*, the voltage and current profiles exhibit a more regular behavior, with a single region in which the pulse energy is consumed by a sequence of short-period voltage/current oscillations, similar to those in *Region III* of a *type I* pulse.

4.2.3 Power analysis

The instantaneous power $\mathrm{P(t)}$ delivered by a discharge pulse to the load is computed from the current and voltage profiles as the product $\mathrm{i(t) \cdot V(t)}$. Several factors, including the length of the cables and the interspacing between the voltage and current probes, contribute to defining a spurious delay τ between $\mathrm{i(t)}$ and $\mathrm{V(t)}$. The quantification of τ is then crucial to correctly determine the energy per pulse, $\mathrm{E_p}$, as

$$\mathrm{E_p} = \int_{\tau_\mathrm{p}} \mathrm{i(t) \cdot V(t+\tau) dt} \tag{4.1}$$

where τ_p is the duration of the pulse. The stray phase shift between the voltage and current signals can be determined by reducing to zero the time integral of the $i(t) \cdot V(t)$ product, in a condition of pure reactive regime. To this end, the reactor must be filled with a high-breakdown voltage gas, such as trichlorotrifluoroethane, that prevents the breakdown [63].

In this thesis, with a less rigorous procedure, τ is determined by minimizing the time delay between the measured current $i(t)$ and the first derivative of the voltage before the breakdown, where the two should be equal as the current is purely capacitive (displacement current). Illustrative profiles are shown in figure 4.6 before and after the minimization, indicating a reactor capacitance of 46 ± 5 pF and a spurious delay of 2.4 ± 0.3 ns. For each discharge condition, a few samples of $i(t)$ and $V(t)$ are recorded

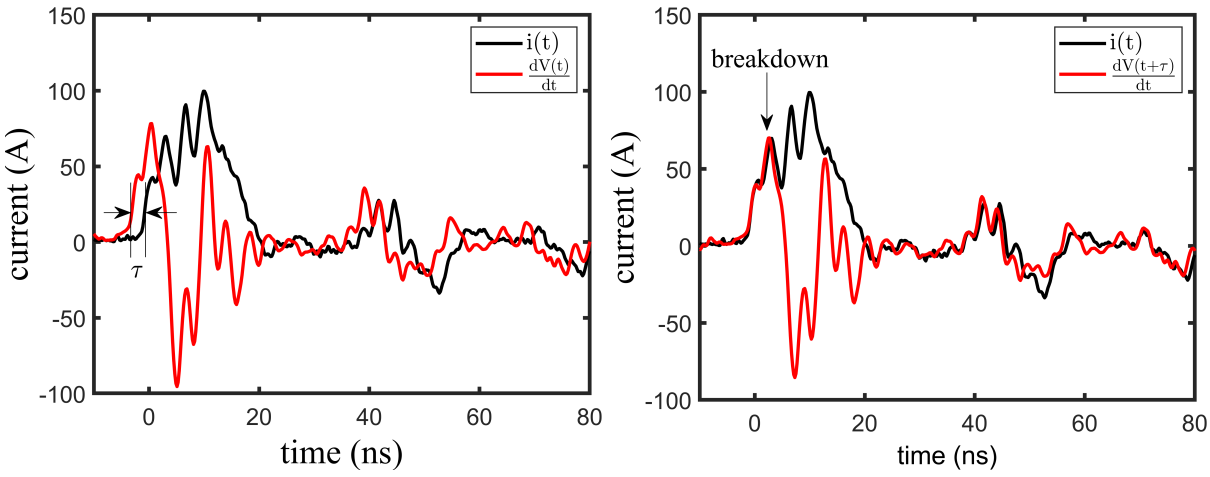

FIGURE 4.6: *left: Current profile and first derivative of the voltage in the first pulse a two-pulse burst. The delay τ is evidenced. The red solid line is rescaled by a factor for pictorial reasons. right: Determination of τ and reactor capacitance C from the time-shifted displacement current.*

to assess the *average energy per pulse* $\tilde{E}_p$. The uncertainty on energy values is the standard deviation of the samples. In the burst mode, the sum of the average energies of the pulses composing the burst determines the total burst energy E_b.

In this thesis, TR-OES studies are limited to burst sequences made of two pulses at $f_p = 90$ kHz and $f_b = 200$ Hz. Three input energy conditions are considered, corresponding to total burst energies of 6.8 ± 0.7 mJ, 9.3 ± 0.9 mJ and 12.9 ± 1.1mJ. The voltage and current profiles of each condition are shown in figure 4.7.

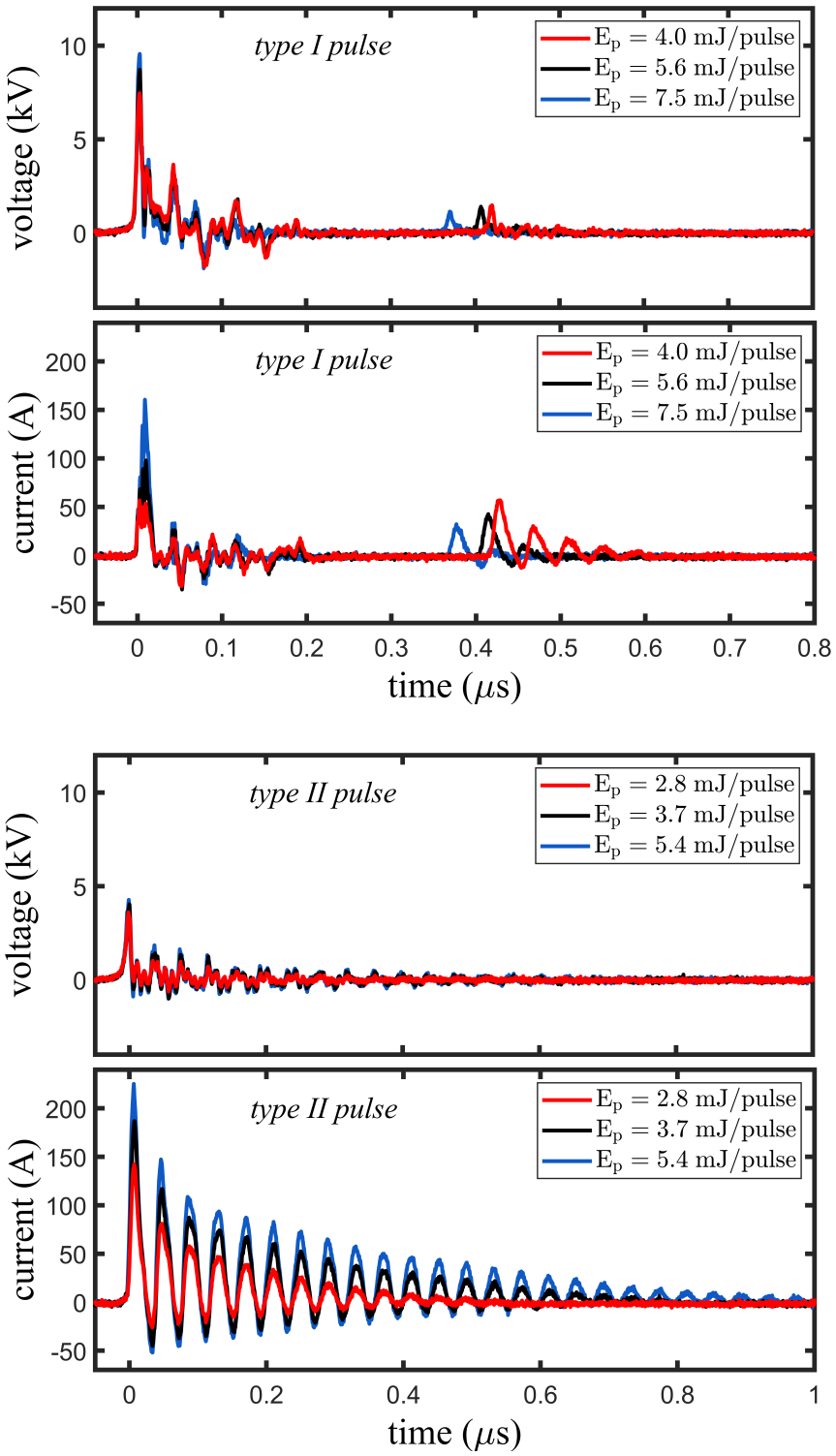

FIGURE 4.7: *Voltage and current characteristics of the first (top) and second (bottom) pulse of a two-pulse burst at* 90 kHz*, burst frequency of* 200 Hz*, and three nominal energy values.*

4.3 Time-resolved OES spectra

The evolution of the discharge kinetics is monitored by recording time-resolved emission spectra at discrete times $\mathrm{t_0}$ after the ns pulse. The temporal resolution is set by the exposure time $\mathrm{t_g}$ of the ICCD, with a lower limit of $2\ \mathrm{ns}$. The time-resolved spectra reveal drastic changes to both the gas mixture composition and the plasma conditions, as evidenced by the appearance of different emitting species and band systems throughout the pulse duration. A detailed overview of the time-resolved features along the different discharge phases is given in the following paragraphs.

4.3.1 *Type I* pulses

Figures 4.10-4.12 show the time-resolved emission spectra recorded at three delays - $\mathrm{t_0} = 0\ \mathrm{ns}$, $\mathrm{t_0} = 400\ \mathrm{ns}$ and $\mathrm{t_0} = 2000\ \mathrm{ns}$ - in a *type I* pulse. These are representative of *Region I*, *Region III* and *Region IV*, respectively, while *Region II* exhibits comparable features to those recorded in *Region III*.

Region I Figure 4.8 shows the spectra recorded upon breakdown ($\mathrm{t_0} = 0\ \mathrm{ns}$) for two conditions:

(a) continuous mode operation at $\mathrm{f_c} = 1\ \mathrm{kHz}$ and injected gas flow $\Phi_{\mathrm{CO_2}} = 100\ \mathrm{sccm}$

(b) continuous mode operation at $\mathrm{f_c} = 200\ \mathrm{Hz}$ and injected gas flow $\Phi_{\mathrm{CO_2}} = 300\ \mathrm{sccm}$

The choice between condition (a) or (b) has an influence on the mixture composition intercepted by the discharge pulses, due to the different residence time $\Delta \mathrm{t_d}$ of the gas molecules in the discharge volume. This quantity should not be confused with the 'true residence time' of the molecules in the reactor volume, $\Delta \mathrm{t_r}$, which cannot be determined in the current conditions as the precise reactor volume is not known. A reasonable estimation of $\Delta \mathrm{t_d}$ is given by

$$\Delta \mathrm{t_d} \approx \frac{\bar{\mathrm{S}} \cdot \mathrm{h}}{\Phi_{\mathrm{CO_2}}} \tag{4.2}$$

where $\Phi_{\mathrm{CO_2}}$ is the gas input flow, h is the inter-electrode gap and $\bar{\mathrm{S}}$ is the average section of the discharge volume, obtained from the inlet/outlet tubes radii. In condition (a), $\Delta \mathrm{t_d}$ is approximately $5.5\ \mathrm{ms}$, significantly larger than the inter-pulse time of $1\ \mathrm{ms}$. Therefore, each discharge pulse occurs in a gas mixture in which some residual $\mathrm{CO_2}$

dissociation products are still present. Conversely, in condition (b), Δt_d is about 1.5 ms, markedly less than the inter-pulse time of 5 ms. Therefore, the discharge pulses act on a gas composition free from CO and O_2 impurities from previous cycles. The energy input is kept approximately constant between the two conditions in order to probe the 'gas refreshing' dependence, independent of any energy input effects.

The spectra are limited to the $200-520$ nm region, as no notable features other than a few O lines appear at higher wavelengths. Five prominent band systems are observed

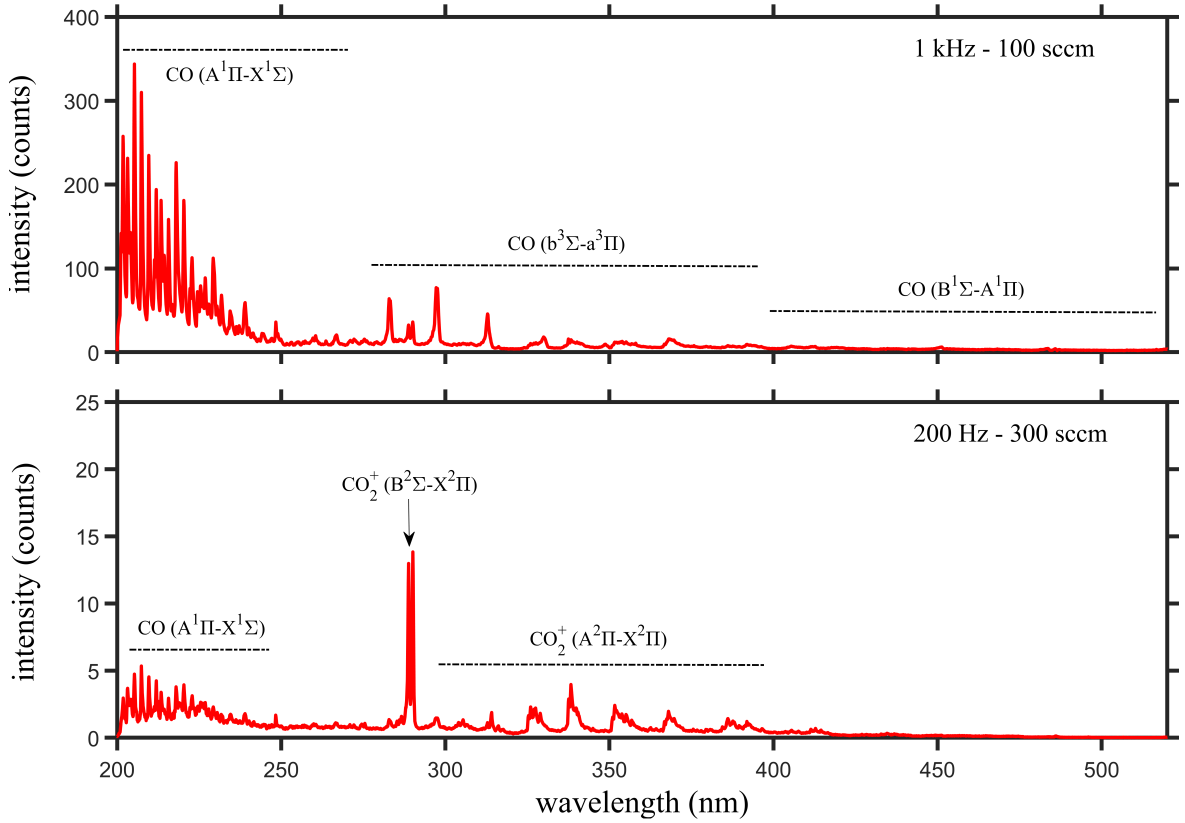

FIGURE 4.8: *Emission spectra recorded at* $t_0 = 0$ ns *(Region I) in a type I pulse.* $t_g = 10$ ns. *top: Discharge running at* 1 kHz *(continuous mode), pulse energy ?,* 100 sccm CO_2, *pressure* 745 Torr. *bottom: Discharge running at* 200 Hz *(continuous mode), pulse energy ?,* 300 sccm CO_2, *pressure* 745 Torr. *Emissions identification from [98] [99] [100] [101].*

[98] [99] [100] [101]:

- the CO $(A\ ^1\Pi \longrightarrow X\ ^1\Sigma)$ *Fourth Positive System* (4PS), appearing as single-headed

bands degrading to the red in the region between $140\ \mathrm{nm}$ and $280\ \mathrm{nm}$;

- the CO $(\mathrm{b}\ ^3\Sigma \longrightarrow \mathrm{a}\ ^3\Pi)$ *Third Positive System* (3PS), appearing as two overlapped progressions in the range $260 - 380\ \mathrm{nm}$. An overview is given in figure 4.27;
- the CO $(\mathrm{B}\ ^1\Sigma \longrightarrow \mathrm{A}\ ^1\Pi)$ *Angstrom System*, a progression of single-headed bands degraded to the violet extending over the region $400 - 550\ \mathrm{nm}$. An overview is given in figure 4.27;
- the $\mathrm{CO_2^+}$ $(\mathrm{A}\ ^2\Pi \longrightarrow \mathrm{X}\ ^2\Pi)$ *Fox Duffendack Barker System* (FDBS), appearing in the range $285 - 450\ \mathrm{nm}$ as narrow bands degraded to the red. An overview is given in figure 4.28;
- the $\mathrm{CO_2^+}$ $(\mathrm{B}\ ^2\Sigma \longrightarrow \mathrm{X}\ ^2\Pi)$ $\lambda\lambda$ $2883 - 2896$ *System* ($\lambda\lambda$), appearing as two peaks of almost line-like sharpness at about $290\ \mathrm{nm}$. An overview is given in figure 4.28.

In the $1\ \mathrm{kHz}$ condition (a), all these systems are readily observed from the onset of the discharge, with the CO emissions being dominant in the whole spectral range of observation. From the previous discussion on the residence time of the gas molecules, the strong CO emissions can be ascribed to a gas mixture still containing some CO, as the gas renewal is slower than the inter-pulse time between two successive discharge pulses. In condition (b), as the gas refreshing between the pulses is essentially complete, only trace amounts of CO and $\mathrm{O_2}$ are expected. This is confirmed experimentally by the rapid decrease in CO systems combined with the absence of emissions from other dissociation products of $\mathrm{CO_2}$. This picture is compatible with a low degree of $\mathrm{CO_2}$ dissociation during this phase. The short duration of *Region I*, and its temporal evolution in line with the profile of the current, suggest that electron impact excitation is the dominant precursor mechanism of the emissions. Notably, the appearance of energetic emission systems in the spectra, such as $\mathrm{CO_2^+}$ FDBS and $\lambda\lambda$, can only be interpreted by a highly non-Boltzmann EEDF, with a relatively large number of energetic electrons.

Regions II-III *Regions II* and *III* exhibit similar emission features to those reported in figure 4.11. The energetic CO and $\mathrm{CO_2^+}$ emission systems observed at the breakdown event are now absent, with no significant differences observed between condition (a)

and (b). These changes are ascribed to a lower degree of electronic excitation, as it cannot be assumed that CO_2 is already completely dissociated. The spectrum is dominated by neutral and ionized atomic lines (C, C^+, C^{++} and O) emerging from two continua that extend between $200 - 350$ nm and $350 - 450$ nm. The presence of intense atomic/ionic lines is still consistent with a low electron energy in the plasma, as atomic lines have typically larger Einstein emission coefficients than molecular bands. In the collision-dominated regime of the discharge, in fact, this results in a quantum yield that is one order of magnitude larger for the atomic emissions than the molecular bands. Representative transitions Einstein coefficients from the available literature are reported in table 4.1.

emission line	$\mathcal{A}$ $(\mathbf{s^{-1}})$	**ref.**
C(I) $-$ 247.86	$2.8 \cdot 10^7$	[102]
C(II) $-$ 251.21	$5.6 \cdot 10^7$	[102]
C(III) $-$ 229.68	$1.4 \cdot 10^8$	[102]
O(I) $-$ 777.42	$3.7 \cdot 10^7$	[102]

emission system	$\mathcal{A}$ $(\mathbf{s^{-1}})$	**ref.**
CO 4PS	$\lesssim 10^7$	[103]
CO 3PS	$\lesssim 10^6$	[103]
CO Angstrom	$\lesssim 10^6$	[103]
C_2 Swan	$\lesssim 10^6$	[103]

TABLE 4.1: *Einstein emission coefficients of selected observed atomic and molecular transitions. For molecules, indicative values corresponding to the most intense emissions of the system are reported.*

The two observe continua are most feasibly assigned to recombination processes. Among these, the recombination chemiluminescence

$$CO + O \longrightarrow CO_2 + h\nu \tag{4.3}$$

gives rise to a strong continuum between 200 and 800 nm with a maximum intensity around 400 nm at room temperature [104] [105] [106] [107]. However, as no correspondence with the experimental spectra has been found, this option should be disregarded. An alternative explanation is electron-ion recombination, but no reference spectra have been found in the literature for comparison. A third possibility is the electron-neutral or electron-ion Bremsstrahlung, produced during elastic collisions of the electrons with both neutral atoms and ions. Bremsstrahlung spectra have been reported for various discharge conditions and electron temperatures in [108] [109] [110] [111] [112] [113] [114]. Although no inconsistencies are observed with the measured

spectra (figure 4.11), further investigation is required for definitive characterization of the continua.

Most bands appearing between 350 and 450 nm cannot be assigned. An overview is given by figure 4.9. One reasonable explanation might be the *Carbon monoxide flame*

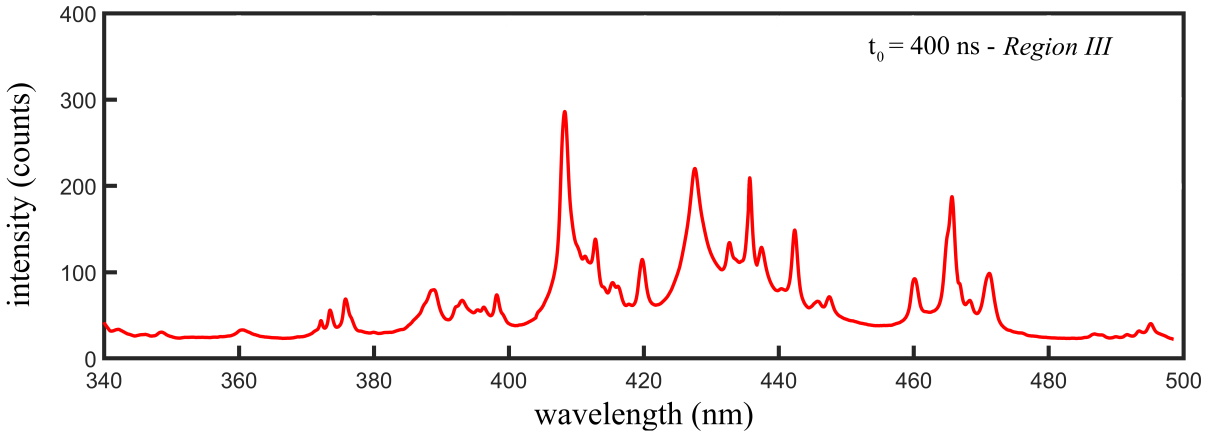

FIGURE 4.9: *Emission spectrum recorded at* $t_0 = 400$ ns *(Region III) in a type I pulse showing the unidentified bands in the region between* 340 *and* 500 nm. $t_g = 10$ ns. *Discharge running at* 200 Hz *(continuous mode),* 300 sccm CO_2, *pressure* 745 Torr.

bands system

$$CO_2\ (\tilde{A}\ ^1B_2\Delta_u \rightarrow\ \tilde{X}\ ^1\Sigma_g^+)$$

which originates from $CO + O$ recombination and appears as distinct bands superimposed on an intense continuous background in the mid-visible range [115] [106] [104]. However, no correspondence between the band head positions has been found. More generally, the time duration of these emissions rules out any $CO + O$ origin since they do not persist in the far after-glow, as one might expect for recombination processes. Because the observed emissions do not match with any known systems of either neutral or ionized CO_2, O_2 or CO, further investigation is needed for their complete characterization.

Region IV Figure 4.12 shows the emission spectrum recorded at $t_0 = 2000$ ns in the post-discharge of a ns pulse. The low current and voltage characterizing this phase justify the assumption of a low electronic excitation and, hence, negligible electron impact

excitation. Long-lived species resulting from either previous excitation or recombination processes are responsible for the observed emissions. The most notable are neutral atomic lines, weak CO bands, and the C_2 Swan System $d\ ^3\Pi_g \longrightarrow a\ ^3\Pi_u$. The latter, in particular, can be mainly attributed to the carbon recombination [116]

$$C\left(^3P\right) + C\left(^3P\right) + M \longrightarrow C_2\left(d\ ^3\Pi_g\right) + M, \tag{4.4}$$

although the role of C_2O should also be taken into consideration [117].

4.3.2 *Type II* pulses

Figure 4.13 shows the time-resolved emission spectra recorded at three successive delays - $t_0 = 5$ ns, $t_0 = 400$ ns and $t_0 = 1200$ ns - in a *type II* pulse of a two-pulse burst at 90 kHz and burst frequency of 200 Hz.

At the pulse onset (top panel, $t_0 = 5$ ns), the spectrum reveals a strong C emission at 247.86 nm, while CO and CO_2^+ bands are either weak or absent. These observations disagree with both the significant degree of CO_2 dissociation measured using CET-LIF in the post-discharge of the ns pulse (section 3.4.1) and the appearance of the energetic CO_2^+ FDBS, both of which would be expected to result in stronger CO emissions. A possible explanation is that CO is fully dissociated at this stage, and recombination only occurs in the late post-discharge. However, given an inter-pulse time of 11 μs, it seems unrealistic that no meaningful recombination to form CO has occurred yet. A second more plausible explanation is that a lower electron temperature prevents both CO and CO_2^+ excitation via electron impact and that the excited CO_2^+ that is observed is the result of alternative processes. This hypothesis is supported by the lack of the $\lambda\lambda$ emissions, which indicates different discharge conditions with respect to the previous pulse. However, further investigation is needed to clarify these aspects.

At $t_0 = 400$ ns and $t_0 = 1200$ ns, the spectrum changes drastically, with new spectral features appearing over the whole domain. Although individual lines have not been assigned, these emissions are a marker of a high O_2 concentration in the gas composition, as they match the emissions observed in a pure oxygen discharge (bottom panel). It should be noted that the different intensity arises purely from the different discharge conditions in the CO_2 and O_2 cases. As these 'O_2-related' emissions appear very weakly at the end of the first pulse, it is reasonable to assume that the O_2 formation is not significant during *Regions I-II* of the first pulse.

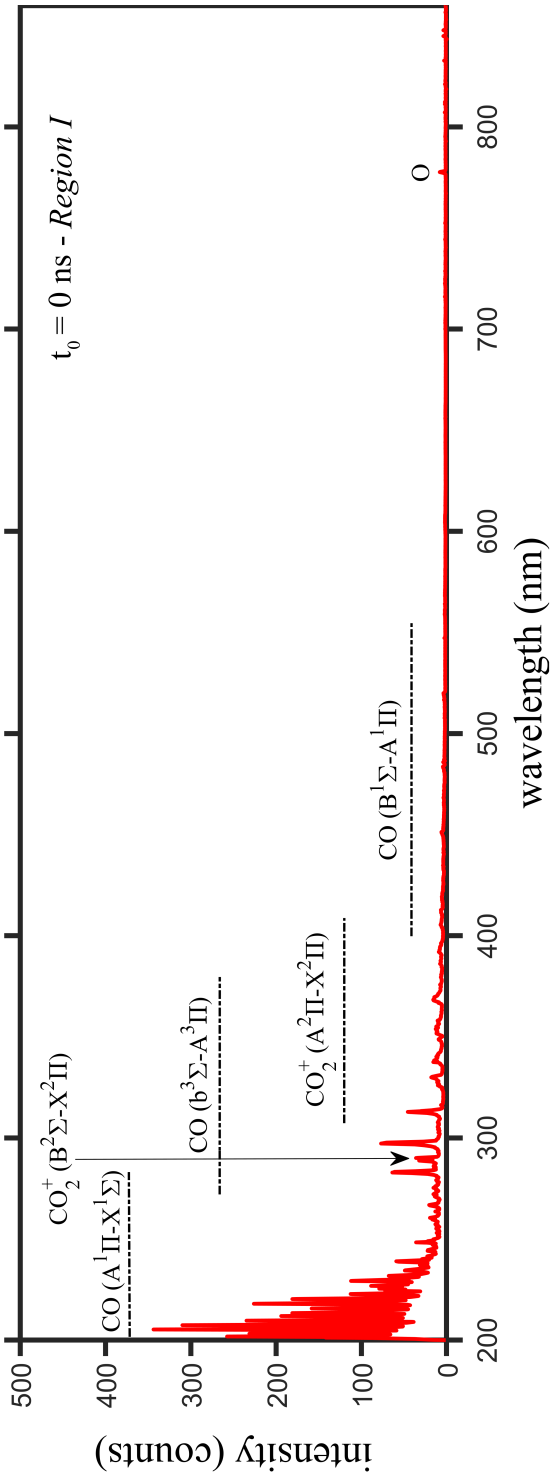

FIGURE 4.10: *Emission spectrum recorded at* $t_0 = 0$ ns *(Region I) in a type I pulse.* $t_g = 10$ ns. *Discharge operating at* 1 kHz *(continuous mode). Experimental conditions:* 100 sccm CO_2, *pressure* 745 Torr. *E?. Emissions identification from [98].*

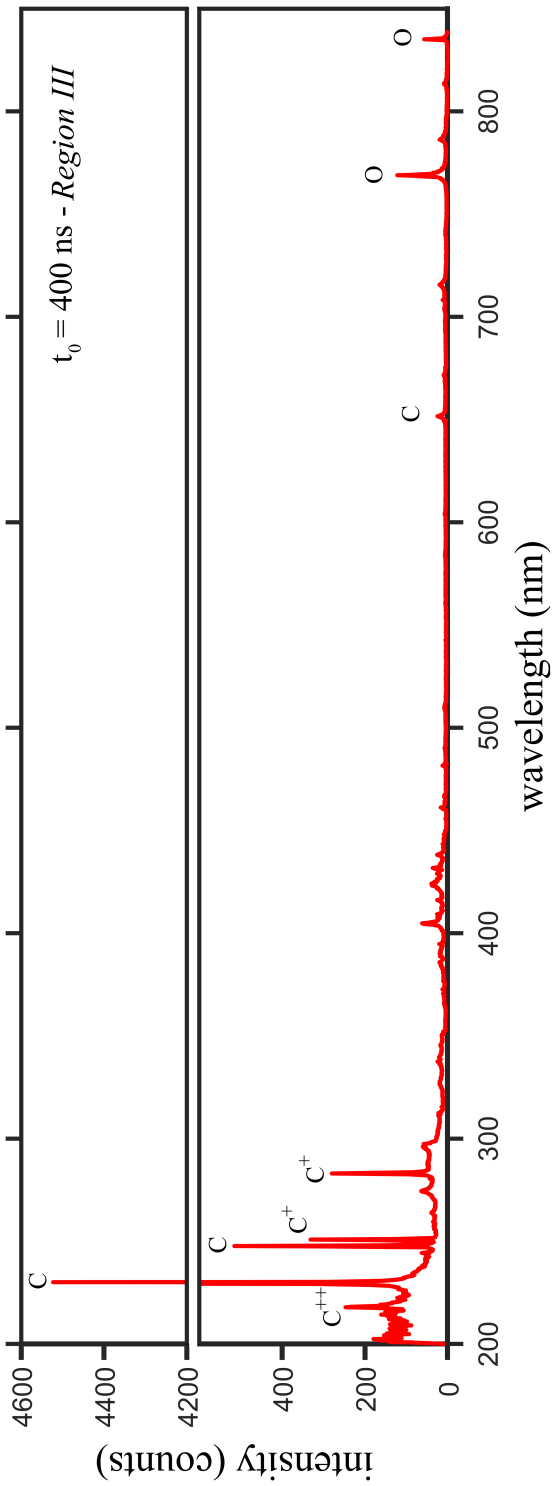

FIGURE 4.11: *Emission spectrum recorded at* $t_0 = 400$ ns *(Region III) in a type I pulse.* $t_g = 10$ ns. *Discharge operating at* 1 kHz *(continuous mode). Experimental conditions:* 100 sccm CO_2*, pressure* 745 Torr. *E?. Emissions identification from [98].*

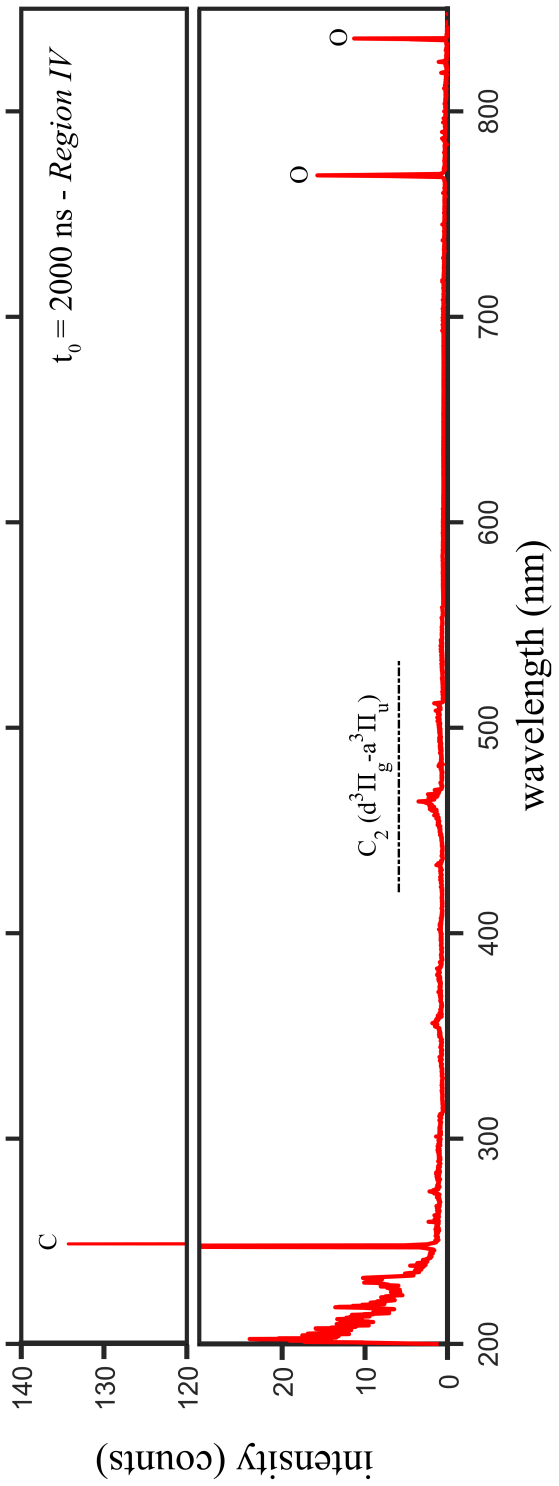

FIGURE 4.12: *Emission spectrum recorded at* $t_0 = 2000$ ns *(Region IV) in a type I pulse.* $t_g = 10$ ns. *Discharge operating at* 1 kHz *(continuous mode). Experimental conditions:* 100 sccm CO_2*, pressure* 745 Torr. *E?. Emissions identification from [98].*

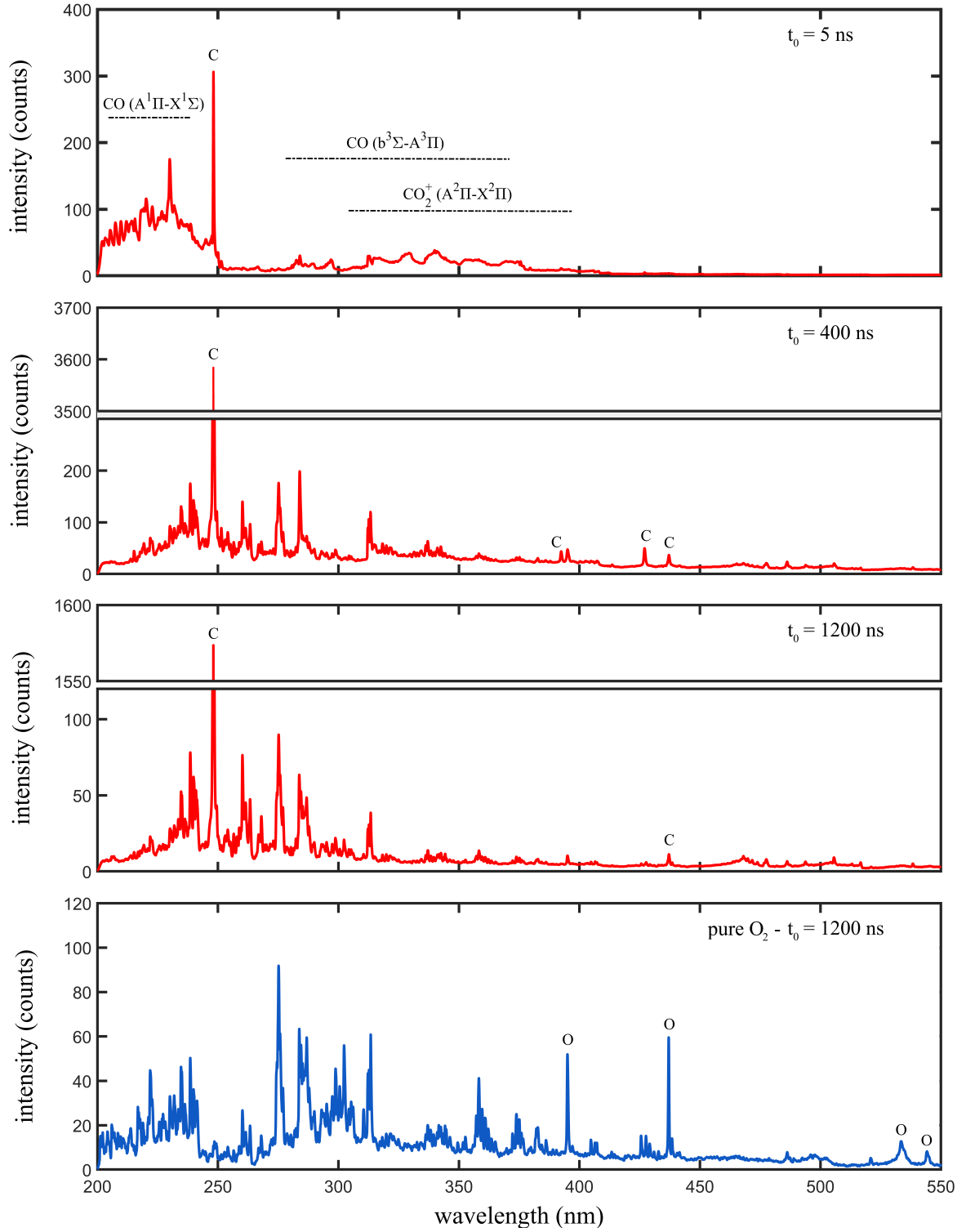

FIGURE 4.13: *Emission spectra recorded at* $t_0 = 5$ ns, $t_0 = 400$ ns *and* $t_0 = 1200$ ns *in the second pulse of a two-pulse burst at* 90 kHz, $f_b = 200$ Hz, *E?.* $t_g = 10$ ns. *Experimental conditions:* 100 sccm CO_2, *pressure* 745 Torr. *Emissions identification from [98]. bottom panel: pure oxygen discharge at* 200 Hz *(continuous mode) and* $p = 745$ Torr.

4.3.3 Atomic lines

The time-resolved spectra of both *type I* and *type II* pulses show a series of intense atomic lines arising from the dissociation of CO_2 into its constituent atoms. The most relevant of which, for the spectroscopic characterization of the discharge, are:

- the C $(2p^2\ ^1P_2 \leftarrow 3s\ ^1P^0_1)$ line at 247.86 nm;
- the $C^+(2p^2\ ^2P_{1/2.3/2} \leftarrow 2p^3\ ^2D^0_{3/2,5/2})$ doublet at 250.91 nm and 251.21 nm;
- the C^{++} $(2p\ ^1P^0_1 \leftarrow 2p^2\ ^1P_2)$ at 229.68 nm;
- the O $(3s\ ^5S^0_2 \leftarrow 3p\ ^5P_{1,2,3})$ triplet at 777.19 nm, 777.42 nm and 777.54 nm.

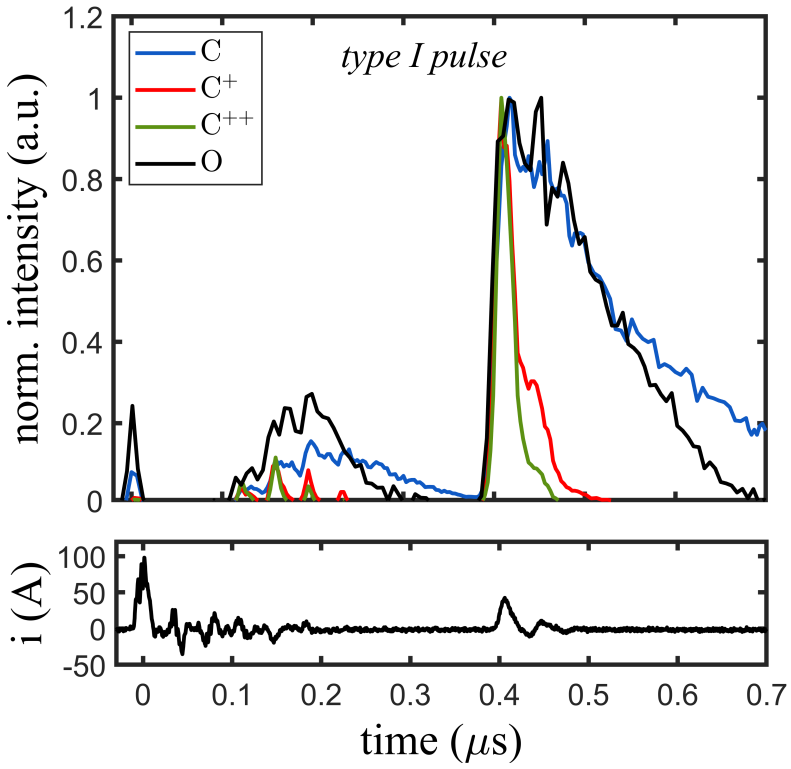

FIGURE 4.14: *Integral of the* C *(247.86 nm),* C^+ *(250.91 nm-251.21 nm),* C^{++} *(229.68 nm) and* O *(777.19 nm-777.42 nm-777.54 nm) lines in the first pulse of a two-pulse burst at* 90 kHz*, burst frequency of* 200 Hz *and burst energy* 9.3 mJ*. Temporal resolution* 3 ns*. The current profile is reported in the bottom panel as a timing reference.*

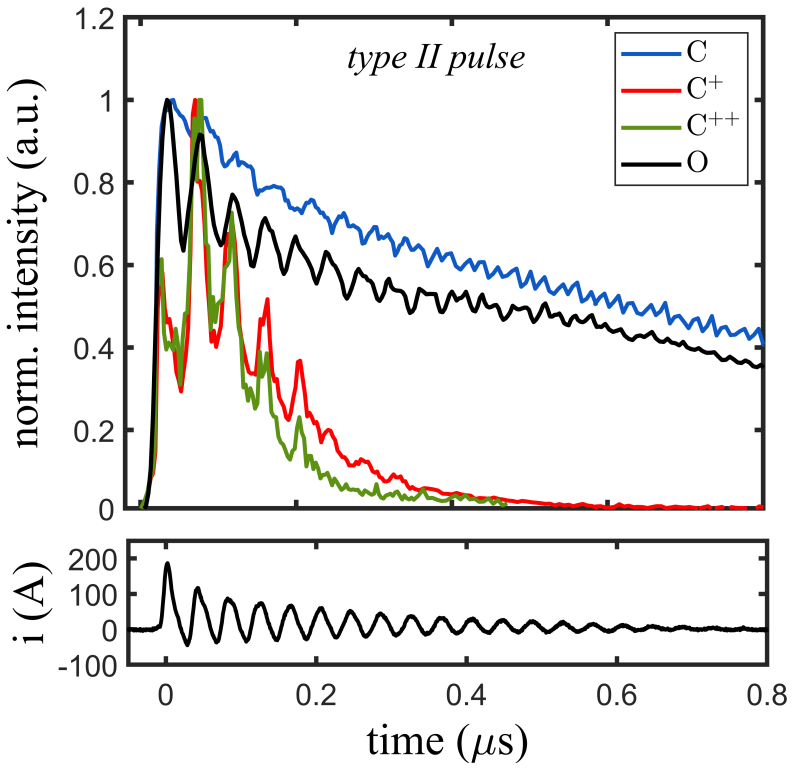

FIGURE 4.15: *Integral of the* C *(247.86 nm), C^+ (250.91 nm-251.21 nm), C^{++} (229.68 nm) and* O *(777.19 nm-777.42 nm-777.54 nm) lines in the second pulse of a two-pulse burst at* 90 kHz*, burst frequency of* 200 Hz *and burst energy* 9.3 mJ*. Temporal resolution* 3 ns*. The current profile is reported in the bottom panel as a timing reference.*

The temporal evolution of these atomic lines is shown in figures 4.14 and 4.15 for the first and second pulse of a two-pulse burst at 90 kHz, respectively. The ionic C^+ and C^{++} lines, appearing in *Regions II* and *III*, evolve in line with the discharge current peaks. This can be reasonably attributed to excitation via electron impact and, in general, to a regime in which the excitation kinetics is dominated by the electrons due to a large ionization degree [118] [119]. The implications of this condition for diagnostic purposes are discussed in section 4.6. Contrary to ionic lines, neutral C and O lines persist beyond the current peaks, suggesting that their formation might be due to recombinations or energy-transfers from long-living species. However, a contribution from electron impact cannot be neglected entirely, especially at the outbreak of *Region I* where electron-mediated processes are prevalent. Since no precursors have been identified for these lines, no conclusive considerations can be drawn at this stage.

4.4 Gas temperature determination

OES is a widely used analytical technique to infer the translational (gas) temperature $\mathrm{T_{gas}}$ from the rotational distribution function of the light-emitting molecules. An extensive review of alternative temperature determination methods based on emission spectra is given in [120]. The spectroscopic determination of $\mathrm{T_{gas}}$ relies on the existence of an equilibrium condition between the vibro-electronic state under consideration, say $|\mathrm{i}\rangle$, and the gas temperature. This being the case, a thermalized population distribution following the Maxwell–Boltzmann statistics is established in $|\mathrm{i}\rangle$ and the intensity radiated by individual rotational levels J'

$$\mathcal{I}_{\mathrm{J}'} \propto \mathcal{A}_{\mathrm{J}'\mathrm{J}''}\, \upsilon_{\mathrm{J}'\mathrm{J}''}\, \mathrm{n}_{\mathrm{J}'} \propto (2\mathrm{J}'+1)\, \mathcal{A}_{\mathrm{J}'\mathrm{J}''}\, \upsilon_{\mathrm{J}'\mathrm{J}''} \exp\left[-\frac{\mathrm{E}_{\mathrm{J}'}}{\mathrm{k_B T'_{rot}}}\right] \tag{4.5}$$

provides a measurement of $\mathrm{T_{gas}}$ via the equilibrium condition $\mathrm{T'_{rot}} \simeq \mathrm{T_{gas}}$. In formula (4.5), the $(2\mathrm{J}'+1)$-fold degeneracy of each rotational state has been taken into account, $\upsilon_{\mathrm{J}'\mathrm{J}''}$ is the frequency of the transition, $\mathcal{A}_{\mathrm{J}'\mathrm{J}''}$ the spontaneous emission Einstein coefficient and $\mathrm{E}_{\mathrm{J}'}$ the rotational energy of levels J' [120]. Primed and double primed quantum numbers refer to the upper and lower states of the transition, respectively.

4.4.1 Rotational distribution of molecules

The translational-rotational equilibrium of a molecular state is achieved when the rates of rotational energy-transfer exceed its overall rate of de-excitation. In other words, collisions are fast enough to allow for thermalization of the state within its lifetime. As the lifetime of the molecules in the ground state is normally significantly longer than the characteristic mean time between two successive collisions, the ground state rotational temperature is usually safely representative of the gas temperature. Conversely, the lifetime of the excited states is often not long enough to allow for rotational thermalization of those states, as in the case of AP discharges of molecular gases. As a result, many emissions arise from states with highly non-thermal rotational distributions, due to exothermic reactions that leave those states with large rotational excitation (chemical recombinations, chemi-luminescent reactions, energy-transfers, dissociations,..). The combination of both factors thus results in unreliable temperature determinations from emission spectra.

From the previous introduction, it becomes evident that selecting the suitable spectral features for $\mathrm{T_{gas}}$ determination urges caution, since the rotational distributions can represent an imprint of the formation process, a signature of the kinetic temperature, or a combination of both. Unless rotational thermalization of the excited state is met, the knowledge of the mechanisms involved in the production of the excited states is requested. It should be noted that even if rotational thermalization of a state is not fulfilled, $\mathrm{T_{gas}}$ is still accessible from OES spectra provided that the rotational temperature of the vibro-electronic state reproduces the gas kinetic temperature.

Take, for instance, the electron impact excitation from the ground state. The rate coefficients of the electron impact excitation are known to drop significantly with the transferred angular momentum $\Delta \mathrm{J}$ [121], with the consequence that one can often assume that the excitation occurs without or little change in the rotational quantum number [120]. Because of this, the excited state rotational distribution mimics the parent ground state rotational distribution, and the association $\mathrm{T_{gas}} \simeq \mathrm{T_{rot}^{M^*}}$ is justified.

Differently from electron impact excitation, several processes produce molecules in the excited states with specific rotational distributions that do not resemble the gas temperature. Dissociation of polyatomic molecules, for example, releases significant excess of energy that is partitioned between the degrees of freedom of the products, i.e. their translation, rotation, vibration and electronic excitation. From a classical point of view, one can consider that rotational excitation can take up the change in the angular momentum imparted by the dissociation process, in the same way as vibrations reflect the change in the bond length of the fragment molecule [122]. An extensive literature is available on various photodissociation mechanisms, electron-induced dissociation, dissociative recombinations and dissociative charge transfers. The reader may refer, for example, to [120] and the references therein.

In this thesis work, three study cases are considered for gas temperature determinations: the $\mathrm{N_2}$ Second Positive System, the CN Violet System and the $\mathrm{C_2}$ Swan System. A discussion concerning their utilisation as diagnostic tools is given in the following paragraphs.

4.4.2 N_2 Second Positive System (SPS)

With vibrational branches ranging between 280 and $500\ \mathrm{nm}$, the SPS is an intense ultraviolet radiation emitted by $N_2\,(C\ ^3\Pi_u)$ state appearing readily in nitrogen-containing plasmas. This emission system, originating from the transitions $C\ ^3\Pi_u \longrightarrow B\ ^3\Pi_g$, is frequently used as a gas temperature monitor by OES, since $C\ ^3\Pi_u$ state fulfills the requirement of rotational-translational equilibrium in many circumstances (see the discussion at the end of this section). N_2 SPS is observed upon injection of $5\%\ N_2$ to the gas feed. This quantity ensures that the nitrogen content does not alter the discharge conditions appreciably. The details of the SPS are shown in figure 4.29.

The gas temperature is determined by fitting the experimental spectrum with simulated profiles obtained with DIATOMIC simulation tool [123]. The fitting is restricted to the $(0,0)$ emission band at $337\ \mathrm{nm}$, due to its significant intensity and little overlap with other emissions. The spectroscopic constants used for the simulation are reported in [124]. One such fit is presented in figure 4.16, where the spectrum measured at $t_0 = 9\ \mathrm{ns}$ in a *type I pulse* of a two-pulse burst at $90\ \mathrm{kHz}$ is shown.

When the intensity of N_2 emissions is strong enough for recording a good quality spectrum, the determination of T_{gas} from OES spectra is possible. As shown in figure 4.17, N_2 emissions are prominent at the beginning of *Region I*, *Region II* and *Region III* of *type I* pulses and at the onset of *type II* pulses, up to about $15\ \mathrm{ns}$ from the breakdown event. In the particular case of a *type II* pulse, because few ns do not suffice for gas heating, the observed temperature gives a reasonable estimation of T_{gas} immediately before the pulse itself. Therefore, by changing the inter-pulse delay between two pulses in a burst, the gas temperature evolution in the post-discharge of the first can be followed by inferring the gas temperature at the onset of the second. The applicability of this procedure is limited by the minimum inter-pulse time of $10\ \mu\mathrm{s}$ achievable with the ns-pulsed power supply.

The gas temperature measurements are shown in figure 4.18. Because N_2 emissions do not allow to sample the whole temporal domain, both the temperature increase in the spark phase and the gas cooling in the post-discharge of a *type I* pulse can be monitored partially. A double exponential function

$$T_{gas}(t) = A \exp\left(-\frac{t}{\tau_1}\right) + B \exp\left(-\frac{t}{\tau_2}\right) \tag{4.6}$$

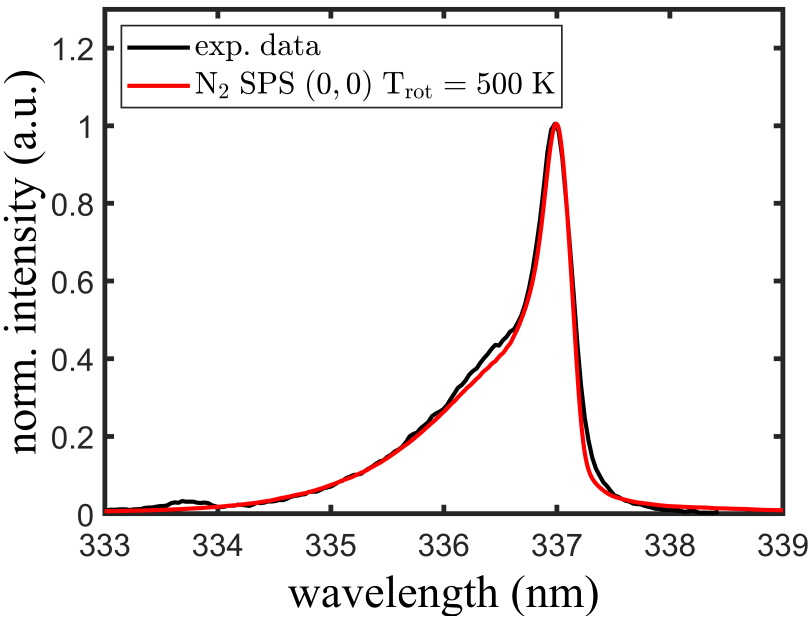

FIGURE 4.16: *Emission spectrum of the* $(0,0)$ *band of the* N_2 *SPS at* 337.1 nm*, obtained upon injection of* 5% *of* N_2 *in a* CO_2 *buffer flow. Total pressure* 745 Torr*. The data are collected at* $t_0 = 9$ ns, $t_g = 3$ ns *in the first pulse of a two-pulse burst at* 90 kHz*, burst frequency of* 200 Hz *and burst energy of* 9.3 mJ*. The simulation is obtained with DIATOMIC software [123] and the spectroscopic constants reported in [124].*

reasonably fits the time decay of T_{gas} in the post-discharge of the initial pulse. Although a complete fluid-dynamic model would be required to draw conclusive statements, it is clear that the cooling of the gas proceeds along two phases. The first, with a characteristic time of $\tau_1 \simeq 17$ μs, is probably due to a rapid expansion following the fast and significant temperature rise in the spark phase; the second, with a characteristic time of $\tau_2 \simeq 500$ μs is attributable to the mixing with the surrounding cold gas that gradually enters the plasma volume. Backward extrapolation in the $2 - 10$ μs interval, where the discharge current is zero, returns a maximum gas temperature of about 2400 K.

Validity of the approach The spectroscopic determination of T_{gas} via the N_2 SPS assumes that the rotational temperature of the $C\ ^3\Pi_u$ state can reproduce the gas kinetic

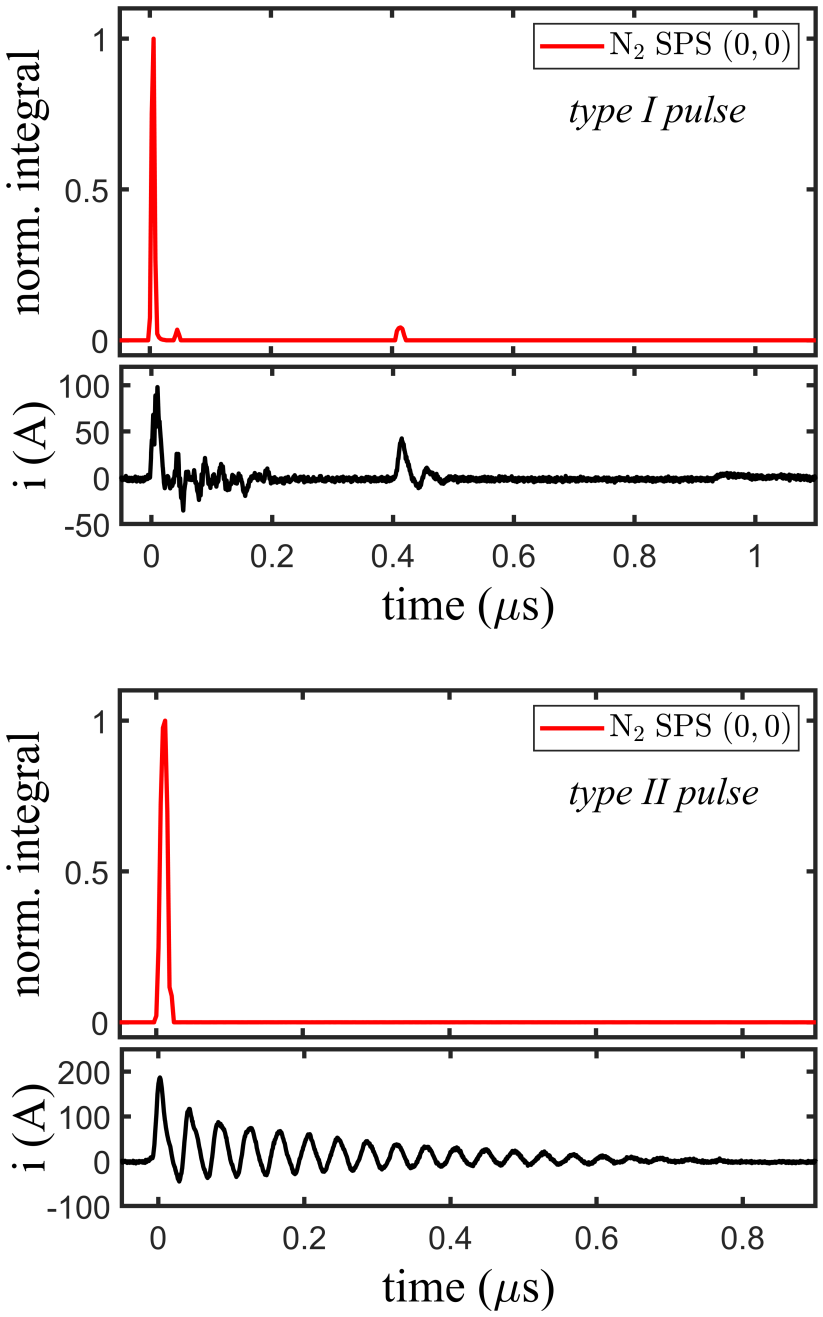

FIGURE 4.17: *Temporal evolution of the* N_2 *SPS* $(0,0)$ *band at* 337.1 nm *along the first (top) and second (bottom) pulses of a two-pulse burst at* 90 kHz*, burst frequency* 200 Hz *and burst energy* 9.3 mJ*. Temporal resolution* 3 ns*.* N_2 *emissions are obtained upon injection of* 5% *of* N_2 *in a* CO_2 *buffer flow. Total pressure* 745 Torr*. The current is reported as timing reference.*

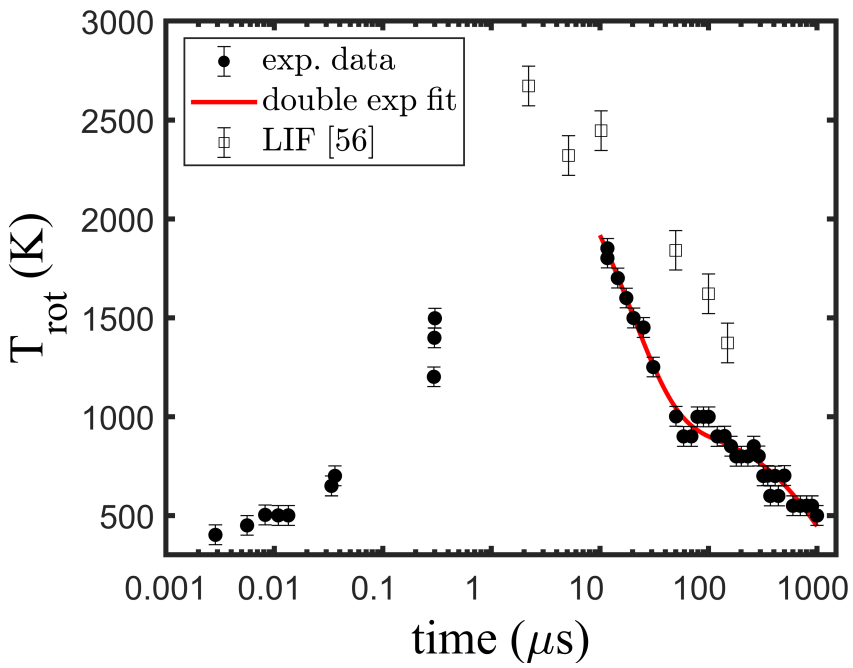

FIGURE 4.18: *Gas temperature evolution in a type I pulse and its post-discharge. Experimental conditions: two-pulse burst at variable frequency up to* 90 kHz, *burst frequency* 200 Hz, *burst energy* 9.3 mJ, CO_2 *gas flow* 300 sccm, *total pressure* 745 Torr. *The experimental data are fitted by a double-exponential function. LIF temperature measurements from [56] are also reported for comparison.*

temperature. This is indeed the case if electron impact excitation from the ground state

$$N_2\left(X\ ^1\Sigma_g^+\right) + e^- \longrightarrow N_2\left(C\ ^3\Pi_u\right) + e^- \tag{4.7}$$

is the sole production mechanism of $C\ ^3\Pi_u$, as the electron excitation can map the ground state rotational distribution on the excited state [120]. The soundness of this hypothesis can be examined by considering the other mechanisms that may come into play in the $C\ ^3\Pi_u$ formation. These are the electron impact excitation from the $N_2\left(A\ ^3\Sigma_u^+\right)$ state

$$N_2\left(A\ ^3\Sigma_u^+\right) + e^- \longrightarrow N_2\left(C\ ^3\Pi_u\right) + e^-, \tag{4.8}$$

the pooling reaction

$$N_2\left(A\ ^3\Sigma_u^+\right) + N_2\left(A\ ^3\Sigma_u^+\right) \longrightarrow N_2\left(C\ ^3\Pi_u\right) + N_2\left(X\ ^1\Sigma_g^+\right), \tag{4.9}$$

and the dissociative recombination

$$\mathrm{N_4^+ + e^- \longrightarrow N_2\left(C\ ^3\Pi_u\right) + N_2\left(X\ ^1\Sigma_g^+\right)} \tag{4.10}$$

(see table 1 in [120]). The assumption of pure electron impact excitation from the ground state might be invalidated by the concurrent formation of the $\mathrm{N_2\,(A\ ^3\Sigma_u^+)}$ metastable state, which leads to reactions (4.8) and (4.9) and unknown nascent rotational distributions in the $\mathrm{C\ ^3\Pi_u}$ state. However, no markers attributable to the $\mathrm{N_2\,(A\ ^3\Sigma_u^+)}$ formation are observed in the emission spectra throughout the whole discharge evolution. Moreover, the typical population inversion between $v' = 1$ and $v' = 0$ states generated by the pooling reaction (4.9) [125] [126] is not observed in the SPS emissions, a further indication that the reaction does not occur. On the contrary, reaction (4.10) cannot be neglected a priori since the formation of $\mathrm{N_4^+}$ is favored in highly reactive environments. However, $\mathrm{N_4^+}$ synthesis is a two-step process [127] and, therefore, only residual at the discharge outbreak when temperature measurements are carried out.

LIF thermometry The temperature measurements obtained by OH LIF excitation spectra in [56] are reported in figure 4.29 for comparison with OES measurements, due to the similar discharge conditions achieved in the two experiments. LIF temperatures are considerably larger than the corresponding OES ones. The following discussion clarifies the discrepancy. LIF thermometry is performed by exciting a few OH ro-vibronic transitions within a specific spectral range, so that the population of different rotational states J″ in the OH ground state is intercepted. The transitions used in [56] are listed in table 4.2. The LIF intensity resulting from the excitation of each transition is proportional to the J″ population according to [120]

$$\mathcal{I}_{\mathrm{LIF,J''}} \propto \mathcal{B}_{\mathrm{J''J'}}\ v_{\mathrm{J'J''}}\ \mathrm{n_{J''}} \propto (2\mathrm{J''}+1)\ \mathcal{B}_{\mathrm{J''J'}}\ v_{\mathrm{J'J''}} \exp\left[-\frac{\mathrm{E_{J''}}}{\mathrm{k_B T''_{rot}}}\right] \tag{4.11}$$

where $\mathcal{B}_{\mathrm{J''J'}}$ is the absorption Einstein coefficient and $\mathrm{T''_{rot}}$ is the rotational temperature of the OH ground state. By recording the fluorescence intensity from several transition lines, the Boltzmann distribution describing the ground state population distribution can be reconstructed and $\mathrm{T''_{rot}}$ ($\simeq \mathrm{T_{gas}}$) is determined. In [56], the derivation of $\mathrm{T_{gas}}$ from OH excitation spectra assumed that the collisional quenching of the upper N″ levels is constant. This assumption was later found to be wrong in the case of poor

	$\mathbf{N'}$	$\mathbf{F'}$	$\mathbf{J'}$	$\mathbf{N''}$	$\mathbf{F''}$	$\mathbf{J''}$	$\mathbf{\Delta J = J' - J''}$	**wavelength (Å)**
$R_2(9)$	10	2	$\frac{19}{2}$	9	2	$\frac{17}{2}$	$+1$	2817.32
$R_1(11)$	12	1	$\frac{23}{2}$	11	1	$\frac{23}{2}$	0	2817.38
$R_2(4)$	5	2	$\frac{9}{2}$	4	2	$\frac{7}{2}$	$+1$	2817.57
$R_{21}(11)$	12	2	$\frac{23}{2}$	11	1	$\frac{23}{2}$	0	2817.59

TABLE 4.2: *Pumped ro-vibronic transitions in [56] and corresponding quantum numbers. The nomenclature is the same adopted by Luque and Crosley in LIFBASE tool [54] (see section 2.5)*

rotational thermalization of the OH excited state (see table 1 in [52] and [70]). For the specific case of [56], a correction factor equal to the ratio of the quenching rate coefficients of $N' = 11$ and $N' = 4$ should be used for the line intensity ratio in the excitation spectra. This ratio, however, is not available in the literature since only low-N' quenching rate coefficients have been measured. A correction of approximately 0.5 makes LIF and OES temperatures coincide in figure 4.18. This value is consistent with the N' dependence of quenching coefficients reported in [70] for low-N' levels.

From the previous discussion, it can be concluded that the discrepancy between LIF and OES temperatures in figure 4.18 is due to an unaware use of collisional data in [56]. The robustness of OES for temperature determinations is confirmed as no assumptions other than the thermalization of the emitting states are required.

4.4.3 CN Violet System (VS)

Typically observed in AP plasma sources containing carbon compounds in air, the CN Violet System is an intense emission system that originates from the radiative transitions $B\ ^2\Sigma^+ \longrightarrow X\ ^2\Sigma^+$. The system appears as three prominent sequences with heads at $421.6\ nm$, $388.3\ nm$ and $359.0\ nm$, degraded to violet. The CN VS is readily observed upon the addition of nitrogen to the CO_2 gas feed. An overview of the $\Delta v = 0$ sequence with band origin assignation is reported in figure 4.30.

VS bands appear at the discharge ignition and, differently from N_2 SPS, they remain intense beyond the discharge current duration. This suggests that the $CN\ (B\ ^2\Sigma^+)$ formation might not be due to electron impact. A study on the mechanisms of CN ex-

citation is performed in [128], where the authors show that the recombination

$$\mathrm{C} + \mathrm{N} + \mathrm{M} \longrightarrow \mathrm{CN}\left(\mathrm{B}\ ^2\Sigma^+\right) + \mathrm{M} \tag{4.12}$$

is a relevant process active in carbon+nitrogen environments. In [128], reaction (4.12) is found to generate supra-thermal vibrational and rotational population distributions in the $\mathrm{CN}\,(\mathrm{B}\ ^2\Sigma^+)$ state, even at atmospheric pressure. This is attributed to exothermic formation reactions, low vibrational relaxation rates, and short lifetimes of the CN excited states. To check whether the Violet System is a good temperature sensor, the CN emissions are simulated with LIFBASE tool. Highly supra-thermal vibrational and rotational distributions are needed to fit the experimental spectrum. As shown in figure 4.19, a rotational temperature of approximately $2500\ \mathrm{K}$ reproduces the CN emissions, in contrast to the $400\ \mathrm{K}$ inferred from $\mathrm{N_2}$ SPS in the same conditions. It can be deduced that the rate of rotational energy-transfer does not guarantee the thermalization of the

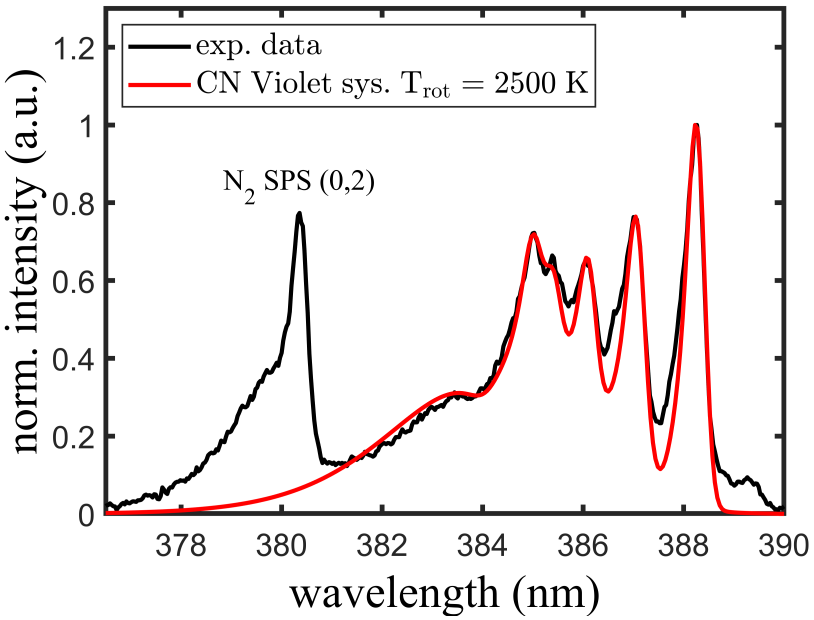

FIGURE 4.19: *Emission spectrum of the $\Delta v = 0$ sequence of the CN Violet System, obtained upon injection of 5% of $\mathrm{N_2}$ in a $\mathrm{CO_2}$ buffer flow. Total pressure $745\ \mathrm{Torr}$. The data are collected at $\mathrm{t_0} = 9\ \mathrm{ns}$, $\mathrm{t_g} = 3\ \mathrm{ns}$ in the first pulse of a two-pulse burst at $90\ \mathrm{kHz}$, burst frequency of $200\ \mathrm{Hz}$ and burst energy of $9.3\ \mathrm{mJ}$. The simulation is obtained with LIFBASE software [54].*

$\mathrm{CN}\,(\mathrm{B}\,^2\Sigma^+)$ within its lifetime and, consequently, CN must be discarded as a temperature monitor.

4.4.4 C_2 Swan System

Among the emission systems of $\mathrm{C_2}$, the most prominent bands in the visible region constitute the Swan System. Easily excited in flames or discharges in carbon-containing gas, these bands result from the $\mathrm{d}\,^3\Pi_\mathrm{g} \longrightarrow \mathrm{a}\,^3\Pi_\mathrm{u}$ electronic transitions. An overview of the system with bands identification is given in figure 4.31.

As with the CN Violet System, the Swan bands appearance does not correlate with the discharge current evolution, as they show up in the tail end of both *type I* and *type II* pulses, where the current approaches zero. A simulation of the experimental spectra is performed with DIATOMIC simulation tool. Two such fits are shown in figure 4.20. A good match with the experimental data is achieved for a rotational temperature of the $\mathrm{C_2}\,(\mathrm{d}\,^3\mathrm{d})$ state of approximately $6000\ \mathrm{K}$. In contrast, lower temperatures fail to reproduce the blue-degrading tail of the sequence. As with CN, a possible explanation for such biased temperature values has to be looked for in the formation mechanisms of the radiating $\mathrm{C_2}\,(\mathrm{d}\,^3\Pi_\mathrm{g})$ state. According to [116], there are several concurring production mechanisms of the state, either via the recombinations of C atoms, for example

$$\mathrm{C}\left(^3\mathrm{P}\right) + \mathrm{C}\left(^3\mathrm{P}\right) + \mathrm{M} \longrightarrow \mathrm{C_2}\left(\mathrm{d}\,^3\Pi_\mathrm{g}\right) + \mathrm{M}, \tag{4.13}$$

or via the $\mathrm{C_2O}$ molecule [117]. In all cases, the excess energy of the chemiluminescence reactions results in a nascent rotational distribution in the excited state that is not equilibrated by RET collisions during the lifetime. Therefore, the Swan System is not suitable for gas temperature determinations.

4.5 Electron density determination

OES is broadly used as a non-intrusive method to infer plasma parameters from the broadening and shift of emission line profiles. Owing to the large Stark effect in plasmas, Stark broadening of emission lines is the ideal tool for electron density measurement once the relationship between spectral lineshapes and charged particle density is known. The earliest attempts to lay the ground for this application date to the

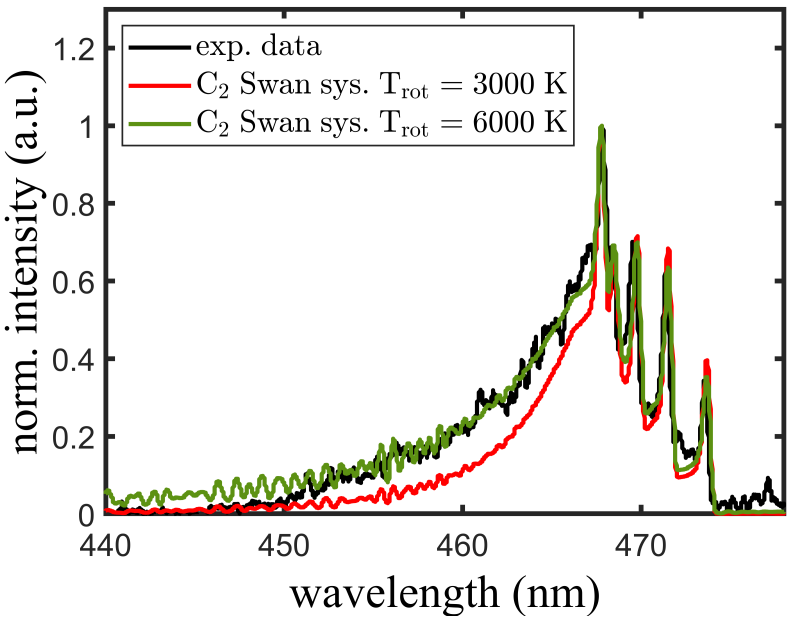

FIGURE 4.20: *Emission spectrum of the* $\Delta v = 1$ *sequences of the* C_2 *Swan System at* $t_0 = 2000$ ns ($t_g = 10$ ns) *in a type I pulse. Discharge running at* 1kHz *(continuous mode) and pulse energy of* 5.6 mJ. *Experimental conditions:* 100 sccm CO_2, *total pressure* 745 Torr. *The simulations are obtained with DIATOMIC software [123] and the spectroscopic constants reported in [103].*

early 1960s, when the first semi-classical calculations of Stark broadening parameters were carried out by Griem and co-workers for isolated non-hydrogenic atomic lines [129] [130].

According to Stark broadening theory, the shapes and shifts of plasma-broadened isolated lines are determined by electron impacts with the radiating atom, with only a minor contribution arising from the electric field generated by essentially static plasma ions [131]. To account for these contributions, the line profile can be obtained by convoluting the electronic and ionic terms, under the assumption of statistical independence and averaging over all possible electric field strengths [132]. This results in a total Lorentzian lineshape, whose full width at half maximum, $\Delta\lambda_S$, may be calculated using the approximate formula [133] [134]

$$\Delta\lambda_S \approx 2\,\omega_e\,n_e \cdot 10^{-16}\left[1 + 1.75 \cdot 10^{-4}\,n_e^{1/4}\,\alpha\left(1 - 0.068\,n_e^{1/6}\,T_{gas}^{-1/2}\right)\right] \tag{4.14}$$

where $\Delta\lambda_S$ has the units of Å, n_e is the electron density (in cm^{-3}), T_{gas} is the gas temperature (in K), ω_e and α are the electron and ion impact parameters (in Å), respectively, which are transition-specific and electron temperature-dependent. Tabulations of calculated electron impact width $\omega_e^{(cal)}$ and ion broadening parameters $\alpha^{(cal)}$ are given for a number of atoms in [134] and [135] for an electron density of $10^{16}\ cm^{-3}$. With the scalings

$$\begin{aligned} \omega_e(\text{Å}) &= 10^{-16} \cdot \omega_e^{(cal)}(\text{Å})\ n_e(cm^{-3}) \\ \alpha(\text{Å}) &= 3.16 \cdot 10^{-6} \cdot \alpha^{(cal)}(\text{Å})\ \left[n_e(cm^{-3})\right]^{1/4} \end{aligned} \tag{4.15}$$

both ω_e and α can be derived for other electron densities n_e.

In this thesis, the electron density is inferred from the Stark broadening of the oxygen $3s\ ^5S_2^0 \leftarrow 3p\ ^5P_{1,2,3}$ line - a triplet at $777.19\ nm$, $777.42\ nm$ and $777.54\ nm$ - and the carbon $2p^2\ ^1S_0 \leftarrow 3s\ ^1P_1^0$ line at $247.85\ nm$. The relevant Stark broadening parameters available in the literature are reported in table 4.3. Since the Stark broadening of the carbon line provides a worse dynamic range than atomic oxygen, the oxygen broadening is used for electron density determinations for the whole range of the measurements. In contrast, carbon data are used for comparison in the conditions of maximum electron density only.

The measurement of n_e from the Stark broadening of selected atomic lines is relatively straightforward if the Stark effect is dominant, with only minor or negligible contributions from other broadening processes. In the present conditions, all broadening mechanisms outside of instrumental and Stark broadening can be neglected, with the consequence that any isolated atomic lineshape is the result of a convolution between the instrumental function and the Lorentzian Stark broadening shape. The validity of this assumption is discussed in section 4.5.1. Provided that the instrumental function is known, the convolution can be simulated, and the width of the Lorentzian component can be varied until a good agreement between the experimental and simulated spectra is found. Examples of fitted lineshapes are shown in figure 4.21 for both a strongly broadened lineshape, with fitted Stark width of $\Delta\lambda_S = 0.51\ nm$ (top panel), and a weakly broadened profile, with $\Delta\lambda_S = 0.20\ nm$ (bottom panel).

The electron density is obtained from the fitted Stark widths via equation (4.14), with the impact parameters reported in table 4.3 and the gas temperature values in-

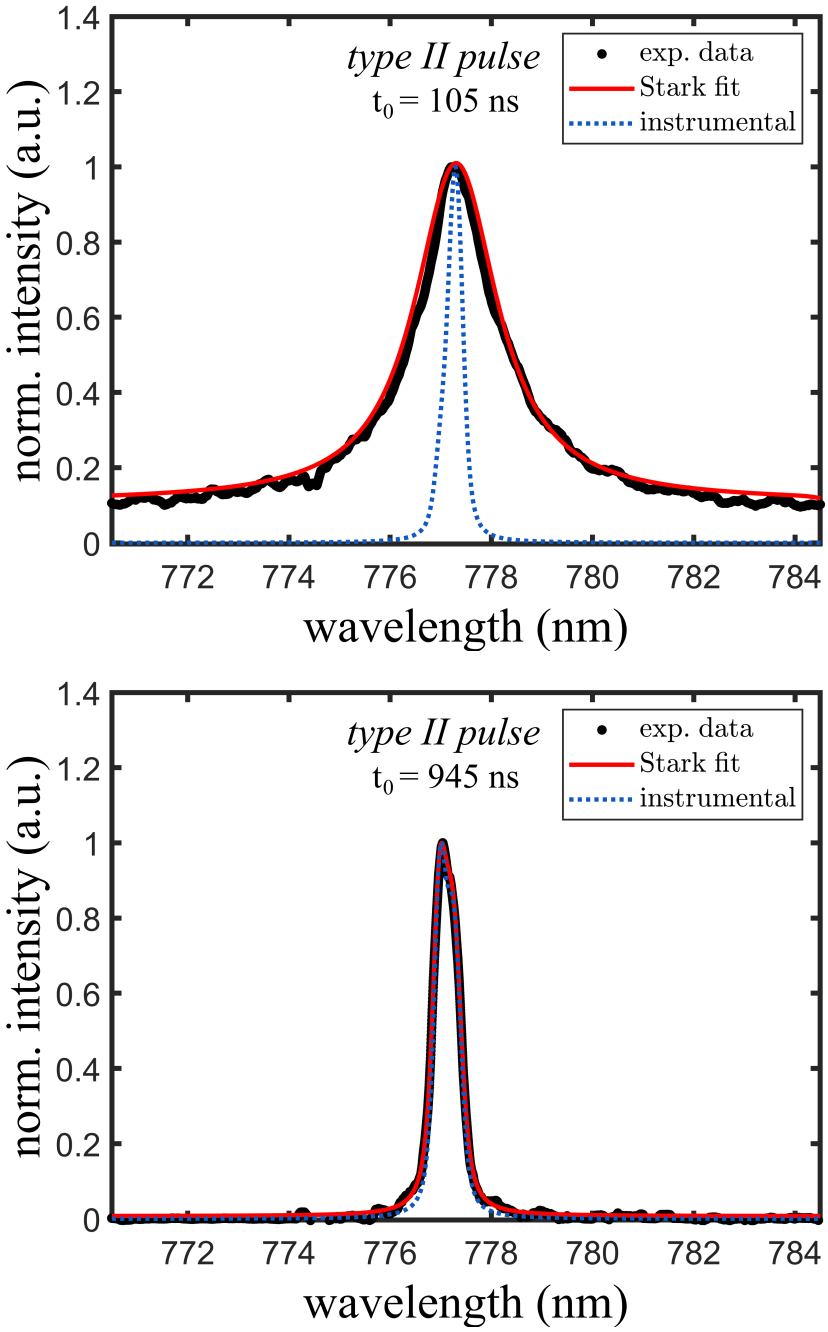

FIGURE 4.21: *Fitted Lorentzian lineshapes in a type II pulse of a two-pulse burst at* 90 kHz, *burst frequency* $f_b = 200$ Hz *and burst energy* $E_b = 12.9$ mJ. *Experimental conditions:* 300 sccm CO_2, *total pressure* $p = 745$ Torr. *Two conditions are presented: a strongly broadened line recorded at the beginning of the post-discharge (top panel,* $t_0 = 105$ ns, $t_g = 3$ ns, $\Delta\lambda = 0.51$ nm*), and a weakly broadened profile, recorded in the far afterglow (bottom panel,* $t_0 = 945$ ns, $t_g = 3$ ns, $\Delta\lambda = 0.20$ nm*). The instrumental function is reported for comparison.*

transition	ref.	$\mathbf{T_e}$ (K)	$\boldsymbol{\omega_e}$ (Å)	$\boldsymbol{\alpha}$ (Å)
O ($3s\ ^5S_2^0 \leftarrow 3p\ ^5P_{1,2,3}$)	NIST-LSJ [135]	5000	$4.74 \cdot 10^{-2}$	$2.45 \cdot 10^{-2}$
		10000	$5.38 \cdot 10^{-2}$	$2.46 \cdot 10^{-2}$
		20000	$7.10 \cdot 10^{-2}$	$2.47 \cdot 10^{-2}$
		40000	$9.88 \cdot 10^{-2}$	$2.48 \cdot 10^{-2}$
O ($3s\ ^5S_2^0 \leftarrow 3p\ ^5P_{1,2,3}$)	TOP-BASE [135]	5000	$5.52 \cdot 10^{-2}$	$3.13 \cdot 10^{-2}$
		10000	$6.30 \cdot 10^{-2}$	$3.14 \cdot 10^{-2}$
		20000	$8.25 \cdot 10^{-2}$	$3.15 \cdot 10^{-2}$
		40000	$1.13 \cdot 10^{-1}$	$3.16 \cdot 10^{-2}$
C ($2p^2\ ^1S_0 \leftarrow 3s\ ^1P_1^0$)	Griem [134]	5000	$6.34 \cdot 10^{-3}$	$2.7 \cdot 10^{-2}$
		10000	$7.22 \cdot 10^{-3}$	$5.3 \cdot 10^{-2}$
		20000	$8.34 \cdot 10^{-3}$	$1.1 \cdot 10^{-1}$
		40000	$9.40 \cdot 10^{-3}$	$2.1 \cdot 10^{-1}$
C ($2p^2\ ^1S_0 \leftarrow 3s\ ^1P_1^0$)	experimental [136]	17600	$7.40 \cdot 10^{-3}$	–

TABLE 4.3: *Electron impact width ω_e and ion impact parameter α for the O triplet at 777.19/777.42/777.54 nm and C line at 247.82 nm in the electron temperature range from 5000 K to 40000 K. Oxygen data are reported from NIST and TOP-BASE [135], carbon data from [134]. In both cases, a constant $n_e = 10^{16}$ cm^{-3} is assumed. Measured data for carbon are reported from [136], where $n_e = 1.08 \cdot 10^{17}$ cm^{-3} is used.*

ferred from the N_2 SPS (see figure 4.18). The gas temperature evolution is assumed to be the same in both the first and the second pulse of the burst, albeit different initial temperatures, 300 K and 1800 K respectively, must be set to account for the gas heating in successive pulses. Figure 4.22 shows the calculated electron density n_e in the first and second pulse of a two-pulse burst at 90 kHz for different input energies, with a temporal resolution of 6 ns and an electron temperature of 20000 K.

The electron density curves reveal a significant ionization of the plasma during both the first and the second pulse of the burst. The electron density values shown in the plots are those for which the emission signal is high enough to ensure a good fit of the experimental data and an additional broadening is safely distinguishable from the instrumental function. Following this criterion, the lower detection limit for n_e can

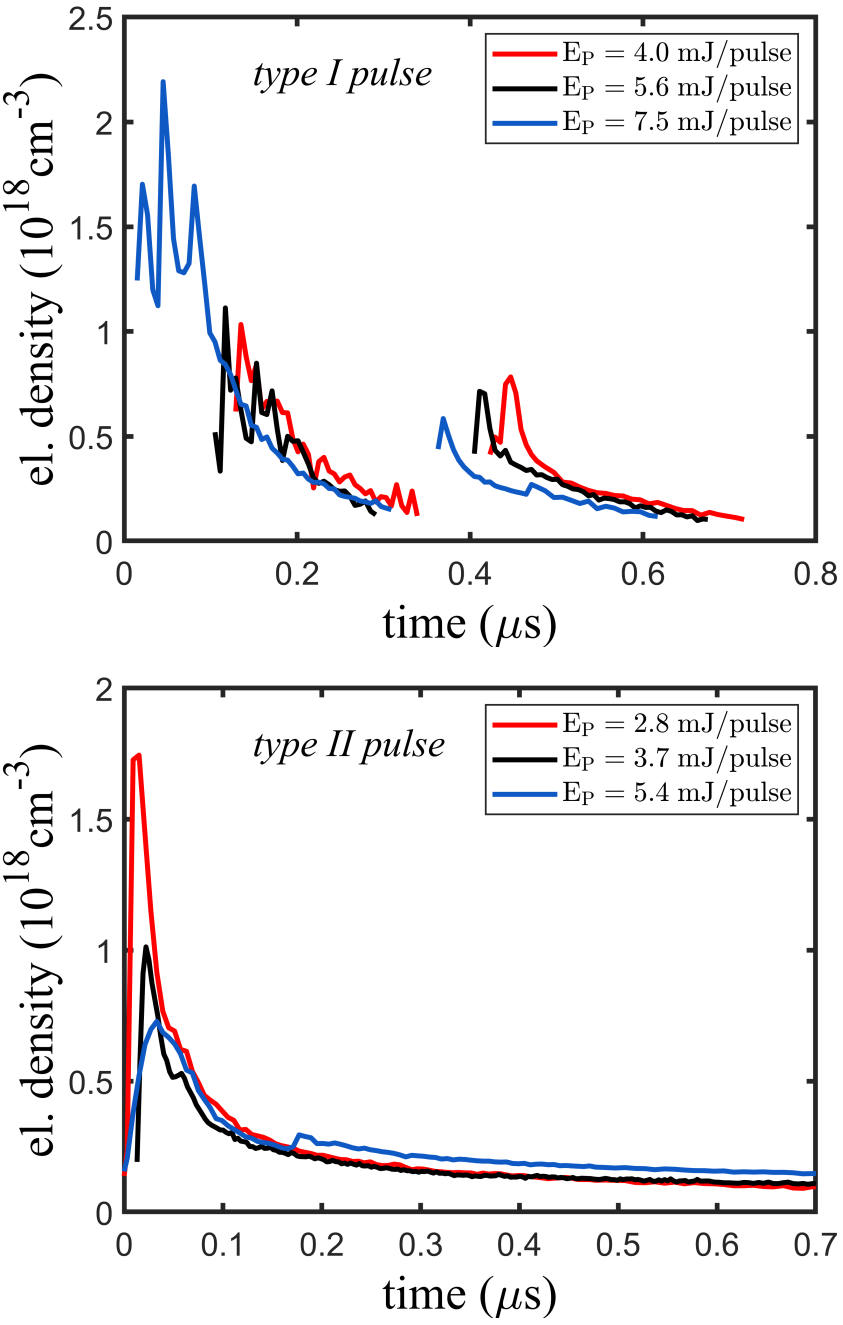

FIGURE 4.22: *Electron density evolution in the first (top) and second (bottom) pulse of a two-pulse burst at* 90 kHz*, burst frequency* $f_b = 200$ Hz *and variable burst energies. Temporal resolution* 6 ns*. Experimental conditions:* 300 sccm CO_2*, total pressure* 745 Torr*. The electron densities are calculated from the gas temperature values inferred from* N_2 *SPS (see figure 4.18) and the average of NIST-LSJ and TOP-BASE broadening parameters at* $T_e = 20000$ K *(see table 4.4).* n_e *values below the lower detection limit of* 10^{17} cm^{-3} *are excluded from the plots. Data uncertainties of* $\sim 60\%$ *are not reported for the sake of clarity.*

be set to $10^{17}\ \mathrm{cm}^{-3}$. During *Region I* of the first pulse, no reliable estimation of $\mathrm{n_e}$ can be given, due to a low spectral resolution of the detection system and electron density values certainly lower than $10^{17}\ \mathrm{cm}^{-3}$. Instead, during *Regions II-III* the electron density raises to approximately $10^{18}\ \mathrm{cm}^{-3}$, which allows for the classification of this regime as *spark*. A clear dependence on the input energy is observed: the spark regime starts progressively at smaller delays with increasing the input energy, up to a condition in which *Region II* and *Region III* are no more distinguishable. Contrary to expectations, higher burst energies result in lower electron densities during the spark phase, probably due to the increasing size of the discharge channel cross-section.

As a cross-check of the validity of the method, the Stark broadening of the carbon $2\mathrm{p}^2\ {}^1\mathrm{S}_0 \leftarrow 3\mathrm{s}\ {}^1\mathrm{P}_1^0$ transition line is measured under the same experimental conditions described for the oxygen triplet. A comparison with oxygen data is given in figure 4.23. The plots are restricted to the first $100\ \mathrm{ns}$ in the second pulse of a two-pulse burst at $90\ \mathrm{kHz}$, as the carbon line intensity is higher, and the broadening is more pronounced. The results obtained for the two species are consistent within an order of magnitude, although the use of different sets of broadening parameters determines a large variability in the outcomes. The influence of the electron temperature should also be considered when assessing the reliability of the measurement, as this affects the choice of the impact parameters to be used in equation (4.14). This is shown in figure 4.24, where $\mathrm{n_e}$ is calculated for electron temperatures of $5000\ \mathrm{K}$, $20000\ \mathrm{K}$ and $40000\ \mathrm{K}$. To account for both the accuracy of the broadening parameters and the uncertainty on $\mathrm{T_e}$, a 60% uncertainty is assigned to the measured electron density values.

4.5.1 Broadening mechanisms

The lineshape of the observed atomic lines is due to natural, resonant, Doppler, Van der Waals and Stark broadening mechanisms. The instrumental broadening, accounting for the spectral response of the light-collection apparatus, must also be considered. In principle, any line in the spectrum can be represented as the convolution of the instrumental function with all non-negligible broadening processes. In the studied conditions, all mechanisms outside of Stark and instrumental are of such size that they can be neglected. This is shown in table 4.4, where the individual contributions to the total broadening of the O $(3\mathrm{s}\ {}^5\mathrm{S}_2^0 \leftarrow 3\mathrm{p}\ {}^5\mathrm{P}_{1,2,3})$ lines are summarized. All contributions

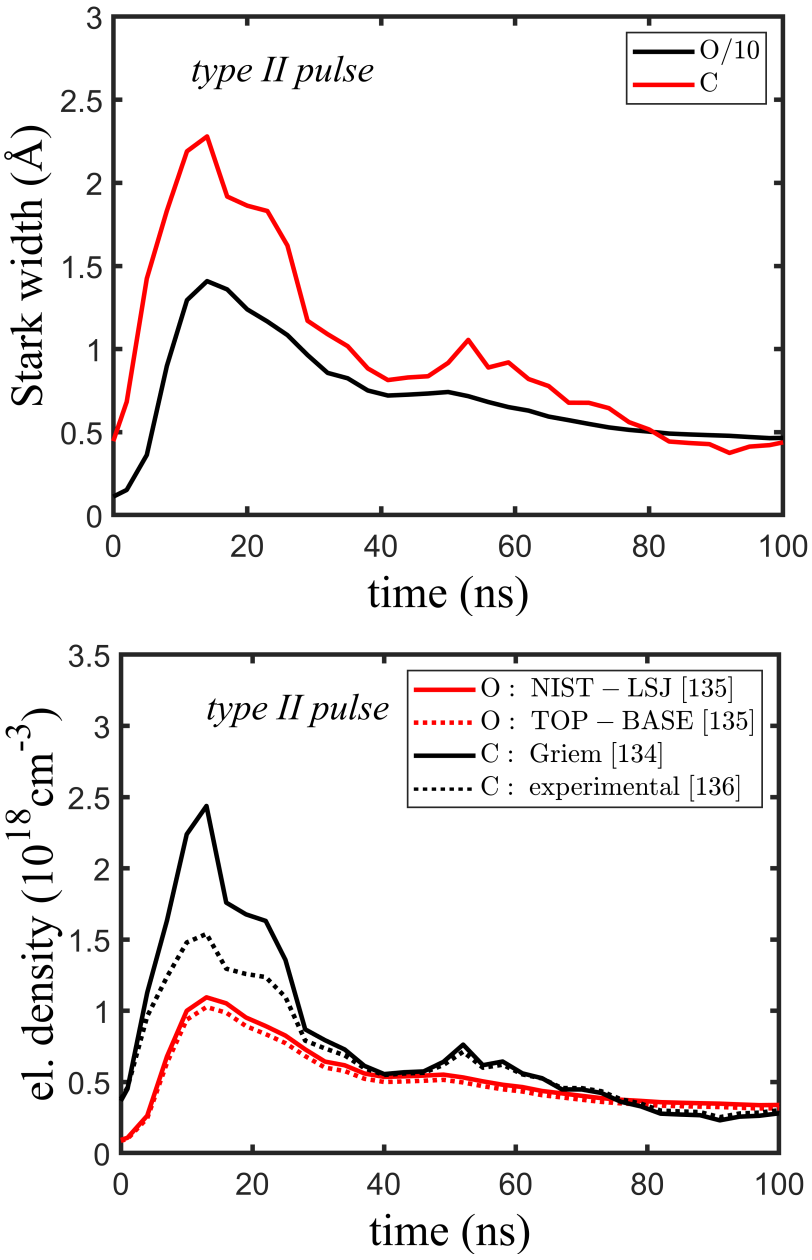

FIGURE 4.23: *Comparison between the Stark width (top) and the electron density (bottom) obtained from* O 3s $^5S^0_2 \leftarrow$ 3p $^5P_{1,2,3}$ *and* C 2p^2 $^1S_0 \leftarrow$ 3s $^1P^0_1$ *lines in the second pulse of a two-pulse burst at* 90 kHz, $f_b = 200$ Hz *and* $E_b = 9.3$ mJ. *Temporal resolution* 6 ns. *The electron density values are calculated from the broadening parameters reported in table 4.4. Experimental conditions:* 300 sccm CO_2, *total pressure* 745 Torr. *The oxygen Stark width is divided by a factor of* 10 *for easier comparison with carbon data.*

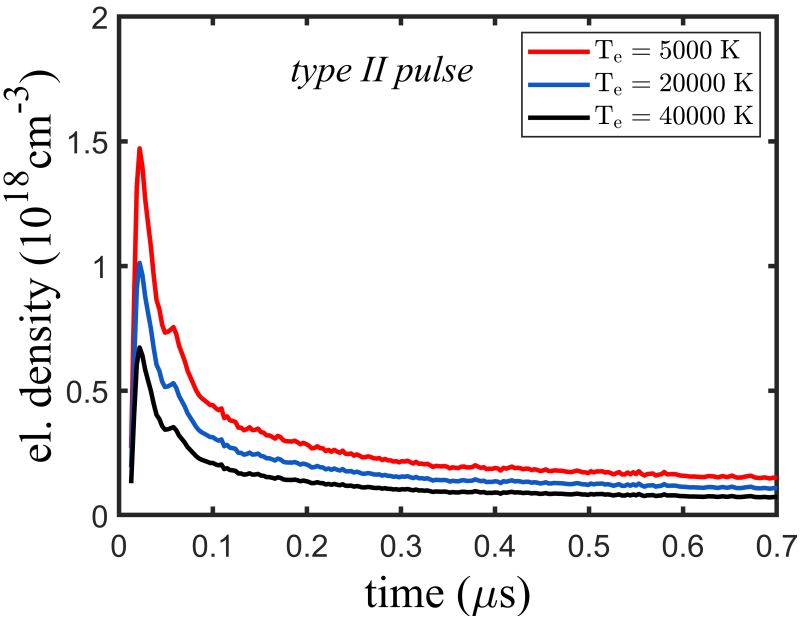

FIGURE 4.24: *Electron density evolution in the second pulse of a two-pulse burst at* 90 kHz *for different electron temperature values. Temporal resolution* 6 ns. n_e *values are calculated from the broadening parameters reported in table 4.4 at various* T_e. *Experimental conditions: burst frequency* $f_b = 200$ Hz, *burst energy* $E_b = 9.3$ mJ, *gas flow* 300 sccm CO_2, *total pressure* 745 Torr.

are calculated according to Kunze's theory [137] and the available parameters from the literature.

The first crucial step to estimate the Stark broadening is the accurate determination of the instrumental function of the collection system. The instrumental broadening is obtained by fitting the oxygen triplet in a condition where no further broadening adds to the (unavoidable) natural widths of the lines. Such a condition is achieved in the Stark-free afterglow of a ns pulse in an O_2 discharge ($t_0 = 4.5$ μs, $t_g = 10$ ns). Given the lack of other broadening sources, each component of the triplet can be fitted by the convolution between a Lorentzian and a Voigt profile to describe natural and instrumental broadening, respectively. The relative line strengths of the individual lines are treated as fit parameters to account for both the intrinsic fine structure of the triplet [138] and the effect of different population mechanisms of the $3p\ ^5P_{0,1,2}$ states [139]. This weighting is crucial to reproduce the measured asymmetric line shape of the triplet in the

broadening	FWHM (nm)	parameters
natural	$\leq 1 \cdot 10^{-5}$	[54]
resonant	$\leq 1 \cdot 10^{-3}$	$\mathrm{n_g} = 2.4 \cdot 10^{19}\ \mathrm{cm^{-3}}$, $\mathrm{p} = 1\ \mathrm{atm}$
Doppler	$\leq 2 \cdot 10^{-2}$	$\mathrm{T_{gas}} = 3500\ \mathrm{K}$ [64]
Van der Waals	$\leq 2 \cdot 10^{-2}$	$\mathrm{T_{gas}} = 300\ \mathrm{K}$, $\mathrm{p} = 1\ \mathrm{atm}$
Stark (min)	$\gtrsim 2.3 \cdot 10^{-2}$	$\mathrm{n_e} = 1 \cdot 10^{16}\ \mathrm{cm^{-3}}$, $\mathrm{T_e} = 40000\ \mathrm{K}$
Stark (max)	$\lesssim 2.1$	$\mathrm{n_e} = 2 \cdot 10^{18}\ \mathrm{cm^{-3}}$, $\mathrm{T_e} = 5000\ \mathrm{K}$
instrumental	0.29 ± 0.01	measured

TABLE 4.4: *Estimated FWHM of the relevant broadening mechanisms of the oxygen triplet* $3\mathrm{s}\ {}^5\mathrm{S}_2^0 \leftarrow 3\mathrm{p}\ {}^5\mathrm{P}_{1,2,3}$*, calculated using the theory from [137]. The parameters are chosen to resemble the discharge conditions. All broadenings are maximized to give the worst-case scenario. For natural broadening, LIFBASE transition probabilities are used [54]; for resonant broadening,* $\mathrm{n_g}$ *is the atomic oxygen ground state density, calculated from the ideal gas law at* $\mathrm{T} = 300\ \mathrm{K}$ *and* $\mathrm{p} = 1\ \mathrm{atm}$*; for Doppler broadening,* $\mathrm{T_{gas}}$ *is the peak gas temperature value in a similar discharge condition [64]; for Van der Waals broadening,* $\mathrm{T_{gas}}$ *and* p *are ambient temperature and atmospheric pressure, respectively; for Stark broadening, the lower and upper limits are obtained by applying formula (4.14) with collision parameters reported in table 4.3.*

conditions where little additional broadening is observed apart from the instrumental broadening (see the bottom panel of figure 4.21). This approach was preferred to the measurement of the lineshape of a narrow bandwidth light source, such as a diode laser, as this would fail to capture the additional instrumental broadening caused by the spatial uncorrelation between subsequent discharge channels. The resulting instrumental function has a FWHM of $(0.29 \pm 0.01)\ \mathrm{nm}$, with Gaussian and Lorentzian components of $\sigma = (85.7 \pm 0.5)\ \mathrm{pm}$ and $\gamma = (71.4 \pm 0.6)\ \mathrm{pm}$, respectively.

4.6 Electron temperature estimate

OES is extensively used to infer the electron temperature $\mathrm{T_e}$ from the line intensity of selected atomic emissions [140]. The spectroscopic determination of $\mathrm{T_e}$ relies on the existence of an equilibrium condition between all collisions and the radiative pro-

cesses in the plasma, known as *thermodynamic equilibrium* (TE). In this condition, the observed line intensities provide the number densities of the excited states, which obey the Boltzmann distribution and display the equilibrium plasma temperature T ($= \mathrm{T_e}$) as the slope of the Boltzmann plot. The same principle can be applied to the ratio of emission lines when absolute line profiles are not achievable (*line-ratio methods*) [140] [131].

4.6.1 Local thermodynamic equilibrium (LTE)

At thermodynamic equilibrium, the principle of *detailed balance* yields to Maxwell, Boltzmann, Saha and Planck balances being established simultaneously [119] [118], and a uniform temperature T can be assigned to all the degrees of freedom of the system. A departure from TE is observed when the principle of *detailed balance* is broken, and the atomic state distribution function (ASDF) deviates from its Saha-Boltzmann equilibrium value. In this condition, the electron temperature cannot be inferred straightforwardly from atomic emissions unless the excitation kinetics in the plasma is known.

Non-equilibrium conditions are met in most laboratory plasmas due to their small linear dimensions and spatial inhomogeneities, so that the TE relations can only be defined on a local scale, i.e, where the gradient effects can be neglected. In this case, a regime of *local thermal equilibrium* (LTE) is established [141]. Radiative non-equilibrium is frequently observed at this stage, as the radiation created by spontaneous decay escapes from the plasma without giving rise to absorption or stimulated emission ($\mathrm{T_{rad}} \neq \mathrm{T}$) [118]. A further degree of departure from TE occurs in NRP discharge plasmas because of the significant temperature differences between the constituent plasma species, usually the electrons ($\mathrm{T_e}$) and the heavy particles ($\mathrm{T_h}$) [11]. In this condition, several temperature regimes are sustained simultaneously, and the competition of the interaction with both the electrons and heavy particles determines the excitation kinetics. The reader may refer to [119] for a comprehensive review on this topic.

4.6.2 Electron excitation kinetics (EEK)

The knowledge of the equilibrium conditions of the system under investigation is crucial to relate the plasma parameters with the emission features in a quantitative

way. All existing methods to derive the electron temperature from atomic emissions use a population model and a set of rate equations to describe the plasma kinetics evolution [142] [140]. A favorable non-equilibrium condition for $\mathrm{T_e}$ determinations is found in NRP discharge plasmas when an *electron excitation kinetic* (EEK) regime is established. Under EEK, in fact, the inelastic collisions with the electrons regulate Boltzmann and Saha balances, and the excitation kinetics is easily modeled by electron-impact excitation only.

In this thesis, the availability of intense atomic lines, together with a large electron density, makes it possible to infer $\mathrm{T_{eq}}$ by OES under the hypothesis of an LTE condition in the spark phase and an EEK regime [143]. The fulfillment of LTE allows using the Saha ionization equilibrium formulas and the Boltzmann distribution to calculate the populations of the electronic levels. The validity of these assumptions is discussed at the end of this section.

Suitable spectral features for $\mathrm{T_e}$ determinations are those excited by electron impact, which allow for the EEK modelization. From the previous discussion on atomic lines (section 4.3.3), this requirement is met by the ionic $\mathrm{C^+}$ and $\mathrm{C^{++}}$ lines at $250.91\ \mathrm{nm}$ and $229.68\ \mathrm{nm}$, respectively. Conversely, the C line at $247.85\ \mathrm{nm}$ and the O triplet at $777.19\ \mathrm{nm}$, $777.42\ \mathrm{nm}$ and $777.54\ \mathrm{nm}$ must be discarded because they result from energy-transfer processes involving long-living species. The electron temperature $\mathrm{T_e}$ is determined by fitting the experimental $\mathrm{C^+}$ and $\mathrm{C^{++}}$ line profiles with a simulated profile obtained by the NIST-LIBS online simulation tool [144]. The simulator uses the LIFBASE data for transition probabilities and line positions to reproduce the populations of the individual electronic states, which are calculated by solving the Saha-Boltzmann equations for a given combination of electron density and electron temperature. The electron density values are incorporated from the measured data (section 4.5) with 60% of uncertainty, and the electron temperature $\mathrm{T_e}$ is varied until the best match with the experimental data is obtained. Two such fits are presented in figure 4.25.

Figure 4.26 shows the electron temperature evolution in the first and second pulse of a two-pulse burst at $90\ \mathrm{kHz}$ and burst energy of $12.9\ \mathrm{mJ}$. For all the studied conditions, the electron temperature evolves in line with the discharge voltage, showing a decrease in *Region II* and *Region III* similar to that of the voltage ringings amplitude. A measurement in *Region I* is not possible due to the lack of electron density data (see fig-

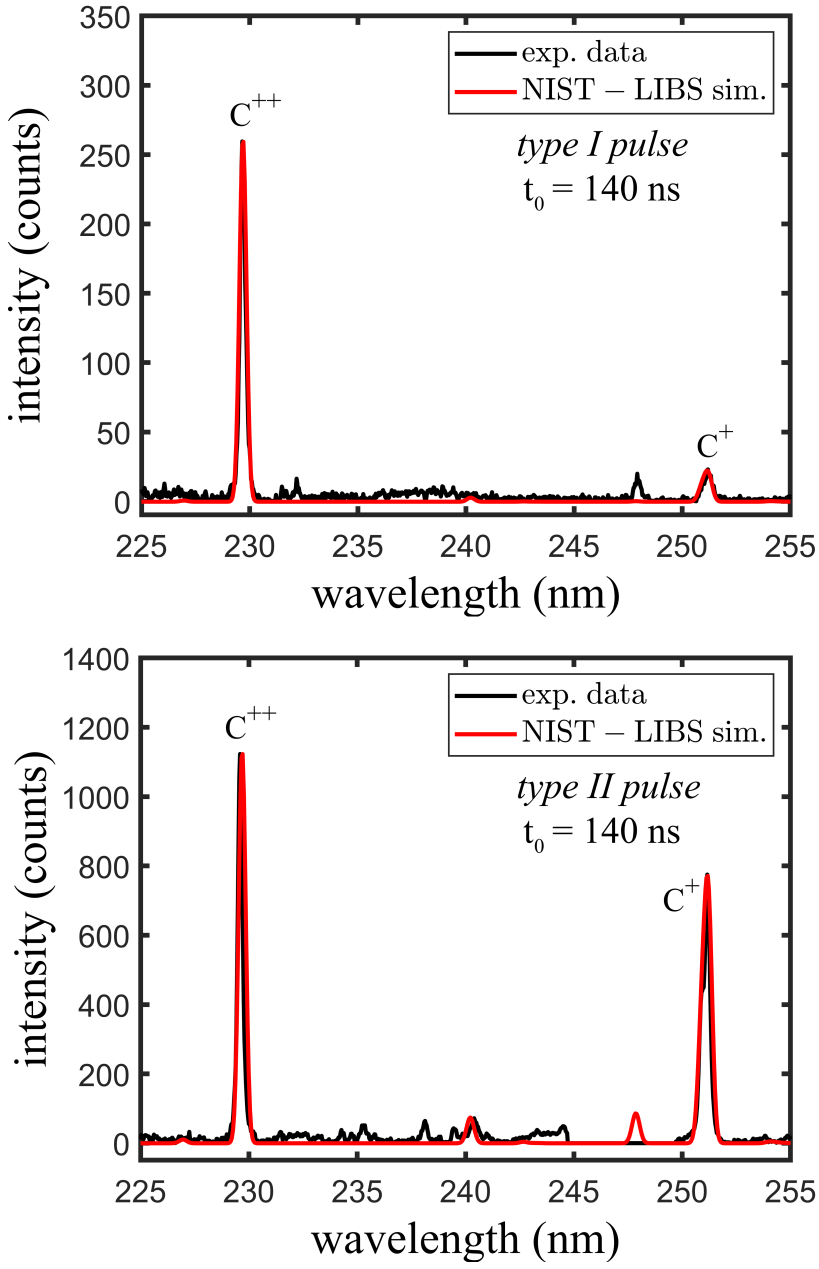

FIGURE 4.25: *Experimental and simulated* C^{+} *and* C^{++} *emission lines at* $t_0 = 140$ ns ($t_g = 3$ ns) *in the first (top) and second pulse (bottom) of a two-pulse* 90 kHz *burst, burst frequency* $f_b = 200$ Hz *and* $E_b = 12.9$ mJ. *Total pressure* 745 Torr, 300 sccm CO_2. *The* C *line at* 247.85 nm *is manually removed from the spectra for the sake of clarity.*

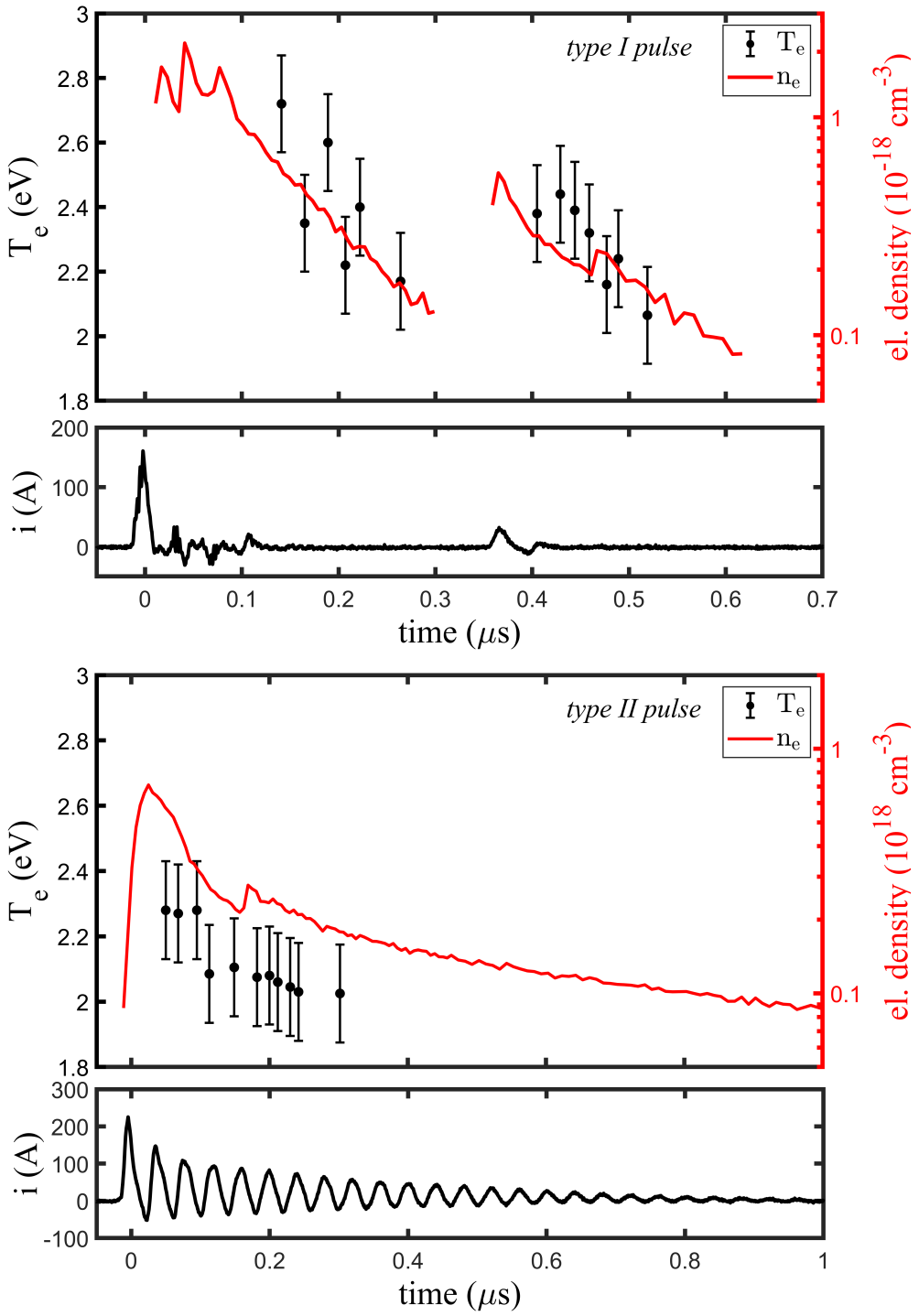

FIGURE 4.26: *Estimated electron temperature from LIBS spectra simulation in the first (top) and second pulse (bottom) of a two-pulse burst at* 90 kHz, *burst frequency* $f_b = 200$ Hz *and* $E_b = 12.9$ mJ. *Experimental conditions:* 300 sccm CO_2, *pressure* 745 Torr. *Confidence intervals are calculated from the uncertainty on* n_e *values, reported for reference.*

ure 4.22). For most of the spark phase, electron temperatures between $2\ \mathrm{eV}$ and $2.5\ \mathrm{eV}$ are found. These values, however, must be regarded as estimates only, since the LIBS calculations are performed in the idealized condition of a pure carbon plasma, which is not met in the investigated conditions.

Assumption of LTE By LTE, one typically refers to a situation allowing the use of TE relations, although the radiation field is much weaker than the blackbody field at $\mathrm{T_e}$ [141]. Essential for an LTE condition is that collisional processes prevail over radiative processes, i.e., the collisional depopulation rates of all the electronic levels of the atoms are higher than the radiative rates between the same states. In this way, the escape of radiative energy is small, and the deviations from TE are negligible [118]. To assess the validity of the LTE assumption, several practical criteria have been introduced based on collisional/radiative models of the plasma kinetics [145] [146] [118]. The most popular one, proposed by McWhirter in [147], sets the minimum electron density $\mathrm{n_e}$ that ensures a collision-dominated regime in the plasma. In the case of a carbon plasma, the criterion is fulfilled for electron densities $\mathrm{n_e} > 10^{17}\ \mathrm{cm^{-3}}$ [118], which are observed in the current experimental conditions (see figure 4.22). At these large ionization degrees, the electron kinetics is dominant, even in the case of a molecular gas mixture at high pressure. In fact, the rate constants of electron-induced energy exchanges between atomic levels are of the order of $10^{-4} - 10^{-5}\ \mathrm{cm^3 s^{-1}}$, to be compared with those of molecular collisions that do not exceed $10^{-9}\ \mathrm{cm^3 s^{-1}}$ [13].

4.7 Summary

Time-resolved optical emission spectroscopy gives an overall description of the discharge characteristics, allowing, in some cases, to identify the mechanisms underlying the $\mathrm{CO_2}$ dissociation pathway. *Type I* pulses, i.e. either the initial pulse of a burst or all the pulses in continuous mode operation mode for pulsing frequencies not exceeding $\sim 10\ \mathrm{kHz}$, present a similar temporal structure, which can be classified into two phases:

1. a breakdown phase (*Region I*), where electron impact is the dominant excitation mechanism. The observation of highly energetic emissions, such as the $\mathrm{CO_2^+}$ FDBS and $\lambda\lambda$ systems, indicates a largely non-Boltzmann EEDF. However, both

the electron temperature and the electron density cannot be assessed by spectroscopic means due to the limited resolution of the detection system. However, the overall picture suggests that the electron density does not exceed $10^{17}\ \mathrm{cm}^{-3}$. The gas temperature evolution, assessed from the N_2, reveals only a minimal gas heating at this stage ($\mathrm{T}_{\mathrm{gas}} < 500\ \mathrm{K}$), consistently with the longer timescales over which VT relaxations operate. Finally, no spectroscopic markers of a significant CO_2 dissociation are observed in this phase, with most of the supplied energy resulting in CO_2 ionization and vibrational excitation via electron impact.

2. a spark phase (*Regions II-IV*), where the inefficient electron-neutral thermal contact allows establishing a two-temperatures LTE regime [148], with electron temperatures between $2 - 2.5\ \mathrm{eV}$ and a gas temperature around $2000\ \mathrm{K}$. The electron density, assessed by the Stark broadening of the O triplet at $\sim 777\ \mathrm{nm}$, ranges between 10^{17} and $10^{18}\ \mathrm{cm}^{-3}$, corresponding to a maximum ionization degree of almost 10%. The observed emissions are dominated by atomic lines resulting from the dissociation of CO_2 into its constituent atoms. These emissions are superimposed on two continua, whose origin needs further clarifications. In the late afterglow ($\sim 2\ \mu s$), the C_2 Swan System is formed due to C atoms recombination, which is favored at high temperatures. No distinguishable emissions ascribable to electron impact are observed at this stage, both because of other stronger emissions and a lower electron temperature with respect to the breakdown phase. Therefore, the lack of CO emissions cannot be straightforwardly associated with a low degree of CO_2 dissociation, but rather to an overall lower excitation condition of the plasma.

Type II pulses exhibit a sudden transition to the spark phase, with electron impact excitation dominating only during the first $\sim 10\ \mathrm{ns}$ of the discharge. Contrary to *type I* pulses, most of the supplied energy is consumed in the spark phase, as confirmed by the lack of intense energetic emissions in the initial breakdown. At the pulse onset, where N_2 SPS is visible, the gas temperature can be assessed via OES thermometry. This gives a reasonable estimation of the gas heating from the previous pulse(s). Both the electron temperature and the electron density are comparable in magnitude to the measured values in the spark regime of a *type I* pulse, indicating a relatively low excitation condition. The appearance of (unidentified) 'oxygen-related' emissions through-

out the whole pulse duration suggests an oxygen-rich initial gas mixture composition, most likely attributable to a significant degree of CO_2 dissociation at this stage.

The combined spectroscopic observations of both pulse types lead to the conclusion that CO_2 dissociation is an ongoing process that starts weakly during the breakdown phase of a *type I* pulse and becomes more significant during the subsequent phases. The appearance of 'O_2-related' bands in the late post-discharge of the pulse suggests that CO_2 dissociation may extend beyond the discharge current has dropped to zero, indicating that a long-lasting excitation mechanism might be active during the spark regime. This picture is justified by both the large electron density and electron temperature values of about $2\ \mathrm{eV}$, which ensure the conditions for the maximum rate coefficients of electron-impact vibrational excitation of CO_2 [149]. The spark regime has then the suitable characteristics for an enhanced role of the vibrational mechanism of CO_2 splitting, which also explains the better performance of the burst mode with respect to the continuous mode operation in terms of energy efficiency [62]. These observations agree with the model calculations reported in [64], where $\sim 67\%$ of the dissociation is found to occur from vibrationally excited CO_2 through electronic excitation, whereas a further $\sim 20\%$ results from the highest antisymmetric stretch levels of CO_2 upon collisions with third bodies. Only a minimal contribution can be attributed to direct electron impact from the ground state, which dominates during the breakdown phase of the pulse (red arrow, figure 1.5). The role of both thermal dissociation and CO_2^+ dissociative recombination [150]

$$\begin{aligned} CO_2^+ + e &\longrightarrow C + O_2 + 2.3\mathrm{eV} \\ CO_2^+ + e &\longrightarrow CO + O + 8.3\mathrm{eV} \end{aligned} \tag{4.16}$$

should also be considered, as they might come into play on account of both the high gas temperature and large ionisation degree. However, the model calculations in [64] evidence their minor contribution to the total dissociation.

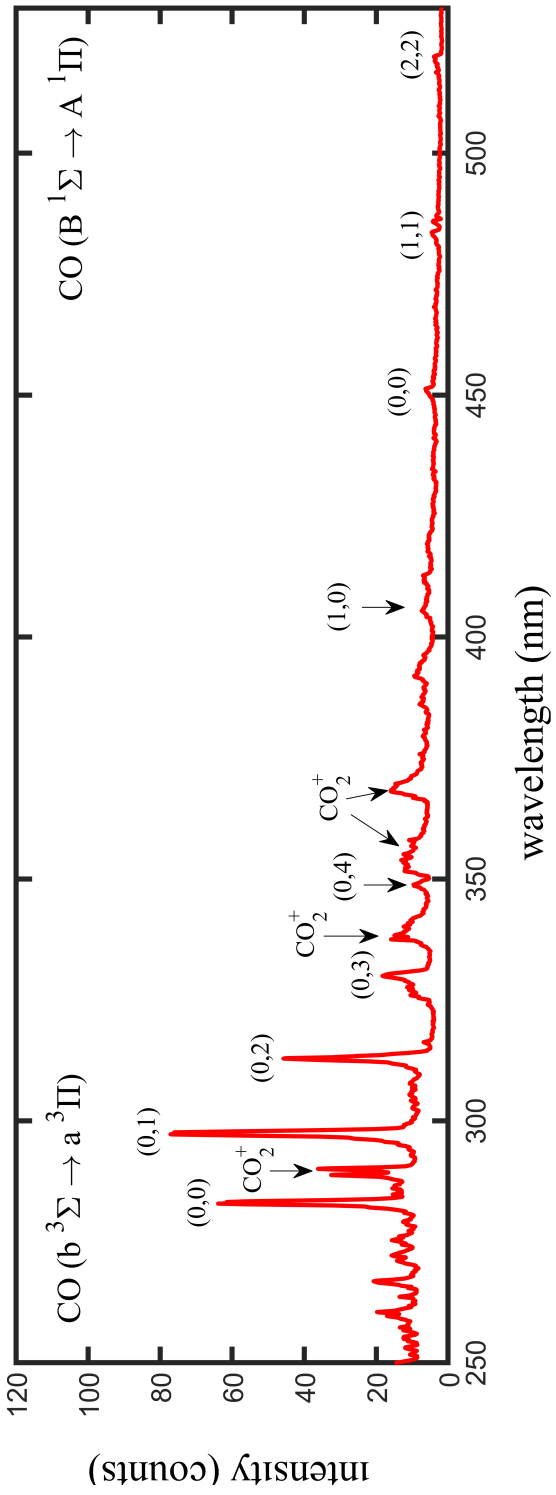

FIGURE 4.27: *Details of the* CO *Fourth Positive System* ($260 - 380$ nm) *and Angstrom System (at* $400 - 550$ nm*), recorded in a type I pulse at* $t_0 = 0$ ns *and* $t_g = 10$ ns. *Discharge operating at* 200 Hz *(continuous mode) and pulse energy of* ? mJ. *Experimental conditions:* 300 sccm CO_2, *pressure* 745 Torr. *Bands identification from [98].*

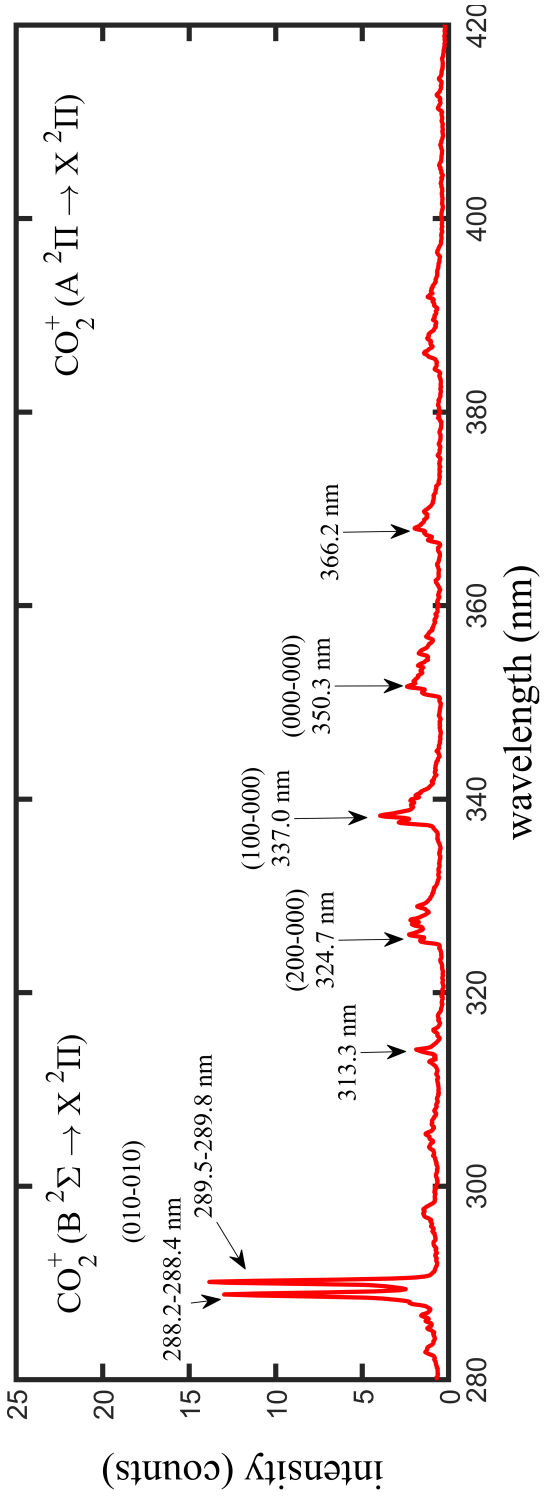

FIGURE 4.28: *Details of the* CO_2^+ *Fox Duffendack Barker System* $(285 - 450\ \mathrm{nm})$ *and* $\lambda\lambda 2883 - 2896$ *System (at* $\sim 290\ \mathrm{nm}$*), recorded in a type I pulse at* $t_0 = 0\ \mathrm{ns}$ *and* $t_g = 10\ \mathrm{ns}$*. Discharge operating at* $1\ \mathrm{kHz}$ *(continuous mode) and pulse energy of* $?\ \mathrm{mJ}$*. Experimental conditions:* $100\ \mathrm{sccm}\ CO_2$*, pressure* $745\ \mathrm{Torr}$*. Band heads reported from [101] and [100].*

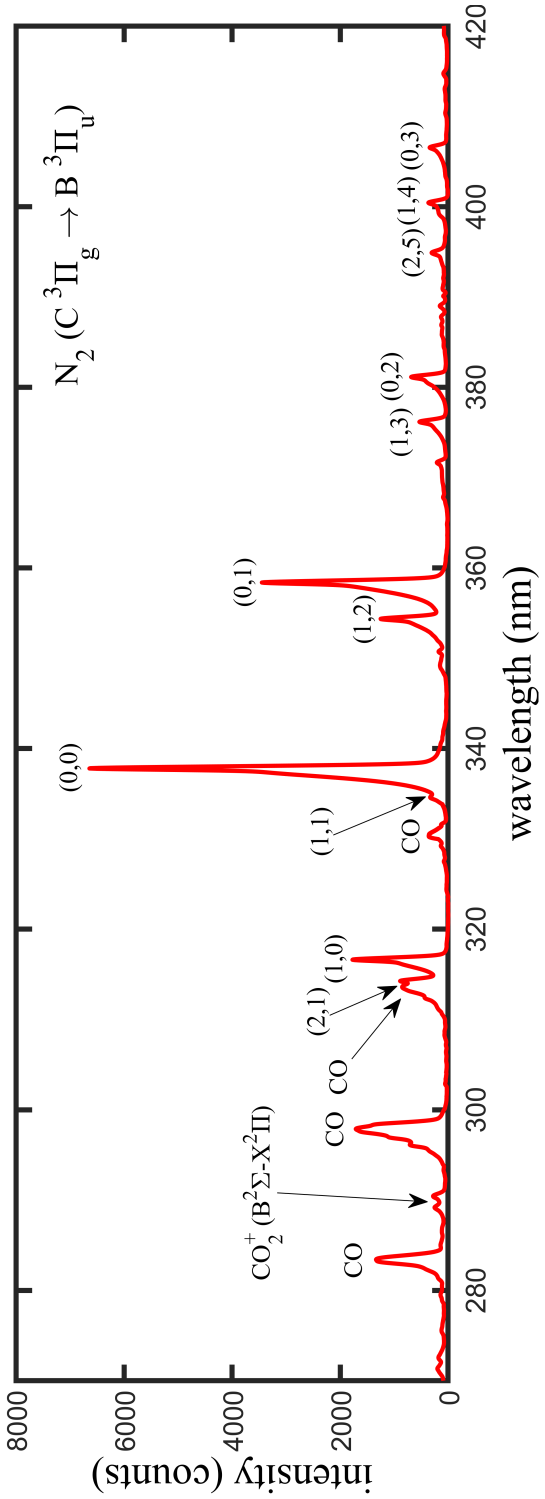

FIGURE 4.29: *Details of the* N_2 *Second Positive System, recorded in a type I pulse at* $t_0 = 0$ ns *and* $t_g = 3$ ns. *Discharge operating at* 1 kHz *(continuous mode) and pulse energy of* 5.6 mJ. *Experimental conditions:* 5% N_2 *in* CO_2 *gas buffer, total gas flow* 100 sccm, *pressure* 745 Torr. *Bands identification from [98].*

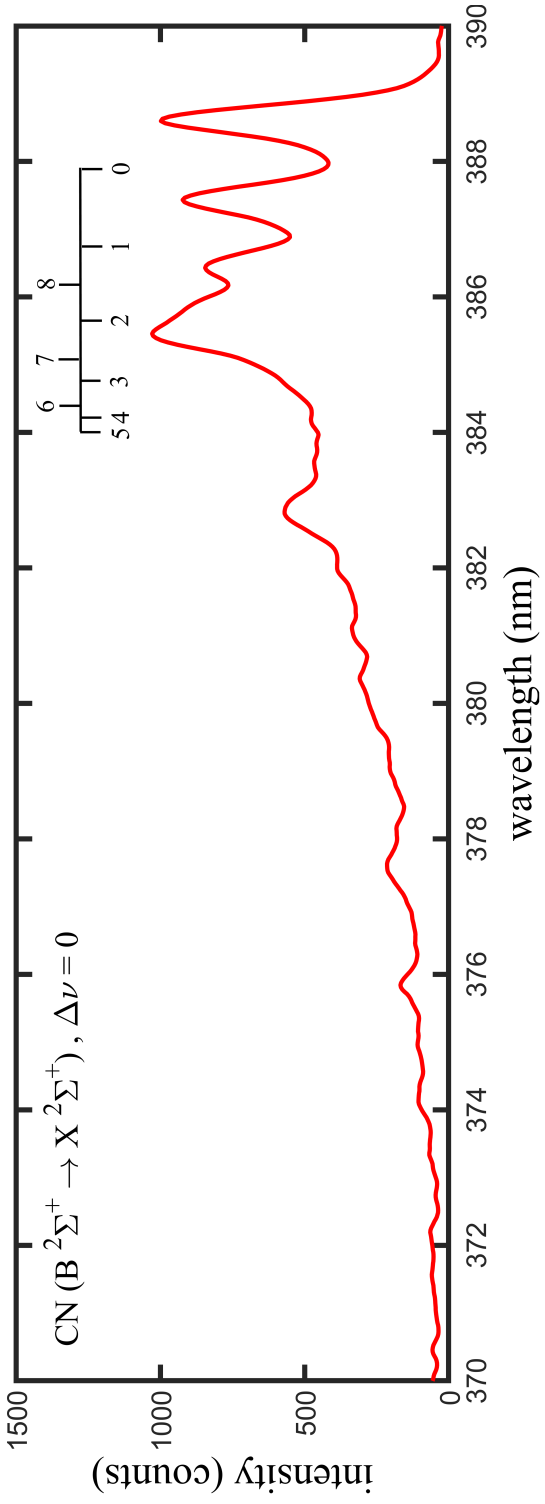

FIGURE 4.30: *Details of the* $\Delta v = 0$ *sequence of the* CN *Violet System, recorded in a type I pulse at* $t_0 = 500$ ns *and* $t_g = 10$ ns. *Discharge operating at* 1 kHz *(continuous mode) and pulse energy of* 5.6 mJ. *Experimental conditions:* 5% N_2 *in* CO_2 *gas buffer, total gas flow* 100 sccm, *pressure* 745 Torr. *Band origins reported from [54].*

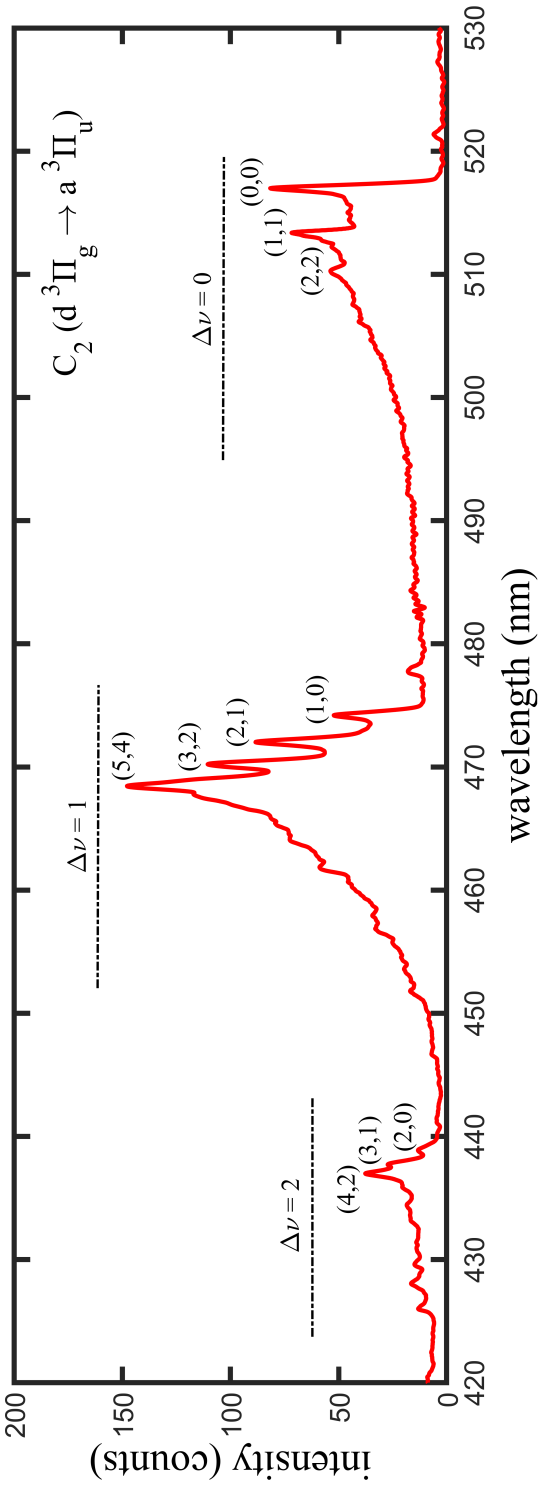

FIGURE 4.31: *Details of the* C_2 *Swan System, recorded in a type I pulse at* $t_0 = 2000$ ns *and* $t_g = 10$ ns. *Discharge operating at* 1 kHz *(continuous mode) and pulse energy of* 5.6 mJ. *Experimental conditions:* 100 sccm CO_2, *pressure* 745 Torr. *Bands identification from [98].*

Chapter 5

Conclusive remarks

Decarbonization of the society and replacement of fossil resources constitute a crucial challenge for the survival of humanity. It has become increasingly more evident that no technology alone can be decisive and universal for all applications, but rather 'tailored' solutions to each particular sector. In this perspective, the capture and re-use of CO_2 is a strategy that tackles simultaneously the greenhouse gases issue and the energy transition towards sustainable resources. Carbon capture and utilization are essential for sectors hard to electrify such as aviation and long-haul transportation. Synthetic fuels produced from CO_2 and H_2 through renewable electricity (e-fuels) are carbon-neutral and provide long-term storage of renewable power in a chemical form, with clear advantages in terms of transportation and distribution.

Reduction of CO_2 to CO and O_2 is a possible strategy to recycle harmful carbon dioxide. Because CO_2 is very stable, its dissociation is challenging. Thermal splitting requires thousands of degrees, which makes the process inefficient, as most of the supplied energy is dissipated as heat. Non-equilibrium conditions allow bypassing thermodynamic limits, to the benefit of the overall conversion efficiency. Discharge plasmas can realize this condition, the electron energy being orders of magnitude higher than that of the gas particles. Also, a hierarchy of molecular temperatures can be established, with the vibrational temperature much higher than the translational one.

In this thesis, the use of nanosecond repetitively pulsed (NRP) discharges has been investigated for dissociating CO_2. In particular, optical diagnostics (LIF and OES) have been implemented to study the temporal evolution of the CO_2 dissociation on the microsecond scale. A novel methodology, Collisional Energy-Transfer Laser-Induced

Fluorescence CET-LIF, has been developed to relate changes of the LIF spectrum of OH with variations of the mixture composition in which OH is embedded, as long as rate coefficients of the energy-transfer collisions are known. The method gives insight into non-equilibrium discharge plasmas employed in the conversion of CO_2, showing versatility and applicability to various devices (NRP, low-pressure glow discharges). Since the rate for rotational thermalization in molecular gases may be low, the energy-transfer processes generally depend on the OH rotational level and are usually unknown. Consequently, a large part of this work was devoted to measuring rate coefficients of vibrational energy transfer and quenching processes with various colliders for $OH(A)$ in selected rotational states.

Time-resolved Optical Emission Spectroscopy has been used to characterize a sequence of close nanosecond discharges pulses, revealing a complex temporal structure along the pulse for both the emitted light and the discharge characteristics. Plasma parameters such as the electron temperature and the electron density were estimated thanks to the presence of atomic neutral and ionic lines and the existence of an electron excitation kinetics condition in the plasma. The addition of N_2 to the CO_2 gas feed allowed for gas temperature determinations. Qualitative guesses on the evolution of the gas mixture could be made from the recording of time-resolved spectra, although definitive confirmation can be given by kinetic modelling and direct measurements (CET-LIF and alternative methods). The spectroscopic observations returned a coherent picture of a discharge evolving from a breakdown phase towards a spark phase, with the latter presenting favourable conditions for enhanced contribution of vibrational pumping to the dissociation of CO_2.

The use of time-resolved optical diagnostics opens new perspectives for the study of plasma discharges. CET-LIF has been validated against models and literature in both a CO_2 NRP discharge and a $CO_2 + 20\%\ H_2O$ low-pressure glow discharge. In the future, application of this method to other gas mixtures, most notably $CO_2 + CH_4$ (dry reforming of methane), can be attempted owing to the measurement of the OH collisional rate coefficients. TR-OES has shed new light on the investigation of CO_2 NRP discharges, as no reference of similar studies could be found in the literature. The new results can then pave the way for modellings and measurements in similar discharge conditions.

Bibliography

[1] IEA, "Global Energy Review," tech. rep., 2021.

[2] Global Climate Change: Evidence., "NASA Global Climate Change and Global Warming: Vital Signs of the Planet. Accessed Feb 2021," tech. rep.

[3] Edenhofer O., Pichs-Madruga R., Sokona Y., Farahani E., Kadner S., Seyboth K., Adler A., Baum I., Brunner S., Eickemeier P., Kriemann, B. Savolainen J., Schlömer S., von Stechow C., Zwickel T. and Minx J.C., "IPCC2014: Climate Change 2014: Mitigation of Climate Change. Contribution of Working Group III to the Fifth Assessment Report of the Intergovernmental Panel on Climate Change," tech. rep., Cambridge University Press, Cambridge, United Kingdom and New York, NY, USA, 2014.

[4] National Oceanic and Atmospheric Administration, "NOAA's Annual Greenhouse Gas Index," tech. rep., 2020.

[5] bp, "Statistical review of world energy," tech. rep., 2021.

[6] R. L. Jaffe and W. Taylor, *The Physics of Energy*. 2018.

[7] bp, "Statistical review of world energy," tech. rep., 2020.

[8] J. Roman, K. S. V. Santhanam, J. Miri Massoud, V. Alla Bailey and A. Gerald Takacs, *Introduction to hydrogen technology*. Hoboken, N.J: John Wiley, 2008.

[9] G. A. Olah, G. K. S. Prakash, and A. Goeppert, "Anthropogenic Chemical Carbon Cycle for a Sustainable Future," *Journal of The American Chemical Society*, vol. 133, pp. 12881–12898, 2011.

[10] https://www.carbonrecycling.is/, "Carbon Recycling International."

[11] F. Taccogna and G. Dilecce, "Non-equilibrium in low-temperature plasmas," *The European Physical Journal D*, vol. 70, 2016.

[12] Y. Itikawa, "Cross Sections for Electron Collisions With Carbon Dioxide," *Journal of Physical and Chemical Reference Data*, vol. 31, pp. 749–767, 2002.

[13] L. C. Pitchford, L. L. Alves, K. Bartschat, S. F. Biagi, M.-C. Bordage, I. Bray, C. E. Brion, M. J. Brunger, L. Campbell, A. Chachereau, B. Chaudhury, L. G. Christophorou, E. Carbone, N. A. Dyatko, C. M. Franck, D. V. Fursa, R. K. Gangwar, V. Guerra, P. Haefliger, G. J. M. Hagelaar, A. Hoesl, Y. Itikawa, I. V. Kochetov, R. P. McEachran, W. L. Morgan, A. P. Napartovich, V. Puech, M. Rabie, L. Sharma, R. Srivastava, A. D. Stauffer, J. Tennyson, J. de Urquijo, J. van Dijk, L. A. Viehland, M. C. Zammit, O. Zatsarinny, and S. Pancheshnyi, "LXCat: an Open-Access, Web-Based Platform for Data Needed for Modeling Low Temperature Plasmas," *Plasma Processes and Polymers*, vol. 14, p. 1600098, 2016.

[14] A. George, B. Shen, M. Craven, Y. Wang, D. Kang, C. Wu, and X. Tu, "A Review of Non-Thermal Plasma Technology: A novel solution for CO_2 conversion and utilization," *Renewable and Sustainable Energy Reviews*, vol. 135, p. 109702, 2021.

[15] B. Ashford and X. Tu, "Non-thermal plasma technology for the conversion of CO_2," *Current Opinion in Green and Sustainable Chemistry*, vol. 3, pp. 45–49, 2017.

[16] R. Snoeckx and A. Bogaerts, "Plasma technology – a novel solution for CO_2 conversion?," *Chemical Society Reviews*, vol. 46, pp. 5805–5863, 2017.

[17] R. W. Wood, "The Fluorescence of Sodium Vapour and the Resonance Radiation of Electrons," *Proceedings of the Physical Society of London*, vol. 19, pp. 764–778, 1905.

[18] W. J. Tango, J. K. Link, and R. N. Zare, "Spectroscopy of K_2 Using Laser−Induced Fluorescence," *The Journal of Chemical Physics*, vol. 49, pp. 4264–4268, 1968.

[19] S. D. Benedictis and G. Dilecce, *Laser-Induced Fluorescence Methods for Transient Species Detection in High- Pressure Discharges*. Boca Raton: CRC Press, 2014.

[20] D. R. Crosley, "Laser−induced fluorescence in spectroscopy, dynamics, and diagnostics," *Journal of Chemical Education*, vol. 59, p. 446, 1982.

[21] J. W. Daily, "Laser induced fluorescence spectroscopy in flames," *Progress in Energy and Combustion Science*, vol. 23, pp. 133–199, 1997.

[22] R. N. Zare, "My Life with LIF: A Personal Account of Developing Laser-Induced Fluorescence," *Annual Review of Analytical Chemistry*, vol. 5, pp. 1–14, 2012.

[23] G. Dilecce, L. M. Martini, M. Ceppelli, M. Scotoni, and P. Tosi, "Progress on laser induced fluorescence in a collisional environment: the case of OH molecules in ns pulsed discharges," *Plasma Sources Science and Technology*, vol. 28, p. 025012, 2019.

[24] K. Kohse-Höinghaus, "Laser techniques for the quantitative detection of reactive intermediates in combustion systems," *Progress in Energy and Combustion Science*, vol. 20, pp. 203–279, 1994.

[25] K. Smyth and D. Crosley, *Detection of minor species with laser techniques*. In Applied Combustion Diagnostics, ed. K Kohse Hoinghaus, JB Jeffries, pp. 9–68. London: Taylor & Francis, 2002.

[26] W. Hack, "Detection methods for atoms and radicals in the gas phase," *International Reviews in Physical Chemistry*, vol. 4, pp. 165–200, 1985.

[27] J. Wolfrum, "Laser spectroscopy for studying chemical processes," *Applied Physics B volume*, vol. 46, pp. 221–236, 1988.

[28] W. Demtröder, *Laser Spectroscopy: Basic concepts and instrumentation*. Springer-Verlag GmbH, 2003.

[29] J. L. Kinsey, "Laser-Induced Fluorescence," *Annual Review of Physical Chemistry*, vol. 28, pp. 349–372, 1977.

[30] R. Altkorn and R. N. Zare, "Effects of Saturation on Laser-Induced Fluorescence Measurements of Population and Polarization," *Annual Review of Physical Chemistry*, vol. 35, pp. 265–289, 1984.

[31] D. B. Graves, "The emerging role of reactive oxygen and nitrogen species in redox biology and some implications for plasma applications to medicine and biology," *Journal of Physics D: Applied Physics*, vol. 45, p. 263001, 2012.

[32] G. Fridman, G. Friedman, A. Gutsol, A. B. Shekhter, V. N. Vasilets, and A. Fridman, "Applied Plasma Medicine," *Plasma Processes and Polymers*, vol. 5, pp. 503–533, 2008.

[33] K.-D. Weltmann and T. von Woedtke, "Plasma medicine—current state of research and medical application," *Plasma Physics and Controlled Fusion*, vol. 59, p. 014031, 2016.

[34] S. M. Starikovskaia, "Plasma assisted ignition and combustion," *Journal of Physics D: Applied Physics*, vol. 39, pp. R265–R299, 2006.

[35] S. W. . J. Y., "Nonequilibrium Plasma-Assisted Combustion: A Review of Recent Progress," *Journal Plasma and Fusion Research*, vol. 89, 208-219, 2013.

[36] R. Ono and T. Oda, "Measurement of hydroxyl radicals in pulsed corona discharge," *Journal of Electrostatics*, vol. 55, pp. 333–342, 2002.

[37] R. Ono and T. Oda, "Dynamics and density estimation of hydroxyl radicals in a pulsed corona discharge," *Journal of Physics D: Applied Physics*, vol. 35, pp. 2133–2138, 2002.

[38] S. Kanazawa, H. Tanaka, A. Kajiwara, T. Ohkubo, Y. Nomoto, M. Kocik, J. Mizeraczyk, and J.-S. Chang, "LIF imaging of OH radicals in DC positive streamer coronas," *Thin Solid Films*, vol. 515, pp. 4266–4271, 2007.

[39] S. Kanazawa, H. Kawano, S. Watanabe, T. Furuki, S. Akamine, R. Ichiki, T. Ohkubo, M. Kocik, and J. Mizeraczyk, "Observation of OH radicals produced by pulsed discharges on the surface of a liquid," *Plasma Sources Science and Technology*, vol. 20, p. 034010, 2011.

[40] Y. Nakagawa, R. Ono, and T. Oda, "Density and temperature measurement of OH radicals in atmospheric-pressure pulsed corona discharge in humid air," *Journal of Applied Physics*, vol. 110, p. 073304, 2011.

[41] Z. Yin, I. V. Adamovich, and W. R. Lempert, "OH radical and temperature measurements during ignition of H_2-air mixtures excited by a repetitively pulsed nanosecond discharge," *Proceedings of the Combustion Institute*, vol. 34, pp. 3249–3258, 2013.

[42] L. M. Martini, N. Gatti, G. Dilecce, M. Scotoni, and P. Tosi, "Rate constants of quenching and vibrational relaxation in the OH ($A^2\Sigma^+, \nu = 0, 1$) manifold with various colliders," *Journal of Physics D: Applied Physics*, vol. 50, p. 114003, 2017.

[43] F. P. Sainct, D. A. Lacoste, M. J. Kirkpatrick, E. Odic, and C. O. Laux, "Temporal evolution of temperature and OH density produced by nanosecond repetitively pulsed discharges in water vapour at atmospheric pressure," *Journal of Physics D: Applied Physics*, vol. 47, p. 075204, 2014.

[44] N. Srivastava and C. Wang, "Effects of water addition on OH radical generation and plasma properties in an atmospheric argon microwave plasma jet," *Journal of Applied Physics*, vol. 110, p. 053304, 2011.

[45] X. Pei, Y. Lu, S. Wu, Q. Xiong, and X. Lu, "A study on the temporally and spatially resolved OH radical distribution of a room-temperature atmospheric-pressure plasma jet by laser-induced fluorescence imaging," *Plasma Sources Science and Technology*, vol. 22, p. 025023, 2013.

[46] S. Yonemori, Y. Nakagawa, R. Ono, and T. Oda, "Measurement of OH density and air–helium mixture ratio in an atmospheric-pressure helium plasma jet," *Journal of Physics D: Applied Physics*, vol. 45, p. 225202, 2012.

[47] J. Voráč, A. Obrusník, V. Procházka, P. Dvořák, and M. Talába, "Corrigendum: Spatially resolved measurement of hydroxyl radical (OH) concentration in argon RF plasma jet by planar laser-induced fluorescence (2014Plasma Sources Sci. Technol. 23 025011)," *Plasma Sources Science and Technology*, vol. 25, p. 059502, 2016.

[48] L. M. Martini, G. Dilecce, G. Guella, A. Maranzana, G. Tonachini, and P. Tosi, "Oxidation of CH_4 by CO_2 in a dielectric barrier discharge," *Chemical Physics Letters*, vol. 593, pp. 55–60, 2014.

[49] G. Dilecce and S. D. Benedictis, "Laser diagnostics of high-pressure discharges: laser induced fluorescence detection of OH in He/Ar–H_2O dielectric barrier discharges," *Plasma Physics and Controlled Fusion*, vol. 53, p. 124006, 2011.

[50] G. Dilecce, P. F. Ambrico, M. Simek, and S. D. Benedictis, "LIF diagnostics of hydroxyl radical in atmospheric pressure He-H_2O dielectric barrier discharges," *Chemical Physics*, vol. 398, pp. 142–147, 2012.

[51] Y. Teramoto, H.-H. Kim, A. Ogata, and N. Negishi, "Measurement of OH ($X^2\Sigma$) in immediate vicinity of dielectric surface under pulsed dielectric barrier discharge at atmospheric pressure using two geometries of laser-induced fluorescence," *The Journal of Applied Physics*, vol. 115, p. 133302, 2014.

[52] M. Ceppelli, L. M. Martini, G. Dilecce, M. Scotoni, and P. Tosi, "Non-thermal rate constants of quenching and vibrational relaxation in the OH ($A^2\Sigma^+, \nu' = 0, 1$) manifold," *Plasma Sources Science and Technology*, vol. 29, p. 065019, 2020.

[53] G. Dilecce, L. M. Martini, P. Tosi, M. Scotoni, and S. D. Benedictis, "Laser induced fluorescence in atmospheric pressure discharges," *Plasma Sources Science and Technology*, vol. 24, p. 034007, 2015.

[54] J. Luque and D. R. Crosley, "LIFBASE: Database and Spectral Simulation Program," 1999. SRI International Report MP 99-009.

[55] R. J. Fallon, I. Tobias, and J. T. Vanderslice, "Potential Energy Curves for OH," *The Journal of Chemical Physics*, vol. 34, pp. 167–168, 1961.

[56] L. M. Martini, S. Lovascio, G. Dilecce, and P. Tosi, "Time-Resolved CO_2 Dissociation in a Nanosecond Pulsed Discharge," *Plasma Chem Plasma Process*, vol. 38, pp. 707–718, 2018.

[57] J. W. Daily, "Use of rate equations to describe laser excitation in flames," *Applied Optics*, vol. 16, p. 2322, 1977.

[58] T. Verreycken, R. Mensink, R. van der Horst, N. Sadeghi, and P. J. Bruggeman, "Absolute OH density measurements in the effluent of a cold atmospheric-pressure Ar–H_2O RF plasma jet in air," *Plasma Sources Science and Technology*, vol. 22, p. 055014, 2013.

[59] M. J. Dunn and A. R. Masri, "A comprehensive model for the quantification of linear and nonlinear regime laser-induced fluorescence of OH under $A^2\Sigma^+ \leftarrow^2 \Pi(1,0)$ excitation," *Applied Physics B*, vol. 101, pp. 445–463, 2010.

[60] L. M. Martini, N. Gatti, G. Dilecce, M. Scotoni, and P. Tosi, "Laser induced fluorescence in nanosecond repetitively pulsed discharges for CO_2 conversion," *Plasma Physics and Controlled Fusion*, vol. 60, p. 014016, 2018.

[61] D. Riès, G. Dilecce, E. Robert, P. F. Ambrico, S. Dozias, and J.-M. Pouvesle, "LIF and fast imaging plasma jet characterization relevant for NTP biomedical applications," *Journal of Physics D: Applied Physics*, vol. 47, p. 275401, 2014.

[62] C. Montesano, S. Quercetti, L. M. Martini, G. Dilecce, and P. Tosi, "The effect of different pulse patterns on the plasma reduction of CO_2 for a nanosecond discharge," *Journal of CO_2 Utilization*, vol. 39, p. 101157, 2020.

[63] M. Scapinello, L. M. Martini, G. Dilecce, and P. Tosi, "Conversion of CH_4/CO_2 by a nanosecond repetitively pulsed discharge," *Journal of Physics D: Applied Physics*, vol. 49, p. 075602, 2016.

[64] S. Heijkers, L. M. Martini, G. Dilecce, P. Tosi, and A. Bogaerts, "Nanosecond Pulsed Discharge for CO_2 Conversion: Kinetic Modeling To Elucidate the Chemistry and Improve the Performance," *The Journal of Physical Chemistry C*, vol. 123, pp. 12104–12116, 2019.

[65] S. Sepka, Y.-K. Chen, J. Marschall, and R. A. Copeland, "Experimental Investigation of Surface Reactions in Carbon Monoxide and Oxygen Mixtures," *Journal of Thermophysics and Heat Transfer*, vol. 14, pp. 45–52, 2000.

[66] A. S. Morillo-Candas, C. Drag, J.-P. Booth, T. C. Dias, V. Guerra, and O. Guaitella, "Oxygen atom kinetics in CO_2 plasmas ignited in a DC glow discharge," *Plasma Sources Science and Technology*, vol. 28, p. 075010, 2019.

[67] G. Dilecce, "Optical spectroscopy diagnostics of discharges at atmospheric pressure," *Plasma Sources Science and Technology*, vol. 23, p. 015011, 2014.

[68] J. Brown, *Rotational spectroscopy of diatomic molecules*. Cambridge New York: Cambridge University Press, 2003.

[69] G. Herzberg, *Molecular spectra and molecular structure, I spectra of diatomic molecules*. New York: Van Nostrand, 1950.

[70] R. A. Copeland, M. J. Dyer, and D. R. Crosley, "Rotational-level-dependent quenching of $A^2\Sigma^+$ OH and OD," *The Journal of Chemical Physics*, vol. 82, pp. 4022–4032, 1985.

[71] R. A. Copeland, M. L. Wise, and D. R. Crosley, "Vibrational energy transfer and quenching of hydroxyl($A^2\Sigma^+$,$\nu = 1$)," *The Journal of Chemical Physics*, vol. 92, pp. 5710–5715, 1988.

[72] A. Jörg, A. D. Esposti, and H. Werner, "Quantum scattering study of rotational energy transfer in OH($A^2\Sigma^+$, $\nu' = 0$) in collisions with He($1S$)," *The Journal of Chemical Physics*, vol. 93, pp. 8757–8763, 1990.

[73] P. Bruggeman, F. Iza, P. Guns, D. Lauwers, M. G. Kong, Y. A. Gonzalvo, C. Leys, and D. C. Schram, "Electronic quenching of OH(A) by water in atmospheric pressure plasmas and its influence on the gas temperature determination by OH(A−X) emission," *Plasma Sources Science and Technology*, vol. 19, p. 015016, 2010.

[74] L. R. Williams and D. R. Crosley, "Collisional vibrational energy transfer of OH ($A^2\Sigma^+$, ν'=1)," *The Journal of Chemical Physics*, vol. 104, pp. 6507–6514, 1996.

[75] I. J. Wysong, J. B. Jeffries, and D. R. Crosley, "Quenching of $A^2\Sigma^+$ OH at 300 K by several colliders," *The Journal of Chemical Physics*, vol. 92, pp. 5218–5222, 1990.

[76] M. Tamura, P. A. Berg, J. E. Harrington, J. Luque, J. B. Jeffries, G. P. Smith, and D. R. Crosley, "Collisional Quenching of CH(A), OH(A), and NO(A) in Low Pressure Hydrocarbon Flames," *Combustion and Flame*, vol. 114, pp. 502–514, 1998.

[77] G. Herzberg, *Molecular spectra and molecular structure, III electronic spectra and electronic structure of polyatomic molecules*. Malabar, Fla: R.E. Krieger Pub. Co, 1991.

[78] Y. L. Yung and W. B. DeMore, *Photochemistry of Planetary Atmospheres*. Oxford University Press, 1998.

[79] H. Okabe, *Photochemistry of small molecules*. New York: Wiley, 1978.

[80] K. Gericke, S. Klee, F. J. Comes, and R. N. Dixon, "Dynamics of H_2O_2 photodissociation: OH product state and momentum distribution characterized by sub-Doppler and polarization spectroscopy," *The Journal of Chemical Physics*, vol. 85, pp. 4463–4479, 1986.

[81] S. C. Farantos and A. Vegiri, "Quantum mechanical study of rotationally inelastic collisions on a helium + hydroxyl ($A^2\Sigma^+$) excited potential energy surface," *The Journal of Physical Chemistry*, vol. 92, pp. 2719–2723, 1988.

[82] K. L. Steffens and D. R. Crosley, "Vibrational energy transfer in OH $A^2\Sigma^+$ between 195 and 295 K," *The Journal of Chemical Physics*, vol. 112, pp. 9427–9432, 2000.

[83] D. E. Heard and D. A. Henderson, "Quenching of OH ($A^2\Sigma^+$,$\nu' = 0$) by several collision partners between 200 and 344 K. Cross-section measurements and model comparisons," *Physical Chemistry Chemical Physics*, vol. 2, pp. 67–72, 2000.

[84] A. E. Bailey, D. E. Heard, P. H. Paul, and M. J. Pilling, "Collisional quenching of OH ($A^2\Sigma^+$, $\nu' = 0$) by N_2, O_2 and CO_2 between 204 and 294 K. Implications for atmospheric measurements of OH by laser−induced fluorescence," *Journal of the Chemical Society, Faraday Transactions*, vol. 93, pp. 2915–2920, 1997.

[85] P. W. Fairchild, G. P. Smith, and D. R. Crosley, "Collisional quenching of A $^2\Sigma^+$ OH at elevated temperatures," *The Journal of Chemical Physics*, vol. 79, pp. 1795–1807, 1983.

[86] P. H. Paul, "Vibrational Energy Transfer and Quenching of OH $A^2\Sigma^+$ ($\nu' = 1$) Measured at High Temperatures in a Shock Tube," *Journal of Physical Chemistry*, vol. 99, pp. 8472–8476, 1995.

[87] J. Yardley, *Introduction to molecular energy transfer*. New York: Academic Press, 1980.

[88] R. Snoeckx, A. Ozkan, F. Reniers, and A. Bogaerts, "The Quest for Value-Added Products from Carbon Dioxide and Water in a Dielectric Barrier Discharge: A Chemical Kinetics Study," *ChemSusChem*, vol. 10, pp. 409–424, 2017.

[89] L. Guo, X. Ma, Y. Xia, X. Xiang, and X. Wu, "A novel method of production of ethanol by carbon dioxide with steam," *Fuel*, vol. 158, pp. 843–847, 2015.

[90] G. Chen, T. Silva, V. Georgieva, T. Godfroid, N. Britun, R. Snyders, and M. P. Delplancke-Ogletree, "Simultaneous dissociation of CO_2 and H_2O to syngas in a surface-wave microwave discharge," *International Journal of Hydrogen Energy*, vol. 40, pp. 3789–3796, 2015.

[91] G. Chen, T. Godfroid, N. Britun, V. Georgieva, M.-P. Delplancke-Ogletree, and R. Snyders, "Plasma-catalytic conversion of CO_2 and CO_2/H_2O in a surface-wave sustained microwave discharge," *Applied Catalysis B: Environmental*, vol. 214, pp. 114–125, 2017.

[92] D. L. Baulch, C. J. Cobos, R. A. Cox, C. Esser, P. Frank, T. Just, J. A. Kerr, M. J. Pilling, J. Troe, R. W. Walker, and J. Warnatz, "Evaluated Kinetic Data for Combustion Modelling," *Journal of Physical and Chemical Reference Data*, vol. 21, pp. 411–734, 1992.

[93] M. A. Damen, L. M. Martini, and R. Engeln, "Vibrational quenching by water in a CO_2 glow discharge measured using quantum cascade laser absorption spectroscopy," *Plasma Sources Science and Technology*, vol. 29, p. 095017, 2020.

[94] M.Budde, L. M. Martini, M. Ceppelli, S. Quercetti, and R. Engeln, "Absolute OH density measurements in a CO_2-H_2O glow discharge by laser-induced fluorescence spectroscopy," *submitted to Plasma Sources Science and Technology*, 2022.

[95] M. A. Damen, D. A. C. M. Hage, A. W. van de Steeg, L. M. Martini, and R. Engeln, "Absolute CO number densities measured using TALIF in a non-thermal plasma environment," *Plasma Sources Science and Technology*, vol. 28, p. 115006, 2019.

[96] B. L. M. Klarenaar, A. S. Morillo-Candas, M. Grofulović, M. C. M. van de Sanden, R. Engeln, and O. Guaitella, "Excitation and relaxation of the asymmetric stretch mode of CO_2 in a pulsed glow discharge," *Plasma Sources Science and Technology*, vol. 28, p. 035011, 2019.

[97] C. Montesano, M. Faedda, L. M. Martini, G. Dilecce, and P. Tosi, "CH_4 reforming with CO_2 in a nanosecond pulsed discharge. The importance of the pulse sequence," *Journal of CO_2 Utilization*, vol. 49, p. 101556, 2021.

[98] R. W. B. Pearse, *The identification of molecular spectra*. London New York: Chapman and Hall Wiley, 1976.

[99] P. H. Krupenie, "The band spectrum of carbon monoxide," tech. rep., 1966.

[100] M. A. Johnson and J. Rostas, "Vibronic structure of the CO_2^+ ion: reinvestigation of the antisymmetric stretch vibration in the $\tilde{X}$, $\tilde{A}$, and $\tilde{B}$ states," *Molecular Physics*, vol. 85, pp. 839–868, 1995.

[101] D. Gauyacq, C. Larcher, and J. Rostas, "The emission spectrum of the CO_2^+ ion: rovibronic analysis of the band system," *Canadian Journal of Physics*, vol. 57, pp. 1634–1649, 1979.

[102] A. Kramida, Yu. Ralchenko, J. Reader, and and NIST ASD Team. NIST Atomic Spectra Database (ver. 5.9), [Online]. Available: `https://physics.nist.gov/asd` [2016, January 31]. National Institute of Standards and Technology, Gaithersburg, MD., 2021.

[103] M. L. da Silva and M. Dudeck, "Arrays of radiative transition probabilities for CO_2-N_2 plasmas," *Journal of Quantitative Spectroscopy & Radiative Transfer*, vol. 102, pp. 348–386, 2006.

[104] G. Raposo, A. W. van de Steeg, E. R. Mercer, C. F. A. M. van Deursen, H. J. L. Hendrickx, W. A. Bongers, G. J. van Rooij, M. C. M. van de Sanden, and F. J. J. Peeters, "Flame bands: CO + O chemiluminescence as a measure of gas temperature," *Journal of Physics D: Applied Physics*, vol. 54, p. 374005, 2021.

[105] H. P. Broida and A. G. Gaydon, "The luminous reaction between carbon monoxide and atomic oxygen," *Transactions of the Faraday Society*, vol. 49, p. 1190, 1953.

[106] A. G. Gaydon, *The Spectroscopy of Flames*. Springer Netherlands, 1974.

[107] C. Rond, A. Bultel, P. Boubert, and B. G. Chéron, "Spectroscopic measurements of nonequilibrium CO_2 plasma in RF torch," *Chemical Physics*, vol. 354, pp. 16–26, 2008.

[108] J. Park, I. Henins, H. W. Herrmann, and G. S. Selwyn, "Neutral bremsstrahlung measurement in an atmospheric-pressure radio frequency discharge," *Physics of Plasmas*, vol. 7, pp. 3141–3144, 2000.

[109] E. Iordanova, N. de Vries, M. Guillemier, and J. J. A. M. van der Mullen, "Absolute measurements of the continuum radiation to determine the electron density in a microwave-induced argon plasma," *Journal of Physics D: Applied Physics*, vol. 41, p. 015208, 2008.

[110] S. Park, W. Choe, S. Y. Moon, and J. Park, "Electron density and temperature measurement by continuum radiation emitted from weakly ionized atmospheric pressure plasmas," *Applied Physics Letters*, vol. 104, p. 084103, 2014.

[111] R. Bazinette, J. Paillol, and F. Massines, "Optical emission spectroscopy of glow, Townsend-like and radiofrequency DBDs in an Ar/NH_3 mixture," *Plasma Sources Science and Technology*, vol. 24, p. 055021, 2015.

[112] D. Z. Pai, S. Stauss, and K. Terashima, "Field-emitting Townsend regime of surface dielectric barrier discharges emerging at high pressure up to supercritical conditions," *Plasma Sources Science and Technology*, vol. 24, p. 025021, 2015.

[113] A. Y. Nikiforov, E.-R. Ionita, G. Dinescu, and C. Leys, "Characterization of a planar 8 mm atmospheric pressure wide radiofrequency plasma source by spectroscopy techniques," *Plasma Physics and Controlled Fusion*, vol. 58, p. 014013, 2016.

[114] Z. Navrátil, T. Morávek, J. Ráheľ, J. Čech, O. Lalinský, and D. Trunec, "Diagnostics of pre-breakdown light emission in a helium coplanar barrier discharge: the presence of neutral bremsstrahlung," *Plasma Sources Science and Technology*, vol. 26, p. 055025, 2017.

[115] R. N. Dixon, "The carbon monoxide flame bands," *Proceedings of the Royal Society of London. Series A. Mathematical and Physical Sciences*, vol. 275, pp. 431–446, 1963.

[116] E. Carbone, F. D'Isa, A. Hecimovic, and U. Fantz, "Analysis of the C_2 ($d^3\Pi_g - a^3\pi$) Swan bands as a thermometric probe in CO_2 microwave plasmas," *Plasma Sources Science and Technology*, vol. 29, p. 055003, 2020.

[117] H. Wallaart, B. Piar, M.-Y. Perrin, and J.-P. Martin, "C_2 formation in vibrationally excited CO," *Chemical Physics Letters*, vol. 246, pp. 587–593, 1995.

[118] G. Cristoforetti, A. D. Giacomo, M. Dell'Aglio, S. Legnaioli, E. Tognoni, V. Palleschi, and N. Omenetto, "Local Thermodynamic Equilibrium in Laser-Induced Breakdown Spectroscopy: Beyond the McWhirter criterion," *Spectrochimica Acta Part B*, vol. 65, pp. 86–95, 2010.

[119] J. van der Mullen, "Excitation equilibria in plasmas; a classification," *Physics Reports*, vol. 191, pp. 109–220, 1990.

[120] P. J. Bruggeman, N. Sadeghi, D. C. Schram, and V. Linss, "Gas temperature determination from rotational lines in non−equilibrium plasmas: a review," *Plasma Sources Science and Technology*, vol. 23, p. 023001, 2014.

[121] S. A. Astashkevich, M. Käning, E. Käning, N. V. Kokina, B. P. Lavrov, A. Ohl, and J. Röpcke, "Radiative characteristics of $3p\ \Sigma, \Pi$; $3d\ \Pi^-, \Delta^-$ states of H_2 and determination of gas temperature of low pressure hydrogen containing plasmas," *Journal of Quantitative Spectroscopy and Radiative Transfer*, vol. 56, pp. 725–751, 1996.

[122] R. Schinke, *Photodissociation Dynamics: Spectroscopyand Fragmentation of Small Polyatomic Molecules*. Cambridge University Press, 1993.

[123] X. Tan, "Diatomic, a spectral simulation program for diatomic molecules on windows platforms," tech. rep., 2006.

[124] F. R. Gilmore, R. R. Laher, and P. J. Espy, "Franck–Condon Factors, r-Centroids, Electronic Transition Moments, and Einstein Coefficients for Many Nitrogen and Oxygen Band Systems," *Journal of Physical and Chemical Reference Data*, vol. 21, pp. 1005–1107, 1992.

[125] S. D. Benedictis and G. Dilecce, "Vibrational relaxation of N_2(C, ν) state in N_2 pulsed rf discharge: electron impact and pooling reactions," *Chemical Physics*, vol. 192, pp. 149–162, 1995.

[126] L. G. Piper, "State-to-state $N_2(A^3\Sigma_u^+)$ energy-pooling reactions. I. The formation of $N_2(C^3\Pi_u)$ and the Herman infrared system," *The Journal of Chemical Physics*, vol. 88, pp. 231–239, 1988.

[127] Y. Akishev, M. Grushin, V. Karalnik, A. Petryakov, and N. Trushkin, "On basic processes sustaining constricted glow discharge in longitudinal N_2 flow at atmospheric pressure," *Journal of Physics D: Applied Physics*, vol. 43, p. 215202, 2010.

[128] G. Dilecce, P. F. Ambrico, G. Scarduelli, P. Tosi, and S. D. Benedictis, "$CN(B^2\Sigma^+)$ formation and emission in a N_2–CH_4 atmospheric pressure dielectric barrier discharge," *Plasma Sources Science and Technology*, vol. 18, p. 015010, 2009.

[129] H. R. Griem, M. Baranger, A. C. Kolb, and G. Oertel, "Stark Broadening of Neutral Helium Lines in a Plasma," *Physical Review*, vol. 125, pp. 177–195, 1962.

[130] H. R. Griem, "Stark Broadening of Isolated Spectral Lines from Heavy Elements in a Plasma," *Physical Review*, vol. 128, pp. 515–523, 1962.

[131] N. Konjević, "Plasma broadening and shifting of non-hydrogenic spectral lines: present status and applications," *Physics Reports*, vol. 316, pp. 339–401, 1999.

[132] F. XU, F. DING, X. CHEN, L. WANG, J. XU, Z. HU, H. MAO, G. LUO, Z. YANG, J. CHEN, and K. LI, "Electron density calculation based on Stark broadening of D Balmer line from detached plasma in EAST tungsten divertor," *Plasma Science and Technology*, vol. 20, p. 105102, 2018.

[133] R. Konjević and N. Konjević, "On the use of non-hydrogenic spectral line profiles for electron density diagnostics of inductively coupled plasmas," *Spectrochimica Acta Part B: Atomic Spectroscopy*, vol. 52, pp. 2077–2084, 1997.

[134] Griem, *Spectral Line Broadening by Plasmas*. Elsevier, 1974.

[135] N. Alonizan, R. Qindeel, N. B. Nessib, S. Sahal-Bréchot, and M. S. Dimitrijević, "Stark Broadening Parameters for Neutral Oxygen Spectral Lines," *Journal of Astrophysics and Astronomy*, vol. 36, 2015.

[136] S. Djeniže, A. Srećković, and S. Bukvić, "The C I 247.8561 nm Resonance Line Stark Broadening Parameters," *Zeitschrift für Naturforschung A*, vol. 61, pp. 91–94, 2006.

[137] H.-J. Kunze, *Introduction to Plasma Spectroscopy*. Springer Berlin Heidelberg, 2009.

[138] N. Alonizan, R. Qindeel, and N. B. Nessib, "Atomic Structure Calculations for Neutral Oxygen," *International Journal of Spectroscopy*, vol. 2016, pp. 1–7, 2016.

[139] V. Milosavljević, A. R. Ellingboe, and S. Daniels, "Influence of plasma chemistry on oxygen triplets," *The European Physical Journal D*, vol. 64, pp. 437–445, 2011.

[140] X.-M. Zhu and Y.-K. Pu, "Optical emission spectroscopy in low-temperature plasmas containing argon and nitrogen: determination of the electron temperature and density by the line-ratio method," *Journal of Physics D: Applied Physics*, vol. 43, p. 403001, 2010.

[141] H. Griem, *Principles of Plasma Spectroscopy*. Cambridge: Cambridge University Press, 2005.

[142] U. Fantz, "Basics of plasma spectroscopy," *Plasma Sources Science and Technology*, vol. 15, pp. S137–S147, 2006.

[143] M. Ceppelli, T. P. W. Salden, L. M. Martini, G. Dilecce, and P. Tosi, "Time-resolved optical emission spectroscopy in CO_2 nanosecond pulsed discharges," *Plasma Sources Science and Technology*, vol. 30, p. 115010, 2021.

[144] A. Kramida, Yu. Ralchenko, J. Reader, and and NIST ASD Team. NIST Atomic Spectra Database (ver. 5.8) https://physics.nist.gov/asd (Gaithersburg, MD National Institute of Standards and Technology) `https://physics.nist.gov/PhysRefData/ASD/LIBS/libs-form.html`, 2020.

[145] H. W. Drawin, "Validity conditions for local thermodynamic equilibrium," *Zeitschrift für Physik*, vol. 228, pp. 99–119, 1969.

[146] R. Wilson, "The spectroscopy on non-thermal plasmas," *Journal of Quantitative Spectroscopy and Radiative Transfer*, vol. 2, pp. 477–490, 1962.

[147] R. McWhirter, *Plasma Diagnostic Techniques*. in: R.H. Huddlestone, S.L. Leonard (Eds.). Academic Press, New York, chapter 5, 1965.

[148] R. M. van der Horst, T. Verreycken, E. M. van Veldhuizen, and P. J. Bruggeman, "Time-resolved optical emission spectroscopy of nanosecond pulsed discharges in atmospheric-pressure N_2 and N_2/H_2O mixtures," *Journal of Physics D: Applied Physics*, vol. 45, p. 345201, 2012.

[149] V. Laporta, J. Tennyson, and R. Celiberto, "Calculated low-energy electron-impact vibrational excitation cross sections for CO_2 molecule," *Plasma Sources Science and Technology*, vol. 25, p. 06LT02, 2016.

[150] A. A. Viggiano, A. Ehlerding, F. Hellberg, R. D. Thomas, V. Zhaunerchyk, W. D. Geppert, H. Montaigne, M. Larsson, M. Kaminska, and F. Österdahl, "Rate constants and branching ratios for the dissociative recombination of CO_2^+," *The Journal of Chemical Physics*, vol. 122, p. 226101, 2005.